Quantitative multi-proxy climate reconstruction for MIS 3 in Central Europe based on precisely dated speleothems from Bleßberg Cave, Germany

Dissertation

for attaining the academic degree of
„Doctor rerum naturalium“ (Dr. rer. nat.)

of the Departments
08 – Physics, Mathematics, and Computer Science,
09 – Chemistry, Pharmaceutics and Geosciences,
10 – Biology,
and University Medicine
of the Johannes Gutenberg University Mainz

by

Jennifer Klose

born 02.05.1992
in Hannover

Johannes Gutenberg University Mainz with the Max Planck Graduate Center
prepared at the Institute of Geosciences
Mainz, May 2024

Faculty director: Prof. Dr. Eva Rentschler

1st supervisor:

2nd supervisor:

Date of oral examination: 02.07.2024

Sworn declaration

I hereby declare that I wrote the dissertation submitted without any unauthorized external assistance and used only sources acknowledged in the work. All textual passages which are appropriated verbatim or paraphrased from published and unpublished texts as well as all information obtained from oral sources are duly indicated and listed in accordance with bibliographical rules. In carrying out this research, I complied with the rules of standard scientific practice as formulated in the statutes of Johannes Gutenberg University Mainz to insure standard scientific practice.

……

Jennifer Klose

Mainz, May 2024

Zusammenfassung

Speläotheme zeichnen sich als sensitive Klimaarchive aus und haben sich in letzten Jahrzehnten als solche etabliert. Sie haben das Potential wertvolle Informationen über das Paläoklima kontinuierlich aufzuzeichnen und können mit den Uran-Ungleichgewichtsmethoden präzise datiert werden. Das Berechnen von unabhängigen Altersmodellen kombiniert mit Analysen verschiedener Klimaproxys, wie $\delta^{18}O$ und $\delta^{13}C$, Spurenelementen oder Tropfwassereinschlüssen ermöglicht es, hochaufgelöste Paläoklimarekonstruktionen zu erstellen.

Dansgaard-Oeschger (DO)-Ereignisse sind kurzfristige Klimaschwankungen über einige hunderte oder wenige tausende Jahre, welche vor allem während der marinen Isotopenstufe 3 (MIS 3, ca. 60 - 30 ka BP) auftraten. Obwohl erste Beweise für die Ereignisse in grönländischen Eisbohrkernen entdeckt wurden, sind sie mittlerweile global nachweisbar. DO-Ereignisse zeichnen sich durch eine rasche Erwärmung, gefolgt von gradueller Abkühlung aus, während das MIS 3 generell als eine kältere Periode definiert ist. Daher wurde die Tatsache, dass bisher kaum zentraleuropäische Speläotheme aus dem MIS 3 gefunden wurden, mit zu kaltem oder trockenem Klima begründet. Im Rahmen dieser Arbeit wurden drei MIS 3 Speläotheme aus der Bleßberg Höhle in Deutschland detailliert untersucht. Durch die Kombination von lösungs-basierter und in-situ Laserablation $^{230}Th/U$-Datierung konnte das komplexe Wachstum der Proben präzise aufgeschlüsselt werden.

Es konnten mehrere Wachstumsepisoden im MIS 3 identifiziert werden, welche primär zeitgleich zu DO-Ereignissen in Grönland auftraten. Die Wachstumsphasen wurde daher als eigenständiger Proxy für günstige Klimabedingungen für Speläothemwachstum etabliert, d.h. Perioden mit ausreichender Boden- und Vegetationsbedeckung über der Höhle und der Möglichkeit das Tropfwasser in die Höhle gelangt. Darüber hinaus wurde eine multi-Proxy Analyse durchgeführt mit dem Ziel möglichst vielfältige Informationen über das MIS 3 in Mitteleuropa zu erhalten. Ein langfristiger Trend zeigt die generelle Verschlechterung des Klimas mit Fortschreiten des MIS 3 auf. Eine besonders warme und kontinuierliche Wachstumsphase trat zeitgleich mit DO14 auf. Außerdem wurden zwei kurzzeitige Kälteereignisse innerhalb des DO14 aufgezeichnet, welches die hohe Sensitivität der Speläotheme aus der Bleßberg Höhle verdeutlicht.

Weitere kurzzeitige Klimaereignisse wurden während des spätglazialen Teils der Speläothem-Proben (ca. 14,5 - 1,7 ka BP) aufgezeichnet und ein hochauflösender multi-Proxy-Datensatz, der das Holozän (11,7 ka BP - rezent) bis 0,6 ka BP abdeckt, wurde erstellt.

Abstract

Speleothems are sensitive paleoclimate archives and have been established as those during the past decades. They have the potential to continuously record valuable information about the past climate and can be precisely dated using U-series disequilibrium methods. The calculation of independent age-depth models and the analyses of various climate proxies, such as $\delta^{18}O$ and $\delta^{13}C$, trace elements or fluid inclusions, allow to constrain high-resolution multi-proxy paleoclimate records.

Dansgaard-Oeschger (DO) events are centennial- to millennial-scale climate oscillations during Marine Isotope Stage 3 (MIS 3, ca. 60 – 30 ka BP). While first discovered in Greenland ice cores evidence of these climate events has been observed on a global scale. DO events are characterised by a rapid warming followed by a gradual cooling, while MIS 3 in general is considered a rather cold period. Therefore, the fact that MIS 3 speleothem records from Central Europe are very limited has been attributed to too cold and dry conditions. Three flowstones from Bleßberg Cave, Germany which grew during MIS 3 were intensively studied during this thesis. A combined approach of solution-based (sampled by handheld drilling and micromilling) and in-situ Laser Ablation $^{230}Th/U$-dating has been used to create precise age models for samples with a complicated growth structure and growth phases smaller than 2 mm.

The samples revealed several episodes of growth during MIS 3 primarily coinciding with DO events. The growth phases were established as its own proxy for favourable conditions for speleothem growth, i.e., periods with sufficient soil and vegetation cover above the cave and liquid water reaching the cave. In addition, a multi-proxy approach was used to gain more information about MIS 3 in Central Europe, which established the climate to deteriorate with ongoing progression of MIS 3. A particularly warm and prolonged growth phase coincided with DO14. Two short-term cold events were recorded within the event, highlighting the high sensitivity of the Bleßberg Cave speleothems.

Several more centennial- to millennial-scale climate events were recorded during the late Glacial part of the speleothem samples (ca. 14.5 – 11.7 ka BP) and a high-resolution multi-proxy record covering the Holocene (11.7 ka BP – recent) until 0.6 ka BP was established.

Table of Contents

List of Figures

Chapter 2: Basics

Chapter 3: Manuscript I

Chapter 3: Supplementary Material for Manuscript I

Chapter 4: Manuscript II

Chapter 4: Supplementary Material for Manuscript II

Chapter 5: Manuscript III

Chapter 5: Supplementary Material for Manuscript III

Chapter 6: Manuscript IV

Chapter 6: Supplementary Material for Manuscript IV

Chapter 7: Conclusion & Outlook

List of Tables

Chapter 3

Chapter 4

Chapter 5

Chapter 6

Chapter 6

Chapter 1: Introduction

Over the course of the past decades, speleothem became well-established as valuable terrestrial archives for paleoclimate reconstructions. They occur worldwide, limited by the availability of karst regions, and can provide extremely well-preserved long and continuous climate records (Fairchild and Baker, 2012). The cave surrounding can be assumed to be a mostly closed and stable system enabling speleothems to primarily record and preserve high-resolution climate signals, such as precipitation or temperature. The most commonly used proxies for that purpose are the stable isotopes of oxygen and carbon (expressed as $\delta^{18}O$ and $\delta^{13}C$) (e.g. Fairchild et al., 2006; Lachniet, 2009; McDermott, 2004) or various trace elements (e.g. Fairchild et al., 2000; Fairchild and Treble, 2009). In addition, one of the main advantages of speleothems in comparison to other archives, such as tree rings or ice cores, is their potential to be dated very precisely and accurately using U-series disequilibrium methods (Richards and Dorale, 2003; Scholz and Hoffmann, 2008).

The $^{230}Th/U$-dating method can be used to date speleothems with unmatchable precision in the range of 600 ka (Richards and Dorale, 2003; Scholz and Hoffmann, 2008). The method relies on the decay of the radioactive U isotopes ^{238}U and ^{234}U to ^{230}Th and is based on the assumption that no initial ^{230}Th ($^{230}Th_i$) is present during the time of speleothem formation (Richards and Dorale, 2003). While U is water soluble and gets transported in the cave with the water infiltrating and finally leading to speleothem formation, Th is highly particle reactive and does not get transported with the water and is ultimately not incorporated in the speleothem's calcite.

In recent years, using multi-proxy approaches to gain a better understanding of past climates has become a more and more common practice. Instead of relying solely on traditional proxies such as stable isotopes of oxygen and carbon or trace elements, different methods are combined to provide more in-depth information. These methods include, for instance, the analysis of water isotopes of fluid inclusions trapped in speleothem's calcite lattice, studies of calcium isotopes to determine precipitation levels at the cave site or examining lignin oxidation products to gain a better insight into the vegetation type and amount above the cave.

In the study for this thesis, a multi-proxy approach was applied to three flowstones from Bleßberg Cave, Germany to investigate Marine Isotope Stage (MIS) 3 in Central Europe. MIS 3 (ca. 60 – 30 ka BP) was characterised by rapid climate oscillations known

as Dansgaard-Oeschger (DO) events (Dansgaard et al., 1993). These events show a rapid increase in temperature followed by a gradual cooling and were first discovered in Greenland ice cores. In those, they are referred to as warm Greenland interstadials (GI) with local temperature increases up to 16.5 °C (± 3 °C) (Kindler et al., 2014) interrupted by cool Greenland stadials (GS) (Dansgaard et al., 1993; Rasmussen et al., 2014). Evidence for these events can be found worldwide with an emphasis on the northern hemisphere (Adolphi et al., 2018; Erhardt et al., 2019) and especially regions dominated by monsoon patterns (Chen et al., 2016; Cheng et al., 2013; Cheng et al., 2016; Kathayat et al., 2016; Wang et al., 2001). In 2021 Corrick et al. (2020) compiled a study focused on speleothem records from the Mediterranean, the Asian Summer Monsoon region, and the South American Monsoon region showing evidence of DO events worldwide and concluded a global synchrony within a century of the events.

The origin and initial trigger of DO events is still a matter of ongoing discussion. Nevertheless, it is believed that these events have their origin in the North Atlantic region. Due to the close proximity to this area, Central Europe provides an excellent study area for observing and studying the timing and progression of DO events. So far, most of the MIS 3 speleothem records from Europe either stem from more southern (Constantin et al., 2007; Genty et al., 2003; Hodge et al., 2008; Pérez-Mejías et al., 2019) and often also more coastal (Budsky et al., 2019b; Denniston et al., 2018; Kudielka et al., 2019; Stoll et al., 2015) or alpine regions (e.g. Moseley et al., 2020; Moseley et al., 2014), where glacier meltwater enabled speleothem growth (Spötl and Mangini, 2002). Therefore, it was previously believed that the Central European region was too cold and/or dry to enable the growth of speleothems. However, the Bleßberg flowstones disprove this assumption and provide new information about MIS 3 in Central Europe. The three more centrally located European speleothem records in existence stem from north-eastern France (Pons-Branchu et al., 2010), eastern Germany (Weber et al., 2018) and Belgium (Peral et al., 2024), but the records either do not provide proxy data, only cover a shorter period of MIS 3 or continuous growth over large parts of MIS3 is assumed but relies on a questionable age model.

In order to provide a reliable age model for the Bleßberg flowstones the combination of several methods was necessary due to the more complicated growth structure of the samples. Flowstones often show short and episodic growth phases, interrupted by growth stops, which complicates the sampling process which, as standard procedures, utilises a hand-held drill or a band saw. Using those standard techniques the prevention of detrital

material may not always be possible. Detrital material accumulates on the surface of the speleothem during growth stops and is covered up and incorporated into the speleothem when the growth of the sample is resumed. This detrital material contains a high concentration of detrital Th, which is normally absent in the speleothem and only a product of the radioactive decay of U. Therefore, if not avoided in the sampling process one of the basic assumptions of the ^{230}Th/U-dating method is not assured and the ^{230}Th/U-ages and resulting age models unreliable and unprecise. During the first part of this thesis (Manuscript I, Chapter 3) a better approach for the dating process of flowstone samples was developed. A combination of hand-held drilling, micromilling and in-situ Laser Ablation (LA) resulted in a few very precise ^{230}Th/U-ages, obtained by standard approaches when practicable, and a very high quantity of LA ^{230}Th/U-ages with a much higher age uncertainty but also very high spatial resolution. This ^{230}Th/U-ages were then used to create very precise age models and identified the most favourable time periods for speleothem growth during MIS 3 in Central Europe.

Using growth phases of speleothems as a proxy for climate reconstructions allows to identify the time periods where liquid water was able to reach the cave and a sufficient soil and vegetation cover was present above the cave. During MIS 3 those time periods mainly coincide with the warm DO events. The Bleßberg growth phases often show a distinct lag to the onset of the DO events as recorded in the Greenland ice cores and cover approximately 70 % of their duration. During the second part of this study (Manuscript II, Chapter 4) the general climatic progression of MIS 3 in Central Europe and one particularly well represented DO event (DO14) were studied in more detail. The multi-proxy approach showed that early MIS 3 was characterised by a generally more humid climate with enhanced vegetation growth. DO14 was identified as the warmest and most prolonged growth phase in the Bleßberg MIS 3 record and its internal structure revealed two short cold events, which have not been identified in a terrestrial Central European record before.

The third part of this thesis (Manuscript III, Chapter 5) focussed on the Holocene (11.7 ka BP – recent) and the Late Glacial part of the three samples. While the main focus of this study was aimed towards MIS 3, all three samples also cover parts of Termination I (15 – 10 ka BP), which describes the transition from the last glacial period to the current warm phase, the Holocene, and the Holocene itself. The MIS 3 part if the study already showed the high sensitivity of the Bleßberg speleothems. Termination I was characterised by several centennial- to millennial-scale climate oscillations (e.g., the Younger Dryas cold

period and the Bølling/Allerød warm phase), which were to a large extent recorded in the flowstones.

The last part of this thesis (Manuscript IV, Chapter 6) shows a more uncommon approach on the dating of speleothems. As already mentioned, the ^{230}Th/U-dating method is limited by the dating range of 600 ka and detrital contamination in the sample. For samples older than 600 ka, the U-Pb-dating method is applicable, which is based on the decay from ^{238}U to stable ^{206}Pb and ^{235}U to stable ^{207}Pb and is not limited by an upper age range. To successfully apply U-Pb dating, similar requirements to those of the ^{230}Th/U-dating are necessary. However, further requirements include accumulating sufficient concentration of radiogenic ^{206}Pb and ^{207}Pb. This is essential to differentiate from the variable initial (common) Pb that is always present at the time of speleothem formation (Woodhead et al., 2012). In Manuscript IV an isothermal thermoluminescence dating method is tested on a sample from Bleßberg Cave, which has been precisely dated using the ^{230}Th/U-dating before and grew during MIS 9 and MIS 11.

Chapter 2: Basics

2.1 Speleothem formation

Speleothems are secondary cave carbonate deposits naturally occurring in karstic environments worldwide, with typical host rocks such as limestone ($CaCO_3$) or dolomite ($CaMg(CO_3)_2$). Their growth is only limited by the availability of liquid water reaching the cave through the aquifer. The cave acts as an isolated environment protecting the speleothems in most cases from erosion and alteration, which allows them to provide continuous proxy records of paleoclimatic and environmental information of even millions of years. Speleothems mainly consist of calcium carbonate ($CaCO_3$) mostly in the form of calcite or aragonite. There are various forms of speleothems used in paleoclimate research, but two of the most commonly used types are stalagmites and flowstones. Stalagmites grow from the cave floor to the ceiling and have a distinct growth stratigraphy. On the other hand, flowstones form from a thin water film that flows along the cave walls or floor and show a slower and more episodic growth pattern compared to stalagmites (Fairchild and Baker, 2012). The geochemistry of speleothems can be influenced by various sources, mainly changes in the climate of the cave region, the vegetation and soil above the cave, the karstic aquifer, the primary speleothem crystal growth, and its secondary alteration (Fairchild et al., 2006).

The principal formation of speleothem starts with meteoric precipitation falling above the cave and seeping through the soil. The soil pCO_2 is several orders of magnitude higher than the one in the atmosphere due to root respiration and microbial activity, which leads to the formation of carbonic acid:

$$CO_2\ (g) + H_2O\ (l) \leftrightarrow H_2O(l) + CO_2\ (aq) \leftrightarrow H_2CO_3\ (aq). \quad (2.1)$$

This acid dissolves the carbonate host rock above the cave, while it seeps further through fissures and joints:

$$H_2CO_3\ (aq) + CaCO_3(s) \leftrightarrow\ Ca^{2+}(aq) + 2\ HCO_3^-\ (aq). \quad (2.2)$$

This solution gets saturated with respect to calcium carbonate. If this solution reaches a cavity or cave, where the pCO_2 is usually several orders of magnitude lower than in the soil and karst above the cave, the excess CO_2 degasses due to the gradient between the

pCO_2 of the solution and the cave atmosphere. This results in a change in the pH value towards higher values and, thus, the predominant carbon species in the dissolved inorganic carbon (DIC) being bicarbonate (HCO_3^-). As a consequence, the solution then reaches supersaturation with respect to calcium carbonate and subsequently, $CaCO_3$ is precipitated, resulting in the growth of speleothems:

$$Ca^{2+}(aq) + 2\,HCO_3^-(aq) \leftrightarrow\ CaCO_3(s) +\ H_2O\ (l) +\ CO_2\ (aq). \tag{2.3}$$

Differences in pCO_2 within the soil, karst aquifer above the cave, and the cave system are main drivers of the calcium carbonate precipitation processes leading to speleothem formation in the cave. Therefore, $CaCO_3$ can precipitate even before the drip water reaches the top of a stalagmite. This process of precipitation of calcite in for instance fractures and cavities in the karst aquifer above the cave, on stalactites or along flowstones prior to precipitation on the top of a stalagmite or sampling site on a flowstone, is defined as prior

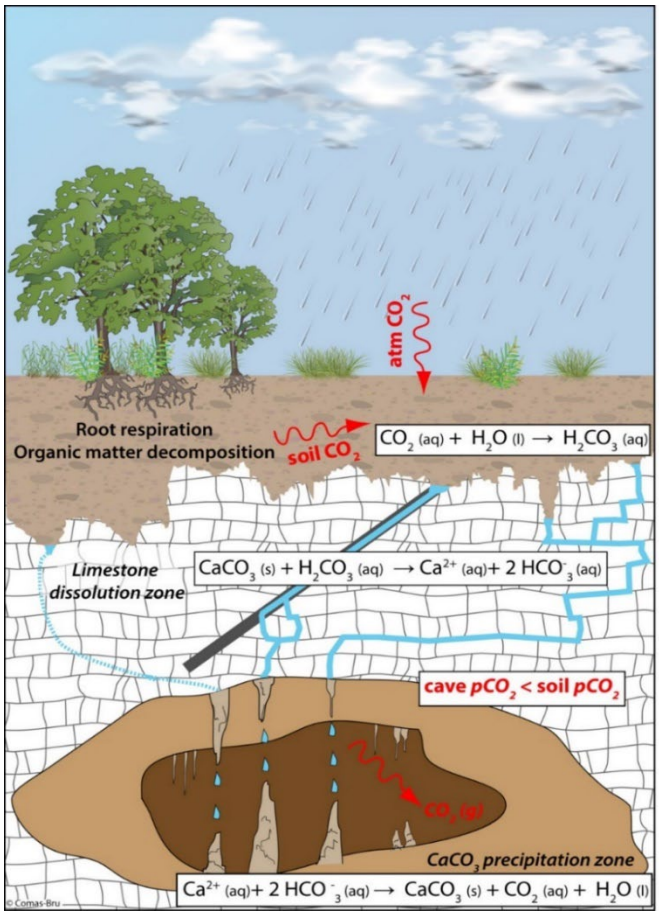

Fig. 2.1: Schematic overview of speleothem formation. It shows the interaction of meteoric precipitation with the CO_2 in the soil released from decaying plant matter and forming weak carbonic acid (H_2CO_3). This acid has the potential to dissolve the carbonate host rock (e.g., limestone or dolomite) and continues to flow through fissures and joints in the host rock. When the water reaches the caves, CO_2 degasses due to differences in the pCO_2 of the cave atmosphere and eventually $CaCO_3$ precipitates (Comas-Bru, 2019).

calcite precipitation (PCP). Due to the nature of flowstones growing from thin water films flowing on the cave wall or floor, these are always affected by PCP. Typically, PCP is enhanced by two processes: higher gradient of pCO_2 between the solution and the cave air or reduced water flows (Fairchild and McMillan, 2007) due to drier conditions and less water filled fissures and cavities in the aquifer above the cave (Fairchild et al., 2000).

2.2 U-series disequilibrium dating methods

Uranium-series disequilibrium methods can be used to precisely date both marine and terrestrial carbonates, such as corals and speleothems, in the range up to 600 ka using the ^{230}Th/U-method or even further in the range of million years using the U-Pb-method (Richards and Dorale, 2003; Scholz and Hoffmann, 2008). Both methods are based on the principle of disrupting the state of naturally reached equilibrium of different U isotopes and their radiogenic daughter nuclides. The ^{230}Th/U-dating method relies on the decay of ^{238}U via ^{234}U to ^{230}Th (Fig. 2.2) while the U-Pb-dating method is based on the decay from ^{238}U to stable ^{206}Pb and ^{235}U to stable ^{207}Pb (Fig. 2.2) and therefore relies on two different decay chains of U (Richards and Dorale, 2003). In this thesis, only the ^{230}Th/U-method is applied and therefore will be the focus of this chapter.

In the continental crust, typical U concentrations range from 0.1 up to 6 µg/g, while ^{238}U is the most abundant isotope reaching 99.27 %. The most abundant Th isotope is ^{232}Th with 99,98 % and the upper continental crust ^{232}Th/^{238}U weight ratio is ~ 3.8 (Wedepohl, 1995). Due to the much longer half-live of ^{238}U ($T_{1/2}$ = 4.4683 x 10^9 a (Cheng et al., 2013)) compared to the radiogenic daughter nuclides (Fig. 2.2), the activities of parent and daughter isotopes reach a state of secular equilibrium in natural systems. The interruption of this state caused by natural processes, such as elemental fractionation due to the geochemically different behaviour of U and Th, is the basis of the U-series disequilibrium dating method (Richards and Dorale, 2003).

In nature, U predominantly occurs in two oxidation states: U^{4+} and U^{6+}. On the earth's surface, it mainly exits as a water-soluble uranyl ion $[UO_2]^{2+}$ in its U^{6+} oxidation state (Ivanovich and Harmon, 1992). Therefore, U is easily mobilised and transported in meteoric waters. However, Th predominantly occurs in its insoluble, highly particle reactive Th^{4+} or Th^{5+} oxidation state and therefore either precipitates or is absorbed onto particles such as clay minerals. Consequently, the relative abundances of U and Th in the

hydrosphere are distinctly different from those in the earth's crust (Richards and Dorale, 2003). During the process of speleothem formation (Chapter 2.1) the drip water reaching the cave will therefore contain U dissolved from the host rock but presumably no Th. Thus, the concentrations of U and Th in secondary deposits, such as speleothems, generally reflect the relative abundances of U in the water seeping into the cave. Uranium will be incorporated in the speleothem $CaCO_3$. While Thorium will not due to the fact that it is not abundant in the water reaching the cave. This results in a strong chemical fractionation and a disequilibrium of U and Th in the speleothem and is a prerequisite that allows the application of the ^{230}Th/U-dating method.

In addition, several more assumptions are made when the ^{230}Th/U- dating method is applied on speleothems:

(1) A closed system is assumed, i.e., no gain or loss of parent or daughter isotopes due to post-depositional diagenetic processes;

(2) ^{230}Th only derives from radioactive decay, hence at the time of speleothem formation t = 0, (^{230}Th/^{238}U) = 0,

(3) No detrital ^{230}Th, ^{234}U or ^{238}U.

The first requirement listed is usually fulfilled due to speleothems growing in well-protected cave environments as well as the supersaturation of the drip water precluding post-depositional dissolution of the speleothem calcite in most cases. The most possible possibility to enable diagenetic processes is corrosive water reaching the speleothem. Several scenarios on the development of corrosive water and the consequences of alteration are described in detail in (Scholz et al., 2014). All scenarios result in either the loss or gain of U resulting in deviating (^{230}Th/^{238}U) activity ratios. Thorium is much more unlikely to be affected by diagenetic processes again due to its insoluble behaviour in water. Deviation in the (^{230}Th/^{238}U) activity ratio will result in erroneous ages calculated and probably disrupted stratigraphic order. The loss of U will result in elevated (^{230}Th/^{238}U) activity ratios and therefore in overestimated and too old ^{230}Th/U-ages. On the contrary, the gain of U will lower the (^{230}Th/^{238}U) activity ratios and calculated ^{230}Th/U-ages will turn out to be too young (Scholz et al., 2014). The second and third fundamental requirements are not always fulfilled, due to detrital material being incorporated in speleothems. Detrital material not only contains ^{232}Th, which is commonly used as an indicator for detrital contamination, but also detrital ^{230}Th. Since ^{230Th} is also part of the ^{238}U decay chain used for the

^{230}Th/U-dating method and the fact that there is no possibility to distinguish between detrital ^{230}Th and ^{230}Th resulting from the decay of the incorporated ^{238}U, detrital contamination can have a huge effect on the calculation of the ^{230}Th/U-ages. The (^{230}Th/^{238}U) activity ratio in this scenario will be elevated and therefore result in apparently too old ^{230}Th/U-ages. The correction for the ^{230}Th is further hampered because there is no universal (^{230}Th/^{232}Th) activity ratio for detrital material (Wedepohl, 1995) and different correction techniques can be applied (Budsky et al., 2019). The episodic growth pattern of flowstones is especially prone to incorporate detrital material which complicates the dating procedure for those samples. In addition, it is necessary to ensure that the decay chain has not been disturbed by diagenetic processes and alteration when using U-series disequilibrium methods. If this cannot be guaranteed, the cave system may become an open system, which will affect and hamper the accuracy of the dating method.

When calculating the individual ages using the ^{230}Th/U-method the (^{234}U/^{238}U) and the (^{230}Th/^{238}U) activity ratios need to be determined. The calculation of the activity ratios is described as the temporal development by the following equations:

$$\left(\frac{234_U}{238_U}\right)(t) = \left(\left(\frac{234_U}{238_U}\right)_{inital} - 1\right) e^{-\lambda_{234} t} + 1, \tag{2.4}$$

$$\left(\frac{230_{Th}}{238_U}\right)(t) = \left(1 - e^{-\lambda_{230} t}\right) + \left(\left(\frac{234_U}{238_U}\right)(t) - 1\right) \frac{\lambda_{230}}{\lambda_{230} - \lambda_{234}} \left(1 - e^{-(\lambda_{230} - \lambda_{234}) t}\right), \tag{2.5}$$

where $\left(\frac{234_U}{238_U}\right)_{inital}$ is the initial (^{234}U/^{238}U) activity ratio, and λ_{234} and λ_{230} are the decay constants for ^{234}U and ^{230}Th. For speleothems, it is not possible to calculate ^{230}Th/U-ages only by using Eq. 2.4 since $\left(\frac{234_U}{238_U}\right)_{inital}$ is generally not known and cannot be measured directly. However, Eq. 2.5 only requires the present (^{230}Th/^{238}U) and (^{234}U/^{238}U) activity ratios, which can both be obtained by analytical procedures. Variations in the (^{234}U/^{238}U) activity ratio can be affected by isotope fractionation between both isotopes, which is caused by α-recoil effects. During the α-decay of ^{238}U to ^{234}U (Fig. 2.2) a He nucleus is emitted which results in displacements in the crystal lattice, which gets damaged by the α-trajectory (Bourdon et al., 2003; Scholz and Hoffmann, 2008). This causes higher (^{234}U/^{238}U) activity ratios in e.g., ground or river water than expected from the equilibrium value, due to the more easily mobilized ^{234}U during e.g., weathering processes. In cave drip water the (^{234}U/^{238}U) activity ratio is strongly influenced by two factors: (i) the age of the

host rock and (ii) the water residence time in the aquifer, where an increased residence time leads to elevated initial ($^{234}U/^{238}U$) activity ratios and vice versa. However, since the initial ($^{234}U/^{238}U$) activity ratio is not relevant for the calculation of $^{230}Th/U$-ages, these processes do not influence the $^{230}Th/U$-dating of speleothem samples.

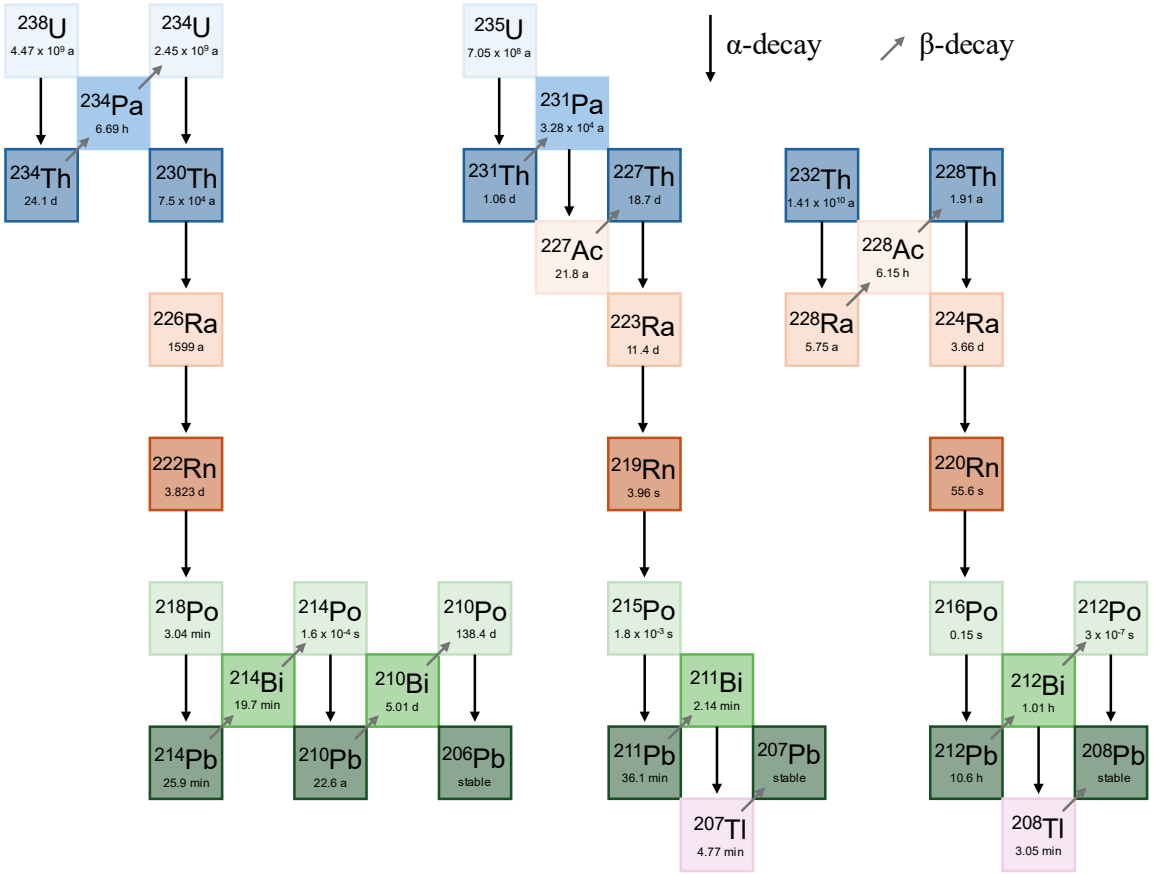

Fig. 2.2: Schematic illustration of the ^{238}U, ^{235}U and ^{232}Th decay chain. Different colours indicate isotopes of the different elements. The half-lives are given for each isotope and the different arrows indicate α-decay (black) or β-decay (grey), the half-lives are given after (Cheng et al., 2013).

First attempts on U-series dating were done using alpha spectrometry in the 1960s and 1970s. The development of thermal ionisation mass spectrometry (TIMS) helped to increase the precision of the measurements significantly and the development of multi-collector - inductively coupled plasma - mass spectrometry (MC-ICP-MS) (Wieser and Schwieters, 2005) further improved the analytical quality and sample throughput. The sample size was drastically reduced, while the analytical precision was further increased. The most recent technical advances of the methods are the combined use of MC-ICP-MS system and Laser Ablation (LA) techniques. While the most common procedure requires a chemical separation of U and Th using ion-exchange resin (see Manuscript I (Chapter 3) for detailed procedure) prior to the analysis, LA techniques allow an *in-situ* sampling and

immediate subsequent measurement, resulting in a fast, less destructive procedure and much higher spatial resolution. Unfortunately, there is a significant reduction in sensitivity due to much lower test portion masses for LA techniques. This limitation can ultimately result in a reduction in the precision of the ages obtained. In addition, only samples with a sufficient U concentration (at least ~ 0.3 µg/g for the setup used in this thesis) can be used due to the limitation in analytical sensitivity. Nevertheless, this sampling approach is especially well suited for samples with exceptionally narrow growth layers such as flowstones with short episodic growth patterns used in this study. Therefore, a combined approach of standard ^{230Th}/U-dating using different sampling techniques (hand-held drilling and micromilling), chemical processing and MC-ICP-MS as well as LA-MC-ICP-MS was used and is described in detail in Manuscript I (Chapter 3).

In order to combine high-resolution proxy data, such as stable isotopes or trace element data (see Chapter 2.3 and 2.4), with the calculated ^{230}Th/U-ages the construction of an appropriate age-depth-model is necessary to generate reliable and robust paleoclimate records. The simplest approach is linear interpolation, which only considers the adjacent ^{230}Th/U-ages when calculating the age-depth relationship in between and therefore potentially puts too much weight on individual ages. Potential age inversions, e.g., measured ages of stalagmites or flowstones that do not follow the constraint of older ages with increasing distance from top (DFT) even within the given age uncertainty, would result in a negative growth rate and therefore need to be discarded. However, the decision which of the two adjacent ^{230}Th/U-ages violates the stratigraphic order is difficult. Therefore, several advanced age-depth-models and algorithms are available in the literature (Breitenbach et al., 2012; Drysdale et al., 2004; Scholz and Hoffmann, 2011; Scholz et al., 2012; Spötl et al., 2008)}, all with different and specific advantages and disadvantages, trying to overcome the limitations of a simple linear interpolation age model. For instance, the age-depth-model algorithm StalAge (Scholz and Hoffmann, 2011) calculates the age models based on Monte Carlo simulations fitting straight lines through at least three data points, improving fundamental limitations of point-to-point linear interpolation models. By rejecting major outliers and increasing the age uncertainty of minor outliers, age inversions are prevented and further improve the final age model. The combined approach of solution-based ^{230}Th/U-dating and LA ^{230}Th/U-dating in this study resulted in a very large amount of individual ^{230}Th/U-ages in very high spatial resolution. The LA ^{230}Th/U- ages are also more likely to result in age inversions (within the age uncertainty) due to the generally

lower analytical precision using this sampling technique. The age uncertainty of LA ^{230}Th/U-ages are larger by a factor > 10 on average in comparison to the solution method. Conventionally used methods for age/depth-modelling as described above are generally designed for ages in the mm to cm spatial resolution range, comparable age uncertainties and only a limited amount of age inversions. Therefore, a modified error-weighted linear regression (i.e., Yorkfit (Ludwig, 2003)) was used for age/depth-modelling in this study. The modified algorithm accounts for uncertainties in the x- and y-direction and excludes negative slopes, which would imply a negative growth rate of the speleothem. The algorithm performs Monte Carlo simulations based on the Yorkfit calculations and provide a median age model including its corresponding 95 %-confidence limits. More details on the age model calculations are given in Manuscript I (Chapter 3).

2.2.1 Thermoluminescence dating

Another potential dating technique which can be applied to speleothems is thermoluminescence dating. Although ^{230}Th/U-dating is widely used for dating purposes, it has some limitations. As previously mentioned, it can only be used for samples within the range of 600 ka and can be significantly impacted by the initial detrital Th present in the speleothem. On the other hand, the U-Pb dating technique is applicable for samples older than 600 ka years but requires samples with high U and low initial (common) Pb, which drastically reduces the number of samples that can be dated using this technique (Richards and Dorale, 2003; Scholz and Hoffmann, 2008). Thermoluminescence dating offers the opportunity to date samples less precisely but within the ^{230}Th/U-dating and U-Pb dating range, without being affected by detrital Th and common Pb (Zhang and Wang, 2020).

Thermoluminescence dating is a process that determines the age of a material by measuring the light emitted from the material after heating it. It is based on the principle that crystalline materials emit light when heated, which is proportional to the amount of ionizing radiation that they have been exposed to (Wintle and Huntley, 1982). While this method is commonly used for sediments and samples of archaeological importance (Aitken, 1989; Roberts, 1997; Wintle, 2008), it is far less established for speleothems. Previous studies have shown that the thermoluminescence signal of calcite can be used to date the crystallization events of limestone (Ninagawa et al., 2001), travertines (Engin and

Güven, 1997) and speleothems (e.g. Debenham and Aitken, 1984; Wintle, 1978). Manuscript IV (Chapter 6) shows a dating comparison of the ^{230}Th/U-method and thermoluminescence dating of a Bleßberg speleothem from MIS 9 and 11.

2.3 Stable oxygen and carbon isotope analysis

The stable isotopes of carbon and oxygen (expressed as $\delta^{18}O$ and $\delta^{13}C$) are the most commonly used paleoclimate proxies in speleothem research. They can be obtained at high resolution, usually reaching the µm scale, by using a MicroMill device (Dettman and Lohmann, 1995) that is ideally adjusted to the growth rate of the speleothem. In some cases, this can even result in a sub-annual resolution record. The measurements are performed using continuous flow isotope ratio mass spectrometer (CF-IRMS). The relative differences in the isotopic ratios can be determined with a much higher precision than absolute ratios, and in 1950 (McKinney et al., 1950) introduced the delta (δ) notation to express the measured ratios:

$$\delta = \left(\frac{R_{sample} - R_{Std}}{R_{Std}}\right) x\ 1000. \tag{2.6}$$

Where R refers to the ratio of the heavy to the light isotope, e.g., $^{18}R_{sample} = (^{18}O/^{16}O)_{sample}$, and Std is the abbreviation for the used standard. Commonly carbonates are calibrated against Vienna Pee Dee Belemnite (VPDB (Craig, 1957)) and water samples against Vienna Standard Mean Ocean Water (VSMOW (Craig, 1961)). Both $\delta^{18}O$ values of the standards are 0 ‰ (Coplen, 1995). The chemical and physical properties of different isotopes of the same element are slightly different, which results in different behaviours of the heavy and light isotopes. Due to small differences in the mass of the atomic nuclei, the lighter isotope shows generally faster responsiveness in chemical reactions in comparison to the heavier isotope, resulting in effects commonly referred to as isotope fractionation. It can be distinguished between different types of isotope fractionation processes. In the case of an isotope flux between two reservoirs equal in both directions it is referred to as equilibrium fractionation. Kinetic fractionation, on the other hand, refers to a one-dimensional, irreversible process. However, fractionation processes in natural systems often cannot be described and characterised by only one of

these two endmember processes. They are more likely a combination of both and are commonly referred to as disequilibrium fractionation (Sharp, 2017).

The $\delta^{18}O$ values in speleothems are in principle controlled by two variables: the temperature of the cave air controlling the fractionation between the drip water and precipitated calcite and the $\delta^{18}O$ value of the drip water itself. However, the drip water $\delta^{18}O$ value is influenced by various environmental processes and therefore, variations in the $\delta^{18}O$ values in speleothems are also influenced by these processes, such as changes in the ocean, atmosphere, soil zone, karst above the cave, and the cave system itself (Lachniet, 2009). This makes it often complex to interpret $\delta^{18}O$ values of speleothems. It is not only essential to understand the equilibrium and kinetic fractions processes of the oxygen isotopes in the drip water (Fig. 2.1), but also site-specific cave processes, such as the infiltration pattern and flow paths of the seeping water, seasonality, or the microclimate of the cave (Lachniet, 2009).

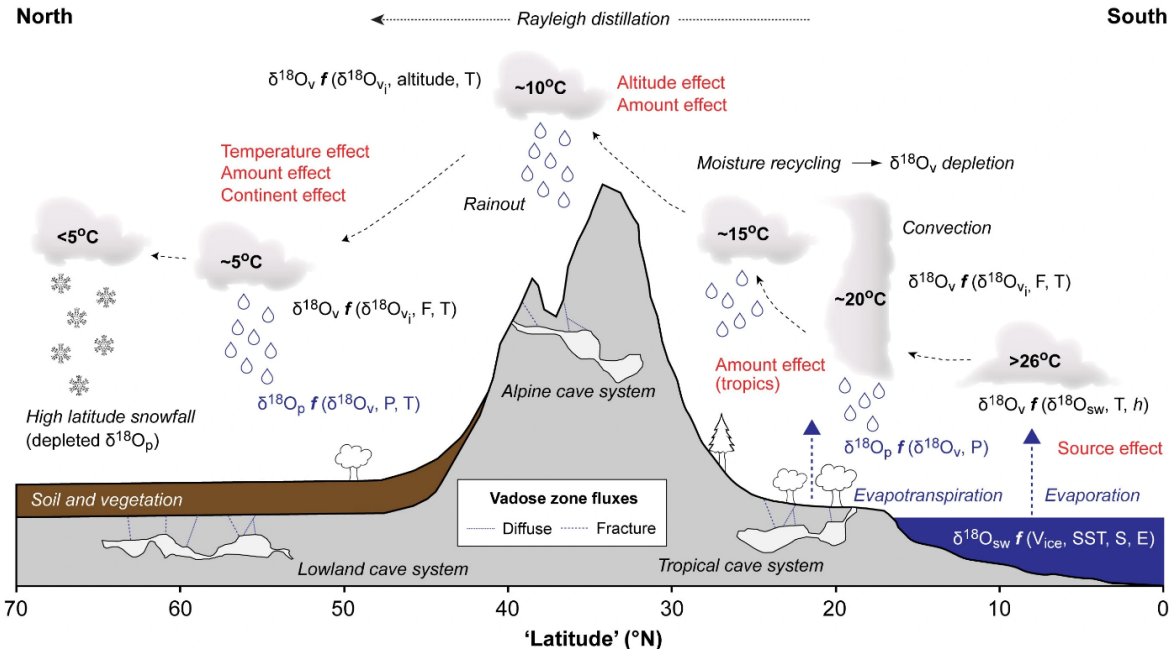

Fig. 2.3: Schematic illustration of primary processes of stable isotope fractionation. The variations in the $\delta^{18}O$ are given as a function f of various variables. The dominant controls are changes in temperature (T) and relative humidity (h) occurring in the ocean, atmosphere, and hydrosphere. More details are given in the text ((Baker, 2014) adapted from (Lachniet, 2009)).

All processes described int the following are illustrated in Fig. 2.3. The $\delta^{18}O$ of seawater ($\delta^{18}O_{SW}$) is influenced by the volume of sea ice (V_{ice}), the sea surface temperature (SST), salinity (S) and evaporation (E), resulting in highly variable $\delta^{18}O$ values, not only spatially but also temporally on an interglacial/glacial timescale. The $\delta^{18}O$ value of the sea water evaporate ($\delta^{18}O_V$) can be described as a function of the

previous $\delta^{18}O_{SW}$, temperature (T) and relative humidity (h), where the lighter isotope is more readily removed from the liquid phase and preferably goes into the vaporous phase. The resulting $\delta^{18}O_V$ values are a result of kinetic fractionation processes and therefore typically represent the source condition, commonly referred to as the source effect. Precipitation (P) and recycling processes of moisture within clouds, due to convective processes, will result in decreasing $\delta^{18}O$ values, i.e., the preferred removal of the heavy isotope. Tropical regions affected by extreme rainfall events will show $\delta^{18}O$ values strongly influenced by this so-called amount effect, i.e., decrease in rainfall $\delta^{18}O$ value with increased rainfall amount. Rain out events (F) in general as well as temperature dependent fractionation processes (temperature effect) will also strongly affect the remaining $\delta^{18}O_v$ as well as the $\delta^{18}O$ of precipitation in higher altitudes (altitude effect, i.e., decrease in $\delta^{18}O$ value values with increasing altitude) and more inland (continent effect, decrease in water $\delta^{18}O$ values with increasing distance from the ocean). All those processes described above influence the $\delta^{18}O$ values of the drip water percolated through the soil above the cave and result in highly variable $\delta^{18}O$ values of the speleothems depending on the location of the cave (Lachniet, 2009).

The $\delta^{18}O$ value of the drip water will mainly represent the $\delta^{18}O$ value of the precipitation when infiltrating the soil zone above the cave (Fig. 2.1), which is altered with increased evaporation leading to increased $\delta^{18}O$ values of the drip water (Lachniet, 2009). Reaching the karst aquifer above the cave (Fig. 2.1) the water is likely to be stored and/or mixed with older water (Willimas, 2008). Flow paths will vary based on the availability of fissures and joints in the host rock and a complicated interplay of them and the recharge flows, allowing for transmitting water laterally and vertically as well as mixing of flows of different origin and variable $\delta^{18}O$ values (Long and Putnam, 2004). In addition, water flows reaching air-filled cavities might evaporate, leading to increasing $\delta^{18}O$ values (Lachniet, 2009). Water entering the cave as drip water from the cave ceiling (Fig. 2.1) is a function of the $\delta^{18}O$ value of the precipitation infiltrating the soil and the combination of processes occurring in the soil zone and the aquifer above the cave (Mattey et al., 2008; Perrin et al., 2003). The $\delta^{18}O$ value of the precipitated speleothem carbonate can be further affected by the humidity and therefore level of evaporation inside the cave and the residence time on the speleothems surface. In addition, kinetic and equilibrium fractionation processes on the surface of the speleothem between the drip water and the carbonate phase further influence the $\delta^{18}O$ value of the precipitate (Dreybrodt, 2008; Dreybrodt and Scholz,

2011; Hansen et al., 2019; Hendy, 1971; Scholz et al., 2009). Concluding, the $\delta^{18}O$ values of speleothem result from a complex interplay of various fractionation processes above the cave and inside the soil-karst aquifer-cave system and are highly dependent on the source of the water, which often complicates their interpretation. Despite that, they can provide valuable information about past climate variability, such as varying moisture sources and atmospheric circulation patterns.

In contrast to the various supra-regional processes potentially influencing the $\delta^{18}O$ values of speleothems, the $\delta^{13}C$ values are mainly affected by local processes above the cave. The density and the type of the vegetation (C3, C4 or CAM plants) as well as the root respiration of the plants and decomposition of organic matter in the soil (Fig. 2.1) strongly influence the $\delta^{13}C$ values of soil CO_2 (McDermott, 2004). Equilibrium fractionation processes between soil CO_2 and the pH driven predominant carbon species (usually bicarbonate (HCO_3^-), see Chapter 2.1 for details) in the karst aquifer further affect the $\delta^{13}C$ value in the seeping water. Furthermore, it must be distinguished between an open or closed system model. In an open system model a continuous equilibration between the soil water and an infinite reservoir of soil CO_2 leads to a monotonic increase of HCO_3^- and an enrichment of solutes in the water. In this case the $\delta^{13}C$ values of the DIC reflect the isotopic composition of only the soil CO_2 without traces of the host rock. In a closed system model the soil water is isolated from the soil CO_2 reservoir with beginning carbonate dissolution processes (Hendy, 1971). During the dissolution of the carbonate host rock the CO_2 is consumed (see Eq. 2.1), and due to the limited and finite soil CO_2 reservoir the DIC reflects the isotopic composition of both the carbonate host rock and the CO_2. However, as described in Chapter 2.2, natural systems are often a combination of both models and most likely to be partially open (McDermott, 2004).

The interpretation of $\delta^{13}C$ values in speleothems can be relatively straightforward, provided that the ratio and shifts between C3 and C4 vegetation can be independently verified, for instance, through pollen records. (McDermott, 2004). However, in regions with temperate climate the interpretation of $\delta^{13}C$ values in speleothems can be more complicated due to the lack of C4 vegetation. Nevertheless, it is possible to obtain higher $\delta^{13}C$ values in speleothems than would be expected from solely C3 type vegetation. Possible processes that would lead to increasing $\delta^{13}C$ values would be a decrease of the drip rate enhancing the disequilibrium fractionation processes on the surface of the speleothem (Scholz et al., 2009), a stronger contribution of the host rock (i.e., more closed

system conditions), enhanced PCP (Fohlmeister et al., 2020) or a reduced soil CO_2 due to a lack of vegetation or climate changes strongly affecting root respiration and microbiological activity in the soil (Cerling, 1984). In conclusion, the interpretation of $\delta^{13}C$ values in speleothems especially in temperate climate zones can be complicated, even though the range of processes that might influence the value in the speleothem are more limited than those potentially influencing the $\delta^{18}O$ values. However, the information based on vegetation density, changes and activity of the local vegetation can still be very valuable for paleoclimate reconstructions, especially in combination with other proxy records such as the $\delta^{18}O$ values or trace elements.

2.4 Trace element analysis

The trace elements of speleothems are commonly applied proxies for paleoclimate studies, although they are less widely used than stable oxygen and carbon isotopes (Fairchild and Treble, 2009). Even though the potential of trace element studies in speleothems is great and they might reflect past precipitation patterns, soil conditions, and other environmental changes and conditions, it is also crucial to understand the cave system and environment to fully utilize the potential of trace elements as paleoclimate proxies. However, even with accompanying cave monitoring studies and a multi-proxy approach, the interpretation of trace elements can remain challenging. One of the major advantages of trace element analyses is the very high spatial resolution in which the data can be obtained using LA-ICP-MS. Using this approach, it is possible to receive datasets in a spatial resolution of tens of µm, allowing for analyses on an annual or even seasonal scale depending on the growth rate of the speleothem, while the analysis itself is almost non-destructive.

The process of incorporating trace elements into the speleothem carbonate can vary. Several trace elements such as Mg, Sr and Ba are incorporated as a substitute for the Ca^{2+}-ion in the carbonate crystal lattice and depend on the mass fraction of the drip water. Therefore, those elements are sensitive to water-soil-rock processes such as the residence time in the karst aquifer, a parameter related to precipitation (Sinclair, 2011) and/or seasonality. Sr and Ba can also be used as an indicator for changes in the growth rate of the speleothem (Fairchild and Treble, 2009; Huang and Fairchild, 2001).

A widely used application of trace elements is the potential identification of PCP indicating drier climate conditions (see Chapter 2.1). During this process, the Ca^{2+} is preferentially precipitated upstream to the drip site of the speleothem, while Mg, Sr and Ba remain in solution due to their partition coefficients being below unity (Huang and Fairchild, 2001). This leads to an enrichment of Mg, Sr, and Ba with respect to Ca^{2+} in the solution and subsequently in the speleothem. A positive correlation between Mg/Ca and Sr/Ca is therefore often attributed to PCP (Sinclair, 2011). This co-enrichment results in a vector with a constant slope (ranging from 0.709 to 1.45 (Wassenburg et al., 2020)) in natural logarithmic cross plots of Sr/Ca vs. Mg/Ca ratios and is commonly referred to as Sinclair test and used to identify PCP in karst-water-systems (Sinclair, 2011; Wassenburg et al., 2020). The growth of flowstones based on a water film rather than a drip point of water also implies that those speleothems are generally affected by PCP.

Additionally, it has been observed that incongruent calcite dissolution (ICD) has a similar effect to PCP. This is caused by the dissolution of calcite host rock and nearly simultaneous precipitation of calcite, which leads to the enrichment of Mg and Sr in the solution and, consequently, the speleothem. As water-to-rock interaction increases, and thus water residence time, this effect becomes more pronounced (Sinclair, 2011).

Other elements such as Al, Y, and P are transported by the drip water as fine detrital particles or colloids which get incorporated in the speleothem (Fairchild and Treble, 2009) and can therefore be useful to determine the (spatial) extent of detrital contamination in speleothems as shown in Chapter 3 (Manuscript I) using either the element concentration itself, or a trace element mapping to visualize the detrital distribution. Detrital contamination usually occurs at the end of a growth phase and detrital components, such as clay minerals, accumulate on the surface of the speleothem sample and therefore occur also as a visual hiatus between two growth periods. When the growth of the speleothem resumes the newly precipitated calcite will then cover the detrital particles. As stated in Chapter 2.1 flowstones often show particularly episodic growth patterns and trace elements marking detrital material in the sample can be a valuable tool to constrain a better growth history of the samples and can provide the understanding of potential limitations and failed measurements of other proxies that are potentially influenced by detrital contamination. One example of this application is shown in Chapter 4 (Manuscript II), where the $\delta^{18}O$ values of fluid inclusions and the associated calculated temperatures might be misleading due to detrital contamination indicated by elevated Al concentrations. In addition, while P

and Y can also hint towards detrital contamination, these elements are also used as proxies for soil activity (Baldini et al., 2002; Fairchild et al., 2001; Huang and Fairchild, 2001).

2.5 Fluid inclusion analysis

The analysis of fluid inclusions water isotope ratios in speleothems, in particular $\delta^{18}O$ and $\delta^{2}H$ values, became a more commonly used proxy in the last decades but is still not as frequently used as e.g., stable carbon and oxygen isotopes of the carbonate or trace elements in speleothems. Nonetheless, they can provide valuable information regarding the isotope composition of meteoric water and potentially the cave temperature at the time of speleothem formation (e.g. Fleitmann et al., 2003; Van Breukelen et al., 2008; Vonhof et al., 2006; Wainer et al., 2011). Several different techniques for fluid inclusion analysis in speleothems were used and developed during the last decades, often based on techniques that have been frequently applied to fluid inclusion in other mineral samples (e.g., pyrite (Ohmoto and Rye, 1974)). The more recent techniques combine a mechanical crusher unit in a heated environment as described in (Vonhof et al., 2006) to a continuous-flow isotope ratio mass spectrometer (CF-IRMS) or use it in combination with cavity ring-down spectroscopy (CRDS). The advantage of CRDS in comparison to IRMS is the ability to measure both $\delta^{18}O$ and $\delta^{2}H$ values of the released water vapour directly without the need to split them into separate water and hydrogen species. The obtained precision also increased to 0.3 ‰ for $\delta^{18}O$ and 1.1 ‰ for $\delta^{2}H$ values in comparison to the 0.4 ‰ for $\delta^{18}O$ and 2.0 ‰ for $\delta^{2}H$ values achievable with IRMS (De Graaf et al., 2020). However, the required sample sizes for analysis, approximately 1 g are much larger than those of other proxies such as stable isotopes or trace elements. As a result, the resolution of fluid inclusion records of speleothems is far lower.

Fluid inclusions are remnants of the paleo-drip water included in the speleothem calcite during the process of speleothem formation (Kendall and Broughton, 1978). As elaborated in Chapter 2.3. the $\delta^{18}O$ values of the seepage water reaching the cave will reflect the $\delta^{18}O$ value of the precipitation above the cave influenced by further processes and fractionation processes in the soil and karst aquifer zone above the cave and the cave itself. If the speleothem grew in thermal isotopic equilibrium and is not affected by re-equilibration, the water isotopes of the fluid inclusion will reflect the precipitation reaching the cave and

forming the speleothem. Comparisons of the measured water isotopes of the fluid inclusion with the Global Meteoric Water Line (GMWL) or a local MWL (LMWL) can help to ensure the thermal isotopic equilibrium and that the sample was not affected by post-depositional fractionation processes with the surrounding calcite phase (Dennis et al., 2001; Schwarcz et al., 1976).

The application of fluid inclusions is the reconstruction of paleotemperature using the oxygen isotope fractionation between the water and calcite. In the case of equilibrium conditions and based on the known temperature-dependent isotope fractionation between calcite and water (Hansen et al., 2019; Kim and O'Neil, 1997; Tremaine et al., 2011) the paleo-temperatures, which are reflected as an annual mean by the cave temperature (Gascoyne, 1992; Wigley and Brown, 1971), can be reconstructed. This approach is especially well suited for speleothems in a mid- and high-latitude continental setting, because of the dominant control of temperature on the isotope composition of the precipitation (Affolter et al., 2019). In this study, the empirical isotope-temperature fractionation relationship for inorganic cave calcite presented by (Tremaine et al., 2011) is used:

$$1000\ ln\ \alpha = \ 16.1\ (10^3 T^{-1}) - 24.6. \tag{2.7}$$

In this equation, the temperature dependent oxygen isotope fractionation (described by the fractionation factor α) is defined as approximately $\Delta\delta^{18}O_{CaCO_3}/\Delta T = -0.177‰/°C$.

As previously mentioned, due to the potential exchange of oxygen isotopes with the surrounding calcite over time, the fluid-inclusion $\delta^{18}O$ values may not accurately reflect the pore-water composition at the time of incorporation in the speleothem calcite (Schwarcz et al., 1976). As a consequence, studies (e.g. Fleitmann et al., 2003; Zhang et al., 2008) based on fluid inclusion temperatures did not directly use the measured $\delta^{18}O$ values for the temperature calculation. Instead, they utilized the $\delta^{2}H$ - $\delta^{18}O$ relationship of the GMWL to estimate the $\delta^{18}O$ of the fluid inclusion based on the measured $\delta^{2}H$, because hydrogen does not exchange with the calcite phase. Other studies, however, showed that in some cases the post-depositional fractionation processes are negligible, relying on the premise that the measured data falls directly or close to the GMWL and/or shows a similar slope and is consistent with modern drip water (Griffiths et al., 2010). In this study all three approaches, i.e., the direct use of measured $\delta^{18}O$ values and estimating the inclusion $\delta^{18}O$ value based

on the GMWL and LMWL, are used. In addition, a modern δ^2H – temperature equation was established based on monthly precipitation data from a Global Network of Isotopes in Precipitation (GNIP) station in close vicinity to the location of the cave and used for temperature calculation using the measured δ^2H fluid inclusion values. All four temperature reconstructions are shown in more detail in Chapter 4 (Manuscript II).

2.6 Calcium isotope analysis

Calcium, as the third major element of calcite, is rarely used as a proxy from speleothems. The isotope fractionation processes of Ca in the cave environment and speleothem have not been studied systematically and are still only relatively poorly understood (Owen et al., 2016). As described in Chapter 2.4. Calcium has the potential to be precipitated prior to speleothem formation, which leads to the enrichment of other trace elements with respect to calcite. During those PCP fractionation processes the light Ca isotope (^{42}Ca) is preferably incorporated into the solid phase, i.e., the prior precipitated calcite, which contradicts other isotope fractionation processes where the heavy isotope is preferentially incorporated into the solid phase. This is caused by the stronger bonding energy to water molecules in solution, which enriches the lighter isotope in the precipitated carbonate (Marriott et al., 2004). Thus, PCP would lead to higher values in the drip water reaching the cave. Ca isotopes in speleothems, reported as $\delta^{44/42}Ca$, would therefore show those higher values if PCP occurs (Owen et al., 2016). PCP is commonly used as an implication for drier climate conditions, which allows the conclusion that lower $\delta^{44/42}Ca$ values can be associated with wetter climate conditions and can be used as a potential proxy for paleo-precipitation reconstructions. The $\delta^{44/42}Ca$ values of speleothems can be measured in a high-resolution using MC-ICP-MS with only a small sample amount (~1 mg) needed, which can be processed by ion exchange chemistry using the automated device prepFAST MC to separate the Ca prior to the measurement in is described in (Weber et al., 2021).

2.7 Strontium isotope analysis

Even though the first studies of Sr isotopes in speleothems were already conducted in 1990 (Avigour et al., 1990) and it is a commonly used proxy in other fields (e.g., palaeontology or archaeology) it is still a more uncommonly used proxy in speleothem science today. The primary source of Sr, that is incorporated in speleothems, is the host rock but several other potential influences have been proposed on this topic like, for instance, the water residence time in the aquifer (Banner et al., 1996; Oster et al., 2010), changes in aeolian input as a response to sea-level fluctuations or atmospheric circulations (Bar-Matthews et al., 1999; Goede et al., 1998), changes in the weathering of the soil and/or host rock as a response to rainfall (Avigour et al., 1990) and several more (Fisher et al., 2010; Frumkin and Stein, 2004). Sr^{2+} ions can get incorporated into the speleothem calcite lattice as a substitute for Ca^{2+} (Banner, 2004) and so far, no isotopic fraction has been observed in the process of speleothem precipitation. The method therefore relies on the assumption, that the $^{87}Sr/^{86}Sr$ ratio in the speleothem corresponds that of the parent solution (Banner and Kaufman, 1994). The $^{87}Sr/^{86}Sr$ ratios can either be measured in a high-resolution using MC-ICP-MS coupled to a Laser Ablation system or with a preceding chemical preparation, more detailed information on both techniques can be found in (Weber et al., 2020; Weber et al., 2017).

2.8 Lignin Oxidation Products analysis

While many inorganic climate proxies have been utilized in speleothem science, the use of organic proxies has been more negligible, even though the analysis of organic matter in speleothems might offer a great opportunity to study additional vegetation and temperature proxies (Blyth et al., 2016). A potential proxy, which has been studied and more frequently applied in recent years, is lignin. Lignin is a biopolymer which is exclusively found in vascular plants and gets transported with the drip water from the soil zone inside the cave. Lignin results, when broken down into its monomeric units by oxidative digestion, in lignin oxidation products (LOPs). These LOPs can be divided into three groups: the vanillyl (V), the syringyl group (S) and the cinnamyl group (C) (Jex et al., 2014). Using those measured values, it is possible to distinguish between angiosperms (flowering plants), gymnosperms (“naked-seed”-bearing plants) or woody and non-woody type plants based on the comparison of the C/V and S/V ratios (Hedges and Mann, 1979). Based on this division,

C/V values between 0 – 0.1 indicate woody vegetation, 0.1 – 0.4 a transition zone and > 0.4 non-woody type vegetation, while S/V values from 0 – 0.2 indicate gymnosperm plants, 0.2 – 0.9 a transition zone and > 0.9 angiosperms. Additionally, the Σ8 value represents the sum of the concentration of all 8 analysed LOPs and can therefore be used as an indicator of the total amount of lignin in the sample. The analysis of LOPs can be done by using a Dionex UltiMate 3000 ultrahigh-performance liquid chromatography system (UHPLC) coupled to a heated electrospray ionization source (ESI) and a Q Exactive Orbitrap high-resolution mass spectrometer (HRMS). A more detailed description of the method and the analysis can be found in (Homann et al., 2022). Unfortunately, the sample amount needed is relatively large (~ 2 g), which results in scarce spatial resolution in comparison with high-resolution proxies like stable isotopes and trace elements.

In conclusion, the analysis of lignin samples incorporated in speleothems provides a great opportunity to achieve more insight into the vegetation type and amount above the cave at the time of speleothem formation. Especially in combination with more traditionally used proxies, such as $\delta^{13}C$ values, or trace elements like P and Y, that can be influenced by soil activity, it is possible to reconstruct a robust paleo-vegetation record and might be a great addition to commonly used paleoclimate proxies.

2.9 References

Adolphi, F., Bronk Ramsey, C., Erhardt, T., Edwards, R.L., Cheng, H., Turney, C.S.M., Cooper, A., Svensson, A., Rasmussen, S.O., Fischer, H. and Muscheler, R., 2018. Connecting the Greenland ice-core and U/Th timescales via cosmogenic radionuclides: testing the synchroneity of Dansgaard–Oeschger events. Climate of the Past, 14(11): 1755-1781.

Affolter, S., Häuselmann, A., Fleitmann, D., Edwards, R.L., Cheng, H. and Leuenberger, M., 2019. Central Europe temperature constrained by speleothem fluid inclusion water isotopes over the past 14,000 years. Science advances, 5(6): eaav3809.

Aitken, M.J., 1989. Luminescence dating: a guide for non-specialists. Archaeometry, 31(pt. 2): 147-159.

Avigour, A., Magaritz, M., Issar, A. and Dodson, M., 1990. Sr isotope study of vein and cave calcites from southern Israel. Chemical geology, 82: 69-81.

Baker, A., 2014. Lagrangian modelling of precipitation and speleothem proxy oxygen isotope systematics in the East Asian Summer Monsoon region, Durham University.

Baldini, J.U., McDermott, F. and Fairchild, I.J., 2002. Structure of the 8200-year cold event revealed by a speleothem trace element record. Science, 296(5576): 2203-2206.

Banner, J.L., 2004. Radiogenic isotopes: systematics and applications to earth surface processes and chemical stratigraphy. Earth-Science Reviews, 65(3-4): 141-194.

Banner, J.L. and Kaufman, J., 1994. The isotopic record of ocean chemistry and diagenesis preserved in non-luminescent brachiopods from Mississippian carbonate rocks, Illinois and Missouri. Geological Society of America Bulletin, 106(8): 1074-1082.

Banner, J.L., Musgrove, M., Asmerom, Y., Edwards, R.L. and Hoff, J.A., 1996. High-resolution temporal record of Holocene ground-water chemistry: Tracing links between climate and hydrology. Geology, 24(11): 1049-1053.

Bar-Matthews, M., Ayalon, A., Kaufman, A. and Wasserburg, G.J., 1999. The Eastern Mediterranean paleoclimate as a reflection of regional events: Soreq cave, Israel. Earth and Planetary Science Letters, 166(1-2): 85-95.

Blyth, A.J., Hartland, A. and Baker, A., 2016. Organic proxies in speleothems–New developments, advantages and limitations. Quaternary Science Reviews, 149: 1-17.

Bourdon, B., Turner, S., Henderson, G.M. and Lundstrom, C.C., 2003. Introduction to U-series geochemistry. Reviews in mineralogy and geochemistry, 52(1): 1-21.

Breitenbach, S.F., Rehfeld, K., Goswami, B., Baldini, J.U., Ridley, H.E., Kennett, D.J., Prufer, K.M., Aquino, V.V., Asmerom, Y. and Polyak, V.J., 2012. Constructing proxy records from age models (COPRA). Climate of the Past, 8(5): 1765-1779.

Budsky, A., Scholz, D., Wassenburg, J.A., Mertz-Kraus, R., Spötl, C., Riechelmann, D.F., Gibert, L., Jochum, K.P. and Andreae, M.O., 2019a. Speleothem $\delta^{13}C$ record suggests enhanced spring/summer drought in south-eastern Spain between 9.7 and 7.8 ka – A circum-Western Mediterranean anomaly? The Holocene, 29(7): 1113-1133.

Budsky, A., Wassenburg, J.A., Mertz-Kraus, R., Spötl, C., Jochum, K.P., Gibert, L. and Scholz, D., 2019b. Western Mediterranean climate response to Dansgaard/Oeschger events: New insights from speleothem records. Geophysical Research Letters, 46(15): 9042-9053.

Cerling, T.E., 1984. The stable isotopic composition of modern soil carbonate and its relationship to climate. Earth and Planetary science letters, 71(2): 229-240.

Chen, S., Wang, Y., Cheng, H., Edwards, R.L., Wang, X., Kong, X. and Liu, D., 2016. Strong coupling of Asian Monsoon and Antarctic climates on sub-orbital timescales. Scientific Reports, 6(1): 32995.

Cheng, H., Edwards, R.L., Shen, C.-C., Polyak, V.J., Asmerom, Y., Woodhead, J., Hellstrom, J., Wang, Y., Kong, X. and Spötl, C., 2013. Improvements in ^{230}Th dating, ^{230}Th and ^{234}U half-life values, and U–Th isotopic measurements by multi-collector inductively coupled plasma mass spectrometry. Earth and Planetary Science Letters, 371: 82-91.

Cheng, H., Edwards, R.L., Sinha, A., Spötl, C., Yi, L., Chen, S., Kelly, M., Kathayat, G., Wang, X. and Li, X., 2016. The Asian monsoon over the past 640,000 years and ice age terminations. nature, 534(7609): 640-646.

Comas-Bru, L., 2019. Palaeoclimate Data Syntheses: Opportunities and Challenges, Climate: Past, Present & Future.

Constantin, S., Bojar, A.-V., Lauritzen, S.-E. and Lundberg, J., 2007. Holocene and Late Pleistocene climate in the sub-Mediterranean continental environment: A speleothem record from Poleva Cave (Southern Carpathians, Romania). Palaeogeography, Palaeoclimatology, Palaeoecology, 243(3-4): 322-338.

Coplen, T.B., 1995. Discontinuance of SMOW and PDB. Nature, 375(6529): 285-285.

Corrick, E.C., Drysdale, R.N., Hellstrom, J.C., Capron, E., Rasmussen, S.O., Zhang, X., Fleitmann, D., Couchoud, I. and Wolff, E., 2020. Synchronous timing of abrupt climate changes during the last glacial period. Science, 369(6506): 963-969.

Craig, H., 1957. Isotopic standards for carbon and oxygen and correction factors for mass-spectrometric analysis of carbon dioxide. Geochimica et cosmochimica acta, 12(1-2): 133-149.

Craig, H., 1961. Standard for reporting concentrations of deuterium and oxygen-18 in natural waters. Science, 133(3467): 1833-1834.

Dansgaard, W., Johnsen, S.J., Clausen, H.B., Dahl-Jensen, D., Gundestrup, N.S., Hammer, C.U., Hvidberg, C.S., Steffensen, J.P., Sveinbjörnsdottir, A.E., Jouzel, J. and Bond, G., 1993. Evidence for general instability of past climate from a 250-kyr ice-core record. Nature, 364: 218 - 220.

De Graaf, S., Lüders, V., Banks, D.A., Sośnicka, M., Reijmer, J.J., Kaden, H. and Vonhof, H.B., 2020. Fluid evolution and ore deposition in the Harz Mountains revisited: isotope and crush-leach analyses of fluid inclusions. Mineralium Deposita, 55: 47-62.

Debenham, N. and Aitken, M., 1984. Thermoluminescence dating of stalagmitic calcite. Archaeometry, 26(2): 155-170.

Dennis, P., Rowe, P. and Atkinson, T., 2001. The recovery and isotopic measurement of water from fluid inclusions in speleothems. Geochimica et Cosmochimica Acta, 65(6): 871-884.

Denniston, R.F., Houts, A.N., Asmerom, Y., Wanamaker Jr, A.D., Haws, J.A., Polyak, V.J., Thatcher, D.L., Altan-Ochir, S., Borowske, A.C. and Breitenbach, S.F., 2018. A stalagmite test of North Atlantic SST and Iberian hydroclimate linkages over the last two glacial cycles. Climate of the Past, 14(12): 1893-1913.

Dettman, D.L. and Lohmann, K.C., 1995. Microsampling carbonates for stable isotope and minor element analysis: Physical separation of samples on a 20 micrometer scale. Journal of Sedimentary Research, 65(3).

Dreybrodt, W., 2008. Evolution of the isotopic composition of carbon and oxygen in a calcite precipitating H_2O–CO_2–$CaCO_3$ solution and the related isotopic composition of calcite in stalagmites. Geochimica et Cosmochimica Acta, 72(19): 4712-4724.

Dreybrodt, W. and Scholz, D., 2011. Climatic dependence of stable carbon and oxygen isotope signals recorded in speleothems: From soil water to speleothem calcite. Geochimica et Cosmochimica Acta, 75(3): 734-752.

Drysdale, R.N., Zanchetta, G., Hellstrom, J.C., Fallick, A.E., Zhao, J.-x., Isola, I. and Bruschi, G., 2004. Palaeoclimatic implications of the growth history and stable isotope (δ^{18}O and δ^{13}C)

geochemistry of a Middle to Late Pleistocene stalagmite from central-western Italy. Earth and Planetary Science Letters, 227(3-4): 215-229.

Engin, B. and Güven, O., 1997. Thermoluminescence dating of Denizli travertines from the southwestern part of Turkey. Applied Radiation and Isotopes, 48(9): 1257-1264.

Erhardt, T., Capron, E., Rasmussen, S.O., Schüpbach, S., Bigler, M., Adolphi, F. and Fischer, H., 2019. Decadal-scale progression of the onset of Dansgaard–Oeschger warming events. Clim. Past, 15(2): 811-825.

Fairchild, I.J. and Baker, A., 2012. Speleothem science: from process to past environments. John Wiley & Sons.

Fairchild, I.J., Baker, A., Borsato, A., Frisia, S., Hinton, R.W., McDERMOTT, F. and Tooth, A.F., 2001. Annual to sub-annual resolution of multiple trace-element trends in speleothems. Journal of the Geological Society, 158(5): 831-841.

Fairchild, I.J., Borsato, A., Tooth, A.F., Frisia, S., Hawkesworth, C.J., Huang, Y., McDermott, F. and Spiro, B., 2000. Controls on trace element (Sr–Mg) compositions of carbonate cave waters: implications for speleothem climatic records. Chemical geology, 166(3-4): 255-269.

Fairchild, I.J. and McMillan, E.A., 2007. Speleothems as indicators of wet and dry periods. International Journal of Speleology, 36(2): 2.

Fairchild, I.J., Smith, C.L., Baker, A., Fuller, L., Spötl, C., Mattey, D. and McDermott, F., 2006. Modification and preservation of environmental signals in speleothems. Earth-Science Reviews, 75(1-4): 105-153.

Fairchild, I.J. and Treble, P.C., 2009. Trace elements in speleothems as recorders of environmental change. Quaternary Science Reviews, 28(5-6): 449-468.

Fisher, E.C., Bar-Matthews, M., Jerardino, A. and Marean, C.W., 2010. Middle and Late Pleistocene paleoscape modeling along the southern coast of South Africa. Quaternary Science Reviews, 29(11-12): 1382-1398.

Fleitmann, D., Burns, S.J., Neff, U., Mangini, A. and Matter, A., 2003. Changing moisture sources over the last 330,000 years in Northern Oman from fluid-inclusion evidence in speleothems. Quaternary Research, 60(2): 223-232.

Fohlmeister, J., Voarintsoa, N.R.G., Lechleitner, F.A., Boyd, M., Brandtstätter, S., Jacobson, M.J. and Oster, J.L., 2020. Main controls on the stable carbon isotope composition of speleothems. Geochimica et Cosmochimica Acta, 279: 67-87.

Frumkin, A. and Stein, M., 2004. The Sahara–East Mediterranean dust and climate connection revealed by strontium and uranium isotopes in a Jerusalem speleothem. Earth and Planetary Science Letters, 217(3-4): 451-464.

Gascoyne, M., 1992. Palaeoclimate determination from cave calcite deposits. Quaternary Science Reviews, 11(6): 609-632.

Genty, D., Blamart, D., Ouahdi, R., Gilmour, M., Baker, A., Jouzel, J. and Van-Exter, S., 2003. Precise dating of Dansgaard–Oeschger climate oscillations in western Europe from stalagmite data. Nature, 421(6925): 833-837.

Goede, A., McCulloch, M., McDermott, F. and Hawkesworth, C., 1998. Aeolian contribution to strontium and strontium isotope variations in a Tasmanian speleothem. Chemical Geology, 149(1-2): 37-50.

Griffiths, M.L., Drysdale, R.N., Vonhof, H.B., Gagan, M.K., Zhao, J.-x., Ayliffe, L.K., Hantoro, W.S., Hellstrom, J.C., Cartwright, I. and Frisia, S., 2010. Younger Dryas–Holocene temperature and rainfall history of southern Indonesia from δ18O in speleothem calcite and fluid inclusions. Earth and Planetary Science Letters, 295(1-2): 30-36.

Hansen, M., Scholz, D., Schöne, B.R. and Spötl, C., 2019. Simulating speleothem growth in the laboratory: Determination of the stable isotope fractionation ($\delta^{13}C$ and $\delta^{18}O$) between H_2O, DIC and $CaCO_3$. Chemical geology, 509: 20-44.

Hedges, J.I. and Mann, D.C., 1979. The characterization of plant tissues by their lignin oxidation products. Geochimica et Cosmochimica Acta, 43(11): 1803-1807.

Hendy, C.H., 1971. The isotopic geochemistry of speleothems—I. The calculation of the effects of different modes of formation on the isotopic composition of speleothems and their applicability as palaeoclimatic indicators. Geochimica et cosmochimica Acta, 35(8): 801-824.

Hodge, E.J., Richards, D.A., Smart, P.L., Andreo, B., Hoffmann, D.L., Mattey, D.P. and González-Ramón, A., 2008. Effective precipitation in southern Spain (~ 266 to 46 ka) based on a speleothem stable carbon isotope record. Quaternary Research, 69(3): 447-457.

Homann, J., Zirbes, M., Arndt-Engelbart, M., Scholz, D., Waldvogel, S.R. and Hoffmann, T., 2022. Development of a Method for Anodic Degradation of Lignin for the Analysis of Paleo-Vegetation Proxies in Speleothems. ChemElectroChem, 9(6): e202101312.

Huang, Y. and Fairchild, I.J., 2001. Partitioning of Sr2+ and Mg2+ into calcite under karst-analogue experimental conditions. Geochimica et Cosmochimica Acta, 65(1): 47-62.

Ivanovich, M. and Harmon, R.S., 1992. Uranium-series disequilibrium: applications to earth, marine, and environmental sciences. 2.

Jex, C.N., Pate, G.H., Blyth, A.J., Spencer, R.G., Hernes, P.J., Khan, S.J. and Baker, A., 2014. Lignin biogeochemistry: from modern processes to Quaternary archives. Quaternary Science Reviews, 87: 46-59.

Kathayat, G., Cheng, H., Sinha, A., Spötl, C., Edwards, R., Zhang, H., Li, X., Yi, L., Ning, Y. and Cai, Y., 2016. Indian monsoon variability on millennial-orbital timescales, Sci. Rep., 6, 24374.

Kendall, A.C. and Broughton, P.L., 1978. Origin of fabrics in speleothems composed of columnar calcite crystals. Journal of Sedimentary Research, 48(2): 519-538.

Kim, S.-T. and O'Neil, J.R., 1997. Equilibrium and nonequilibrium oxygen isotope effects in synthetic carbonates. Geochimica et cosmochimica acta, 61(16): 3461-3475.

Kindler, P., Guillevic, M., Baumgartner, M., Schwander, J., Landais, A. and Leuenberger, M., 2014. Temperature reconstruction from 10 to 120 kyr b2k from the NGRIP ice core. Clim. Past, 10(2): 887-902.

Kudielka, G., Bar-Matthews, M., Gilmour, M., Ayalon, A., Koeberl, C. and Montanari, A., 2019. Implications for central Italy paleoclimate from 95,000 yr BP until the early Holocene as evident from Frasassi Cave speleothems.

Lachniet, M.S., 2009. Climatic and environmental controls on speleothem oxygen-isotope values. Quaternary Science Reviews, 28(5-6): 412-432.

Long, A.J. and Putnam, L.D., 2004. Linear model describing three components of flow in karst aquifers using 18O data. Journal of hydrology, 296(1-4): 254-270.

Ludwig, K., 2003. Mathematical–statistical treatment of data and errors for $^{230}Th/U$ geochronology. Reviews in Mineralogy and Geochemistry, 52(1): 631-656.

Marriott, C.S., Henderson, G.M., Belshaw, N.S. and Tudhope, A.W., 2004. Temperature dependence of δ7Li, δ44Ca and Li/Ca during growth of calcium carbonate. Earth and Planetary Science Letters, 222(2): 615-624.

Mattey, D., Lowry, D., Duffet, J., Fisher, R., Hodge, E. and Frisia, S., 2008. A 53 year seasonally resolved oxygen and carbon isotope record from a modern Gibraltar speleothem: reconstructed drip water and relationship to local precipitation. Earth and Planetary Science Letters, 269(1-2): 80-95.

McDermott, F., 2004. Palaeo-climate reconstruction from stable isotope variations in speleothems: a review. Quaternary Science Reviews, 23(7-8): 901-918.

McKinney, C.R., McCrea, J.M., Epstein, S., Allen, H. and Urey, H.C., 1950. Improvements in mass spectrometers for the measurement of small differences in isotope abundance ratios. Review of Scientific Instruments, 21(8): 724-730.

Moseley, G.E., Spötl, C., Brandstätter, S., Erhardt, T., Luetscher, M. and Edwards, R.L., 2020. NALPS19: Sub-orbital-scale climate variability recorded in northern Alpine speleothems during the last glacial period. Climate of the Past, 16(1): 29-50.

Moseley, G.E., Spötl, C., Svensson, A., Cheng, H., Brandstätter, S. and Edwards, R.L., 2014. Multi-speleothem record reveals tightly coupled climate between central Europe and Greenland during Marine Isotope Stage 3. Geology, 42(12): 1043-1046.

Ninagawa, K., Kitahara, T., Toyoda, S., Hayashi, K., Nishido, H., Kinjo, M. and Kawana, T., 2001. Thermoluminescence dating of the Ryukyu Limestone. Quaternary Science Reviews, 20(5-9): 829-833.

Ohmoto, H. and Rye, R.O., 1974. Hydrogen and oxygen isotopic compositions of fluid inclusions in the Kuroko deposits, Japan. Economic Geology, 69(6): 947-953.

Oster, J.L., Montanez, I.P., Guilderson, T.P., Sharp, W.D. and Banner, J.L., 2010. Modeling speleothem $\delta^{13}C$ variability in a central Sierra Nevada cave using 14C and 87Sr/86Sr. Geochimica et Cosmochimica Acta, 74(18): 5228-5242.

Owen, R., Day, C., Hu, C.-Y., Liu, Y.-H., Pointing, M., Blättler, C. and Henderson, G., 2016. Calcium isotopes in caves as a proxy for aridity: Modern calibration and application to the 8.2 kyr event. Earth and Planetary Science Letters, 443: 129-138.

Peral, M., Marchegiano, M., Verheyden, S., Goderis, S., Van Helden, T., Vanhaecke, F., Van Acker, T., Jia, X., Cheng, H. and Fiebig, J., 2024. A new insight of the MIS 3 Dansgaard-Oeschger climate oscillations in western Europe from the study of a Belgium isotopically equilibrated speleothem. Quaternary Science Reviews, 329: 108564.

Pérez-Mejías, C., Moreno, A., Sancho, C., Martín-García, R., Spötl, C., Cacho, I., Cheng, H. and Edwards, R.L., 2019. Orbital-to-millennial scale climate variability during Marine Isotope Stages 5 to 3 in northeast Iberia. Quaternary Science Reviews, 224: 105946.

Perrin, J., Jeannin, P.-Y. and Zwahlen, F., 2003. Epikarst storage in a karst aquifer: a conceptual model based on isotopic data, Milandre test site, Switzerland. Journal of hydrology, 279(1-4): 106-124.

Pons-Branchu, E., Hamelin, B., Losson, B., Jaillet, S. and Brulhet, J., 2010. Speleothem evidence of warm episodes in northeast France during Marine Oxygen Isotope Stage 3 and implications for permafrost distribution in northern Europe. Quaternary Research, 74(2): 246-251.

Rasmussen, S.O., Bigler, M., Blockley, S.P., Blunier, T., Buchardt, S.L., Clausen, H.B., Cvijanovic, I., Dahl-Jensen, D., Johnsen, S.J., Fischer, H., Gkinis, V., Guillevic, M., Hoek, W.Z., Lowe, J.J., Pedro, J.B., Popp, T., Seierstad, I.K., Steffensen, J.P., Svensson, A.M., Vallelonga, P., Vinther, B.M., Walker, M.J.C., Wheatley, J.J. and Winstrup, M., 2014. A stratigraphic framework for abrupt climatic changes during the Last Glacial period based on three synchronized Greenland ice-core records: refining and extending the INTIMATE event stratigraphy. Quaternary Science Reviews, 106: 14-28.

Richards, D.A. and Dorale, J.A., 2003. Uranium-series chronology and environmental applications of speleothems. Reviews in Mineralogy and Geochemistry, 52(1): 407-460.

Roberts, R.G., 1997. Luminescence dating in archaeology: from origins to optical. Radiation measurements, 27(5-6): 819-892.

Scholz, D. and Hoffmann, D., 2008. ^{230}Th/U-dating of fossil corals and speleothems. E&G Quaternary Science Journal, 57(1/2): 52-76.

Scholz, D. and Hoffmann, D.L., 2011. StalAge–An algorithm designed for construction of speleothem age models. Quaternary Geochronology, 6(3-4): 369-382.

Scholz, D., Hoffmann, D.L., Hellstrom, J. and Ramsey, C.B., 2012. A comparison of different methods for speleothem age modelling. Quaternary Geochronology, 14: 94-104.

Scholz, D., Mühlinghaus, C. and Mangini, A., 2009. Modelling δ^{13}C and δ^{18}O in the solution layer on stalagmite surfaces. Geochimica et Cosmochimica Acta, 73(9): 2592-2602.

Scholz, D., Tolzmann, J., Hoffmann, D.L., Jochum, K.P., Spötl, C. and Riechelmann, D.F., 2014. Diagenesis of speleothems and its effect on the accuracy of ^{230}Th/U-ages. Chemical Geology, 387: 74-86.

Schwarcz, H.P., Harmon, R.S., Thompson, P. and Ford, D.C., 1976. Stable isotope studies of fluid inclusions in speleothems and their paleoclimatic significance. Geochimica et Cosmochimica Acta, 40(6): 657-665.

Sharp, Z., 2017. Principles of stable isotope geochemistry.

Sinclair, D.J., 2011. Two mathematical models of Mg and Sr partitioning into solution during incongruent calcite dissolution: implications for dripwater and speleothem studies. Chemical Geology, 283(3-4): 119-133.

Spötl, C. and Mangini, A., 2002. Stalagmite from the Austrian Alps reveals Dansgaard–Oeschger events during isotope stage 3:: Implications for the absolute chronology of Greenland ice cores. Earth and Planetary Science Letters, 203(1): 507-518.

Spötl, C., Scholz, D. and Mangini, A., 2008. A terrestrial U/Th-dated stable isotope record of the Penultimate Interglacial. Earth and Planetary Science Letters, 276(3-4): 283-292.

Stoll, H., Mendez-Vicente, A., Gonzalez-Lemos, S., Moreno, A., Cacho, I., Cheng, H. and Edwards, R.L., 2015. Interpretation of orbital scale variability in mid-latitude speleothem δ18O: Significance of growth rate controlled kinetic fractionation effects. Quaternary Science Reviews, 127: 215-228.

Tremaine, D.M., Froelich, P.N. and Wang, Y., 2011. Speleothem calcite farmed in situ: Modern calibration of δ^{18}O and δ^{13}C paleoclimate proxies in a continuously-monitored natural cave system. Geochimica et Cosmochimica Acta, 75(17): 4929-4950.

Van Breukelen, M., Vonhof, H., Hellstrom, J., Wester, W. and Kroon, D., 2008. Fossil dripwater in stalagmites reveals Holocene temperature and rainfall variation in Amazonia. Earth and Planetary Science Letters, 275(1-2): 54-60.

Vonhof, H.B., Van Breukelen, M.R., Postma, O., Rowe, P.J., Atkinson, T.C. and Kroon, D., 2006. A continuous-flow crushing device for on-line δ^{2}H analysis of fluid inclusion water in speleothems. Rapid Communications in Mass Spectrometry: An International Journal Devoted to the Rapid Dissemination of Up-to-the-Minute Research in Mass Spectrometry, 20(17): 2553-2558.

Wainer, K., Genty, D., Blamart, D., Daëron, M., Bar-Matthews, M., Vonhof, H., Dublyansky, Y., Pons-Branchu, E., Thomas, L. and Van Calsteren, P., 2011. Speleothem record of the last 180 ka in Villars cave (SW France): Investigation of a large δ^{18}O shift between MIS6 and MIS5. Quaternary Science Reviews, 30(1-2): 130-146.

Wang, Y.-J., Cheng, H., Edwards, R.L., An, Z., Wu, J., Shen, C.-C. and Dorale, J.A., 2001. A high-resolution absolute-dated late Pleistocene monsoon record from Hulu Cave, China. Science, 294(5550): 2345-2348.

Wassenburg, J.A., Riechelmann, S., Schröder-Ritzrau, A., Riechelmann, D.F., Richter, D.K., Immenhauser, A., Terente, M., Constantin, S., Hachenberg, A. and Hansen, M., 2020. Calcite Mg and Sr partition coefficients in cave environments: Implications for interpreting

prior calcite precipitation in speleothems. Geochimica et Cosmochimica Acta, 269: 581-596.

Weber, K., Weber, M., Menneken, M., Kral, A.G., Mertz-Kraus, R., Geisler, T., Vogl, J. and Tütken, T., 2021. Diagenetic stability of non-traditional stable isotope systems (Ca, Sr, Mg, Zn) in teeth–An in-vitro alteration experiment of biogenic apatite in isotopically enriched tracer solution. Chemical Geology, 572: 120196.

Weber, M., Scholz, D., Schröder-Ritzrau, A., Deininger, M., Spötl, C., Lugli, F., Mertz-Kraus, R., Jochum, K.P., Fohlmeister, J., Stumpf, C.F. and Riechelmann, D.F.C., 2018. Evidence of warm and humid interstadials in central Europe during early MIS 3 revealed by a multi-proxy speleothem record. Quaternary Science Reviews, 200: 276-286.

Weber, M., Tacail, T., Lugli, F., Clauss, M., Weber, K., Leichliter, J., Winkler, D.E., Mertz-Kraus, R. and Tütken, T., 2020. Strontium uptake and intra-population 87Sr/86Sr variability of bones and teeth—controlled feeding experiments with rodents (Rattus norvegicus, Cavia porcellus). Frontiers in Ecology and Evolution, 8: 569940.

Weber, M., Wassenburg, J.A., Jochum, K.P., Breitenbach, S.F., Oster, J. and Scholz, D., 2017. Sr-isotope analysis of speleothems by LA-MC-ICP-MS: High temporal resolution and fast data acquisition. Chemical Geology, 468: 63-74.

Wedepohl, K.H., 1995. The composition of the continental crust. Geochimica et cosmochimica Acta, 59(7): 1217-1232.

Wieser, M.E. and Schwieters, J.B., 2005. The development of multiple collector mass spectrometry for isotope ratio measurements. International Journal of Mass Spectrometry, 242(2-3): 97-115.

Wigley, T. and Brown, C., 1971. Geophysical applications of heat and mass transfer in turbulent pipe flow. Boundary-layer meteorology, 1(3): 300-320.

Willimas, P.W., 2008. The role of the epikarst in karst and cave hydrogeology: a review.

Wintle, A., 1978. A thermoluminescence dating study of some Quaternary calcite: potential and problems. Canadian Journal of Earth Sciences, 15(12): 1977-1986.

Wintle, A. and Huntley, D., 1982. Thermoluminescence dating of sediments. Quaternary Science Reviews, 1(1): 31-53.

Wintle, A.G., 2008. Fifty years of luminescence dating. Archaeometry, 50(2): 276-312.

Woodhead, J., Hellstrom, J., Pickering, R., Drysdale, R., Paul, B. and Bajo, P., 2012. U and Pb variability in older speleothems and strategies for their chronology. Quaternary Geochronology, 14: 105-113.

Zhang, J. and Wang, L., 2020. Thermoluminescence dating of calcite–Alpha effectiveness and measurement protocols. Journal of Luminescence, 223: 117205.

Zhang, R., Schwarcz, H.P., Ford, D.C., Schroeder, F.S. and Beddows, P.A., 2008. An absolute paleotemperature record from 10 to 6 Ka inferred from fluid inclusion D/H ratios of a stalagmite from Vancouver Island, British Columbia, Canada. Geochimica et Cosmochimica Acta, 72(4): 1014-1026.

Chapter 3: Manuscript I

Precisely dated speleothem growth phases as a proxy for particularly warm climate conditions during MIS 3 in Central Europe

Jennifer Klose[1*], Michael Weber[1], Denis Scholz[1]

*corresponding author: jeklose@uni-mainz.de

[1]Institute for Geosciences, Johannes Gutenberg University, Mainz, Germany

under revision in communications earth & environment

Abstract

Speleothems provide exceptional age control, and the sensitivity of their growth to climatic conditions makes them a valuable archive for identification of particularly warm phases in temperate climates. Here we present a speleothem composite record from Germany, which shows episodic growth during the last glacial period, coinciding with several Dansgaard-Oeschger (DO) events. Using a combined approach of high-resolution solution and in-situ laser ablation ^{230}Th/U-dating, we were able to precisely constrain the timing and duration of several particularly warm phases during Marine Isotope Stage 3. The inception of speleothem growth in Central Europe lags the onset of DO events in Greenland and covers only approximately 70 % of the total duration, documenting a climatic threshold of favourable conditions for the initiation and termination of speleothem growth. This suggests that our record reflects the warmest conditions of the corresponding DO events and in general during Marine Isotope Stage 3 in Central Europe.

3.1 Introduction

The last glacial period and especially Marine Isotope Stage (MIS) 3 was characterised by several events of abrupt climate change known as warm Greenland Interstadials (GI) and cold Greenland Stadials (GS), or Dansgaard-Oeschger (DO) events (Dansgaard et al., 1993; NGRIP Project members, 2004; Rasmussen et al., 2014). The DO events are visible as rapid shifts in the $\delta^{18}O$ and $\delta^{15}N$ values of Greenland ice cores (Rasmussen et al., 2014) reflecting regional temperature increases of up to 16 °C (± 3 °C), coinciding with almost a doubling of the local snow accumulation (Andersen et al., 2006) and rapid changes in aerosol concentrations (Erhardt et al., 2019). These shifts towards warmer conditions often occurred within only a few decades (Dansgaard et al., 1993; Johnsen et al., 1992; Kindler et al., 2014). The DO events have been linked with rapid changes in ocean and atmospheric circulation in the North Atlantic region (Birchfield and Broecker, 1990; Boers et al., 2018; Broecker et al., 1985; Dansgaard et al., 1993; Menviel et al., 2014; Sime et al., 2019; Zhang et al., 2017; Zhang et al., 2014) and were associated with a reduction and retraction of North Atlantic sea ice, a strong Atlantic Meridional Overturning Circulation (AMOC) and a reduced influence of Antarctic Bottom Water (AABW) (Henry et al., 2016). However, their main trigger still remains a topic of debate (Corrick et al., 2020; Fohlmeister et al., 2023; Vettoretti et al., 2022).

The DO events show a supra-regional character with sites ranging from the North Atlantic to Asia as well as monsoon regions in the southern hemisphere (Adolphi et al., 2018; Bond et al., 1993; Erhardt et al., 2019; Kathayat et al., 2016; Spötl and Mangini, 2002), and have been identified in numerous climate archives, such as ocean sediment cores from the Atlantic (Barker et al., 2015; Barker et al., 2009; Peterson et al., 2000; Sachs and Lehman, 1999) and terrestrial records from monsoon regions (Kanner et al., 2012; Wang et al., 2006). These records indicate that the timing of climate change was synchronous in the North Atlantic, the Asian and South American Monsoon regions (Corrick et al., 2020) as well as in the low to mid-latitudes (Adolphi et al., 2018; Moseley et al., 2020).

Due to the short duration and rapid onset of the DO events, the determination of their precise timing remains challenging. For the Greenland ice cores, the commonly used GICC05 time scale (Svensson et al., 2008), which was constructed by counting continuously accumulating annual layers, the accumulative counting errors progressively increase from 0.8 ka (at ~28 ka BP) to 2.5 ka (at ~ 60 ka BP) (Rasmussen et al., 2014). This

uncertainty hampers the cross-dating and general comparability with other records, including the identification of potential leads and lags between regions and climate subsystems. This is further complicated by the low temporal resolution and dating accuracy achievable in many climate archives. Speleothems offer the exceptional possibility to establish precise and accurate independent age models based on U-series dating (Richards and Dorale, 2003; Scholz and Hoffmann, 2008). Corrick et al. (2020) compiled 63 published speleothem records from the European Mediterranean region, the Asian Summer Monsoon region, and the South American Monsoon realm, constructed a Speleothem Interstadial Onset Compilation data set (SIOC19) and compared it with the GICC05 chronology of DO onsets. The SIOC19 chronology does not include any speleothems from Central Europe. Most MIS 3 speleothem records from Europe stem from the Alps, where liquid water underneath temperate glaciers and pyrite oxidation allowed for speleothem growth even in case of absence of soil cover (Moseley et al., 2014; Spötl and Mangini, 2002). Additional speleothem records covering MIS 3 come from caves located in southwestern Europe (Budsky et al., 2019b; Genty et al., 2003). So far, the northernmost speleothem MIS 3 proxy record from Central Europe is from Bunker Cave, western Germany (49°N, 7°E, Fig. S3.1), where two relatively short growth phases during MIS 3 have been identified (Weber et al., 2018), but this record does not provide proxy data covering an entire DO event.

Located in close vicinity to and downwind of Greenland and the North Atlantic, Central Europe is highly susceptible to climatic perturbations in higher latitudes, and the influence of the DO events has been recorded in other palaeoclimate archives from the region (Prud'homme et al., 2022; Sirocko et al., 2021). However, it has proven challenging to constrain the precise timing of the DO events in Central Europe due to the lack of independently dated records (i.e., not tuned to GICC05). The lack of speleothem records from Central Europe during MIS 3 may have numerous reasons, including flooding or infilling of cave passages, drought, permafrost conditions, or a general lack of vegetation above the cave. To enable speleothem growth, liquid water as well as soil and vegetation cover are required, which may not have been continuously available during MIS 3 due to the cold and dry periglacial climate (Vandenberghe et al., 2014).

Ground temperature thus is a key factor for speleothem growth, which when falling below zero for more than two consecutive years initiates permafrost conditions (Atkinson et al., 1978; Vaks et al., 2013). The extent of periglacial periods and (continuous)

permafrost conditions during MIS 3, as for instance documented by the occurrence of cryogenic cave calcites in Central Europe (Richter et al., 2018), is, however, both spatially and temporally poorly constrained. It is also uncertain whether the (short) warming during the DO events was able to initiate sufficient permafrost thaw to allow active infiltration and speleothem deposition. These questions highlight the need for precisely and absolutely dated last glacial climate records from Central Europe.

Here we present three exceptionally precisely dated speleothems from Bleßberg Cave, Central Germany, which show several distinctively separated growth phases during MIS 3 aligning with specific DO events. Due to the complex growth characteristics on the µm-scale, we applied a variety of sampling approaches, including in-situ techniques.

3.2 Results and Discussion

Three flowstones (BB-9, BB-10, and BB-15) were retrieved from Bleßberg Cave, Central Germany (Fig. S3.1, ca. 500 m above sea level, 50°25'28'' N and 11°01'13'' E, see supplement for details). All flowstones are composed of calcite and show distinct growth intervals, interrupted by episodes of deposition of detrital material. ^{230}Th/U-dating reveals that speleothem growth occurred episodically during MIS 3 when environmental conditions were favourable. The uppermost parts of all samples cover the Late Glacial and early Holocene, which is not part of this study. All three samples grew discontinuously between 60 and 33 ka BP. BB-10 and BB-15 more prominently cover the earlier phases of MIS 3 between ca. 60 and 50 ka BP and show only sporadic growth in the later phases of MIS 3 (ca. 39 – 33 ka BP). BB-9 covers a longer, but strongly intermittent period during the middle and late part of MIS 3 (ca. 47 – 33 ka BP), with shorter growth phases interrupted by many growth stops (hiatuses) (Fig. S3.2).

The episodic growth pattern of the samples is characterised by alternating bright (continuous growth phases) and dark (hiatuses) sections. Some of the bright sections - especially of sample BB-9 - only have a thickness of 0.6 – 2 mm (Fig. 3.1). The hiatuses are often associated with detrital material, such as clay, deposited during periods without speleothem growth. These periods coincide with phases of colder climate, and we interpret them as growth stops forced by climatic changes and limited water availability inside the cave. Since Th preferably sticks to clay minerals, the hiatuses show elevated Th

concentrations. The ^{230}Th/U-dating method relies on the decay of ^{238}U and ^{234}U to ^{230}Th, with the assumption of the absence of initial ^{230}Th (Richards and Dorale, 2003). Due to the high content of detrital Th, this assumption is violated for the hiatuses and results in apparently overestimated ages. Accurate ^{230}Th/U-dating of these sections is thus challenging and requires precise determination of the spatial extent of the detrital layers.

Macro- or microscopic assessment of the spatial extent of the detrital layers is difficult due to their spatially heterogeneous character (Fig. 3.1). The detrital content of speleothem calcite is also reflected by elevated concentrations of specific trace elements (such as Th or Al). We measured trace elements applying conventional line scan analysis for samples BB-9 and -10 as well as trace element mapping for sample BB-9 (Fig. 3.1a – c). The line scan data were used for a principal component analysis (PCA), with the first principal component (PC1) representing the elements related to detrital contamination (Fig. 3.1a). PC1 was then used to precisely constrain the spatial extent of the detrital layers (Grey bars in Fig. 3.1). The trace element maps also show the spatial heterogeneity of the layers (Figs. 3.1b and c), especially in close vicinity to the hiatuses. Based on these data, we used a combination of different approaches for the sampling and ^{230}Th/U-dating (handheld drilling, micromilling, and Laser Ablation (LA)) to avoid contaminated areas. Samples obtained by handheld drilling or micromilling will further be referred to as solution ^{230}Th/U-ages.

For the solution ^{230}Th/U-ages, sampling of detrital material often could not be avoided. This is reflected by low (^{230}Th/^{232}Th) activity ratios (Table S7) and results in increased age uncertainties due to the correction for detrital contamination, which is conventionally applied to all ^{230}Th/U-ages. To construct a reliable age model, at least three precise ^{230}Th/U-ages for each individual growth phase are required. However, in many cases, only 1 - 2 high-precision solution ages per growth phase could be obtained, in particular for very thin growth sections. Therefore, we performed high-spatial-resolution LA ^{230}Th/U-dating along the growth layers (Fig. S3.2b) on samples BB-9 and -10. In addition, we measured continuous LA ^{230}Th/U-dating line scans perpendicularly to the growth layers (Fig. S3.2c) on all three samples. The latter were then used to calculate further ^{230}Th/U-ages based on the obtained data (Fig. 3.1 h and i, see methods for details). These individual LA line scan ^{230}Th/U-ages were calculated at 0.2 mm resolution and represent a mean ^{230}Th/U-age of the corresponding material. This combination of a few very precise solution ^{230}Th/U-ages (age uncertainties $\leq$ 0.4 %) and a large number of LA ^{230}Th/U ages with larger uncertainty

(~ 5 – 10 %) but very high spatial resolution (0.2 mm) enables us to calculate age models for all growth phases of the three flowstone samples. In total, 566 ^{230}Th/U-ages (BB-9: solution n = 22, LA n = 101; BB-10 solution n = 13, LA n = 259; BB-15 solution n = 8, LA n = 163) were determined and used for age modelling.

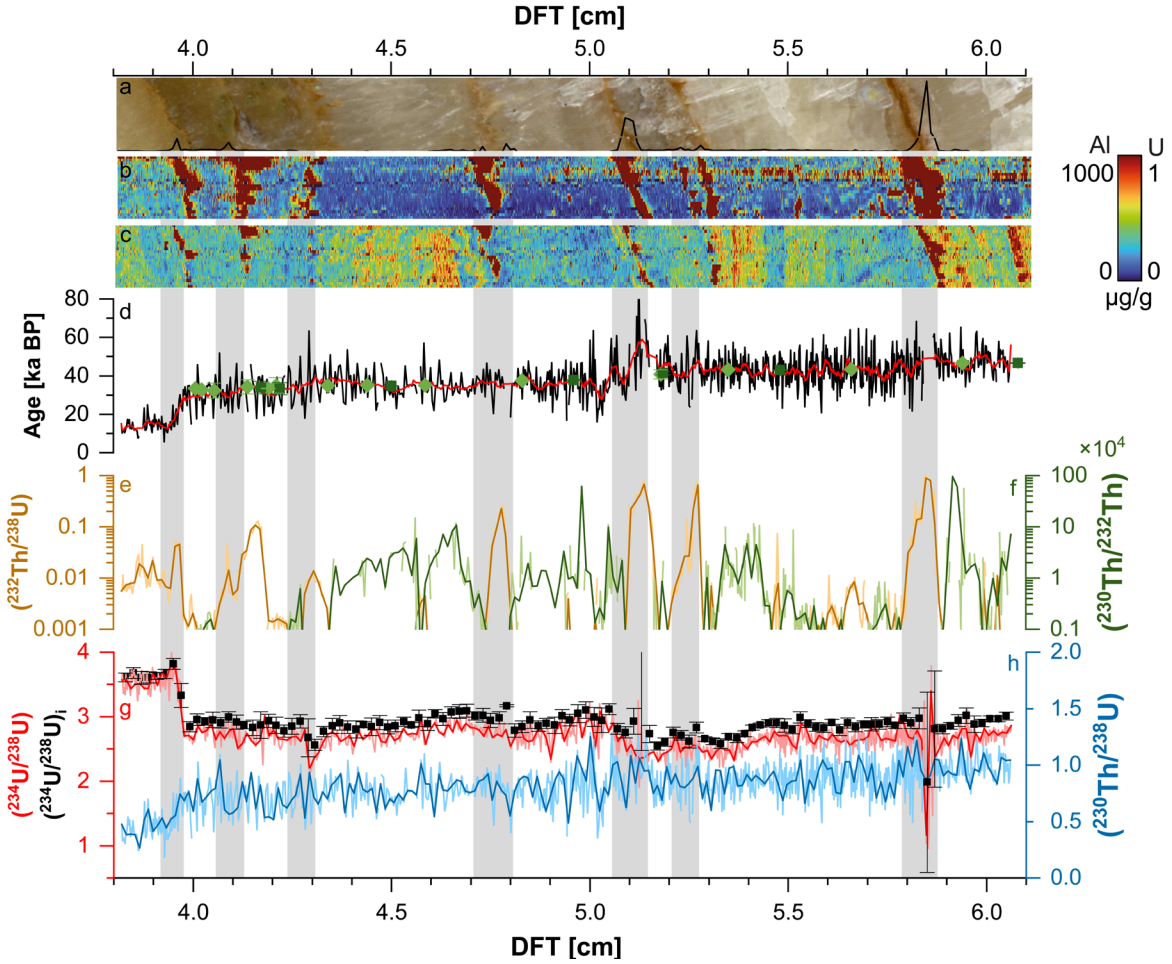

Fig. 3.1: Overview of several applied measurements of sample BB-9. Grey bars indicate the defined width of the hiatuses. a detrital component of the trace element principal component analysis (black line) on a scan of the sample showing the area of the trace element concentration mapping of Al (b) and U (c) highlights the spatial heterogeneity across the sample and especially around the hiatuses. d shows corrected ^{230}Th/U-ages obtained by laser ablation line scan analyses in high resolution (black) and smoothed by a 10pt Adjacent-Averaging (red). Solution ages are given in light green (micromilling) and dark green (handheld drill). e and f indicate the degree of detrital contamination within the sample obtained by laser ablation, g and h show the laser ablation line scan data of (^{234}U/^{238}U) (red) and (^{230}Th/^{238}U) (blue), which were used to calculate the ages in d, the black dots indicate (^{234}U/^{238}U)$_i$ at 0.2 mm resolution.

The high-resolution LA ^{230}Th/U-data also provide detailed information about the distribution of U and Th across the samples. The concentration of ^{232}Th is an indicator for detrital contamination, whereas high (^{232}Th/^{238}U) and low (^{230}Th/^{232}Th) ratios reflect a high degree of contamination. This is the case around and within the hiatuses (Fig. 3.1e and f), and the corresponding LA ^{230}Th/U-ages are apparently too old (Fig. 3.1d). These data support our observations based on the trace element data. Initial (^{234}U/^{238}U) activity

ratios, $(^{234}U/^{238}U)_i$, also show distinct changes around the hiatuses (Fig. 3.1h), and can thus also be used as an indicator for growth stops, even if they do not coincide with a visible detrital layer. Based on this observation, we identified two further growth stops in apparently continuous growth phases of samples BB-10 and -15. These are also reflected by apparently too old LA ^{230}Th/U-ages (Fig. S3.4).

The age models for all three samples (Figs. S3.8 – S3.10) were calculated using a section-wise linear fit based on a Monte-Carlo simulation (Fig. 3.2a and b, see methods for details), which weights precise ages more strongly and does not only provide the age-depth model and its 95 % confidence intervals but also a distribution of all calculated ages (Figs. 3.2c – d and 3.3c – e). The number of bins for the histograms was set to 20 for all growth phases (Fig. 3.3). Therefore, the width of the individual bins and the histogram reflect the precision of the age model for the individual growth phases. Even for sample BB-9, which proved to be the most challenging sample due to the very thin growth layers, we obtained precise age models for the majority of the individual growth phases (Fig. 3.3c). This highlights the great potential of our dating approach for flowstone samples with particularly thin growth layers, which are often considered as less suitable climate archives due to their episodic growth pattern. Unfortunately, in a few cases, even our approach resulted in relatively imprecise age models, and a clear assignment to a specific DO event was not possible. The reason for the lower precision of the corresponding age models is a lack of precise solution ages, either due to unavoidable detrital contamination (e.g., growth phase 4 of BB-9 or growth phase 3 of BB-15) or due to a lower spatial resolution in case of longer growth phases (e.g., growth phase 1.3 of sample BB-10). Thus, our dating approach works best with a few high-precision solution ages that can be used as anchor points for the high-resolution LA ^{230}Th/U-ages with larger age uncertainties.

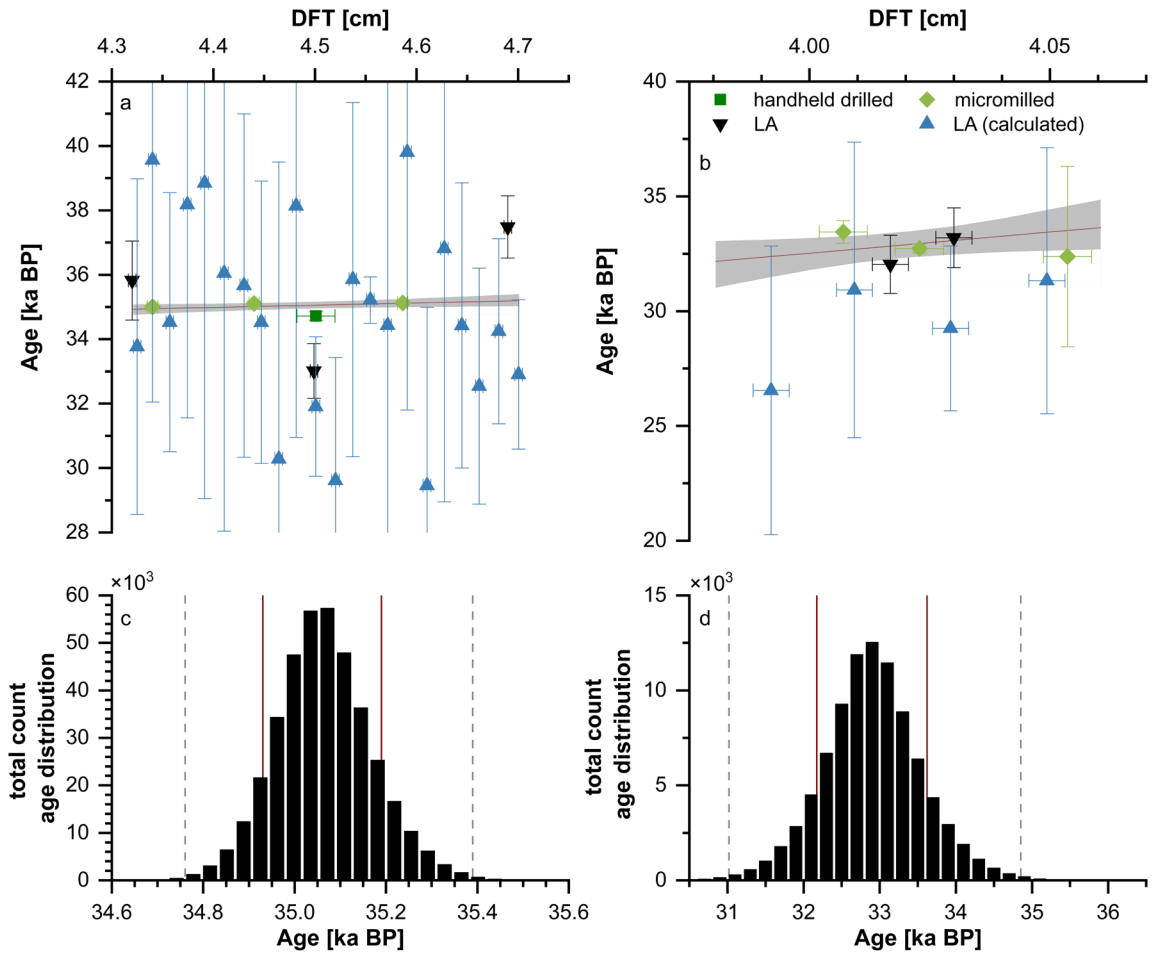

Fig. 3.2: Age models and age distributions for two growth phases of sample BB-9. a and **b:** Age models (red line) for growth phases 6 (**a)** and 8 (**b)** of sample BB-9 and the corresponding 95 % confidence intervals (grey area). Both are also indicated by the red and dashed lines in **c** and **d**. All ages used for the calculations are also shown including their depth uncertainty (handheld drilled (dark green squares, depth uncertainty: ± 0.1875 (1σ)), micromilled (light green diamonds, depth uncertainty: ± 0.05 (1σ)), LA ^{230}Th/U-ages parallel (black upside-down triangles, depth uncertainty: ± 0.0375 (1σ)) and perpendicular (blue triangles, depth uncertainty: ± 0.0375 (1σ)) to the growth layers **c** and **d:** Histograms showing the individual ages calculated for growth phases 6 (**c**) and 8 (**d**) during the Monte-Carlo simulation. The number of bins for each histogram was set to 30.

Based on their age models, most of the Bleßberg flowstone growth periods can be unambiguously assigned to DO events recorded in the Greenland ice cores (Figs. 3.3 and Figs. S3.5 – S3.10). This clearly shows that flowstone growth in Bleßberg Cave during MIS 3 preferentially occurred during DO events. This is reasonable considering that speleothem growth requires both liquid water and a vegetation cover above the cave. In case of less precise age models (e.g., growth phases 4 and 8 of BB-9), the timing of the corresponding growth phases is constrained by the surrounding growth phases (Fig. 3.3). In combination with the reasonable assumption that flowstone growth was inhibited during cold stadial periods, we assigned most growth phases to specific DO events based on the

most frequently simulated Monte-Carlo ages (i.e., the center bins of the age distribution, Fig. 3.3, Table S3.5). Our samples show growth during DO events 17 – 5, the only exception being DO 9, which shows the smallest temperature increase in Greenland 6.5°C (Kindler et al., 2014) and is the second shortest (260 years) DO event during MIS 3 (Rasmussen et al., 2014).

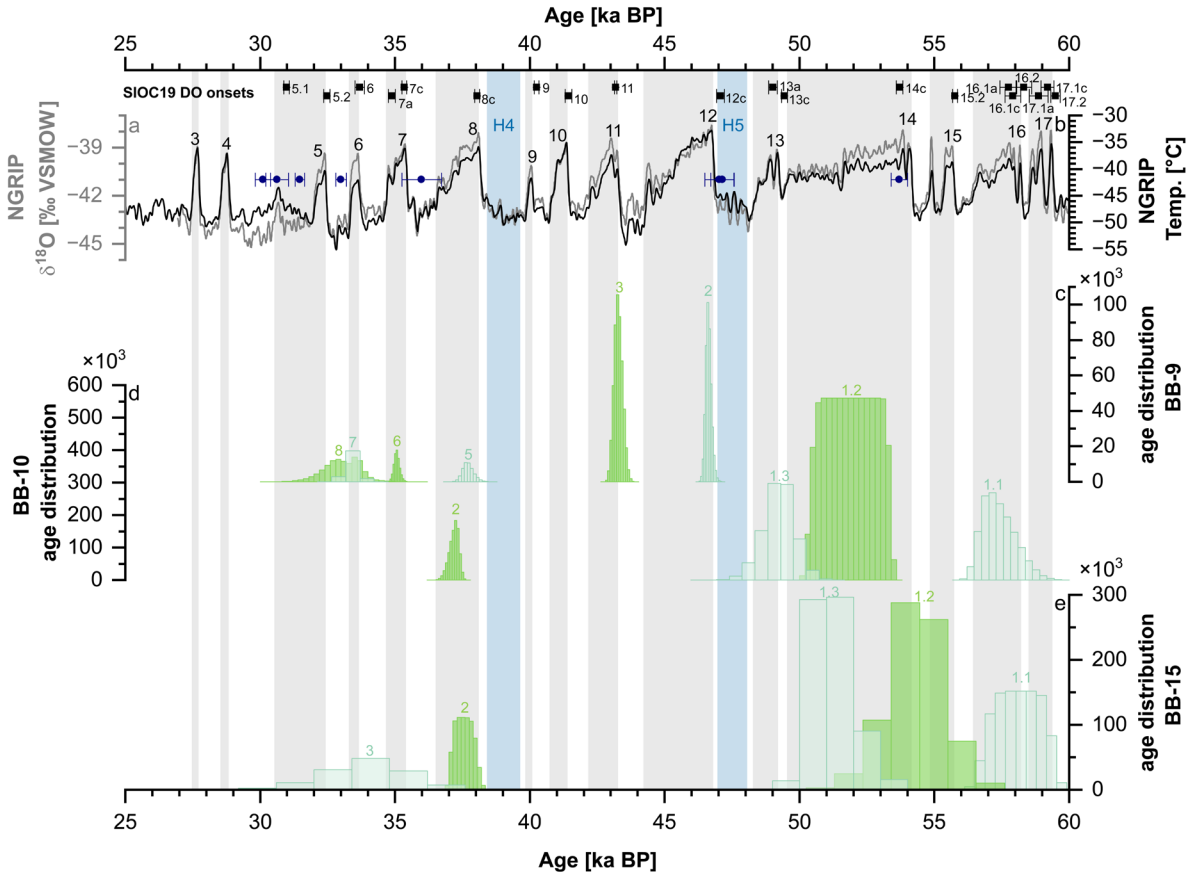

Fig. 3.3: Distribution of ages for all three Bleßberg flowstone samples plotted in comparison with DO and Heinrich events The timing of the DO events (grey bars) is based on the NGRIP GICC05 $\delta^{18}O$ values (grey line) (Rasmussen et al., 2014) and temperature reconstruction (black line) (Kindler et al., 2014). Because there is no exact agreement regarding the timing and duration of Heinrich events (Goni and Harrison, 2010; Hemming, 2004; Kindler et al., 2014) the blue bars for these events are based on the stadial in which they took place which is based on the NGRIP GICC05 chronology. The black dots represent speleothem DO onsets based on the SICC09 record (Corrick et al., 2020) and $^{230}Th/U$-ages of cryogenic cave calcites (blue dots) (Richter et al., 2018). The histograms representing the different growth phases (numbered) consist of 20 bins. The width of the histogram and the individual bins thus represent the precision of the age model.

Previous studies showed that speleothem proxy data can be used to precisely determine the onset of individual DO (sub-)events (Corrick et al., 2020). However, this is only possible if growth is continuous over the transition from stadial to interstadial conditions (i.e., the onset of the event). This can be the case for monsoon systems (Cheng et al., 2016) or underneath temperate glaciers (Moseley et al., 2014). Based on these data, the onset of

the DO events appears to be synchronous worldwide (Corrick et al., 2020). For the Bleßberg speleothems, however, growth is strongly related to the climatic conditions above the cave and thus restricted to warm phases. During phases of comparably warm and wet climate, such as the Holocene, continuous speleothem growth in Bleßberg Cave is possible as shown in previous studies (Breitenbach et al., 2019). During MIS 3, however, the short-lived warm DO events are interrupted by cold stadial conditions when speleothem growth is inhibited. The short duration of favourable conditions in combination with small growth rates (~ 10 µm/a) of the flowstone samples causes very thin growth layers associated with individual DO events. Given the proximity to Greenland and the North Atlantic, it is reasonable to assume that the climate signal reaches central Europe relatively quickly. However, there is still a debate about whether there is a delay (~ 200 years) before these changes are recorded (Lane et al., 2013; Rach et al., 2014) or whether they coincide, as suggested for both central Europe (Reinig et al., 2021) and globally (Corrick et al., 2020).

The timing of the individual Bleßberg speleothem growth phases often appear to be slightly delayed in comparison to the onset of the DO events in Greenland. This could be related to a general lag of the response of the climate signal in Central Europe but may also be due to permafrost and/or the absence or a strongly reduced vegetation cover above the cave at the onset of the event. Permafrost conditions in Central Europe can be derived from the formation of cryogenic cave calcites, which requires an ice body inside the cave (Richter et al., 2010). The occurrence of cryogenic cave calcites in Central Europe (Richter et al., 2015; Richter et al., 2018; Žák et al., 2012) thus shows that the climate conditions during MIS 3 stadials were, at least temporarily, cold enough to form permafrost (Fig. 3.3). During such periods, no liquid water will reach the cave and the vegetation will be absent, both prohibiting speleothem formation. After the onset of a DO event in Greenland, the initiation of speleothem growth will thus be delayed – even if the warming will reach Central Europe relatively quickly – due to the buffered of the warming by the karst above the cave as well as the time required for permafrost thawing and vegetation development.

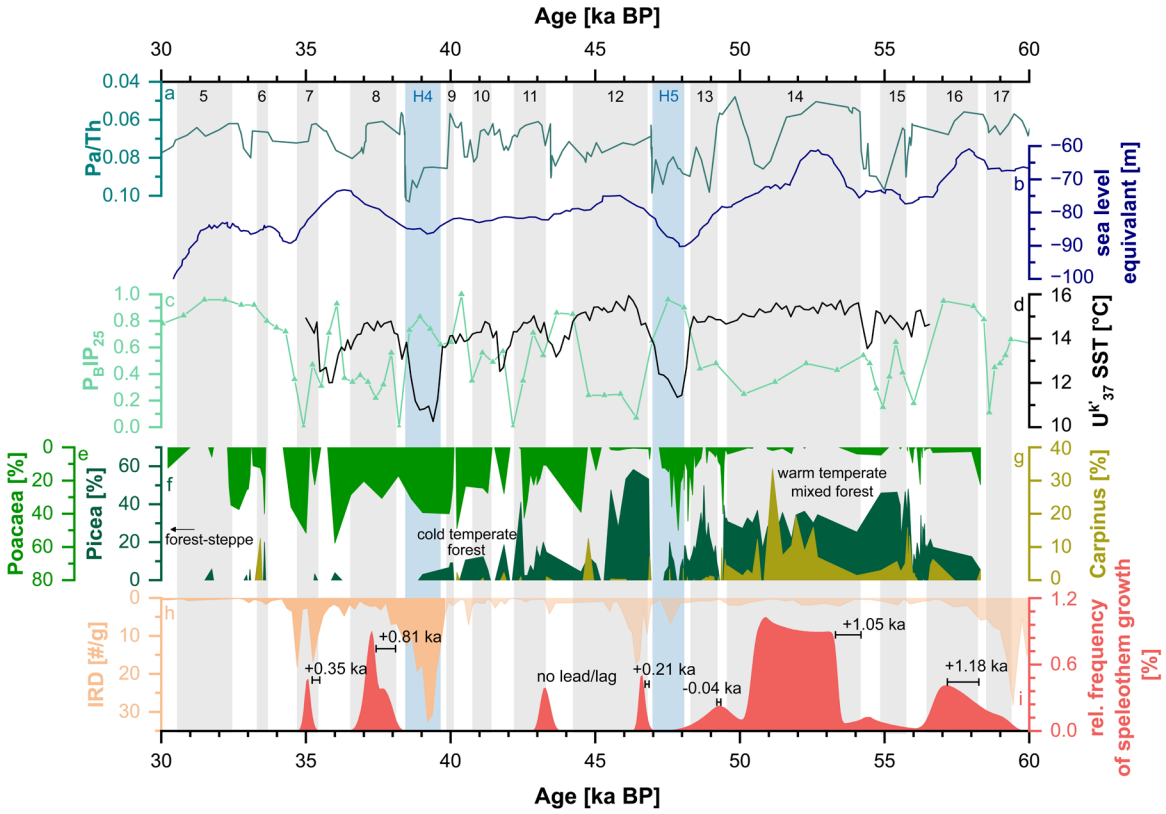

Fig. 3.4: Bleßberg speleothem growth phases in comparison to other climate records. a AABW reconstruction based on a Pa/Th record from core CDH19 from the Bermuda Rise (dark turquoise line) (Henry et al., 2016). **b** Red Sea sea level reconstruction (dark blue line) (Grant et al., 2014). **c** North Atlantic sea ice cover reconstruction based on P_bIP_{25} (brassicasterol C25 isoprenoid lipid) from the SE Norwegian Sea (light turquoise line with triangles) (Hoff et al., 2016). **d** Summer alkenone-based SST ($U^{k'}_{37}$) from core MD01-2444 at the Iberian Margin (37°N, black line) (Martrat et al., 2007). **e, f** and **g** Vegetation reconstructions based on pollen data from *Poacaea* (green), *Picea* (dark green) and *Carpinus* (yellow-green) from different Eifel Maar cores (AU3, AU4, HM4) (Sirocko et al., 2022). **h** Ice rafted debris (IRD) record from core MD01-2040 at the Iberian Margin (40°N, light orange) (Schönfeld et al., 2003) **i** Combined relative frequency of growth of all three Bleßberg flowstone samples with more than 30 % positives slopes during the age model calculation (red. See Table S3.8 for an overview on the percentages of the positives slops). The leads/lags between the onsets of the DO events in Greenland (Fig. 3) and the onset of speleothem growth in Bleßberg Cave are indicated. DO (grey) and Heinrich (blue) events are indicated by the coloured bars.

We created a combined density plot using the age distribution counts of all three flowstone samples (Fig. 3.4d – f) and the Frequency Counts function provided by the software Origin. This reduces the impact of less well-constrained growth phases. For instance, growth phase 4 of BB-9, which is probably associated with DO 10, is not visible in the combined record due to the large age scatter spanning multiple DO events (Fig. 3.4d). Growth during DO 15, associated with growth phase 1.2 of BB-15 (Fig. 3.4f), is still visible in the combined record, but the corresponding peak is small and shifted towards the stadial period. The composite record represents phases of exceptionally warm and wet climate in Central Europe based on the Bleßberg speleothem growth phases (Fig. 3.4i). In total, nine

growth phases can be identified, with eight of them distinctively correlating with DO events 16, 14 – 11 and 8 – 6.

These growth phases correlate with periods of a strong AMOC and diminished influence of AABW (Fig. 3.4a) (Henry et al., 2016), higher sea level (Fig. 3.4b) (Grant et al., 2014), warm sea surface temperatures (SST, Fig. 3.4c) (Martrat et al., 2007), reduced sea ice cover (Fig. 3.4d) (Hoff et al., 2016) and the absence of ice-rafted debris (IRD, Fig. 3.4h) (Schönfeld et al., 2003). Vegetation records from the Eifel Maar lakes (Figs. 3.4e – g and S3.1) (Sirocko et al., 2022), which are located approximately 300 km from Bleßberg Cave (Fig. S3.1), indicate a warm temperate mixed forest during early MIS 3 (around 60 – 48 ka BP), which was characterized by an increased abundance of *Picea* and *Carpinus* and a low abundance of *Poacaea*. This phase is also characterised by a very low abundance of IRD and correlates with the longer growth phases of the Bleßberg speleothems during DO events 16, 14 and 13 (Fig. 3.4i). Speleothem growth was absent during Heinrich event 5 (H5) and the increased abundance of *Poacaea* suggest generally cold climate. This is supported by reduced SST a peak in the IRD record and increased sea ice cover (Fig. 3.4). The middle part of MIS 3 (ca. 47 – 40 ka BP) was characterised by a continuous abundance of *Picea* and sporadic abundance of *Carpinus*. During DO 12, the abundance of *Poacaea* briefly decreased, but then increased again indicating a cold temperate forest. Speleothem growth during this phase was restricted to two short growth phases corresponding to DO events 12 and 11. Speleothem growth was absent during H4, which was preceded by relatively short DO events and is characterised by a large peak in IRD. The vegetation was sparse and dominated by *Poacaea*. During late MIS 3 (38 – 32 ka BP), the vegetation in the Eifel region was dominated by a *Poacaea* dominated grassland. Nevertheless, we observe three speleothem growth phases, which occurred during times of reduced abundance of *Poacaea*. In general, the most prominent speleothem growth phases occurred during phases of low IRD, reduced sea ice and higher SST (Fig. 3.4).

The most prominent growth phase of the Bleßberg composite record (Fig. 3.4i) is from ca. 53.5 – 50.5 ka BP and corresponds with DO 14, which is the longest (4.6 ka) DO event during MIS 3. DO 14 is characterised by persistently high summer SSTs (Fig. 3.4d), a reduced sea ice cover (Fig. 3.4c) and a persistently, relatively high (~ 50 %) abundance of *Picea* (Fig. 3.4f). The abundance of *Carpinus* reaches the highest level (~ 30 %) of MIS 3 during DO 14, suggesting the warmest climate conditions of MIS 3. The onset of DO 14 is

characterised by a sharp decrease in AABW contribution into the Atlantic and a delayed, but substantial (ca. 10 m) rise in sea level. The prominent Bleßberg growth phase (Fig. 3.4i) correlates very well with these observations, documenting that long, continuous speleothem growth phases in Bleßberg Cave were only possible during the warmest and most stable phase of MIS 3. This is supported by the observation that speleothem growth stopped coincidently with the high abundance of *Carpinus*, even if the abundance of *Picea*, which needs less warm conditions, remained on the same level.

The only growth phase of the composite record, which is contained in all three speleothem samples, is the growth phase concordant with DO 8. This DO event followed H4, and the vegetation was dominated by grassland and trees suggesting colder conditions (Sirocko et al., 2022). H4 is reflected by a substantial amount of IRD (Fig. 3.4h), which gradually reduced with the beginning of our speleothem growth phase associated with DO 8. The timing of the growth phase is in agreement with the peak of summer SST and the reduction of AABW.

During DO 7, a short growth phase at Bleßberg Cave was recorded, which fits very well with a short reduction of IRD in the middle of the DO event. Similarly, the timing of the growth phase is in agreement with a brief reduction in the abundance of *Poacaea* and the minimum of sea ice cover during the DO event. DO 7 is one of the shortest events (0.74 ka), when speleothem growth in Bleßberg cave was recorded. In addition, the vegetation reconstruction from the Eifel maar lakes does not indicate particularly warm conditions. This suggests that short speleothem growth phases can even occur without a well-established vegetation cover and during very short phases of stable climate conditions and highlights their potential as a climate proxy.

The growth phase during DO 12 is relatively short (0.74 ka), even if DO 12 is the second longest event (2.6 ka) of MIS 3 and associated with the highest summer SST (Fig. 3.4). The timing of our growth phase is consistent with the warmest phase of the event, as suggested by a minimum in sea ice cover and the peak abundance of *Picea* (ca. 60 %). Interestingly, the stop of speleothem growth coincides with a large IRD peak (Fig. 3.4). This may indicate a climatic reason for the cessation of speleothem growth. It can, however, not be excluded that the IRD peak corresponds to H5 and thus occurred prior to our growth phase. A peak in the abundance of *Carpinus* towards the end of DO 12 (ca. 45 ka BP) suggests a short phase of warm climate, but speleothem growth did not

resume. This shows that speleothem growth may also be affected by other processes than climate, such as re-routing of the drip water within the aquifer. Thus, the absence of growth does not necessarily indicate cold and/or dry conditions. The occurrence of speleothem growth, however, certainly shows that the climatic conditions were favourable (i.e., no permafrost and at least some vegetation cover above the cave).

The majority of the Bleßberg speleothem growth phases show a lag (between 0.16 to 1.18 ka) compared to the DO onsets recorded in Greenland ice cores (Fig. 3.4). For one growth phase, we observe a lead of 0.04 ka, and the timing of DO 11 is synchronous with the onset in the ice core. The magnitude of the lag is not related to the magnitude or length of the cold periods prior to the event (e.g., for Heinrich events). Similarly, we do not observe a relationship with the magnitude of the temperature increase of the corresponding DO event. The absence of the shortest and coldest DO events in the Bleßberg speleothem record suggests that the delay of the Bleßberg growth phases is rather related to the time required to establish favourable conditions for speleothem growth than the time required to transfer the climate signal from the North Atlantic to Central Europe. This includes the availability of liquid water, the thawing of permafrost, and the development of soil and vegetation cover above the cave.

In addition, the total duration of the Bleßberg speleothem growth phases is generally shorter than the duration of the corresponding DO events in Greenland ice cores. On average, the duration of the speleothem growth phases covers approximately 70 % of the total duration of the DO events (Table S3.6). This suggests that during the onset of the DO events in Greenland, the climate in Central Europe was still too cold, and potential permafrost conditions in combination with a strongly reduced or absent vegetation cover above the cave prohibited speleothem growth. The beginning of speleothem growth in Bleßberg Cave marks the crossing of a certain temperature threshold, and the following growth period reflects the warmest conditions during the corresponding event in Central Europe. In most cases, speleothem growth ceased prior to the end of the corresponding DO event in Greenland, indicating that non-favourable conditions for speleothem formation returned towards the end of the event.

In summary, the flowstones from Bleßberg cave can provide a better understanding of the timing and duration of DO events even if our data suggest a systematic lag between the onset of the speleothem growth phases and the DO events recorded in Greenland ice cores.

Similarly, the duration of our growth phases seems to be systematically shorter than that of the corresponding DO events suggesting that the speleothems only record the peak warming of the events. The record of Bleßberg speleothem growth phases can thus be interpreted as snapshots of the particularly warm phases of MIS 3, and our results highlight that large portions of MIS 3 in Central Europe had favourable conditions to enable speleothem growth. Speleothem growth phases from temperate climate zones generally have great potential to determine favourable climatic conditions. However, due to the complex growth characteristics on the µm-scale, a variety of sampling and analytical techniques is required to make use of the full potential of this climate archive.

3.3 Methods

3.3.1 Sampling procedure

All sampling procedures and measurements described in the following were conducted at the Institute for Geosciences, Johannes Gutenberg University Mainz.

Due to the typically very thin growth layers of our flowstone samples, we applied different sampling techniques. Since BB-10 and BB-15 show longer/thicker sections of continuous growth, the majority of samples was taken using a handheld drill (sample sizes of approximately 50 mg). For BB-9, the thickness of the individual MIS 3 growth phases is much thinner and varies between 3.9 to 0.6 mm. Therefore, we used a MicroMill device (Dettman and Lohmann, 1995) with a drill bit of 300 or 500 µm thickness for sampling (approximately 15 mg). However, even with these sampling techniques, it was not always possible to completely avoid detrital contamination, indicated by ($^{230}Th/^{232}Th$) < 200 (compare Table S7).

3.3.2 Solution $^{230}Th/U$-dating

Powdered samples were processed in a clean room laboratory for chemical separation of U and Th (see Table S1 for details). All acids used during chemical treatment were of trace-metal grade quality. Samples were weighed, dissolved in 7N HNO_3 and subsequently spiked with a previously calibrated ^{229}Th-^{233}U-^{236}U spike solution. The spike was

gravimetrically prepared and then calibrated against IRMM074/10(Richter et al., 2009) and a solution prepared from speleothem sample WM 1 from Wilder Mann Cave, which has an approximate age of 2.02 Ma (Meyer et al., 2009) and is therefore in secular equilibrium (Cheng et al., 2013) i.e., ($^{234}U/^{238}U$) = ($^{230}Th/^{238}U$) = 1. The samples were evaporated to dryness and treated with concentrated HNO_3, HCl and H_2O_2 in order to destroy any organic material prior to chemical separation. The samples were then evaporated again, dissolved in 7N HNO_3 and passed through ion exchange columns filled with 1.5 mL of Bio-Rad AG 1-X8 (200 – 400 mesh size) anion exchange resin to separate U and Th. The procedure (Table S1) was carried out twice and followed a method developed at the Berkely Geochronology Center, which is based on the procedure described in Edwards et al. (1987). With each sample set, a subsample of the WM 1 solution was prepared and analysed for quality control, yielding activity ratios of ($^{230}Th/^{238}U$) = 1.00001 ± 0.00038 and ($^{234}U/^{238}U$) = 0.99997 ± 0.00021 (2SE, n = 55, within a 12-month period).

Mass spectrometric analyses of U and Th were conducted using a Thermo Fischer Scientific Neptune Plus multi-collector inductively coupled plasma mass spectrometer (MC-ICP-MS) equipped with an Elemental Scientific Apex Omega HF desolvator. U and Th were measured separately in a standard-bracketing procedure and the data were corrected offline using an in-house R-script (Team, 2023) correcting for mass fractionation, ion counter yield, instrumental drift and tailing. Each sample is analysed in standard-sample-bracketing (SBB) mode, accounting for instrumental drift during the analytical session. For U, the CRM112-A Uranium Isotopic Standard is analysed prior to and after each sample, while for Th an in-house Th standard solution with known isotope ratios of ^{229}Th, ^{230}Th and ^{232}Th is analysed. Mass fractionation is determined for each standard by analysing $^{235}U/^{238}U$ or $^{229}Th/^{232}Th$, respectively. Within the same analysis, ion counter yield for IC1 is determined by analysing $^{234}U/^{238}U$ or $^{230}Th/^{232}Th$, both previously corrected for mass fractionation. Tailing is determined externally by analysing a concentrated CRM 112-A U solution (containing ^{234}U, ^{235}U, ^{238}U) or a natural Th solution (containing ^{232}Th) at the beginning and at the end of each analytical session. Abundance sensitivity is calculated and corrected for isotopes of ^{229}Th, ^{230}Th, ^{233}U and ^{236}U.

All ages were calculated using the half-lives reported by Cheng et al. (2013). Due to the very thin growth layers of our flowstone samples (especially BB-9), some samples show ($^{230}Th/^{232}Th$) < 10 (Table S7) and are thus significantly affected by detrital contamination. This is particularly the case for samples close to hiatuses. To better constrain the

($^{232}Th/^{238}U$) activity ratio of the detrital material, we applied the approach of Budsky et al. (2019a) to the solution data. This algorithm minimises the sum of all apparent age inversions by iteratively varying the ($^{232}Th/^{238}U$) activity ratio of the detrital material, $(^{232}Th/^{238}U)_d$ (Klaes et al., 2022). The resulting $(^{232}Th/^{238}U)_d$ is 0.953 ± 0.477, which is in agreement within uncertainty with the conventionally used correction factor of $(^{232}Th/^{238}U)_d$ = 1.243 ± 0.622 based on the global mean ratio of the upper crust.

3.3.3 Laser Ablation MC-ICP-MS ^{230}Th/U-dating

In-situ analyses for ^{230}Th/U-dating have been performed using the Neptune Plus MC-ICP-MS coupled to an ESI New Wave NWR 193 nm ArF excimer laser ablation system (LA-MC-ICP-MS) with a TwoVol2 cell. To enhance sensitivity and introduce N_2 for signal stabilisation, an ESI Apex Omega HF desolvator system was additionally coupled with the sample outlet being connected with a Y-connector to the sample gas line originating from the laser ablation system. Instrumental details are summarised in Table S3.3.

Due to the low abundance of the decay products ^{234}U and ^{230}Th, both isotopes are monitored using the central ion counter. Therefore, two separate line scans are necessary to calculate ^{230}Th ages with the instrumental setup during this study (cup configuration in Table S3.4). Prior to each analysis, 30 s of background data was collected without the laser firing and subtracted from the signals monitored during sample ablation. Speleothem sample WM 1 was used as bracketing standard, as this speleothem is in secular equilibrium. A first line scan (line scan 1, Table S4) performed on WM 1 was used to determine the mass fractionation factor β based on the naturally invariant $^{235}U/^{238}U$, and a correction factor for ($^{230}Th/^{238}U$) correcting for mass fractionation, ion counter yield and inter-element fractionation, which was then applied to the unknown speleothem samples. Similarly, a second line scan (line scan 2, Table S3.4) on WM 1 was used to determine a correction factor for ($^{234}U/^{238}U$), correcting for mass fractionation and ion counter yield. Similar to the solution ^{230}Th/U-dating, the ($^{232}Th/^{238}U$) from the speleothem samples was used to correct for detrital contamination, using the previously determined detrital correction factor of $(^{232}Th/^{238}U)_d$ = 0.953 ± 0.477.

LA-MC-ICP-MS allows fast data acquisition and less destructive sampling compared to the drilling techniques. For each age determination, two line scans parallel to the growth

layers were conducted (1000 µm length, 150 mm spot size, 100 Hz laser frequency) in close proximity to determine ($^{230}Th/^{238}U$) and ($^{234}U/^{238}U$) in two separate measurements. LA-MC-ICP-MS ^{230}Th-dating was applied to samples BB-9 and -10. A global correction factor for $^{230}Th/^{238}U$ and $^{234}U/^{238}U$ was determined for each standard of WM 1. The obtained isotope ratios of $^{230}Th/^{238}U$ and $^{234}U/^{238}U$ were calculated into activity ratios using the decay constants from Cheng et al. (2013), resulting in a global correction factor accounting for mass bias, ion counter yield and inter-element fractionation. This correction factor was then applied to sample activity ratios of ($^{230}Th/^{238}U$) and ($^{234}U/^{238}U$).

In addition to the line scan measurements along the growth layers, several line scans were conducted parallel to the growth axis (i.e., vertical to the growth layers) across the hiatuses (Fig. S3.2). The data from these transects was used to calculate mean $^{230}Th/U$-ages at 0.2 mm spatial resolution between a selected depth, which increased the number of individual ages. Large and rapid changes (Fig. S3.4) in the calculated initial ($^{234}U/^{238}U$) activity ratios, $(^{234}U/^{238}U)_i$, calculated as $(^{234}U/^{238}U)_i = (^{234}U/^{238}U) * \exp(l_{234} * t)$, where t is the $^{230}Th/U$-age, were used to determine growth stops, which are not visible or reflected by changes in the trace element data.

3.3.4 Trace element analysis and mapping

Trace element analysis was conducted by LA-ICP-MS using an ESI New Wave NWR 193 nm ArF Excimer laser system coupled to an Agilent 7500ce ICP-MS. A continuous line scan from top to bottom was conducted for samples BB-9 and BB-10 with the intensities of ^{27}Al, ^{232}Th and ^{238}U monitored. The laser parameters used were a rectangular spot size of 130 x 50 µm, a transition rate of 10 µm/s and a laser repetition rate of 10 Hz, resulting in a fluence of 3.5 J/cm^2. For calibration purposes, NIST SRM 610 was analysed several times during the analyses, together with several other quality control materials including NIST SRM 612, BCR-2G and MACS3. For all analyses, ^{43}Ca was used as an internal reference, and data evaluation was performed offline following the calculations presented in Mischel et al. (2017). Prior to each analysis, a pre-ablation was performed. A principal component analysis (PCA) of the trace element data was conducted using the prcomp() function of the statistical software R (Team, 2020) in order to identify the detrital component within the trace elements.

The mapping of the trace element distribution (^{27}Al, ^{238}U) was performed using the Matlab script MapIT! (Sforna and Lugli, 2017) using the same instrumental LA-ICP-MS setup as described above. NIST SRM 610 was used for calibration purposes. The final map consists of a total number of 33 line scans with a circular spot size of 80 µm resulting in a mapping area of 25,000 x 2640 µm. A transition rate of 50 µm/s was used. No pre-ablation was performed prior to the mapping.

3.3.5 Age-depth modelling

The individual growth phases of our flowstone samples are exceptionally thin. For the majority of growth phases, it is, thus, not possible to determine several high-precision solution $^{230}Th/U$-ages, even if sampling is conducted using the MicroMill. In addition, the solution ages are often affected by detrital contamination resulting in substantially increased uncertainties. This is particularly problematic for the thinnest growth phases. However, for all growth phases several high-resolution LA-MC-ICP-MS $^{230}Th/U$-ages are available, even if those are associated with much larger uncertainties than the solution ages (Fig. 3.2 a and b). The age data for the individual flowstone growth phases, thus, usually consist of a few (sometimes only a single) high-precision solution ages and several less precise LA-MC-ICP-MS ages. The uncertainty of the LA-MC-ICP-MS ages is, on average, larger by a factor of > 10 compared to the solution ages. This also implies that each growth phase shows various age inversions within uncertainty (Fig. 3.2a and b).

The conventionally used methods for age-depth modelling in speleothems are designed for ages with a spatial resolution of a few mm to a few cm, comparable age uncertainty and only a limited number of age inversions (for details see Comas-Bru et al., 2020; Scholz et al., 2012). Thus, these algorithms, such as linear interpolation, StalAge (Scholz and Hoffmann, 2011) or COPRA (Breitenbach et al., 2012) cannot be applied to the very high-spatial resolution age data of our flowstone samples.

Here we use a modified version of an error-weighted linear regression (i.e. the York fit (York et al., 2004)), which accounts for uncertainties in both x- and y-direction (i.e., the york() function implemented in R-package IsoplotR (Vermeesch, 2018)). Since the growth rate of the speleothem cannot be negative (i.e., it needs to become progressively older with increasing distance from top), negative slopes of the fit must be excluded. To account for

this, we perform a Monte-Carlo simulation with the results of the York-fit (i.e., slope, intercept and the corresponding covariance) and exclude those simulations with a negative slope. Based on these simulations, we also calculate the Mean Square of Weighted Deviates (MSWD) and the probability of fit for the fits with a positive slope (Table S3.8). These two parameters allow to assess whether the assumptions of a linear regression are justified by the assigned analytical errors i.e., if the observed scatter around the regression is comparable with the age uncertainties, for a detailed discussion see Ludwig (Ludwig, 2003). In case of probabilities of fit < 0.05, indicating excess scatter, we use the established methods for excess scatter isochrons and expand the uncertainties by the square root of MSWD and the corresponding Student's t factor for a confidence level of 95 % (Ludwig, 2003). In other words, if the ages and uncertainties suggest that the age data of a growth phase cannot be described by a linear regression (e.g., due to a change in the growth rate), the uncertainties of the age model are increased accordingly.

We then use the results of our Monte-Carlo simulations to calculate the median age model, the corresponding 95 %-confidence limits and the probability distributions/histograms of the simulated age data (Figs. 3.2 and 3.3).

3.4 Data availability

The ^{230}Th/U data compiled for this study are provided in Supplementary Table S3.7.

3.5 Acknowledgements

Financial support for this project was provided by the Deutsche Forschungsgemeinschaft through grant SCHO 1274/14-1 to DS and WE 7074/1-1 to MW. We also acknowledge financial support from the Max Planck Graduate Center Mainz. The authors would like to thank Viktoria Blumrich for assistance with the measurement of the ^{230}Th/U-ages and Sebastian Breitenbach for helpful discussions regarding this manuscript and the project in general. We would also like to thank the Thüringer Höhlenverein e.V. for supporting the project and providing insight into the cave and speleothem samples.

3.6 Author Contributions

DS designed the study. JK conducted the sampling, the chemical preparation for the solution ^{230}Th/U analysis and the measurement for solution ^{230}Th/U-dating. MW set up the LA ^{230}Th/U dating method, MW and JK conducted the measurements of the LA ^{230}Th/U ages, MW evaluated the data. Trace element measurements and evaluation were performed by JK, and the trace element mapping was done by MW and JK, MW evaluated the data. The script for age modelling was developed and written by DS, and JK constructed the age models. All authors contributed to the discussion and interpretation of the data, and the writing of the manuscript.

3.7 Competing interests

The authors declare no competing interests.

3.9 References

Adolphi, F., Bronk Ramsey, C., Erhardt, T., Edwards, R.L., Cheng, H., Turney, C.S.M., Cooper, A., Svensson, A., Rasmussen, S.O., Fischer, H. and Muscheler, R., 2018. Connecting the Greenland ice-core and U/Th timescales via cosmogenic radionuclides: testing the synchroneity of Dansgaard–Oeschger events. Climate of the Past, 14(11): 1755-1781.

Andersen, K.K., Svensson, A., Johnsen, S.J., Rasmussen, S.O., Bigler, M., Röthlisberger, R., Ruth, U., Siggaard-Andersen, M.-L., Peder Steffensen, J. and Dahl-Jensen, D., 2006. The Greenland Ice Core Chronology 2005, 15–42ka. Part 1: constructing the time scale. Quaternary Science Reviews, 25(23-24): 3246-3257.

Atkinson, T., Harmon, R., Smart, P. and Waltham, A., 1978. Palaeoclimatic and geomorphic implications of ^{230}Th/^{234}U dates on speleothems from Britain. Nature, 272(5648): 24-28.

Barker, S., Chen, J., Gong, X., Jonkers, L., Knorr, G. and Thornalley, D., 2015. Icebergs not the trigger for North Atlantic cold events. Nature, 520(7547): 333-336.

Barker, S., Diz, P., Vautravers, M.J., Pike, J., Knorr, G., Hall, I.R. and Broecker, W.S., 2009. Interhemispheric Atlantic seesaw response during the last deglaciation. Nature, 457(7233): 1097-1102.

Birchfield, G.E. and Broecker, W.S., 1990. A salt oscillator in the glacial Atlantic? 2. A "scale analysis" model. Paleoceanography, 5(6): 835-843.

Boers, N., Ghil, M. and Rousseau, D.-D., 2018. Ocean circulation, ice shelf, and sea ice interactions explain Dansgaard–Oeschger cycles. Proceedings of the National Academy of Sciences, 115(47): E11005-E11014.

Bond, G., Broecker, W., Johnsen, S., McManus, J., Labeyrie, L., Jouzel, J. and Bonani, G., 1993. Correlations between climate records from North Atlantic sediments and Greenland ice. Nature, 365(6442): 143-147.

Breitenbach, S.F., Plessen, B., Waltgenbach, S., Tjallingii, R., Leonhardt, J., Jochum, K.P., Meyer, H., Goswami, B., Marwan, N. and Scholz, D., 2019. Holocene interaction of maritime and

continental climate in Central Europe: New speleothem evidence from Central Germany. Global and Planetary Change, 176: 144-161.

Breitenbach, S.F., Rehfeld, K., Goswami, B., Baldini, J.U., Ridley, H.E., Kennett, D.J., Prufer, K.M., Aquino, V.V., Asmerom, Y. and Polyak, V.J., 2012. Constructing proxy records from age models (COPRA). Climate of the Past, 8(5): 1765-1779.

Broecker, W.S., Peteet, D.M. and Rind, D., 1985. Does the ocean–atmosphere system have more than one stable mode of operation? Nature, 315(6014): 21-26.

Budsky, A., Scholz, D., Wassenburg, J.A., Mertz-Kraus, R., Spötl, C., Riechelmann, D.F., Gibert, L., Jochum, K.P. and Andreae, M.O., 2019a. Speleothem $\delta^{13}C$ record suggests enhanced spring/summer drought in south-eastern Spain between 9.7 and 7.8 ka – A circum-Western Mediterranean anomaly? The Holocene, 29(7): 1113-1133.

Budsky, A., Wassenburg, J.A., Mertz-Kraus, R., Spötl, C., Jochum, K.P., Gibert, L. and Scholz, D., 2019b. Western Mediterranean climate response to Dansgaard/Oeschger events: New insights from speleothem records. Geophysical Research Letters, 46(15): 9042-9053.

Cheng, H., Edwards, R.L., Shen, C.-C., Polyak, V.J., Asmerom, Y., Woodhead, J., Hellstrom, J., Wang, Y., Kong, X. and Spötl, C., 2013. Improvements in ^{230}Th dating, ^{230}Th and ^{234}U half-life values, and U–Th isotopic measurements by multi-collector inductively coupled plasma mass spectrometry. Earth and Planetary Science Letters, 371: 82-91.

Cheng, H., Edwards, R.L., Sinha, A., Spötl, C., Yi, L., Chen, S., Kelly, M., Kathayat, G., Wang, X. and Li, X., 2016. The Asian monsoon over the past 640,000 years and ice age terminations. nature, 534(7609): 640-646.

Comas-Bru, L., Rehfeld, K., Roesch, C., Amirnezhad-Mozhdehi, S., Harrison, S.P., Atsawawaranunt, K., Ahmad, S.M., Brahim, Y.A., Baker, A. and Bosomworth, M., 2020. SISALv2: a comprehensive speleothem isotope database with multiple age–depth models. Earth System Science Data, 12(4): 2579-2606.

Corrick, E.C., Drysdale, R.N., Hellstrom, J.C., Capron, E., Rasmussen, S.O., Zhang, X., Fleitmann, D., Couchoud, I. and Wolff, E., 2020. Synchronous timing of abrupt climate changes during the last glacial period. Science, 369(6506): 963-969.

Dansgaard, W., Johnsen, S.J., Clausen, H.B., Dahl-Jensen, D., Gundestrup, N.S., Hammer, C.U., Hvidberg, C.S., Steffensen, J.P., Sveinbjörnsdottir, A.E., Jouzel, J. and Bond, G., 1993. Evidence for general instability of past climate from a 250-kyr ice-core record. Nature, 364: 218 - 220.

Dettman, D.L. and Lohmann, K.C., 1995. Microsampling carbonates for stable isotope and minor element analysis: Physical separation of samples on a 20 micrometer scale. Journal of Sedimentary Research, 65(3).

Edwards, R.L., Chen, J. and Wasserburg, G., 1987. $^{238}U^{234}U^{230}Th^{232}Th$ systematics and the precise measurement of time over the past 500,000 years. Earth and Planetary Science Letters, 81(2-3): 175-192.

Erhardt, T., Capron, E., Rasmussen, S.O., Schüpbach, S., Bigler, M., Adolphi, F. and Fischer, H., 2019. Decadal-scale progression of the onset of Dansgaard–Oeschger warming events. Clim. Past, 15(2): 811-825.

Fohlmeister, J., Sekhon, N., Columbu, A., Vettoretti, G., Weitzel, N., Rehfeld, K., Veiga-Pires, C., Ben-Yami, M., Marwan, N. and Boers, N., 2023. Global reorganization of atmospheric circulation during Dansgaard–Oeschger cycles. Proceedings of the National Academy of Sciences, 120(36): e2302283120.

Genty, D., Blamart, D., Ouahdi, R., Gilmour, M., Baker, A., Jouzel, J. and Van-Exter, S., 2003. Precise dating of Dansgaard–Oeschger climate oscillations in western Europe from stalagmite data. Nature, 421(6925): 833-837.

Goni, M.F.S. and Harrison, S.P., 2010. Millennial-scale climate variability and vegetation changes during the Last Glacial: Concepts and terminology. Quaternary Science Reviews, 29(21-22): 2823-2827.

Grant, K., Rohling, E., Ramsey, C.B., Cheng, H., Edwards, R., Florindo, F., Heslop, D., Marra, F., Roberts, A. and Tamisiea, M.E., 2014. Sea-level variability over five glacial cycles. Nature communications, 5(1): 5076.

Hemming, S.R., 2004. Heinrich events: Massive late Pleistocene detritus layers of the North Atlantic and their global climate imprint. Reviews of Geophysics, 42(1).

Henry, L., McManus, J., Curry, W., Roberts, N., Piotrowski, A. and Keigwin, L., 2016. North Atlantic ocean circulation and abrupt climate change during the last glaciation. Science, 353(6298): 470-474.

Hoff, U., Rasmussen, T.L., Stein, R., Ezat, M.M. and Fahl, K., 2016. Sea ice and millennial-scale climate variability in the Nordic seas 90 kyr ago to present. Nature communications, 7(1): 12247.

Johnsen, S., Clausen, H., Dansgaard, W., Fuhrer, K., Gundestrup, N., Hammer, C., Iversen, P., Jouzel, J., Stauffer, B. and Steffensen, J., 1992. Irregular glacial interstadials recorded in a new Greenland ice core. Nature, 359(6393): 311-313.

Kanner, L.C., Burns, S.J., Cheng, H. and Edwards, R.L., 2012. High-latitude forcing of the South American summer monsoon during the last glacial. Science, 335(6068): 570-573.

Kathayat, G., Cheng, H., Sinha, A., Spötl, C., Edwards, R., Zhang, H., Li, X., Yi, L., Ning, Y. and Cai, Y., 2016. Indian monsoon variability on millennial-orbital timescales, Sci. Rep., 6, 24374.

Kindler, P., Guillevic, M., Baumgartner, M., Schwander, J., Landais, A. and Leuenberger, M., 2014. Temperature reconstruction from 10 to 120 kyr b2k from the NGRIP ice core. Clim. Past, 10(2): 887-902.

Klaes, B., Wörner, G., Kremer, K., Simon, K., Kronz, A., Scholz, D., Mueller, C.W., Höschen, C., Struck, J. and Arz, H.W., 2022. High-resolution stalagmite stratigraphy supports the Late Holocene tephrochronology of southernmost Patagonia. Communications Earth & Environment, 3(1): 23.

Lane, C.S., Brauer, A., Blockley, S.P. and Dulski, P., 2013. Volcanic ash reveals time-transgressive abrupt climate change during the Younger Dryas. Geology, 41(12): 1251-1254.

Ludwig, K., 2003. Mathematical–statistical treatment of data and errors for ^{230}Th/U geochronology. Reviews in Mineralogy and Geochemistry, 52(1): 631-656.

Martrat, B., Grimalt, J.O., Shackleton, N.J., de Abreu, L., Hutterli, M.A. and Stocker, T.F., 2007. Four climate cycles of recurring deep and surface water destabilizations on the Iberian margin. Science, 317(5837): 502-507.

Menviel, L., Timmermann, A., Friedrich, T. and England, M., 2014. Hindcasting the continuum of Dansgaard–Oeschger variability: mechanisms, patterns and timing. Climate of the Past, 10(1): 63-77.

Meyer, M., Cliff, R., Spötl, C., Knipping, M. and Mangini, A., 2009. Speleothems from the earliest Quaternary: Snapshots of paleoclimate and landscape evolution at the northern rim of the Alps. Quaternary Science Reviews, 28(15-16): 1374-1391.

Mischel, S.A., Mertz-Kraus, R., Jochum, K.P. and Scholz, D., 2017. TERMITE: An R script for fast reduction of laser ablation inductively coupled plasma mass spectrometry data and its application to trace element measurements. Rapid Communications in Mass Spectrometry, 31(13): 1079-1087.

Moseley, G.E., Spötl, C., Brandstätter, S., Erhardt, T., Luetscher, M. and Edwards, R.L., 2020. NALPS19: Sub-orbital-scale climate variability recorded in northern Alpine speleothems during the last glacial period. Climate of the Past, 16(1): 29-50.

Moseley, G.E., Spötl, C., Svensson, A., Cheng, H., Brandstätter, S. and Edwards, R.L., 2014. Multi-speleothem record reveals tightly coupled climate between central Europe and Greenland during Marine Isotope Stage 3. Geology, 42(12): 1043-1046.

NGRIP Project members, 2004. High-resolution record of Northern Hemisphere climate extending into the last interglacial period. Nature, 431(7005): 147-151.

Peterson, L.C., Haug, G.H., Hughen, K.A. and Rohl, U., 2000. Rapid changes in the hydrologic cycle of the tropical Atlantic during the last glacial. Science, 290(5498): 1947-1951.

Prud'homme, C., Fischer, P., Jöris, O., Gromov, S., Vinnepand, M., Hatté, C., Vonhof, H., Moine, O., Vött, A. and Fitzsimmons, K.E., 2022. Millennial-timescale quantitative estimates of climate dynamics in central Europe from earthworm calcite granules in loess deposits. Communications Earth & Environment, 3(1): 267.

Rach, O., Brauer, A., Wilkes, H. and Sachse, D., 2014. Delayed hydrological response to Greenland cooling at the onset of the Younger Dryas in western Europe. Nature Geoscience, 7(2): 109-112.

Rasmussen, S.O., Bigler, M., Blockley, S.P., Blunier, T., Buchardt, S.L., Clausen, H.B., Cvijanovic, I., Dahl-Jensen, D., Johnsen, S.J., Fischer, H., Gkinis, V., Guillevic, M., Hoek, W.Z., Lowe, J.J., Pedro, J.B., Popp, T., Seierstad, I.K., Steffensen, J.P., Svensson, A.M., Vallelonga, P., Vinther, B.M., Walker, M.J.C., Wheatley, J.J. and Winstrup, M., 2014. A stratigraphic framework for abrupt climatic changes during the Last Glacial period based on three synchronized Greenland ice-core records: refining and extending the INTIMATE event stratigraphy. Quaternary Science Reviews, 106: 14-28.

Reinig, F., Wacker, L., Jöris, O., Oppenheimer, C., Guidobaldi, G., Nievergelt, D., Adolphi, F., Cherubini, P., Engels, S. and Esper, J., 2021. Precise date for the Laacher See eruption synchronizes the Younger Dryas. Nature, 595(7865): 66-69.

Richards, D.A. and Dorale, J.A., 2003. Uranium-series chronology and environmental applications of speleothems. Reviews in Mineralogy and Geochemistry, 52(1): 407-460.

Richter, D., Meissner, P., Immenhauser, A., Schulte, U. and Dorsten, I., 2010. Cryogenic and non-cryogenic pool calcites indicating permafrost and non-permafrost periods: a case study from the Herbstlabyrinth-Advent Cave system (Germany). The Cryosphere, 4(4): 501-509.

Richter, D.K., Goll, K., Grebe, W., Niedermayr, A., Platte, A. and Scholz, D., 2015. Weichselzeitliche Kryocalcite als Hinweise für Eisseen in der Hüttenbläserschachthöhle (Iserlohn/NRW). E&G Quaternary Science Journal, 64(2): 67-81.

Richter, D.K., Scholz, D., Jöns, N., Neuser, R.D. and Breitenbach, S.F., 2018. Coarse-grained cryogenic aragonite as end-member of mineral formation in dolomite caves. Sedimentary Geology, 376: 136-146.

Richter, S., Alonso, A., Aregbe, Y., Eykens, R., Kehoe, F., Kühn, H., Kivel, N., Verbruggen, A., Wellum, R. and Taylor, P., 2009. A new series of uranium isotope reference materials for investigating the linearity of secondary electron multipliers in isotope mass spectrometry. International Journal of Mass Spectrometry, 281(3): 115-125.

Sachs, J.P. and Lehman, S.J., 1999. Subtropical North Atlantic temperatures 60,000 to 30,000 years ago. Science, 286(5440): 756-759.

Scholz, D. and Hoffmann, D., 2008. ^{230}Th/U-dating of fossil corals and speleothems. E&G Quaternary Science Journal, 57(1/2): 52-76.

Scholz, D. and Hoffmann, D.L., 2011. StalAge–An algorithm designed for construction of speleothem age models. Quaternary Geochronology, 6(3-4): 369-382.

Scholz, D., Hoffmann, D.L., Hellstrom, J. and Ramsey, C.B., 2012. A comparison of different methods for speleothem age modelling. Quaternary Geochronology, 14: 94-104.

Schönfeld, J., Zahn, R. and de Abreu, L., 2003. Surface and deep water response to rapid climate changes at the Western Iberian Margin. Global and Planetary Change, 36(4): 237-264.

Sforna, M.-C. and Lugli, F., 2017. MapIT!: a simple and user-friendly MATLAB script to elaborate elemental distribution images from LA-ICP-MS data. Journal of Analytical Atomic Spectrometry, 32(5): 1035-1043.

Sime, L.C., Hopcroft, P.O. and Rhodes, R.H., 2019. Impact of abrupt sea ice loss on Greenland water isotopes during the last glacial period. Proceedings of the National Academy of Sciences, 116(10): 4099-4104.

Sirocko, F., Albert, J., Britzius, S., Dreher, F., Martínez-García, A., Dosseto, A., Burger, J., Terberger, T. and Haug, G., 2022. Thresholds for the presence of glacial megafauna in central Europe during the last 60,000 years. Scientific reports, 12(1): 20055.

Sirocko, F., Martínez-García, A., Mudelsee, M., Albert, J., Britzius, S., Christl, M., Diehl, D., Diensberg, B., Friedrich, R., Fuhrmann, F., Muscheler, R., Hamann, Y., Schneider, R., Schwibus, K. and Haug, G.H., 2021. Muted multidecadal climate variability in central Europe during cold stadial periods. Nature Geoscience, 14(9): 651-658.

Spötl, C. and Mangini, A., 2002. Stalagmite from the Austrian Alps reveals Dansgaard–Oeschger events during isotope stage 3:: Implications for the absolute chronology of Greenland ice cores. Earth and Planetary Science Letters, 203(1): 507-518.

Svensson, A., Andersen, K.K., Bigler, M., Clausen, H.B., Dahl-Jensen, D., Davies, S., Johnsen, S.J., Muscheler, R., Parrenin, F. and Rasmussen, S.O., 2008. A 60 000 year Greenland stratigraphic ice core chronology. Climate of the Past, 4(1): 47-57.

Team, R.C., 2020. R Core Team R: a language and environment for statistical computing. Foundation for Statistical Computing.

Team, R.C., 2023. R Development Core Team R: A Language and Environment for Statistical Computing 2023. R Core Team: Vienna, Austria.

Vaks, A., Gutareva, O.S., Breitenbach, S.F., Avirmed, E., Mason, A.J., Thomas, A.L., Osinzev, A.V., Kononov, A.M. and Henderson, G.M., 2013. Speleothems reveal 500,000-year history of Siberian permafrost. Science, 340(6129): 183-186.

Vandenberghe, J., French, H.M., Gorbunov, A., Marchenko, S., Velichko, A.A., Jin, H., Cui, Z., Zhang, T. and Wan, X., 2014. The L ast P ermafrost M aximum (LPM) map of the N orthern H emisphere: permafrost extent and mean annual air temperatures, 25–17 ka BP. Boreas, 43(3): 652-666.

Vermeesch, P., 2018. IsoplotR: A free and open toolbox for geochronology. Geoscience Frontiers, 9(5): 1479-1493.

Vettoretti, G., Ditlevsen, P., Jochum, M. and Rasmussen, S.O., 2022. Atmospheric CO_2 control of spontaneous millennial-scale ice age climate oscillations. Nature Geoscience, 15(4): 300-306.

Wang, X., Auler, A.S., Edwards, R.L., Cheng, H., Ito, E. and Solheid, M., 2006. Interhemispheric anti-phasing of rainfall during the last glacial period. Quaternary Science Reviews, 25(23-24): 3391-3403.

Weber, M., Scholz, D., Schröder-Ritzrau, A., Deininger, M., Spötl, C., Lugli, F., Mertz-Kraus, R., Jochum, K.P., Fohlmeister, J., Stumpf, C.F. and Riechelmann, D.F.C., 2018. Evidence of warm and humid interstadials in central Europe during early MIS 3 revealed by a multi-proxy speleothem record. Quaternary Science Reviews, 200: 276-286.

York, D., Evensen, N.M., Martínez, M.L. and De Basabe Delgado, J., 2004. Unified equations for the slope, intercept, and standard errors of the best straight line. American journal of physics, 72(3): 367-375.

Žák, K., Richter, D., Filippi, M., Živor, R., Deininger, M., Mangini, A. and Scholz, D., 2012. Coarsely crystalline cryogenic cave carbonate–a new archive to estimate the Last Glacial minimum permafrost depth in Central Europe. Climate of the Past, 8(6): 1821-1837.

Zhang, X., Knorr, G., Lohmann, G. and Barker, S., 2017. Abrupt North Atlantic circulation changes in response to gradual CO_2 forcing in a glacial climate state. Nature Geoscience, 10(7): 518-523.

Zhang, X., Lohmann, G., Knorr, G. and Purcell, C., 2014. Abrupt glacial climate shifts controlled by ice sheet changes. Nature, 512(7514): 290-294.

Supplementary Material for

Precisely dated speleothem growth phases as a proxy for particularly warm climate conditions during MIS 3 in Central Europe

Jennifer Klose[1*], Michael Weber[1], Denis Scholz[1]

*corresponding author: jeklose@uni-mainz.de

[1]Institute for Geosciences, Johannes Gutenberg University, Mainz, Germany

under revision in communications earth & environment

Cave setting

Bleßberg Cave was first discovered in 2008 during the construction works of the Bleßberg tunnel for a new high-speed rail line between Berlin and Munich. The NW-SE oriented cave is located close to the town Eisfeld in Germany at 50°25'28'' N and 11°01'13'' E (Fig. S1) at ca. 500 m above sea level at the southern fringe of the Thuringian schist mountains and developed in Triassic marly limestones (Lower Muschelkalk/Anisium). Bleßberg Cave is covered by 12 to 50 m of marly limestone (Lower and Middle Muschelkalk) and the vegetation above the cave is characterized by anthropogenically altered farmland and mixed deciduous and pine forests towards more uphill areas (Breitenbach et al., 2019). The modern climate at Bleßberg Cave can be characterised as Cfb climate in the Köppen-Geiger classification.

Before its discovery, the absence of a natural entrance prevented the cave from any human or animal disturbances. The cave atmosphere is relatively stable, but the ventilation of the cave might be influenced by a small stream running through the main passage of the cave (Breitenbach et al., 2019). During the discovery of the cave, construction workers tried to close the newfound cave entrance with concrete which led to flooding of the cave and a now disturbed cave system. In addition, the new rail line tunnel runs through the cave and now divides it into two sections. The eastern part of the cave system is not accessible anymore but was reopened once to obtain additional.

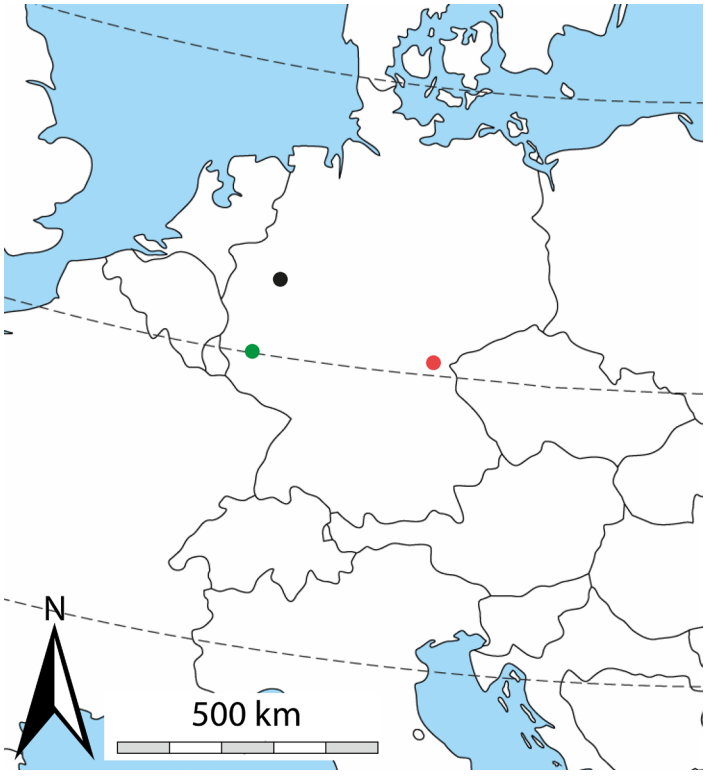

Fig. S3.1: Map of Central Europe. The red dot indicates the location of Bleßberg Cave (this study). The black dot indicates Bunker Cave, and the green dot indicates the location of the Eifel Maar lakes.

Samples BB-9, BB-10 and BB-15

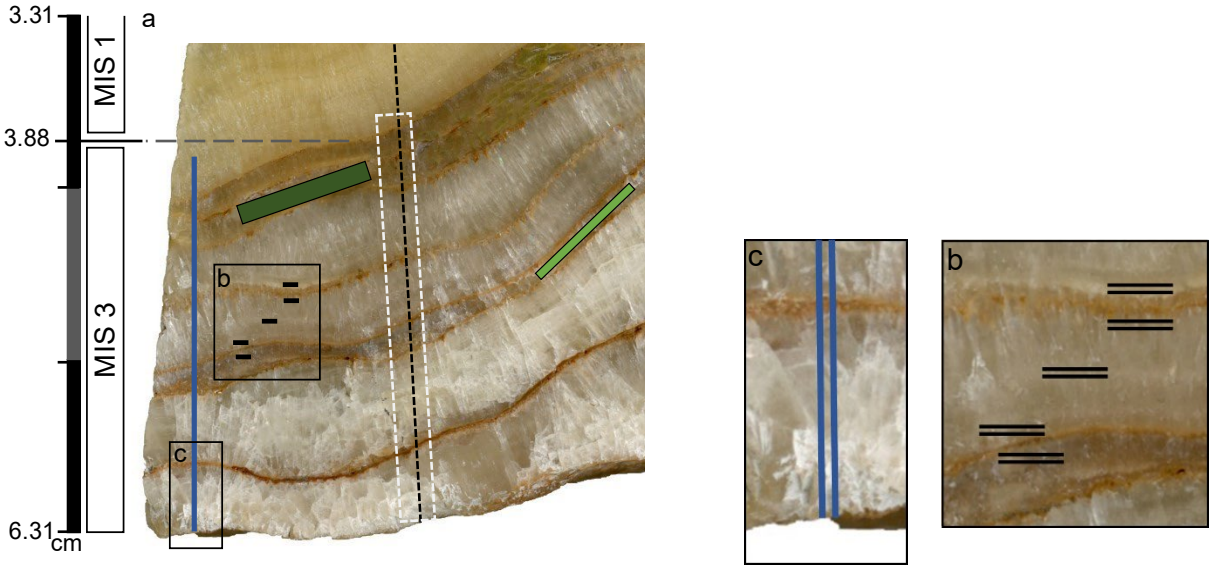

Fig. S3.2: Shows sample BB-9 and several sampling techniques for the ^{230}Th/U dating. Handheld drilling using a 1 mm drill bit (dark green), MicroMilling (light green) using a 300 or 500 µm drill bit as well as two different LA techniques, within the growth layer (black line) and parallel to the growth axis (blue line). The black dotted line represents the trace element track, and the white box highlights the trace element mapping area. b and c show a close-up of the LA techniques.

Fig. S3.3: Shows sample BB-10 a and -15 b. BB-10 on the left is a continuous sample but broken into several pieces. Both samples show several different drilling techniques for the ^{230}Th/U-dating sampling, see Fig. S3.2 for more information. The black boxes highlight growth during MIS 3.

^{230}Th/U-dating

Chemical Preparation

Prior to the procedure shown in Table S1, the samples were weighed, dissolved in 7N HNO_3 and subsequently spiked with a drop (~ 0.03 g) of previously calibrated ^{229}Th-^{233}U-^{236}U spike solution. The samples were evaporated to dryness and treated with concentrated HNO_3, HCl and H_2O_2 to destroy any organic material. The samples were then evaporated again and dissolved in 0.375 mL 7N HNO_3.

Table S3.1: Summary of chemical separation procedures for solution ^{230}Th/U-ages. The fractions of Th and U are each collected in respective beakers for each sample. The procedure to elute Th and U (and the waste fraction of Ca) is carried out twice. If the samples are very clean this might not be necessary. In that case, the procedure can be concluded after the first separation cycle, and it can proceed with the dissolution of the sample fitting for the used MC-ICP-MS. The used resin and columns were cleaned before the procedure and only used once and therefore discarded after the separation process.

resin volume (1 CV)	Bio-Rad AG1-X8 1.5 mL
rinse resin	4 CV 0.5N HCl 2CV H_2O 1 CV 7N HNO_3 add each step at once
load sample on column (U +Th) in	0.375 mL 7N HNO_3
elute Ca (waste)	2 CV 7N HNO_3 add stepwise
elute Th (collect)	5 CV 8N HCl add stepwise
elute U (collect)	4 CV 0.5 HCl add stepwise
dry samples down	
dissolve both fractions in	0.375 mL 7N HNO_3
add Th fraction to U beaker	
rinse resin	6N HCl H_2O 7N HNO_3 fill columns up to the top
load sample on column (U +Th in U beaker)	
elute Ca (waste)	2 CV 7N HNO_3 add stepwise and rinse the beakers with the first CV (all U and Th beakers)
elute Th (collect, final fraction)	5 CV 8N HCl add stepwise
elute U (collect, final fraction)	4 CV 0.5 HCl add stepwise
dry samples down	
dissolve in	0.26 mL 7N HNO_3
dissolve on a heating plate and ultrasound bath	
For the final concentration for MC-ICP-MS add	1.99 mL H_2O

Instrument Settings

Table S3.2: Cup Configuration for solution ^{230}Th/U-dating.

Uranium cup configuration					
Cup	L1	C	H1	H2	H3
Amplifier	$10^{11}\Omega$ or $10^{13}\Omega$	SEM	$10^{11}\Omega$	$10^{11}\Omega$	$10^{11}\Omega$ or $10^{10}\Omega$
m/z	^{233}U	^{234}U	^{235}U	^{236}U	^{238}U

Thorium cup configuration			
Cup	L1	C	H1
Amplifier	$10^{11}\Omega$ or $10^{13}\Omega$	SEM	$10^{11}\Omega$ or $10^{13}\Omega$
m/z	^{229}Th	^{230}Th	^{232}Th

Table S3.3: Instrument Settings for LA ^{230}Th/U-dating.

Neptune Plus MC-ICP-MS	
RF Power	1200 W
Ar cooling [L/min]	15
Auxiliar gas [L/min]	0.73
Integration Time	1.049
Interface cones	Jet-X

NWR 193 nm Laser Ablation system	
Line length [µm]	1000
He [L/min]	0.80
Frequency [Hz]	20
Translation rate [µm/s]	10
Spot size [µm]	150

Table S3.4: Cup Configuration for LA ^{230}Th/U-dating.

Uranium cup configuration						
Cup	L1	C	H1	H2	H3	H4
Amplifier	$10^{13}\Omega$	SEM	$10^{11}\Omega$	$10^{11}\Omega$	$10^{13}\Omega$	$10^{11}\Omega$
Line scan 1		^{230}Th	^{232}Th		^{235}U	^{238}U
Line scan 2	^{232}Th	^{234}U		^{236}U		

$(^{234}U/^{238}U)_i$ activity ratios as growth stop indicator

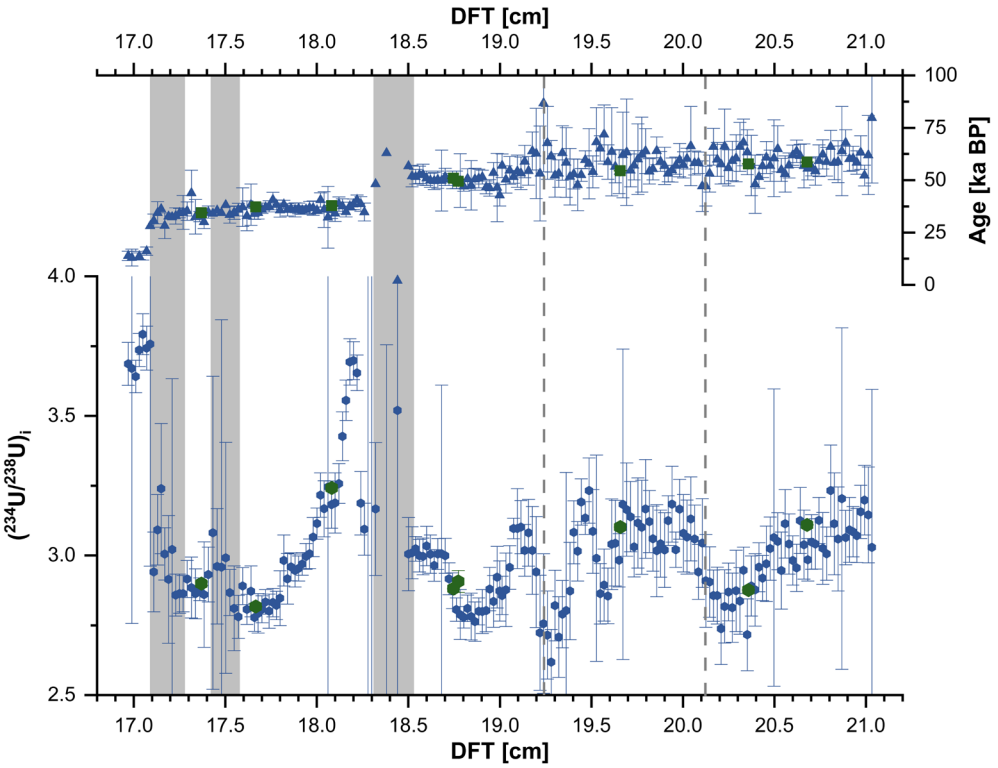

Fig. S3.4 LA ^{230}Th/U-ages and $(^{234}U/^{238}U)_i$ activity ratios of sample BB-15. **a** LA ^{230}Th/U-ages (blue triangles) and solution ages (green squares) of sample BB-15; **b** corresponding $(^{234}U/^{238}U)_i$. Grey bars indicate hiatuses, which were identified macroscopically and based on the trace element data. The dotted grey lines indicate two hiatuses, which were identified based on changes in $(^{234}U/^{238}U)_i$.

Speleothem growth phases and assigned DO events

Table S3.5: Comparison of speleothem growth phases and the respective DO event.

Speleothem sample	growth phase No.	DO event (Rasmussen et al., 2014)
BB-9	2	12
BB-9	3	11
BB-9	4	10
BB-9	5	8
BB-9	6	7
BB-9	7	6
BB-9	8	5
BB-10	1.1	16
BB-10	1.2	14
BB-10	1.3	13
BB-10	2	8
BB-15	1.1	16 or 17
BB-15	1.2	14 or 15
BB-15	1.3	14
BB-15	2	8
BB-15	3	6 or 7

Table S3.6: Comparison of the duration between NGRIP and Bleßberg growth phases.

DO event	Duration NGRIP [ka] (Rasmussen et al., 2014)	duration Bleßberg [ka] (this study)	Offset
16	1.78	1.28	72 %
14	4.62	3.38	73 %
13	0.94	1.11	118 %
12	2.58	0.74	29 %
11	1.1	0.84	76 %
8	1.59	1.03	65 %
7	0.74	0.5	68 %
6	0.38	0.37	97 %

Comparison of individual growth phases with NGRIP $\delta^{18}O$ and temperature

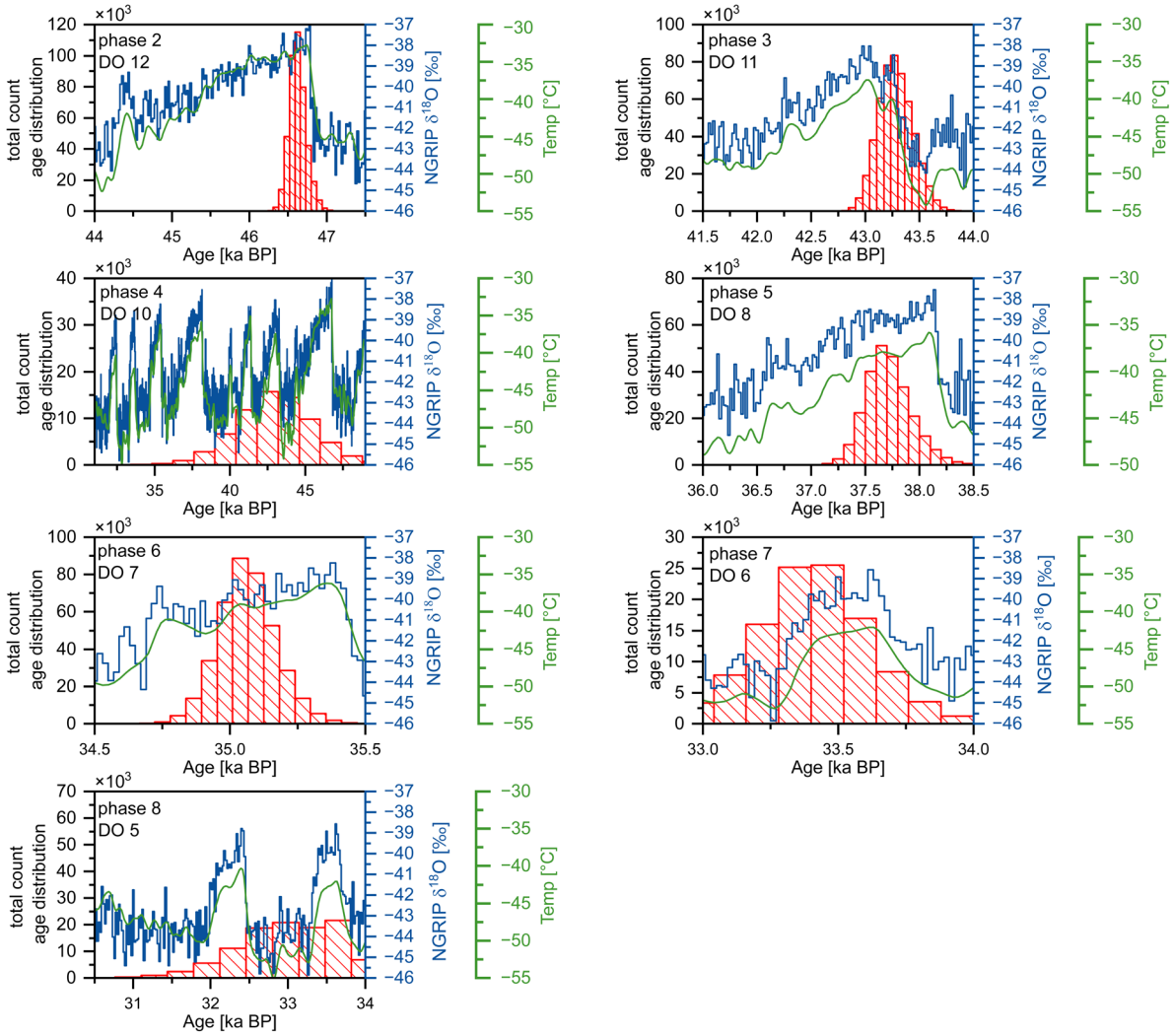

Fig. S3.5 Comparison of the growth phases of BB-9 and their respective DO events. Given are the $\delta^{18}O$ record (blue) and Temperature reconstruction (green) from the NGRIP (Kindler et al., 2014; Rasmussen et al., 2014). The BB-9 growth phases are given as the total age distribution (red histograms) of the Monte-Carlo simulations of the age model calculations in a 0.1 mm resolution.

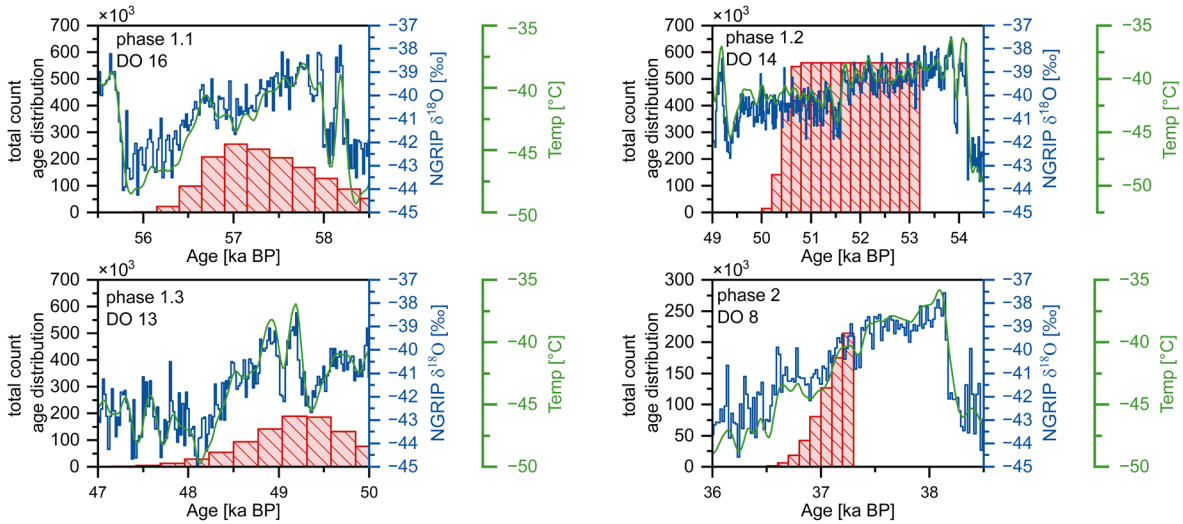

Fig. S3.6 Comparison of the growth phases of BB-10 and their respective DO events. Given are the $\delta^{18}O$ record (blue) and Temperature reconstruction (green) from the NGRIP (Kindler et al., 2014; Rasmussen et al., 2014). The BB-10 growth phases are given as the total age distribution (red histograms) of the Monte-Carlo simulations of the age model calculations in a 0.1 mm resolution.

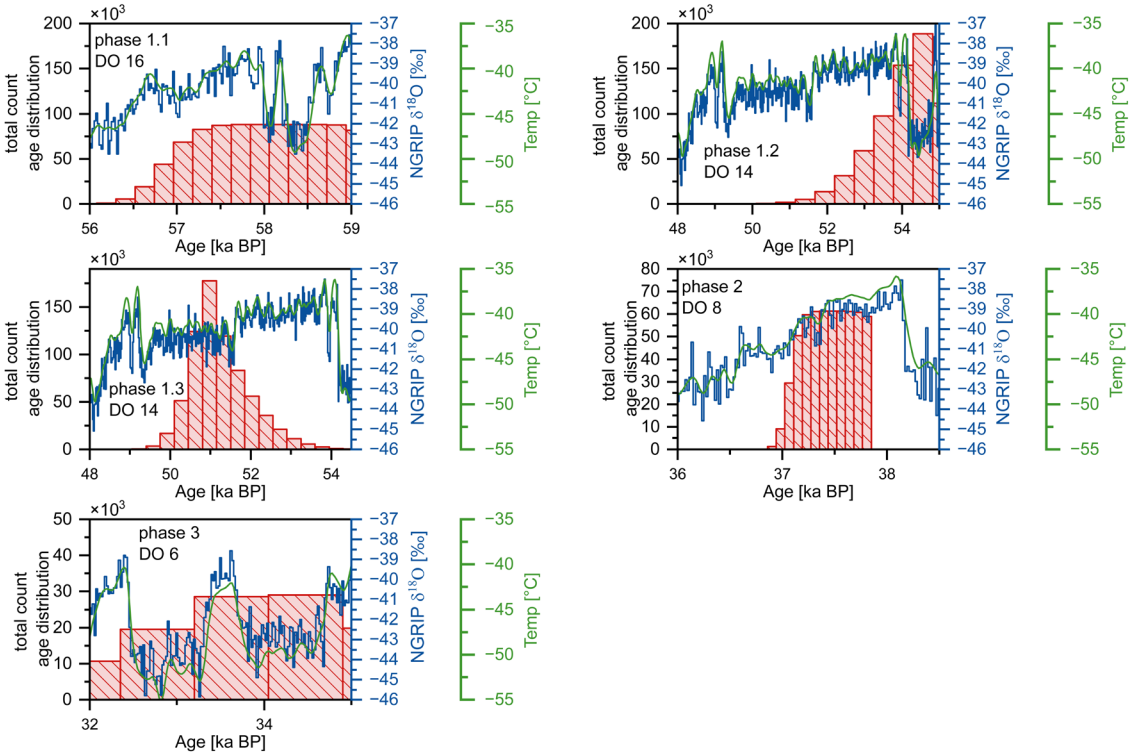

Fig. S3.7 Comparison of the growth phases of BB-15 and their respective DO events. Given are the $\delta^{18}O$ record (blue) and Temperature reconstruction (green) from the NGRIP (Kindler et al., 2014; Rasmussen et al., 2014). The BB-15 growth phases are given as the total age distribution (red histograms) of the Monte-Carlo simulations of the age model calculations in a 0.1 mm resolution.

Table S3.7a: Results of the solution-based ^{230}Th/U-dating for sample BB-9. Activity ratios ate indicated by parentheses and sampling method is given in the third column.

smpl ID	DFT [cm]		^{238}U [µg/g]	^{232}Th [ng/g]	(^{234}U/^{238}U)	(^{230}Th/^{238}U)	(^{234}U/^{238}U)$_{initial}$	(^{230}Th/^{232}Th)	uncorrected age [ka BP]	corrected age [ka BP]
LL181	4.01	MM	0.3392 ± 0.0033	34.39 ± 0.33	2.709 ± 0.023	0.7437 ± 0.0042	2.880 ± 0.023	23.436 ± 0.076	34.75 ± 0.13	33.75 ± 0.39
JK105	4.02	MM	0.3031 ± 0.0023	10.47 ± 0.08	2.7329 ± 0.0078	0.7323 ± 0.0027	2.9015 ± 0.0082	67.35 ± 0.21	33.16 ± 0.13	32.83 ± 0.17
JK130	4.05	MM	0.3079 ± 0.0033	217.24 ± 2.31	2.91 ± 0.21	0.822 ± 0.020	3.11 ± 0.21	3.830 ± 0.011	42.11 ± 0.15	34.76 ± 3.12
JK131	4.14	MM	0.2357 ± 0.0025	153.74 ± 1.62	2.80 ± 0.18	0.826 ± 0.018	3.00 ± 0.18	4.146 ± 0.013	43.59 ± 0.17	36.63 ± 2.87
JK91	4.17	hh	0.2952 ± 0.0020	166.12 ± 1.24	2.79 ± 0.16	0.807 ± 0.017	2.98 ± 0.16	4.538 ± 0.025	41.97 ± 0.22	35.82 ± 2.46
JK104	4.19	MM	0.3040 ± 0.0029	5.860 ± 0.055	2.7524 ± 0.0048	0.7494 ± 0.0029	2.9261 ± 0.0049	123.27 ± 0.46	33.61 ± 0.15	33.43 ± 0.16
LL182	4.21	MM	0.3309 ± 0.0028	228.30 ± 1.91	2.80 ± 0.19	0.840 ± 0.017	3.00 ± 0.19	3.983 ± 0.011	44.82 ± 0.16	37.39 ± 3.11
JK84	4.22	hh	0.2913 ± 0.0019	169.04 ± 1.24	2.84 ± 0.17	0.810 ± 0.018	3.03 ± 0.17	4.419 ± 0.023	41.59 ± 0.21	35.32 ± 2.57
LL183	4.34	MM	0.4374 ± 0.0037	5.629 ± 0.048	2.7682 ± 0.0033	0.7858 ± 0.0020	2.9525 ± 0.0033	193.48 ± 0.48	35.17 ± 0.10	35.05 ± 0.11
JK103	4.44	MM	0.5761 ± 0.0038	0.2732 ± 0.0019	2.8043 ± 0.0010	0.7974 ± 0.0016	2.9926 ± 0.0012	5324.26 ± 15.62	35.11 ± 0.08	35.108 ± 0.085
JK80	4.50	hh	0.6015 ± 0.0037	9.202 ± 0.061	2.8473 ± 0.0038	0.8028 ± 0.0024	3.0387 ± 0.0039	160.556 ± 0.572	34.95 ± 0.12	34.81 ± 0.13
JK102	4.59	MM	0.5068 ± 0.0037	1.2209 ± 0.0090	2.9556 ± 0.0014	0.8417 ± 0.0017	3.1599 ± 0.0015	1106.42 ± 2.16	35.16 ± 0.08	35.135 ± 0.082
JK101	4.83	MM	0.2235 ± 0.0017	1.2370 ± 0.0097	2.8098 ± 0.0026	0.8477 ± 0.0028	3.0127 ± 0.0028	485.12 ± 1.60	37.63 ± 0.15	37.58 ± 0.15
JK90	4.96	hh	0.2331 ± 0.0015	1.1224 ± 0.0083	2.8579 ± 0.0020	0.8656 ± 0.0031	3.0677 ± 0.0023	549.50 ± 2.84	37.82 ± 0.16	37.78 ± 0.16
JK128	5.18	MM	0.3307 ± 0.0036	130.90 ± 1.41	2.496 ± 0.084	0.8289 ± 0.0099	2.685 ± 0.083	6.763 ± 0.017	46.56 ± 0.16	42.13 ± 1.78
JK106	5.19	MM	0.3296 ± 0.0026	46.65 ± 0.36	2.431 ± 0.027	0.8018 ± 0.0045	2.611 ± 0.028	18.097 ± 0.053	43.37 ± 0.16	41.83 ± 0.61
JK100	5.35	MM	0.6053 ± 0.0044	0.790 ± 0.006	2.5340 ± 0.0012	0.8596 ± 0.0017	2.7332 ± 0.0014	2084.45 ± 4.23	43.20 ± 0.10	43.19 ± 0.10
JK82	5.48	hh	0.5015 ± 0.0030	1.530 ± 0.010	2.6664 ± 0.0011	0.9012 ± 0.0028	2.8821 ± 0.0015	903.13 ± 3.53	43.03 ± 0.16	43.00 ± 0.16
LL177	5.66	MM	0.3916 ± 0.0027	2.741 ± 0.019	2.6730 ± 0.0020	0.9128 ± 0.0018	2.8918 ± 0.0021	412.925 ± 0.793	43.53 ± 0.10	43.46 ± 0.11
LL176	5.94	MM	0.6241 ± 0.0040	3.339 ± 0.022	2.7655 ± 0.0015	1.0013 ± 0.0034	3.0137 ± 0.0019	592.57 ± 2.04	46.60 ± 0.19	46.55 ± 0.19
JK83	6.08	hh	0.7286 ± 0.0044	2.171 ± 0.014	2.8241 ± 0.0010	1.0242 ± 0.0031	3.0818 ± 0.0014	1050.67 ± 4.02	46.71 ± 0.17	46.68 ± 0.17
LL184	6.21	MM	0.5493 ± 0.0045	34.50 ± 0.28	2.781 ± 0.015	1.0083 ± 0.0024	3.0320 ± 0.0148	50.823 ± 0.118	47.20 ± 0.14	46.62 ± 0.32

Table S3.7b: Results of the LA ^{230}Th/U-dating for sample BB-9. Activity ratios ate indicated by parentheses. BP = before present, i.e., 1950 CE. TS indicates calculated LA ages, LA individually measured ages.

smpl ID	DFT [cm]	$(^{234}U/^{238}U)$	$(^{230}Th/^{238}U)$	$(^{234}U/^{238}U)_{initial}$	$(^{230}Th/^{232}Th)$	uncorrected age [ka BP]	corrected age [ka BP]
BB9-TS-1	3.99	2.71 ± 0.07	0.60 ± 0.12	2.844 ± 0.078	392.34 ± 159.92	26.71 + 10.2111 - 9.4453	26.55 ± 6.09
BB9-TS-2	4.01	2.790 ± 0.083	0.71 ± 0.13	2.953 ± 0.093	626.12 ± 221.00	30.95 ± 6.43	30.92 ± 6.43
BB9-2 (LA)	4.02	2.734 ± 0.051	0.533 ± 0.022	2.903 ± 0.051	215.11 ± 27.02	23.20 ± 1.15	30.92 ± 6.67
BB9-TS-3	4.03	2.776 ± 0.053	0.671 ± 0.073	2.929 ± 0.057	1180.44 ± 274.19	30.92 ± 6.43	29.25 ± 3.55
BB9-3 (LA)	4.03	2.694 ± 0.021	0.711 ± 0.025	2.866 ± 0.022	415.41 ± 56.51	32.39 ± 1.33	32.31 ± 1.27
BB9-TS-4	4.05	2.78 ± 0.12	0.72 ± 0.11	2.95 ± 0.12	1123.17 ± 506.68	31.35 ± 5.81	31.32 ± 5.78
BB9-4 (LA)	4.14	2.711 ± 0.029	0.670 ± 0.023	2.886 ± 0.029	267.81 ± 34.48	30.09 ± 1.16	34.23 ± 1.23
BB9-TS-5	4.14	2.716 ± 0.094	0.78 ± 0.17	2.90 ± 0.11	15.01 ± 8.71	37.09 + 41.3078 - 14.5852	35.50 + 9.42 - 8.8674
BB9-5 (LA)	4.15	2.778 ± 0.026	0.742 ± 0.026	2.943 ± 0.028	263.79 ± 47.39	32.84± 1.33	33.92 ± 1.37
BB9-TS-6	4.16	2.71 ± 0.11	0.72 ± 0.14	2.87 ± 0.11	6.77 ± 1.73	34.09± 6.44	32.42 ± 7.14
BB9-TS-7	4.18	2.73 ± 0.24	0.72 ± 0.10	2.90 ± 0.25	439.96 ± 426.45	32.52 + 6.8115 - 5.7158	32.13 + 6.4498 - 5.6983
BB9-TS-8	4.20	2.743 ± 0.092	0.622 ± 0.098	2.883 ± 0.099	387.15 ± 62.71	27.34 ± 4.79	27.25 ± 4.82
BB9-TS-9	4.22	2.619 ± 0.092	0.70 ± 0.12	2.776 ± 0.098	415.45 ± 87.91	32.78 ± 6.59	32.66 ± 6.54
BB9-TS-10	4.24	2.660 ± 0.057	0.74 ± 0.12	2.829 ± 0.067	1024.38 ± 484.79	34.24 + 21.8461 - 10.4342	34.1 4± 6.60
BB9-6 (LA)	4.32	2.384 ± 0.027	0.746 ± 0.022	2.762 ± 0.029	-5784.24 ± 3764.77	39.47 ± 1.46	35.8 7± 1.22
BB9-TS-11	4.32	2.530 ± 0.057	0.693 ± 0.093	2.683 ± 0.063	114.80 ± 40.72	34.22 ± 5.25	33.7 7± 5.16
BB9-TS-12	4.34	2.59 ± 0.10	0.81 ± 0.13	2.77 ± 0.11	562.79 ± 523.41	39.59 + 8.0254 - 7.1234	39.56 + 7.6849 - 7.0803
BB9-TS-13	4.36	2.760 ± 0.068	0.773 ± 0.079	2.941 ± 0.072	14180.11 ± 12833.83	34.53 ± 4.03	34.53 ± 4.08
BB9-TS-14	4.37	2.70 ± 0.11	0.83 ± 0.12	2.90 ± 0.12	5745.84 ± 1662.59	38.18 ± 7.01	38.18 ± 6.89

Table S3.7b: Results of the LA ^{230}Th/U-dating for sample BB-9. Activity ratios ate indicated by parentheses. BP = before present, i.e., 1950 CE. TS indicates calculated LA ages, LA individually measured ages.

smpl ID	DFT [cm]	(^{234}U/^{238}U)	(^{230}Th/^{238}U)	(^{234}U/^{238}U)$_{initial}$	(^{230}Th/^{232}Th)	uncorrected age [ka BP]	corrected age [ka BP]
BB9-TS-15	4.39	2.62 ± 0.07	0.81 ± 0.18	2.813 ± 0.085	NA	38.85 + 10.5316 - 9.4283	38.85 + 10.5934 - 9.5531
BB9-TS-16	4.41	2.63 ± 0.12	0.76 ± 0.14	2.80 ± 0.13	12097.41 ± 0.00	36.06 + 8.3678 - 7.8455	36.05 + 8.3923 - 7.7737
BB9-TS-17	4.43	2.696 ± 0.033	0.776 ± 0.098	2.876 ± 0.044	15260.29 ± 8027.47	35.67 ± 5.15	35.67 ± 5.14
BB9-TS-18	4.45	2.71 ± 0.11	0.759 ± 0.076	2.89 ± 0.11	22757.49± 0.00	34.53 ± 4.17	34.52 ± 4.16
BB9-TS-19	4.46	2.71 ± 0.15	0.68 ± 0.18	2.86 ± 0.16	10435.28 ± 7378.86	31.51 ± 7.33	30.28 + 9.4559 - 8.7805
BB9-TS-20	4.48	2.617 ± 0.095	0.80 ± 0.12	2.80 ± 0.10	13761.59 ± 10691.61	38.14 ± 7.12	38.13 + 7.4475 - 6.7276
BB9-17(LA)	4.50	2.796 ± 0.020	0.764 ± 0.016	2.961 ± 0.021	4358.32 ± 17480.58	33.58 ± 0.86	33.01 ± 0.84
BB9-TS-21	4.50	2.701 ± 0.068	0.705 ± 0.037	2.862 ± 0.070	28989.24 ± 2613.04	31.91 ± 2.15	31.91 ± 2.13
BB9-TS-22	4.52	2.75 ± 0.10	0.671 ± 0.074	2.90 ± 0.11	23521.57 ± 13593.37	29.62 ± 3.86	29.61 ± 3.86
BB9-TS-23	4.54	2.751 ± 0.041	0.80 ± 0.11	2.938 ± 0.051	37931.13 ± 17435.44	35.86 ± 5.59	35.85 ± 5.54
BB9-TS-24	4.55	2.678 ± 0.039	0.76 ± 0.01	2.854 ± 0.040	78409.34 ± 99189.26	35.18 ± 0.63	35.22 ± 0.71
BB9-TS-25	4.57	2.83 ± 0.12	0.79 ± 0.21	3.02 ± 0.13	326.92 ± 201.53	34.45 + 20.2169 - 17.0275	34.43 + 11.0717 - 10.4181
BB9-TS-26	4.59	2.690 ± 0.093	0.85 ± 0.14	2.89 ± 0.10	10556.47 ± 13993.73	39.80 + 8.2305 - 7.5522	39.80 + 8.529 - 7.4729
BB9-TS-27	4.61	2.879 ± 0.057	0.70 ± 0.12	3.042 ± 0.066	25683.08 ± 12934.30	29.46 ± 5.57	29.45 ± 5.55
BB9-TS-28	4.63	2.732 ± 0.030	0.81 ± 0.15	2.922 ± 0.054	80642.90 ± 0.00	36.82 ± 8.02	36.82 + 8.4062 - 7.7653
BB9-TS-29	4.64	2.910 ± 0.076	0.813 ± 0.089	3.105 ± 0.082	27142.83 ± 0.00	34.43 ± 4.45	34.43 ± 4.46
BB9-TS-30	4.66	2.88 ± 0.11	0.765 ± 0.072	3.06 ± 0.11	73799.31 ± 50060.00	32.54 ± 3.83	32.54 ± 3.68

Table S3.7b: Results of the LA ^{230}Th/U-dating for sample BB-9. Activity ratios ate indicated by parentheses. BP = before present, i.e., 1950 CE. TS indicates calculated LA ages, LA individually measured ages.

smpl ID	DFT [cm]	$(^{234}U/^{238}U)$	$(^{230}Th/^{238}U)$	$(^{234}U/^{238}U)_{initial}$	$(^{230}Th/^{232}Th)$	uncorrected age [ka BP]	corrected age [ka BP]
BB9-TS-31	4.68	2.883 ± 0.099	0.802 ± 0.052	3.07 ± 0.10	11170.99 ± 3195.80	34.25 ± 2.86	34.24 ± 2.98
BB9-7(LA)	4.69	2.730 ± 0.029	0.820 ± 0.015	2.911 ± 0.030	212.03 ± 78.66	37.81 ± 0.88	37.63 ± 0.92
BB9-TS-32	4.70	2.87 ± 0.12	0.771 ± 0.036	3.06 ± 0.12	9926.04 ± 9085.47	32.92 ± 2.34	32.91 ± 2.38
BB9-TS-33	4.82	2.655 ± 0.098	0.797 ± 0.049	2.84 ± 0.10	15177.22 ± 20602.14	37.63 ± 3.19	37.46 ± 3.08
BB9-TS-34	4.84	2.69 ± 0.11	0.844 ± 0.062	2.88 ± 0.12	13151.51 ± 7667.65	39.52 ± 4.04	39.50 ± 4.04
BB9-8 (LA)	4.85	2.588 ± 0.060	0.826 ± 0.057	2.770 ± 0.064	12.10 ± 275.13	44.58 ± 2.56	40.95 ± 3.37
BB9-TS-35	4.86	2.743 ± 0.095	0.783 ± 0.074	2.926 ± 0.098	13444.98 ± 10254.08	35.31 ± 4.00	35.30 ± 4.03
BB9-TS-36	4.88	2.679 ± 0.078	0.696 ± 0.056	2.837 ± 0.081	11080.12 ± 8251.69	31.78 ± 3.11	31.77 ± 3.12
BB9-TS-37	4.90	2.67 ± 0.12	0.79 ± 0.11	2.85 ± 0.13	8027.81 ± 5744.32	36.94 ± 6.19	36.92 ± 6.11
BB9-18 (LA)	4.91	2.778 ± 0.028	0.800 ± 0.024	2.966 ± 0.029	2344.56 ± 8475.07	35.65 ± 1.30	36.91 ± 1.33
BB9-TS-38	4.92	2.837 ± 0.051	0.800 ± 0.084	3.027 ± 0.058	9476.53 ± 2131.82	34.84 ± 4.24	34.83 ± 4.33
BB9-TS-39	4.94	2.736 ± 0.084	0.77 ± 0.15	2.916 ± 0.094	10345.04 ± 9860.75	34.78 + 12.077 - 11.4606	34.74 ± 8.22
BB9-TS-40	4.96	2.79 ± 0.12	0.891 ± 0.087	3.01 ± 0.12	17507.07 ± 14358.85	40.21 + 5.1919 - 4.6562	40.19 ± 5.00
BB9-TS-41	4.98	2.839 ± 0.095	0.82 ± 0.10	3.04 ± 0.10	166964.49 ± 277282.34	35.87 ± 5.44	35.84 ± 5.47
BB9-TS-42	5.00	2.96 ± 0.12	0.87 ± 0.17	3.17 ± 0.13	11743.95 ± 1051.24	36.61 ± 8.23	36.56 + 8.5249 - 7.972
BB9-9 (LA)	5.01	2.665 ± 0.029	0.872 ± 0.034	3.040 ± 0.031	2979.81 ± 12941.83	41.39 ± 1.99	40.10 ± 1.82
BB9-TS-43	5.02	2.74 ± 0.18	0.65 ± 0.13	2.88 ± 0.19	1933.75 ± 1489.62	28.62 ± 6.61	28.52 + 7.0571 - 6.244
BB9-TS-44	5.04	2.866 ± 0.076	0.73 ± 0.10	3.038 ± 0.082	18429.97 ± 28392.86	31.23 ± 5.11	31.20 ± 5.00

Table S3.7b: Results of the LA ^{230}Th/U-dating for sample BB-9. Activity ratios ate indicated by parentheses. BP = before present, i.e., 1950 CE. TS indicates calculated LA ages, LA individually measured ages.

smpl ID	DFT [cm]	(^{234}U/^{238}U)	(^{230}Th/^{238}U)	(^{234}U/^{238}U)$_{initial}$	(^{230}Th/^{232}Th)	uncorrected age [ka BP]	corrected age [ka BP]
BB9-TS-45	5.06	2.77 ± 0.13	0.99 ± 0.12	3.01 ± 0.14	14815.20 ± 7503.92	46.18 + 7.8525 - 6.8177	46.14 + 7.511 - 6.9692
BB9-10(LA)	5.16	2.142 ± 0.033	0.869 ± 0.032	2.643 ± 0.035	398.89 ± 154.15	55.72 ± 5.55	46.91± 2.16
BB9-TS-46	5.16	2.458 ± 0	0.83 ± 0.11	2.647 ± 0.031	1879.63 ± 2260.49	46.06 + 7.85 - 7.1623	43.07 ± 6.77
BB9-TS-47	5.18	2.388 ± 0.039	0.769 ± 0.077	2.557 ± 0.046	7982.16 ± 6868.34	40.78 ± 4.80	40.75 ± 4.72
BB9-11 (LA)	5.19	2.506 ± 0.029	0.811 ± 0.024	2.698 ± 0.031	107.68 ± 62.56	41.64 ± 1.48	41.77 ± 1.57
BB9-TS-48	5.20	2.470 ± 0.078	0.901 ± 0.091	2.680 ± 0.086	668.33 ± 370.81	47.28 ± 5.96	47.18 + 6.3908 - 5.8086
BB9-TS-49	5.29	2.467 ± 0.032	0.825 ± 0.062	2.655 ± 0.038	6188.44 ± 3889.77	42.62 ± 3.86	42.57 ± 3.81
BB9-TS-50	5.31	2.437 ± 0.047	0.809 ± 0.056	2.619 ± 0.051	1373.80 ± 466.12	42.21 + 9.0551 - 8.0473	42.17 ± 3.60
BB9-TS-51	5.33	2.405 ± 0.071	0.794 ± 0.063	2.582 ± 0.075	8318.09 ± 4370.57	41.96 ± 4.18	41.95 ± 4.17
BB9-12 (LA)	5.33	2.452 ± 0.012	0.824 ± 0.017	2.643 ± 0.013	2683.52 ± 18385.18	42.80 ± 1.05	42.80 ± 1.10
BB9-TS-52	5.35	2.493 ± 0.051	0.851 ± 0.046	2.689± 0.054	24856.66 ± 17917.40	43.57 ± 2.96	43.57 ± 2.95
BB9-TS-53	5.37	2.478 ± 0.065	0.836 ± 0.053	2.670 ± 0.069	13800.12 ± 6147.33	42.98 ± 3.52	42.97 ± 3.42
BB9-TS-54	5.39	2.522 ± 0.042	0.895 ± 0.045	2.732 ± 0.045	30787.53 ± 14888.29	45.65 ± 2.82	45.64 ± 2.84
BB9-TS-55	5.41	2.634 ± 0.033	0.837 ± 0.059	2.830 ± 0.038	43573.68 ± 22250.32	39.99 ± 3.22	39.99 ± 3.33
BB9-TS-56	5.43	2.661 ± 0.032	0.877 ± 0.033	2.869 ± 0.034	21272.80 ± 15069.20	41.74 ± 1.91	41.74 ± 1.94
BB9-TS-57	5.45	2.683 ± 0.044	0.916 ± 0.056	2.903 ± 0.049	2723.30 ± 857.89	43.54 ± 3.17	43.52 ± 3.21
BB9-TS-58	5.47	2.690 ± 0.065	0.888 ± 0.077	2.902 ± 0.070	387.87 ± 146.49	42.03 ± 4.26	41.81 ± 4.47
BB9-19 (LA)	5.48	2.625 ± 0.017	0.888 ± 0.025	2.830 ± 0.019	5918.58 ± 73204.72	43.06 ± 1.51	44.02 ± 1.48
BB9-TS-59	5.49	2.659 ± 0.097	0.862 ± 0.076	2.86 ± 0.10	4948.56 ± 2565.41	41.04 ± 4.61	40.95 ± 4.54

Table S3.7b: Results of the LA ^{230}Th/U-dating for sample BB-9. Activity ratios ate indicated by parentheses. BP = before present, i.e., 1950 CE. TS indicates calculated LA ages, LA individually measured ages.

smpl ID	DFT [cm]	(^{234}U/^{238}U)	(^{230}Th/^{238}U)	(^{234}U/^{238}U)$_{initial}$	(^{230}Th/^{232}Th)	uncorrected age [ka BP]	corrected age [ka BP]
BB9-TS-60	5.51	2.593 ± 0.062	0.875 ± 0.057	2.798 ± 0.066	12746.08 ± 15663.00	42.98 ± 3.56	42.93 ± 3.56
BB9-TS-61	5.53	2.768 ± 0.085	0.903 ± 0.070	2.987 ± 0.089	1485.53 ± 347.18	41.31 ± 4.05	41.22 ± 4.04
BB9-TS-62	5.55	2.693 ± 0.054	0.847 ± 0.090	2.893 ± 0.061	1641.44 ± 488.71	39.66 ± 5.09	39.54 ± 5.00
BB9-13 (LA)	5.56	2.630 ± 0.028	0.888 ± 0.036	2.847 ± 0.031	2861.67 ± 2735.45	43.02 ± 2.03	43.90 ± 2.08
BB9-TS-63	5.57	2.627 ± 0.060	0.893 ± 0.069	2.839 ± 0.065	1181.37 ± 469.53	43.43 ± 4.23	43.30 ± 4.04
BB9-TS-64	5.59	2.614 ± 0.064	0.90 ± 0.12	2.827 ± 0.075	854.48 ± 242.45	44.04 + 7.1962 - 6.4355	43.91 ± 6.72
BB9-TS-65	5.61	2.689 ± 0.044	0.918 ± 0.067	2.911 ± 0.049	357.36 ± 88.83	43.66 ± 3.84	43.53 ± 3.90
BB9-20 (LA)	5.62	2.588 ± 0.023	0.929 ± 0.039	2.812 ± 0.027	1166.26 ± 1270.32	46.33 ± 2.47	48.38 ± 2.43
BB9-TS-66	5.63	2.605 ± 0.081	0.818 ± 0.069	2.795 ± 0.086	792.23 ± 320.05	39.66 ± 4.08	39.50 ± 4.21
BB9-TS-67	5.65	2.665 ± 0.072	0.969 ± 0.080	2.902 ± 0.078	230.84 ± 88.98	47.13 ± 4.87	46.88 ± 4.82
BB9-TS-68	5.67	2.621 ± 0.066	0.903 ± 0.073	2.836 ± 0.073	148.79 ± 44.71	44.35 ± 4.42	44.00 ± 4.39
BB9-TS-69	5.69	2.667 ± 0.049	0.892 ± 0.093	2.880 ± 0.056	490.31 ± 113.37	42.72 + 10.0544 - 9.1353	42.50 ± 5.25
BB9-TS-70	5.71	2.668 ± 0.096	0.89 ± 0.11	2.88 ± 0.10	1085.14 ± 360.62	42.81 ± 6.30	42.57 ± 6.24
BB9-14 (LA)	5.72	2.319 ± 0.024	0.889 ± 0.038	2.900 ± 0.026	1180.21 ± 572.86	50.19 ± 2.66	42.84 ± 2.16
BB9-TS-71	5.73	2.682 ± 0.072	0.842 ± 0.062	2.880 ± 0.075	3434.04 ± 1233.65	39.66 ± 3.70	39.45 ± 3.58
BB9-TS-72	5.75	2.719 ± 0.073	0.842 ± 0.071	2.919 ± 0.078	2142.83 ± 1231.28	39.00 ± 4.07	38.78 ± 3.94
BB9-TS-73	5.77	2.672 ± 0.070	0.951 ± 0.083	2.904 ± 0.076	1097.46 ± 359.50	45.93 ± 4.93	45.72 ± 5.03
BB9-TS-74	5.89	2.583 ± 0.073	0.939 ± 0.059	1877.60 ± 1315.92	2.808 ± 0.075	47.05 ± 3.96	46.94 ± 3.92
BB9-TS-75	5.91	2.628 ± 0.047	0.949 ± 0.065	340010.06 ± 480924.51	2.857 ± 0.051	46.51 ± 3.90	46.50 ± 3.89
BB9-15 (LA)	5.92	2.155 ± 0.017	0.922 ± 0.023	2.719 ± 0.019	24.9 1± 20.63	58.49 ± 4.15	48.53 ± 1.50

Table S3.7b: Results of the LA ^{230}Th/U-dating for sample BB-9. Activity ratios ate indicated by parentheses. BP = before present, i.e., 1950 CE. TS indicates calculated LA ages, LA individually measured ages.

smpl ID	DFT [cm]	(^{234}U/^{238}U)	(^{230}Th/^{238}U)	(^{234}U/^{238}U)$_{initial}$	(^{230}Th/^{232}Th)	uncorrected age [ka BP]	corrected age [ka BP]
BB9-TS-76	5.93	2.713 ± 0.079	0.974 ± 0.068	113788.14 ± 179274.07	2.952 ± 0.083	46.16 ± 4.28	46.16 ± 4.21
BB9-TS-77	5.95	2.72 ± 0.16	0.927 ± 0.074	106999.98 ± 163606.25	2.95 ± 0.17	43.33 + 5.3937 - 4.7458	43.31 + 5.5367 - 4.8
BB9-TS-78	5.97	2.679 ± 0.075	1.021 ± 0.069	21120.00 ± 6733.85	2.932 ± 0.080	49.61 ± 4.34	49.61 ± 4.38
BB9-TS-79	5.99	2.670 ± 0.054	1.021 ± 0.057	6422.32 ± 6812.08	2.923 ± 0.058	49.84 ± 3.65	49.84 ± 3.63
BB9-TS-80	6.01	2.708 ± 0.047	0.975 ± 0.049	3525.74 ± 2358.43	2.948 ± 0.050	46.3 ± 2.92	46.33 ± 2.96
BB9-TS-81	6.03	2.736 ± 0.034	1.009 ± 0.070	17095.19 ± 19996.81	2.986 ± 0.042	47.72 + 11.7018 - 10.5016	47.69 ± 3.97
BB9-TS-82	6.05	2.768 ± 0.056	0.97 ± 0.057	15030.37± 5874.36	3.009 ± 0.061	45.19 ± 3.34	45.19 ± 3.31
BB9-16 (LA)	6.15	2.769 ± 0.024	1.014 ± 0.017	3,023 ± 0.025	202.15 ± 155.01	47.50 ± 1.02	47.26 ± 1.07

Table S3.7e: Results of the solution-based ^{230}Th/U-dating for sample BB-10. Activity ratios ate indicated by parentheses. BP = before present, i.e., 1950 CE.

smpl ID	DFT [cm]		^{238}U [µg/g]	^{232}Th [ng/g]	(^{234}U/^{238}U)	(^{230}Th/^{238}U)	(^{234}U/^{238}U)$_{initial}$	(^{230}Th/^{232}Th)	uncorrected age [ka BP]	corrected age [ka BP]
JK122	6.93	MM	0.3979 ± 0.0034	53.32 ± 0.45	2.612 ± 0.028	0.7853 ± 0.0043	2.793 ± 0.029	18.720 ± 0.043	38.84 ± 0.12	37.06 ± 0.69
JK92	7.47	hh	0.4491 ± 0.0027	0.3664 ± 0.0027	2.6365 ± 0.0011	0.7883 ± 0.0022	2.8187 ± 0.0013	2953.16 ± 14.67	37.29 ± 0.12	37.23 ± 0.12
JK132	7.76	MM	0.2589 ± 0.0022	6.19 ± 0.05	2.7701 ± 0.0057	0.8334 ± 0.0023	2.9679 ± 0.0058	110.28 ± 0.27	37.69 ± 0.12	37.38 ± 0.17
JK123	7.77	MM	0.2909 ± 0.0026	102.19 ± 0.90	2.996 ± 0.098	0.9377 ± 0.0044	3.229 ± 0.098	8.498 ± 0.025	42.41 ± 0.16	38.14 ± 1.94
JK93	8.62	hh	0.5840 ± 0.0034	23.84 ± 0.14	2.7393 ± 0.0095	1.0328 ± 0.0025	2.9977 ± 0.0097	77.31 ± 0.19	49.33 ± 0.15	48.76 ± 0.31
JK85	9.51	hh	0.7272 ± 0.0044	0.7342 ± 0.0051	2.72426 ± 0.00076	1.0552 ± 0.0035	2.9896 ± 0.0014	3194.25 ± 14.23	50.58 ± 0.21	50.50 ± 0.20
JK86	10.75	hh	0.6504 ± 0.0041	0.2114 ± 0.0019	2.69215 ± 0.00078	1.0480 ± 0.0040	2.9543 ± 0.0016	9854.03 ± 71.82	50.90 ± 0.24	50.83 ± 0.23
JK94	12.39	hh	0.5699 ± 0.0036	0.2169 ± 0.0021	2.67673 ± 0.00078	1.0588 ± 0.0034	2.9420 ± 0.0014	8505.17 ± 67.03	51.91 ± 0.21	51.84 ± 0.20
JK125	14.92	hh	0.7324 ± 0.0050	0.08646 ± 0.00066	2.79248 ± 0.00070	1.1156 ± 0.0018	3.0786 ± 0.0009	29916.79 ± 106.91	52.40 ± 0.10	52.40 ± 0.10
JK95	15.38	hh	0.7406 ± 0.0046	0.1823 ± 0.0017	2.79030 ± 0.00097	1.1172 ± 0.0035	3.0777 ± 0.0015	13871.11 ± 107.96	52.62 ± 0.20	52.55 ± 0.20
JK126	15.85	hh	0.3405 ± 0.0033	0.04118 ± 0.00050	2.74764 ± 0.00086	1.1078 ± 0.0017	3.0301 ± 0.0010	23190.25 ± 48.80	53.02 ± 0.10	53.00 ± 0.10
JK96	17.55	hh	0.2766 ± 0.0019	0.4875 ± 0.0040	2.5293 ± 0.0011	1.0757 ± 0.0034	2.7962 ± 0.0016	1865.56 ± 9.30	56.88 ± 0.22	56.78 ± 0.22
JK127	18.17	hh	0.3028 ± 0.0020	26.30 ± 0.17	2.648 ± 0.019	1.1540 ± 0.0028	2.944 ± 0.019	41.932 ± 0.066	59.27 ± 0.14	58.16 ± 0.71

Table S3.7d: Results of the LA ^{230}Th/U-dating for sample BB-10. Activity ratios ate indicated by parentheses. BP = before present, i.e., 1950 CE. TS indicates calculated LA ages, LA individually measured ages. NA = no data available.

smpl ID	DFT [cm]	(^{234}U/^{238}U)	(^{230}Th/^{238}U)	(^{234}U/^{238}U)$_{initial}$	(^{230}Th/^{232}Th)	uncorrected age [ka BP]	corrected age [ka BP]
BB10-2 (LA)	6.97	2.54 ± 0.23	0.95 ± 0.10	2.77 ± 0.24	1.740 ±.22	56.34 ± 2.00	43.16 + 17.846 - 14.054
BB10-3 (LA)	7.41	2.642 ± 0.017	0.786 ± 0.014	2.825 ± 0.018	6846.75 ±12519.20	37.09 ±0 .80	37.09 ± 0.82
BB10-TS-1	7.43	2.62 ± 0.48	0.777 ± 0.058	2.80 ± 0.48	54.07 ± 8.54	37.06 + 10.3441 - 7.196	36.98 + 10.6205 - 7.0817
BB10-TS-2	7.45	2.66 ± 0.19	0.786 ± 0.036	2.85 ± 0.20	49.04 ± 12.16	36.84 + 4.0039 - 3.4067	36.73 + 3.9812 - 3.4739
BB10-TS-3	7.47	2.622 ± 0.065	0.788 ± 0.043	2.804 ± 0.067	62.80 ± 43.85	37.57 ± 2.63	37.50 ± 2.64
BB10-TS-4	7.49	2.666 ± 0.045	0.790 ± 0.050	2.849 ± 0.047	44.06 ± 9.35	36.91 ± 2.81	36.88 ± 2.76
BB10-TS-5	7.51	2.69 ± 0.56	0.804 ± 0.054	2.88 ± 0.58	39.71 ± 8.57	37.30 + 13.4737 - 7.6787	37.24 + 12.541 - 7.8152
BB10-TS-6	7.53	2.615 ± 0.054	0.809 ± 0.036	2.802 ± 0.054	47.72 ± 14.31	38.82 ± 2.25	38.78 ± 12-24
BB10-TS-7	7.55	2.663 ± 0.041	0.819 ± 0.029	2.855 ± 0.042	37.28 ± 15.43	38.56 ± 1.71	38.53 ± 1.75
BB10-TS-8	7.57	2.677 ± 0.032	0.777 ± 0.029	2.857 ± 0.034	132.73 ± 98.15	36.07 + 13.5035 - 7.9634	36.04 ± 1.58
BB10-TS-9	7.59	2.64 ± 0.55	0.829 ± 0.042	2.83 ± 0.58	392.34 ± 159.92	39.48 ±2.79	39.44 + 13.5325 - 7.9551
BB10-TS-10	7.61	2.644 ± 0.043	0.808 ± 0.049	2.832 ± 0.046	626.12 ± 221.00	38.28 ±2.91	38.24 ± 2.79
BB10-TS-11	7.63	2.711 ± 0.042	0.818 ± 0.053	2.903 ± 0.046	1180.44 ± 274.19	37.70 + 16.6719 - 8.916	37.67 ± 2.88
BB10-TS-12	7.65	2.70 ± 0.68	0.816 ± 0.029	2.89 ± 0.72	1123.17 ± 506.68	37.80 + 16.6719 - 8.916	37.71 + 16.1788 - 8.8644
BB10-TS-13	7.67	2.75 ± 0.58	0.773 ± 0.059	2.94 ± 0.60	219.05 ± 104.91	34.68 + 12.1962 - 7.1256	34.64 + 11.7903 - 7.2909
BB10-TS-14	7.69	2.746 ±0.060	0.803 ± 0.040	2.935 ± 0.063	64.29 ± 25.79	36.49 ± 2.35	36.28 ± 2.31
BB10-TS-15	7.71	2.746 ± 0.049	0.828 ± 0.056	2.942 ± 0.054	113.82 ± 45.44	37.68 ± 3.08	37.64 ± 3.03
BB10-TS-16	7.73	2.768 ± 0.041	0.834 ± 0.047	2.966 ± 0.045	24.40 ± 6.35	37.59 ± 2.45	37.57 ± 2.44
BB10-TS-17	7.75	2.779 ± 0.042	0.878 ± 0.050	2.991 ± 0.046	8.65 ± 1.80	39.74 ± 2.72	39.71 ± 2.71

Table S3.7d: Results of the LA ^{230}Th/U-dating for sample BB-10. Activity ratios ate indicated by parentheses. BP = before present, i.e., 1950 CE. TS indicates calculated LA ages, LA individually measured ages. NA = no data available.

smpl ID	DFT [cm]	(^{234}U/^{238}U)	(^{230}Th/^{238}U)	(^{234}U/^{238}U)$_{initial}$	(^{230}Th/^{232}Th)	uncorrected age [ka BP]	corrected age [ka BP]
BB10-4 (LA)	7.75	2.787 ± 0.018	0.862 ± 0.022	3.001 ± 0.019	1777.80 ± 2252.59	38.74 ± 1.18	38.73 ± 1.19
BB10-TS-18	7.77	2.826 ± 0.028	0.805 ± 0.049	3.017 ± 0.032	9.47 ± 6.03	35.30 ± 2.46	35.23 ± 2.48
BB10-TS-19	7.79	2.741 ± 0.053	0.875 ± 0.069	2.951 ± 0.057	573.71 ± 218.93	40.27 ± 3.88	40.18 ± 3.84
BB10-TS-20	8.03	2.702 ± 0.068	1.067 ± 0.049	2.971 ± 0.073	15260.29 ± 8027.47	51.84 ± 3.30	51.80 ± 3.27
BB10-7 (LA)	8.04	2.719 ± 0.020	1.073 ± 0.029	2.989 ± 0.023	9.28 ± 12.00	52.77 ± 1.34	51.24 ± 1.95
BB10-TS-21	8.05	2.702 ± 0.049	1.032 ± 0.056	2.959 ± 0.053	22757.49 ± NA	49.71 ± 3.46	49.70 ± 3.46
BB10-TS-22	8.07	2.675 ± 0.024	1.007 ± 0.054	2.924 ± 0.029	18603.96 ± 12722.56	48.87 ± 3.12	48.86 ± 3.17
BB10-TS-23	8.09	2.720 ± 0.070	1.00 ± 0.24	2.97 ± 0.11	13436.13 ± 10163.70	47.60 + 14.4109 - 13.1181	47.56 + 14.6476 - 12.7711
BB10-TS-24	8.11	2.695 ± 0.033	1.026 ± 0.047	2.950 ± 0.037	31434.99 ± 1398.09	49.78 ± 2.87	49.52 ± 2.83
BB10-TS-25	8.13	2.740 ± 0.043	0.991 ± 0.060	2.985 ± 0.048	37027.25 ± 18908.65	46.80 ± 3.49	46.58 ± 3.51
BB10-TS-26	8.15	2.732 ± 0.044	1.015 ± 0.031	2.985 ± 0.047	12446.59 ± 5903.84	49.21 ± 2.10	48.10 ± 2.02
BB10-TS-27	8.17	2.684 ± 0.567	1.045 ± 0.043	2.94 ± 0.57	29970.89 ± 53028.98	51.22 + 18.6637 - 10.8988	50.94 + 18.4117 - 10.907
BB10-TS-28	8.19	2.740 ± 0.060	1.065 ± 0.032	3.009 ± 0.063	10556.47 ± 13993.73	50.79 ± 2.28	50.76 ± 2.31
BB10-TS-29	8.21	2.760 ± 0.036	1.011 ± 0.029	3.012 ± 0.038	25683.08 ± 12934.30	47.23 ± 1.80	47.23 ± 1.80
BB10-TS-30	8.23	2.740 ± 0.030	1.034 ± 0.056	2.999 ± 0.036	53892.86 ± 37830.26	48.99 ± 3.28	48.99 ± 3.24
BB10-TS-31	8.25	2.735 ± 0.045	1.074 ± 0.026	3.007 ± 0.048	51341.28 ± 51110.95	51.41 ± 1.82	51.41 ± 1.84
BB10-TS-32	8.27	2.752 ± 0.041	1.007 ± 0.049	3.003 ± 0.045	49484.54 ± 56588.51	47.19 ± 2.87	47.19 ± 2.83
BB10-TS-33	8.29	2.711 ± 0.039	1.020 ± 0.029	2.965 ± 0.041	12079.20 ± 5790.48	48.86 ± 1.92	48.86 ± 1.91
BB10-TS-34	8.31	2.71± 0.57	1.04 ± 0.13	2.97 ± 0.59	3703.54 ± 1127.24	50.30 + 19.3591 - 12.0767	50.30 + 20.0361 - 12.2588
BB10-TS-35	8.33	2.71 ± 0.51	1.074 ± 0.060	2.98 ± 0.53	1531.15 ± 953.10	52.03 + 16.8507 - 10.2879	52.03 + 16.9704 - 10.5478
BB10-TS-36	8.35	2.682 ± 0.052	1.029 ± 0.059	2.938 ± 0.058	300.13 ± 464.76	50.02 ± 3.75	50.02 ± 3.63

Table S3.7d: Results of the LA ^{230}Th/U-dating for sample BB-10. Activity ratios ate indicated by parentheses. BP = before present, i.e., 1950 CE. TS indicates calculated LA ages, LA individually measured ages. NA = no data available.

smpl ID	DFT [cm]	(^{234}U/^{238}U)	(^{230}Th/^{238}U)	(^{234}U/^{238}U)$_{initial}$	(^{230}Th/^{232}Th)	uncorrected age [ka BP]	corrected age [ka BP]
BB10-TS-37	8.37	2.725 ± 0.034	1.034 ± 0.067	2.983 ± 0.041	5.46 ± 1.98	49.34 ± 3.99	49.34 ± 3.92
BB10-TS-38	8.39	2.732 ± 0.034	1.034 ± 0.039	2.990 ± 0.038	22.91 ± 21.30	49.18 ± 2.31	49.17 ± 2.38
BB10-TS-39	8.41	2.722 ± 0.058	1.13 ± 0.16	3.013 ± 0.082	4596.20 ± 3744.92	55.21 + 10.2978 - 9.5436	55.21 + 10.3424 - 9.5511
BB10-TS-40	8.43	2.712 ± 0.019	1.057 ± 0.042	2.978 ± 0.024	18065.6 ± 21447.25	50.97 ± 2.54	50.97 ± 2.47
BB10-TS-41	8.45	2.768 ± 0.045	1.046 ± 0.057	3.031 ± 0.050	15949.28 ± 9282.33	49.05 ± 3.42	49.05 ± 3.36
BB10-TS-42	8.47	2.783 ± 0.052	1.08 ± 0.23	3.058 ± 0.093	7144.75 ± 2686.24	50.73 + 13.9495 - 12.1573	50.73 + 13.8511 - 12.5843
BB10-TS-43	8.49	2.740 ± 0.046	0.996 ± 0.034	2.986 ± 0.049	13232.44 ± 3445.53	46.83 ± 2.16	46.83 ± 2.15
BB10-TS-44	8.51	2.72 ± 0.57	1.068 ± 0.040	2.99 ± 0.59	1301.06 ± NA	51.40 + 18.9404 - 10.9518	51.39 + 19.1517 - 10.9927
BB10-TS-45	8.53	2.759 ± 0.044	1.071 ± 0.037	3.031 ± 0.046	15961.58 ± 8263.02	50.67± 2.34	50.68 ± 2.38
BB10-TS-46	8.55	2.722 ± 0.029	1.080 ± 0.054	2.995 ± 0.036	10583.46 ± 14479.40	52.10 ± 3.26	52.10 ± 3.29
BB10-TS-47	8.57	2.767 ± 0.040	1.079 ± 0.024	3.041 ± 0.042	166471.03 ± 277497.74	50.99 ± 1.62	50.99 ± 1.68
BB10-TS-48	8.59	2.752 ± 0.034	1.085 ± 0.036	3.027 ± 0.038	10396.82 ± 6382.38	51.64 ± 2.20	51.64 ± 2.21
BB10-TS-49	8.61	2.770 ± 0.042	1.101 ± 0.045	3.052 ± 0.046	5200.37 ± 4849.71	52.17 ± 2.78	52.17 ± 2.74
BB10-TS-50	8.63	2.766 ± 0.037	1.080 ± 0.046	3.041 ± 0.042	2184.09 ± 1285.22	51.05 ± 2.80	51.05 ± 2.76
BB10-TS-51	8.65	2.738 ± 0.052	1.074 ± 0.038	3.010 ± 0.055	21865.92 ± 24225.76	51.33 ± 2.48	51.33 ± 2.46
BB10-TS-52	8.67	2.763 ± 0.051	1.070 ± 0.052	3.034 ± 0.056	16411.51 ± 9014.16	50.55 ± 3.16	50.55 ± 3.18
BB10-TS-53	8.69	2.731 ± 0.033	1.073 ± 0.046	3.002 ± 0.037	5386.44 ± 6326.56	51.48 ± 2.87	51.48 ± 2.81
BB10-TS-54	8.71	2.765 ± 0.035	1.031 ± 0.032	3.024 ± 0.037	2.64 ± 0.98	48.30 ± 1.91	48.30 ± 1.98
BB10-TS-55	8.73	2.740 ± 0.046	1.077 ± 0.040	3.013 ± 0.048	1.85 ± 0.33	51.47 ± 2.51	51.47 ± 2.52
BB10-TS-56	8.75	2.774 ± 0.036	1.050 ± 0.040	3.038 ± 0.039	4.58 ± 2.11	49.16 ± 2.43	49.16 ± 2.44
BB10-TS-57	8.77	2.735 ± 0.057	1.069 ± 0.044	3.005 ± 0.060	3312.49 ± 2951.97	51.12 ± 2.79	51.12 ± 2.88

Table S3.7d: Results of the LA ^{230}Th/U-dating for sample BB-10. Activity ratios ate indicated by parentheses. BP = before present, i.e., 1950 CE. TS indicates calculated LA ages, LA individually measured ages. NA = no data available.

smpl ID	DFT [cm]	(^{234}U/^{238}U)	(^{230}Th/^{238}U)	(^{234}U/^{238}U)$_{initial}$	(^{230}Th/^{232}Th)	uncorrected age [ka BP]	corrected age [ka BP]
BB10-TS-58	8.79	2.751 ± 0.033	1.094 ± 0.028	3.029 ± 0.035	6639.07 ± 7042.79	52.20 ± 1.76	52.20 ± 1.82
BB10-TS-59	8.81	2.718 ± 0.028	1.112 ± 0.054	3.002 ± 0.033	225.43 ± 95.17	54.07 ± 3.28	54.07 ± 3.31
BB10-TS-60	8.83	2.755 ± 0.047	1.02 ± 0.11	3.009 ± 0.060	59.50 ± 17.72	47.78 ± 6.41	47.76 ± 6.39
BB10-TS-61	8.85	2.74 ± 0.76	1.102 ± 0.048	3.02 ± 0.78	30.02 ± 17.44	53.03 + 30.6055 - 14.1516	52.97 + 27.859 - 13.5322
BB10-TS-62	8.87	2.76 ± 0.52	1.064 ± 0.032	3.03 ± 0.54	2.55 ± 1.15	50.25 + 15.5433 - 9.788	50.27 + 16.2426 - 9.6435
BB10-TS-63	8.89	2.771 ± 0.033	1.081 ± 0.041	3.046 ± 0.035	5676.06 ± 3851.24	51.01 ± 2.48	51.01 ± 2.45
BB10-TS-64	8.91	2.728 ± 0.031	1.056 ± 0.041	2.993 ± 0.034	1373.80 ± 466.12	50.51 ± 2.52	50.51 ± 2.47
BB10-TS-65	8.93	2.743 ± 0.022	1.054 ± 0.038	3.009 ± 0.026	8318.09 ± 4370.57	50.06 ± 2.24	50.06 ± 2.23
BB10-TS-66	8.95	2.736 ± 0.042	1.077 ± 0.054	3.009 ± 0.047	24856.66 ± 17917.40	51.57 ± 3.26	51.57 ± 3.25
BB10-TS-67	8.97	2.691 ± 0.032	1.066 ± 0.052	2.959 ± 0.037	13800.12 ± 6147.33	51.98 ± 3.19	51.98 ± 3.24
BB10-TS-68	8.99	2.700 ± 0.034	1.088 ± 0.032	2.976 ± 0.037	30787.53 ± 14888.29	53.04 ± 2.09	53.04 ± 2.12
BB10-TS-69	9.01	2.745 ± 0.054	1.081 ± 0.040	3.019 ± 0.056	43573.68 ± 22250.32	51.58 ± 2.62	51.58 ± 2.69
BB10-TS-70	9.03	2.73 ± 0.69	1.092 ± 0.030	3.00 ± 0.71	21272.80 ± 15069.20	52.69 + 24.9669 - 12.7524	52.68 + 25.9816 - 12.6131
BB10-TS-71	9.05	2.738 ± 0.033	1.042 ± 0.058	2.999 ± 0.039	2723.30 ± 857.89	49.50 ± 3.45	49.50 ± 3.51
BB10-TS-72	9.07	2.706 ± 0.047	1.072 ± 0.017	2.977 ± 0.048	387.87 ± 146.49	51.97 ± 1.52	51.97 ± 1.53
BB10-TS-73	9.09	2.692 ± 0.048	1.021 ± 0.068	2.945 ± 0.053	4948.56 ± 2565.41	49.34 ± 4.13	49.33 ± 4.10
BB10-8 (LA)	9.10	2.691 ± 0.012	1.079 ± 0.025	2.961 ± 0.015	9559.56 ± 63989.00	52.76 ± 1.54	52.76 ± 1.54
BB10-TS-74	9.11	2.702 ± 0.031	1.052 ± 0.066	2.966 ± 0.038	12746.08 ± 15663.00	50.90 ± 3.87	50.90 ± 3.97
BB10-TS-75	9.13	2.683 ± 0.042	1.01 ± 0.20	2.933 ± 0.076	1485.53 ± 347.18	48.94 + 11.8467 - 10.8197	48.94 ± 11.46
BB10-TS-76	9.15	2.654 ± 0.038	1.10 ± 0.080	2.934 ± 0.047	1641.44 ± 488.71	55.27 ± 4.99	55.25 ± 5.15
BB10-TS-77	9.17	2.653 ± 0.036	1.021 ± 0.046	2.905 ± 0.039	1181.37 ± 469.53	50.21 ± 2.83	50.21 ± 2.87

Table S3.7d: Results of the LA ^{230}Th/U-dating for sample BB-10. Activity ratios ate indicated by parentheses. BP = before present, i.e., 1950 CE. TS indicates calculated LA ages, LA individually measured ages. NA = no data available.

smpl ID	DFT [cm]	(^{234}U/^{238}U)	(^{230}Th/^{238}U)	(^{234}U/^{238}U)$_{initial}$	(^{230}Th/^{232}Th)	uncorrected age [ka BP]	corrected age [ka BP]
BB10-TS-78	9.19	2.722 ± 0.056	1.046 ± 0.330	2.98 ± 0.12	854.48 ± 242.45	50.07 + 20.5211 - 18.3414	50.07 + 20.9994 - 18.1471
BB10-TS-79	9.21	2.697 ± 0.048	1.091 ± 0.037	2.973 ± 0.050	357.36 ± 88.83	53.33 ± 2.54	53.33 ± 2.55
BB10-TS-80	9.23	2.738 ± 0.039	1.090 ± 0.051	3.015 ± 0.043	792.23 ± 320.05	52.25 ± 3.07	52.25 ± 3.07
BB10-TS-81	9.25	2.703 ± 0.038	1.013 ± 0.079	2.954 ± 0.046	230.84 ± 88.98	48.62 ± 4.69	48.62 ± 4.56
BB10-TS-82	9.27	2.722 ± 0.031	1.057 ± 0.064	2.988 ± 0.038	148.79 ± 44.71	50.76 ± 3.75	50.76 ± 3.72
BB10-TS-83	9.29	2.679 ± 0.039	1.069 ± 0.050	2.948 ± 0.044	490.31 ± 113.37	52.49 ± 3.16	52.49 ± 3.21
BB10-TS-84	9.31	2.742 ± 0.037	1.047 ± 0.040	3.005 ± 0.040	1085.14 ± 360.62	49.68 ± 2.43	49.68 ± 2.43
BB10-TS-85	9.33	2.724 ± 0.032	1.090 ± 0.059	3.001 ± 0.039	3434.04 ± 1233.65	52.60 ± 3.54	52.59 ± 3.57
BB10-TS-86	9.35	2.676 ± 0.047	1.10 ± 0.23	2.956 ± 0.094	2142.83± 1231.28	54.54 + 15.4151 - 13.2353	54.54 + 15.2985 - 13.2036
BB10-TS-87	9.37	2.715 ± 0.025	1.100 ± 0.044	2.994 ± 0.030	1039.37 ± 370.21	53.44 ± 2.73	53.44 ± 2.63
BB10-TS-88	9.39	2.72 ± 0.57	1.048 ± 0.028	2.99 ± 0.59	416.85 ± 149.89	50.21 + 18.3944 - 10.2318	50.20 + 17.6264 - 10.1636
BB10-TS-89	9.40	2.699 ± 0.052	1.069 ± 0.090	2.968 ± 0.061	22.4 ± 8.01	51.99 ± 5.42	51.99 ± 5.59
BB10-TS-90	15.55	2.721 ± 0.030	1.138 ± 0.069	3.014 ± 0.039	3671.47 ± 400.88	55.58 ± 4.25	55.58 ± 4.28
BB10-TS-91	15.56	2.76 ± 0.99	1.065 ± 0.031	3.03 ± 1.03	3183.70 ± 1713.30	50.33 + 36.9531 - 15.6045	50.28 + 40.3007 - 15.3068
BB10-TS-92	15.59	2.831 ± 0.017	1.046 ± 0.039	3.096 ± 0.021	6657.35 ± 1965.64	47.74 ± 2.18	47.73 ± 2.18
BB10-TS-93	15.61	2.798 ± 0.055	1.171 ± 0.060	3.104 ± 0.059	4233.55 ± 3141.50	55.56 ± 3.81	55.56 ± 3.80
BB10-TS-94	15.63	2.704 ± 0.027	1.094 ± 0.086	2.982 ± 0.040	15681.78 ± 5651.96	53.33 ± 5.24	53.32 ± 5.32
BB10-TS-95	15.64	2.791 ± 0.051	1.111 ± 0.039	3.077 ± 0.053	5217.60 ± 2141.50	52.25 ± 2.48	52.23 ± 2.50
BB10-TS-96	15.67	2.745 ± 0.042	1.115 ± 0.023	3.030 ± 0.043	6067.32 ± 955.90	53.57 ± 1.74	53.55 ± 1.72
BB10-TS-97	15.69	2.814 ± 0.034	1.140 ± 0.078	3.109 ± 0.043	9710.74 ± 4398.68	53.36 ± 4.49	53.35 ± 4.54
BB10-TS-98	15.71	2.785 ± 0.067	1.163 ± 0.026	3.088 ± 0.070	8710.72 ± 2233.22	55.42 ± 2.28	55.42 ± 2.29

Table S3.7d: Results of the LA ^{230}Th/U-dating for sample BB-10. Activity ratios ate indicated by parentheses. BP = before present, i.e., 1950 CE. TS indicates calculated LA ages, LA individually measured ages. NA = no data available.

smpl ID	DFT [cm]	(^{234}U/^{238}U)	(^{230}Th/^{238}U)	(^{234}U/^{238}U)$_{initial}$	(^{230}Th/^{232}Th)	uncorrected age [ka BP]	corrected age [ka BP]
BB10-TS-99	15.72	2.777 ± 0.039	1.105 ± 0.044	3.060 ± 0.043	14593.23 ± 5684.59	52.25 ± 2.71	52.25 ± 2.64
BB10-TS-100	15.75	2.788 ± 0.029	1.140 ± 0.066	3.083 ± 0.038	13639.15 ± 4813.80	53.96 ± 3.81	53.96 ± 3.78
BB10-TS-101	15.77	2.768 ± 0.056	1.161 ± 0.058	3.070 ± 0.061	12133.00 ± 3500.38	55.74 ± 3.78	55.7 ± 3.76
BB10-TS-102	15.79	2.745 ± 0.044	1.164 ± 0.098	3.047 ± 0.056	19548.96 ± 11199.67	56.46 ± 6.00	56.46 ± 6.19
BB10-TS-103	15.80	2.807 ± 0.060	1.153 ± 0.098	3.107 ± 0.069	NA	54.02 ± 5.53	54.24 ± 5.79
BB10-TS-104	15.83	2.789 ± 0.034	1.067 ± 0.046	3.059 ± 0.037	45316.81 ± 43989.87	49.77 ± 2.69	49.77 ± 2.70
BB10-TS-105	15.85	2.800 ± 0.033	1.134 ± 0.016	3.094 ± 0.034	17900.49 ± 3587.09	53.32 ± 1.22	53.32 ± 1.23
BB10-TS-106	15.87	2.777 ± 0.042	1.119 ± 0.048	3.065 ± 0.046	83513.19 ± 119987.56	52.99 ± 2.92	53.00 ± 3.02
BB10-TS-107	15.88	2.801 ± 0.065	1.12 ± 0.40	3.09 ± 0.15	NA	52.71 + 24.7896 - 21.0351	52.71 + 25.56 - 21.2771
BB10-TS-108	15.90	2.723 ± 0.051	1.144 ± 0.025	3.018 ± 0.052	31848.58 ± 11718.90	55.87 ± 2.03	55.87 ± 2.03
BB10-TS-109	15.93	2.720 ± 0.044	1.127 ± 0.061	3.009 ± 0.050	13317.55 ± 11307.44	54.92 ± 3.77	54.92 ± 3.85
BB10-TS-110	15.94	2.728 ± 0.089	1.113 ± 0.088	3.013 ± 0.098	4447.87 ± 1853.15	53.88 ± 5.64	53.88 + 6.0073 - 5.5044
BB10-TS-111	15.96	2.673 ± 0.080	1.092 ± 0.075	2.949 ± 0.086	6032.01 ± 1934.70	53.98 ± 5.10	53.98 ± 5.00
BB10-TS-112	15.98	2.760 ± 0.049	1.125 ± 0.045	3.049 ± 0.053	10163.61 ± 2493.24	53.78 ± 2.98	53.78 ± 2.89
BB10-TS-113	16.01	2.769 ± 0.028	1.074 ± 0.056	3.042 ± 0.034	20964.06 ± 8021.96	50.65 ± 3.22	50.64 ± 3.31
BB10-TS-114	16.03	2.829 ± 0.062	1.092 ± 0.042	3.109 ± 0.066	21584.52 ± 18140.33	50.32 ± 2.70	50.31 ± 2.68
BB10-TS-115	16.05	2.855 ± 0.078	1.107 ± 0.096	3.140 ± 0.086	12507.53 ± 7254.91	50.54 ± 5.43	50.54 ± 5.56
BB10-TS-116	16.06	2.87 ± 0.15	1.19 ± 0.11	3.18 ± 0.16	7531.90 ± 4799.05	54.91 + 7.7067 - 7.1518	54.90 + 7.6109 - 6.9503
BB10-TS-117	16.09	2.825 ± 0.028	1.070 ± 0.038	3.097 ± 0.032	6911.56 ± 1919.43	49.15 ± 2.18	49.15 ± 2.15
BB10-TS-118	16.11	2.739 ± 0.090	1.121 ± 0.053	3.027 ± 0.093	NA	54.11 ± 3.88	54.11 ± 3.88
BB10-TS-119	16.13	2.877 ± 0.097	1.175 ± 0.062	3.186 ± 0.100	15303.81 ± 9651.91	53.88 ± 4.17	53.88 ± 4.28

Table S3.7d: Results of the LA ^{230}Th/U-dating for sample BB-10. Activity ratios ate indicated by parentheses. BP = before present, i.e., 1950 CE. TS indicates calculated LA ages, LA individually measured ages. NA = no data available.

smpl ID	DFT [cm]	(^{234}U/^{238}U)	(^{230}Th/^{238}U)	(^{234}U/^{238}U)$_{initial}$	(^{230}Th/^{232}Th)	uncorrected age [ka BP]	corrected age [ka BP]
BB10-TS-120	16.14	2.87 ± 0.13	1.13 ± 0.17	3.17 ± 0.14	12771.84 ± 10211.75	51.60 + 10.1414 - 9.2516	51.57 + 10.6898 - 9.6745
BB10-TS-121	16.17	2.81 ± 1.01	1.149 ± 0.097	3.11 ± 1.05	10547.59 ± 7056.52	53.88 + 48.0894 - 17.2423	53.88 + 48.3497 - 17.1355
BB10-TS-122	16.19	2.730 ± 0.083	1.078 ± 0.094	3.002 ± 0.090	11192.22 ± 2769.73	51.77 + 6.1335 - 5.608	51.76 + 6.0732 - 5.5354
BB10-TS-123	16.21	2.738 ± 0.080	1.056 ± 0.097	3.004 ± 0.087	5960.87 ± 2006.27	50.33 ± 5.95	50.32 ± 5.93
BB10-TS-124	16.22	2.787 ± 0.068	1.15 ± 0.42	3.08 ± 0.17	13399.52 ± 7091.61	54.43 + 27.3938 - 23.0078	54.43 + 27.5354 - 22.2006
BB10-TS-125	16.25	2.86 ± 0.12	1.163 ± 0.049	3.17 ± 0.13	15491.07 ± 10032.65	53.58 ± 3.88	53.58 ± 3.93
BB10-TS-126	16.27	2.919 ± 0.074	1.100 ± 0.052	3.203 ± 0.078	20531.85 ± 13005.84	48.82 ± 3.18	48.82 ± 3.17
BB10-TS-127	16.29	2.944 ± 0.027	1.096 ± 0.076	3.227 ± 0.037	87136.84 ±125902.04	48.11 ± 4.07	48.11 ± 3.99
BB10-TS-128	16.30	2.832 ± 0.030	1.164 ± 0.017	3.136 ± 0.032	27806.32 ± 16851.39	54.30 ± 1.21	54.29 ± 1.23
BB10-TS-129	16.33	2.773 ± 0.072	1.214 ± 0.072	3.093 ± 0.079	NA	58.75 ± 4.67	58.75 ± 4.67
BB10-TS-130	16.35	2.843 ± 0.041	1.199 ± 0.044	3.159 ± 0.043	NA	56.07 ± 2.76	56.07 ± 2.75
BB10-TS-131	16.36	2.876 ± 0.074	1.23 ± 0.16	3.204 ± 0.096	NA	56.94 + 10.0167 - 8.664	56.94 + 9.8704 - 9.1955
BB10-TS-132	16.38	2.759 ± 0.097	1.143 ± 0.070	3.05 ± 0.10	9659.41 ± 6407.48	54.90 ± 4.72	54.86 ± 4.75
BB10-TS-133	16.40	2.78 ± 0.11	1.174 ± 0.097	3.09 ± 0.12	16794.64 ± 13557.84	56.12 + 6.7383 - 6.135	56.12 + 6.832 - 6.0853
BB10-TS-134	16.43	2.75 ± 0.12	1.24 ± 0.10	3.08 ± 0.12	15261.86 ± 10064.15	61.31 + 7.4947 - 6.874	61.32 + 7.4475 - 6.8204
BB10-TS-135	16.45	2.738 ± 0.082	1.089 ± 0.083	3.014 ± 0.088	26031.32 ± 30973.49	52.20 ± 5.23	52.20 + 5.7028 - 4.983
BB10-TS-136	16.47	2.740 ± 0.078	1.04 ± 0.45	3.00 ± 0.17	NA	48.43 ± 2.79	49.56 + 28.5796 - 23.8116
BB10-TS-137	16.48	2.709 ± 0.056	1.11 ± 0.40	2.99 ± 0.15	10507.5± 5742.10	54.19 + 25.6855 - 22.3483	54.19 + 26.8193 - 22.4522
BB10-TS-138	16.51	2.745 ± 0.079	1.25 ± 0.46	3.08 ± 0.20	NA	61.50	61.54

Table S3.7d: Results of the LA ^{230}Th/U-dating for sample BB-10. Activity ratios ate indicated by parentheses. BP = before present, i.e., 1950 CE. TS indicates calculated LA ages, LA individually measured ages. NA = no data available.

smpl ID	DFT [cm]	(^{234}U/^{238}U)	(^{230}Th/^{238}U)	(^{234}U/^{238}U)$_{initial}$	(^{230}Th/^{232}Th)	uncorrected age [ka BP]	corrected age [ka BP]
						+ 32.6103 - 26.6087	+ 33.264 - 26.2658
BB10-TS-139	16.53	2.733 ± 0.091	1.153 ± 0.070	3.032 ± 0.096	23701.84 ± 22828.89	56.16 ± 4.88	56.16 ± 4.90
BB10-TS-140	16.55	2.75 ± 0.14	0.967 ± 0.060	2.99 ± 0.14	12197.83 ± 5764.91	45.02 ± 4.26	45.02 ± 4.32
BB10-TS-141	16.56	2.77 ± 0.11	1.045 ± 0.050	3.03 ± 0.11	NA	48.96 ± 3.66	48.96 ± 3.71
BB10-TS-142	16.59	2.772 ± 0.074	1.05 ± 0.13	3.035 ± 0.085	19995.45 ± 11587.00	48.96 + 7.6304 - 6.8601	48.96 ± 7.27
BB10-TS-143	16.61	2.735 ± 0.094	1.07 ± 0.39	3.00 ± 0.16	14382.28 ± 19322.86	50.98 + 25.2201 - 20.4145	50.98 + 24.8172 - 21.5581
BB10-TS-144	16.63	2.759 ± 0.031	1.009 ± 0.034	3.010 ± 0.033	54541.09 ± 59930.49	47.17 ± 2.00	47.17 ± 1.99
BB10-TS-145	16.64	2.69 ± 0.15	1.157 ± 0.050	2.99 ± 0.15	17923.81 ± 7175.03	57.49 + 5.2716 - 4.7041	57.48 + 5.3766 - 4.549
BB10-TS-146	16.67	2.716 ± 0.051	1.074 ± 0.032	2.987 ± 0.053	22422.15 ± 16623.95	51.85 ± 2.20	51.85 ± 2.25
BB10-TS-147	16.69	2.797 ± 0.062	1.22 ± 0.11	3.122 ± 0.073	28782.51 ± 22647.7	58.76 + 6.9034 - 6.3702	58.75 ± 6.73
BB10-TS-148	16.71	2.763 ± 0.023	1.134 ± 0.097	3.055 ± 0.041	35764.84 ± 37353.58	54.26 ± 5.81	54.26 ± 5.74
BB10-TS-149	16.72	2.771 ± 0.052	1.091 ± 0.039	3.049 ± 0.054	NA	51.56 ± 2.57	51.56 ± 2.51
BB10-TS-150	16.75	2.814 ± 0.052	1.198 ± 0.065	3.130 ± 0.058	23832.45 ± 13756.51	56.72 ± 4.00	56.72 ± 4.01
BB10-TS-151	16.77	2.720 ± 0.094	1.075 ± 0.090	2.99 ± 0.10	13227.36 ± 3367.84	51.82 ± 5.69	51.82 + 5.9272 - 5.3632
BB10-TS-152	16.78	2.700 ± 0.058	1.021 ± 0.024	2.953 ± 0.059	128399.65± 116736.78	49.13 ± 1.86	49.13 ± 1.88
BB10-TS-153	16.80	2.756 ± 0.090	1.090 ± 0.066	3.034 ± 0.094	NA	51.88 ± 4.34	51.84 ± 4.45
BB10-TS-154	16.82	2.86 ± 0.13	1.210 ± 0.060	3.19 ±0.13	NA	56.13 ± 4.55	56.13 ± 4.61
BB10-TS-155	16.85	2.866 ± 0.061	1.101 ± 0.066	3.149 ± 0.066	10748.22 ± 4719.00	50.03 ± 3.85	50.03 ± 3.90
BB10-TS-156	16.87	2.773 ± 0.064	1.146 ± 0.082	3.070 ± 0.070	7178.19 ± 4018.40	54.72 ± 4.96	54.72 ± 5.09
BB10-TS-157	16.89	2.86 ± 0.22	1.012 ± 0.031	3.11 ± 0.22	2395.55 ± 1034.04	45.31 + 4.9766 - 4.132	45.31 + 5.0008 - 4.1436

Table S3.7d: Results of the LA ^{230}Th/U-dating for sample BB-10. Activity ratios ate indicated by parentheses. BP = before present, i.e., 1950 CE. TS indicates calculated LA ages, LA individually measured ages. NA = no data available.

smpl ID	DFT [cm]	(^{234}U/^{238}U)	(^{230}Th/^{238}U)	(^{234}U/^{238}U)$_{initial}$	(^{230}Th/^{232}Th)	uncorrected age [ka BP]	corrected age [ka BP]
BB10-TS-158	16.90	2.801 ± 0.077	1.155 ± 0.049	3.101 ± 0.082	16784.07 ± 10648.45	54.57 ± 3.49	54.56 ± 3.33
BB10-TS-159	16.93	2.666 ± 0.054	1.110 ± 0.078	2.948 ± 0.061	23678.78 ± 27800.86	55.31 ± 4.95	55.28 ± 4.99
BB10-TS-160	16.95	2.774 ± 0.083	1.130 ± 0.048	3.066 ± 0.084	NA	53.73 ± 3.48	53.73 ± 3.44
BB10-TS-161	16.97	2.788 ± 0.043	1.103 ± 0.076	3.070 ± 0.052	44392.30 ±4 9136.96	51.88 ± 4.44	51.88 ± 4.34
BB10-TS-162	16.98	2.792 ± 0.081	1.148 ± 0.023	3.090 ± 0.082	27773.0 ± 14956.07	54.35 ± 2.39	54.34 ± 2.40
BB10-TS-163	17.01	2.724 ± 0.044	1.14 ± 0.41	3.02 ± 0.15	NA	55.43 + 27.1926 - 23.5704	55.43 + 27.5122 - 22.1724
BB10-TS-164	17.03	2.819 ± 0.060	1.129 ± 0.022	3.112 ± 0.062	4727.72 ± 1918.55	52.63 ± 1.87	52.63 ± 1.87
BB10-TS-165	17.05	2.747 ± 0.058	1.259 ± 0.092	3.083 ± 0.067	17669.96 ± 5030.69	62.30 ± 5.97	62.30 + 6.2115 - 5.6577
BB10-TS-166	17.06	2.686 ± 0.055	1.158 ± 0.071	2.985 ± 0.060	20412.47 ± 8573.52	57.74 ± 4.67	57.74 ± 4.66
BB10-TS-167	17.09	2.714 ± 0.070	1.16 ± 0.42	3.01 ± 0.16	10405.95 ± 3692.70	56.86 + 27.3425 - 23.6375	56.80 + 29.6461 - 23.6337
BB10-TS-168	17.11	2.77 ± 0.99	1.27 ± 0.47	3.12 ± 1.02	NA	62.21 + 74.9381 - 30.0943	62.16 + 80.6656 - 30.1459
BB10-TS-169	17.13	2.714 ± 0.026	1.047 ± 0.030	2.976 ± 0.028	19728.72 ± 13460.85	50.33 ± 1.85	50.32 ± 1.80
BB10-TS-170	17.14	2.777 ± 0.079	1.117 ± 0.077	3.064 ± 0.085	NA	52.90 ± 4.87	52.90 ± 4.82
BB10-TS-171	17.17	2.700 ± 0.020	1.059 ± 0.079	2.966 ± 0.033	62413.15 ± 21214.04	51.38 ± 4.61	51.38 ± 4.69
BB10-TS-172	17.19	2.713 ± 0.076	1.159 ± 0.050	3.012 ± 0.080	24895.27 ± 11592.43	57.03 ± 3.61	57.03 ± 3.62
BB10-TS-173	17.20	2.738 ± 0.072	1.121 ± 0.026	3.026 ± 0.074	19442.53 ± 20468.78	54.12 ± 2.35	54.12 ± 2.39
BB10-TS-174	17.22	2.463 ± 0.095	0.97 ± 0.38	2.70 ± 0.15	NA	52.09 + 27.1755 - 22.3482	52.07 + 27.3454 - 22.9836
BB10-TS-175	17.24	2.56 ± 0.14	0.92 ±0 .15	2.78 ± 0.15	3723.90 ± 979.83	46.01 + 9.5501 - 8.8823	46.00 + 10.2013 - 9.0123
BB10-TS-176	17.27	2.591 ± 0.064	1.12 ± 0.10	2.87 6± 0.075	5218.49 ± 3062.25	58.25 ± 6.96	58.25 + 7.2644 - 6.6362
BB10-TS-177	17.29	2.72 ± 0.15	1.09 ± 0.18	3.00 ± 0.16	3338.83 ± 2517.21	52.44	52.41

Table S3.7d: Results of the LA ^{230}Th/U-dating for sample BB-10. Activity ratios ate indicated by parentheses. BP = before present, i.e., 1950 CE. TS indicates calculated LA ages, LA individually measured ages. NA = no data available.

smpl ID	DFT [cm]	(^{234}U/^{238}U)	(^{230}Th/^{238}U)	(^{234}U/^{238}U)$_{initial}$	(^{230}Th/^{232}Th)	uncorrected age [ka BP]	corrected age [ka BP]
						+ 11.725 - 10.8433	+ 12.2371 - 10.975
BB10-TS-178	17.31	2.783 ± 0.059	1.09 ± 0.16	3.061 ± 0.080	NA	51.28 + 9.9023 - 9.1252	51.27 + 9.7948 - 9.1571
BB10-TS-179	17.32	2.72 ± 0.11	1.203 ± 0.063	3.03 ± 0.11	7338.18 ± 2528.36	59.66 ± 4.93	59.66 + 5.2675 - 4.7453
BB10-TS-180	17.35	2.61 ± 0.20	1.03 ± 0.11	2.87 ± 0.21	2384.10 ± 1115.08	51.98 + 9.247 - 8.2018	51.97 + 9.4457 - 8.098
BB10-TS-181	17.37	2.697 ± 0.065	1.08 ± 0.10	2.968 ± 0.076	2943.12 ± 1264.78	52.51 + 6.6549 - 5.9062	52.45 + 6.5471 - 6.015
BB10-TS-182	17.39	2.562 ± 0.076	1.19 ± 0.52	2.87 ± 0.21	NA	63.52 + 42.929 - 31.2172	63.46 + 42.2669 - 31.9916
BB10-TS-183	17.40	2.646 ± 0.054	1.121 ± 0.025	2.931 ± 0.055	1001.64 ± 633.91	56.51 ± 2.10	56.48 ± 2.13
BB10-TS-184	17.43	2.574 ± 0.057	1.09 ± 0.40	2.85 ± 0.15	2279.14 ± 1220.83	56.51 + 29.1347 - 23.7531	56.50 + 28.8828 - 23.4688
BB10-TS-185	17.45	2.53 ± 0.11	1.151 ± 0.070	2.83 ± 0.11	2036.44 ± 1122.83	61.83 ± 5.78	61.72 ± 5.95
BB10-TS-186	17.47	2.461 ± 0.054	0.926 ± 0.085	2.679 ± 0.060	6712.95 ± 2022.41	49.00 ± 5.56	48.98 ± 5.62
BB10-TS-187	17.48	2.407 ± 0.097	1.010 ± 0.069	2.65 ± 0.10	5850.06 ± 3533.61	56.04 + 5.6878 - 5.0685	56.03 ± 5.51
BB10-TS-188	17.51	2.43 ± 0.11	1.052 ± 0.099	2.68 ± 0.12	5562.39 ± 8151.09	58.34 + 8.2325 - 7.111	58.32 ± 7.66
BB10-TS-189	17.53	2.343 ± 0.041	1.040 ± 0.066	2.593 ± 0.047	12253.28 ± 5219.19	60.17 ± 4.89	60.17 ± 5.02
BB10-TS-190	17.55	2.46 ± 0.11	1.062 ± 0.040	2.72 ± 0.12	3835.63 ± 3875.30	58.08 + 4.8787 - 4.2196	58.09 + 4.8172 - 4.242
BB10-TS-191	17.56	2.510 ± 0.075	1.02 ± 0.45	2.76 ± 0.17	5019.22 ± 3017.93	54.07 + 32.2784 - 26.1778	53.94 + 33.1723 - 26.6335
BB10-TS-192	17.59	2.459 ± 0.098	1.087 ± 0.077	2.73 ± 0.11	59.74 + 6.4911 - 5.9611	59.74 + 6.4609 - 5.8473	59.74 + 6.4609 - 5.8473
BB10-TS-193	17.61	2.46 ± 0.10	0.984 ± 0.026	2.70 ± 0.11	16122.41 ± 5249.87	52.74 ± 3.30	52.74 ± 3.34
BB10-TS-194	17.63	2.563 ± 0.083	1.081 ± 0.070	2.832 ± 0.088	4283.95 ± 996.58	56.27 ± 5.15	56.26 ± 5.07

Table S3.7d: Results of the LA ^{230}Th/U-dating for sample BB-10. Activity ratios ate indicated by parentheses. BP = before present, i.e., 1950 CE. TS indicates calculated LA ages, LA individually measured ages. NA = no data available.

smpl ID	DFT [cm]	(^{234}U/^{238}U)	(^{230}Th/^{238}U)	(^{234}U/^{238}U)$_{initial}$	(^{230}Th/^{232}Th)	uncorrected age [ka BP]	corrected age [ka BP]
BB10-TS-195	17.64	2.444 ± 0.055	1.004 ± 0.089	2.685 ± 0.066	20444.30 ± 21720.47	54.51 ± 6.20	54.50 ± 6.15
BB10-TS-196	17.66	2.56 ± 0.19	1.068 ± 0.087	2.82 ± 0.20	NA	55.53 + 8.5208 - 7.2276	55.53 + 8.4618 - 7.0885
BB10-TS-197	17.69	2.564 ± 0.072	1.060 ± 0.033	2.826 ± 0.074	17093.44 ± 25817.49	54.8 7± 2.92	54.87 ± 2.93
BB10-TS-198	17.71	2.582 ± 0.065	1.08 ± 0.14	2.852 ± 0.081	8209.41 ± 5001.56	55.79 ± 9.19	55.79 + 9.5407 - 8.8118
BB10-TS-199	17.73	2.655 ± 0.034	1.15 ± 0.58	2.95 ± 0.21	21949.24 ± 15821.89	58.32 + 42.4038 - 33.135	58.32 + 41.7232 - 31.8739
BB10-TS-200	17.74	2.620 ± 0.072	1.30 ± 0.47	2.97 ± 0.20	NA	68.80 + 36.5961 - 29.7514	68.78 + 38.5036 - 30.3528
BB10-TS-201	17.77	2.496 ± 0.071	1.217 ± 0.093	2.812 ± 0.081	4829.79 ± 616.14	67.75 + 7.448 - 6.9312	67.70 ± 7.22
BB10-TS-202	17.79	2.618 ± 0.059	1.170 ± 0.088	2.920 ± 0.067	6582.48 ± 5554.31	60.4 9± 6.21	60.46 ± 6.05
BB10-TS-203	17.81	2.508 ± 0.047	1.151 ± 0.052	2.801 ± 0.050	2199.20 ± 2965.84	62.57 ± 3.90	62.60 ± 3.96
BB10-TS-204	17.82	2.595 ± 0.089	1.108 ± 0.072	2.875 ± 0.094	4581.32 ± 2907.64	57.11 + 5.4179 - 4.9063	57.11 ± 5.18
BB10-TS-205	17.85	2.629 ± 0.061	1.082 ± 0.069	2.901 ± 0.067	13086.19 ± 7960.01	54.52 ± 4.60	54.52 ± 4.61
BB10-TS-206	17.87	2.672 ± 0.065	1.101 ± 0.093	2.951 ± 0.073	9504.71 ± 4651.72	54.60 ±5.89	54.60 ± 5.79
BB10-TS-207	17.89	2.672 ± 0.051	1.15 ± 0.13	2.969 ± 0.069	25075.37 ± 17972.02	57.87 + 8.5997 - 8.0679	57.86 ± 8.15
BB10-TS-208	17.90	2.488 ± 0.060	1.038 ± 0.095	2.741 ± 0.070	8602.73 ± 4685.18	55.54 + 6.8168 - 6.2076	55.54 + 6.9614 - 6.3196
BB10-TS-209	17.93	2.427 ± 0.053	1.044 ± 0.018	2.681 ± 0.056	15925.50 ± 5122.69	57.75 ± 2.09	57.74 ± 2.05
BB10-TS-210	17.95	2.534 ± 0.058	1.135 ± 0.082	2.821 ± 0.067	7795.58 ± 1803.89	60.68 ± 5.71	60.67 ± 5.72
BB10-TS-211	17.97	2.53 ± 0.11	1.061 ± 0.090	2.79 ± 0.12	9394.11 ± 3124.56	55.80 + 6.9983 - 6.3275	55.80 ± 6.65
BB10-TS-212	17.98	2.548 ± 0.067	1.07 ± 0.11	2.814 ± 0.079	14824.31 ± 3185.48	56.03 + 7.7737 - 6.9322	56.03 + 7.5814 - 6.9879
BB10-TS-213	18.01	2.54 ± 0.10	1.089 ± 0.044	2.81 ± 0.11	9768.46 ± 8159.44	57.42	57.42 ± 4.14

Table S3.7d: Results of the LA ^{230}Th/U-dating for sample BB-10. Activity ratios ate indicated by parentheses. BP = before present, i.e., 1950 CE. TS indicates calculated LA ages, LA individually measured ages. NA = no data available.

smpl ID	DFT [cm]	(^{234}U/^{238}U)	(^{230}Th/^{238}U)	(^{234}U/^{238}U)$_{initial}$	(^{230}Th/^{232}Th)	uncorrected age [ka BP]	corrected age [ka BP]
						+ 4.5447 - 3.9206	
BB10-TS-214	18.03	2.525 ± 0.077	1.127 ± 0.032	2.809 ± 0.082	14623.22 ± 8392.11	60.40 ± 3.22	60.39 ± 3.26
BB10-TS-215	18.05	2.58 ± 1.12	1.12 ± 0.11	2.86 ± 1.15	21152.87 ± 12998.64	58.30 + 73.0606 - 21.5145	58.15 + 76.8485 - 21.179
BB10-TS-216	18.06	2.581 ± 0.087	1.077 ± 0.083	2.850 ± 0.097	9356.60 ± 4305.09	55.45 ± 5.81	55.45 ± 5.78
BB10-TS-217	18.08	2.609 ± 0.074	1.177 ± 0.076	2.913 ± 0.081	33536.55 ± 13001.35	61.12 ± 5.50	61.11 ± 5.36
BB10-TS-218	18.11	2.598 ± 0.097	1.18 ± 0.17	2.90 ± 0.12	7293.01 ± 5491.92	61.61 + 12.4149 - 11.4481	61.59 + 12.5509 - 10.9396
BB10-TS-219	18.13	2.652 ± 0.069	1.042 ± 0.055	2.911 ± 0.074	5997.51 ± 2368.50	51.51 ± 3.83	51.50 ± 3.64
BB10-TS-220	18.15	2.60 ± 0.14	1.162 ± 0.023	2.90 ± 0.14	14878.47 ± 18187.71	60.51 + 4.714 - 3.9765	60.51 ± 4.38
BB10-TS-221	18.16	2.646 ± 0.048	1.21 ± 0.45	2.96 ± 0.18	NA	62.27 + 33.2769 - 26.8085	62.32 + 33.0856 - 26.9682
BB10-TS-222	18.19	2.60 ±0.93	1.08 ± 0.12	2.88 ± 0.96	6966.10 ± 3526.13	55.36 + 49.5657 - 18.3638	55.32 + 51.8222 - 18.0289
BB10-TS-223	18.21	2.626 ± 0.021	1.112 ± 0.044	2.908 ± 0.026	13766.99 ± 11060.52	56.47 ± 2.84	56.46 ± 2.82
BB10-TS-224	18.23	2.62 ± 0.11	1.164 ± 0 .083	2.92 ± 0.12	7615.28 ± 3619.98	59.86 + 6.8068 - 6.0168	59.86 + 6.6501 - 5.8159
BB10-TS-225	18.24	2.650 ± 0.052	1.112 ± 0.065	2.933 ± 0.059	2378.80 ± 569.98	55.84 ± 4.27	55.83 ± 4.29
BB10-TS-226	18.27	2.642 ± 0.039	1.150 ± 0.055	2.938 ± 0.044	1078.24 ± 511.51	58.43 ± 3.62	58.41 ± 3.74
BB10-TS-227	18.29	2.608 ± 0.084	1.094 ± 0.056	2.884 ± 0.089	3618.91 ± 2102.57	55.83 ± 4.22	55.81 ± 4.13
BB10-TS-228	18.31	2.56 ± 0.14	1.07 ± 0.15	2.82 ± 0.15	7323.50 ± 1354.71	55.68 + 11.2114 - 9.964	55.66 + 11.2884 - 9.8884
BB10-TS-229	18.32	2.643 ± 0.063	1.109 ± 0.082	2.924 ± 0.071	4670.86 ± 1297.97	55.82 ± 5.39	55.82 ± 5.41
BB10-TS-230	18.35	2.683 ± 0.066	1.077 ± 0.082	2.954 ± 0.075	4520.07 ± 2283.72	52.84 ± 5.28	52.83 ± 5.39
BB10-TS-231	18.37	2.706 ± 0.063	1.113 ± 0.081	2.991 ± 0.069	4345.05 ± 3029.70	54.44 ± 5.13	54.43 ±5.27
BB10-TS-232	18.39	2.698 ± 0.069	1.184 ± 0.084	3.007 ± 0.078	9530.38 ± 4999.48	59.01 ± 5.59	59.01 ± 5.48

Table S3.7d: Results of the LA ^{230}Th/U-dating for sample BB-10. Activity ratios ate indicated by parentheses. BP = before present, i.e., 1950 CE. TS indicates calculated LA ages, LA individually measured ages. NA = no data available.

smpl ID	DFT [cm]	(^{234}U/^{238}U)	(^{230}Th/^{238}U)	(^{234}U/^{238}U)$_{initial}$	(^{230}Th/^{232}Th)	uncorrected age [ka BP]	corrected age [ka BP]
BB10-TS-233	18.40	2.574 ± 0.023	1.148 ± 0.044	2.867 ± 0.028	32564.16 ± 6208.87	60.30 ± 2.97	60.30 ± 3.04
BB10-TS-234	18.43	2.609 ± 0.034	1.083 ± 0.081	2.881 ± 0.044	82121.30 ± 95712.81	55.12 ± 5.08	55.11 ± 5.04
BB10-TS-235	18.45	2.592 ± 0.100	1.155 ± 0.060	2.89 ± 0.10	41647.94 ± 28734.13	60.21 ± 4.96	60.20 + 5.2095 - 4.559
BB10-TS-236	18.47	2.560 ± 0.058	1.193 ± 0.065	2.868 ± 0.064	NA	63.80 ± 5.01	63.80 ± 4.97
BB10-TS-237	18.48	2.643 ± 0.098	1.22 ± 0.44	2.9 ± 0.19	NA	63.23 + 32.0633 - 26.6014	63.21 + 33.3184 - 26.3017
BB10-TS-238	18.50	2.65 ± 0.95	1.140 ± 0.053	2.94 ± 0.98	26834.17 ± 7790.13	57.59 + 52.7373 - 17.9194	57.57 + 51.5989 - 18.4132
BB10-TS-239	18.53	2.71 ± 0.97	1.080 ± 0.074	2.98 ± 0.99	15968.30 ± 5342.45	52.33 + 43.4178 - 16.7614	52.35 + 46.7693 - 16.3346
BB10-TS-240	18.54	2.676 ± 0.089	1.212 ± 0.526	2.99 ± 0.22	8850.36 ± 2258.49	61.39 + 38.9549 - 30.5697	61.38 + 36.891 - 30.3627
BB10-TS-241	18.56	2.748 ± 0.078	1.098 ± 0.077	3.028 ± 0.084	9072.15 ± 3252.60	52.50 + 5.1542 - 4.6399	52.48 ± 4.85
BB10-TS-242	18.58	2.638 ± 0.067	1.146 ± 0.093	2.931 ± 0.075	29076.73 ± 24046.15	58.33 ± 6.24	58.32 ± 6.27
BB10-TS-243	18.61	2.588 ± 0.040	1.076 ± 0.067	2.857 ± 0.047	10559.25 ± 2360.54	55.24 ± 4.37	55.23 ± 4.25
BB10-TS-244	18.63	2.602 ± 0.041	1.054 ± 0.094	2.864 ± 0.052	9451.07 ± 4289.51	53.49 ± 5.95	53.47 ± 6.07
BB10-TS-245	18.65	2.737 ± 0.067	1.02 ± 0.11	2.992 ± 0.075	4879.44 ± 2017.46	48.57 ± 6.18	48.54 ± 6.10
BB10-TS-246	18.66	2.579 ± 0.074	1.18 ± 0.11	2.885 ± 0.085	4419.82 ± 3622.34	62.65 + 8.2466 - 7.6832	62.59 ± 8.03
BB10-TS-247	18.69	2.381 ± 0.047	1.068 ± 0.026	2.641 ± 0.050	1295.53 ± 1089.59	62.31 ± 3.30	60.97 ± 2.49
BB10-TS-248	18.71	2.525 ± 0.094	1.046 ± 0.036	2.782 ± 0.099	16838.81 ± 15417.22	55.23 ± 3.47	55.05 ± 3.41
BB10-TS-249	18.73	2.626 ± 0.051	1.052 ± 0.084	2.888 ± 0.059	6870.13 ± 3881.84	52.76 ± 5.18	52.75 ± 5.21
BB10-TS-250	18.74	2.499 ± 0.039	1.063 ± 0.062	2.761 ± 0.046	7521.25 ± 2021.74	56.93± 4.29	56.92 ± 4.28
BB10-TS-251	18.77	2.72 ± 0.19	1.228 ± 0.078	3.04 ± 0.19	2865.45 ± 1456.73	61.23 + 7.8419 - 6.7254	61.21 + 7.8818 - 6.6524

Table S3.7d: Results of the LA ^{230}Th/U-dating for sample BB-10. Activity ratios ate indicated by parentheses. BP = before present, i.e., 1950 CE. TS indicates calculated LA ages, LA individually measured ages. NA = no data available.

smpl ID	DFT [cm]	(^{234}U/^{238}U)	(^{230}Th/^{238}U)	(^{234}U/^{238}U)$_{initial}$	(^{230}Th/^{232}Th)	uncorrected age [ka BP]	corrected age [ka BP]
BB10-TS-252	18.79	2.718 ± 0.041	1.25 ± 0.14	3.051 ± 0.065	5879.07 ± 3373.83	62.77 + 9.3497 - 8.5402	62.67 + 9.3872 - 8.553
BB10-TS-253	18.81	2.77 ± 0.12	1.07 ± 0.10	3.05 ± 0.13	3686.08 ± 1377.63	50.58 ± 6.38	50.27 ± 6.45
BB10-TS-254	18.82	2.578 ± 0.074	1.10 ± 0.18	2.855 ± 0.095	1036.39 ± 1054.85	57.62 + 12.007 - 10.9617	57.29 + 12.3327 - 11.4965

Table S3.7e: Results of the solution-based ^{230}Th/U-dating for sample BB-15. Activity ratios ate indicated by parentheses. BP = before present, i.e., 1950 CE, MM = MicroMill, hh = handheld

smpl ID	DFT [cm]		^{238}U [µg/g]	^{232}Th [ng/g]	(^{234}U/^{238}U)	(^{230}Th/^{238}U)	(^{234}U/^{238}U)$_{initial}$	(^{230}Th/^{232}Th)	uncorrected age [ka BP]	corrected age [ka BP]
SB 5	17.67	hh	0.3943 ± 0.0025	0.9425 ± 0.0060	2.6353 ± 0.0010	0.7873 ± 0.0013	2.8167 ± 0.0011	1042.92 ± 1.60	37.23 ± 0.069	37.20 ± 0.07
SB14	18.08	hh	0.2621 ± 0.0018	0.10273 ± 0.00074	3.0144 ± 0.0013	0.9150 ± 0.0021	3.2416 ± 0.0014	7391.89 ± 22.02	37.79 ± 0.10	37.79 ± 0.10
SB15	18.75	hh	0.3933 ± 0.0024	2.19 ± 0.01	2.6291 ± 0.0015	1.0238 ± 0.0017	2.8810 ± 0.0016	581.17 ± 0.91	50.95 ± 0.10	50.88 ± 0.11
SB 6	18.77	hh	0.4550 ± 0.0028	76.70 ± 0.46	2.66 ± 0.04	1.0175 ± 0.0014	2.9068 ± 0.0390	19.100 ± 0.023	51.537 ± 0.085	49.36 ± 1.13
SB16	19.66	hh	0.2083 ± 0.0013	0.2256 ± 0.0015	2.8023 ± 0.0015	1.1544 ± 0.0026	3.1017 ± 0.0017	3375.01 ± 7.80	54.41 ± 0.15	54.40 ± 0.15
SB17	20.36	hh	0.1935 ± 0.0012	0.2045 ± 0.0013	2.5937 ± 0.0012	1.1184 ± 0.0028	2.8760 ± 0.0016	3350.76 ± 8.60	57.73 ± 0.18	57.72 ± 0.18
SB 7	20.68	hh	0.2674 ± 0.0017	0.3135 ± 0.0020	2.7878 ± 0.0010	1.2186 ± 0.0015	3.1095 ± 0.0012	3291.13 ± 4.50	58.576 ± 0.097	58.562 ± 0.096

Table S3.7f: Results of the LA ^{230}Th/U-dating for sample BB-15. Activity ratios ate indicated by parentheses. BP = before present, i.e., 1950 CE. TS indicates calculated LA ages, LA individually measured ages. NA = no data available.

smpl ID	DFT [cm]	(^{234}U/^{238}U)	(^{230}Th/^{238}U)	(^{234}U/^{238}U)$_{initial}$	(^{230}Th/^{232}Th)	uncorrected age [ka BP]	corrected age [ka BP]
BB15-TS-7	17.29	2.734 ± 0.061	0.778 ± 0.082	2.916 ± 0.066	7.14 ± 3.35	36.87 + 4.36	35.19 ± 4.34
BB15-TS-8	17.31	2.665 ± 0.091	0.92 ± 0.19	2.88 ± 0.11	38.29 ± 64.15	44.96 + 11.5714 - 10.5006	43.81 + 11.3 - 10.4923
BB15-TS-9	17.34	2.700 ± 0.075	0.71 ± 0.16	2.863 ± 0.089	50.24 ± 49.90	32.89± 8.21	32.44 + 8.5248 - 7.9693
BB15-TS-10	17.36	2.713 ± 0.038	0.721 ± 0.046	2.879 ± 0.041	1867.22 ± 817.13	32.57 ± 2.46	32.55 ± 2.43
BB15-TS-11	17.38	2.71 ± 0.18	0.669 ± 0.041	2.86 ± 0.19	778.88 ± 524.41	30.05 ± 3.10	29.98 ± 3.14
BB15-TS-12	17.41	2.751 ± 0.094	0.773 ± 0.049	2.931 ± 0.096	1671.39 ± 357.32	34.74 ± 2.85	34.70 ± 2.90
BB15-TS-13	17.60	2.702 ± 0.043	0.80 ± 0.18	2.890 ± 0.067	NA	37.1 ± 9.24	37.08 + 9.6252 - 8.8874
BB15-TS-14	17.62	2.646 ± 0.037	0.71 ± 0.14	2.807 ± 0.053	7947.1 2± 4269.79	32.91 ± 7.21	32.89 + 7.5121 - 6.786
BB15-TS-15	17.64	2.680 ± 0.071	0.82 ± 0.18	2.871 ± 0.089	NA	38.24 + 10.2862 - 9.287	38.22 + 10.1785 - 9.5083
BB15-TS-16	17.66	2.615 ± 0.048	0.718 ± 0.045	2.778 ± 0.050	NA	33.86 ± 2.46	33.84 ± 2.54
BB15-TS-17	17.68	2.627 ± 0.066	0.730 ± 0.051	2.792 ± 0.070	1997.38 ± 1198.72	34.30 ± 2.93	34.28 ± 2.94
BB15-TS-18	17.70	2.632 ± 0.046	0.763 ± 0.031	2.807 ± 0.047	1230.05 ± 334.37	35.98 ± 1.81	35.95 ± 1.81
BB15-TS-19	17.72	2.652 ± 0.043	0.786 ± 0.036	2.833 ± 0.043	3458.63 ± 1743.93	36.95 ± 2.07	36.90 ± 2.12
BB15-TS-20	17.74	2.619 ± 0.059	0.786 ± 0.044	2.800 ± 0.061	NA	37.49 ± 2.55	37.44 ± 2.67
BB15-TS-21	17.76	2.633 ± 0.047	0.846 ± 0.061	2.831 ± 0.051	NA	40.60 ± 3.46	40.55 ± 3.52
BB15-TS-22	17.78	2.635 ± 0.047	0.804 ± 0.039	2.821 ± 0.049	NA	38.23 ± 2.27	38.16 ± 2.36
BB15-TS-23	17.80	2.670 ± 0.096	0.768 ± 0.058	2.85 ± 0.10	3246.69 ± 1001.33	35.70 ± 3.39	35.63 ± 3.39
BB15-TS-24	17.82	2.778 ± 0.091	0.852 ± 0.025	2.982 ± 0.093	NA	38.45 ± 1.97	38.35 ± 1.98
BB15-TS-25	17.84	2.731 ± 0.088	0.789 ± 0.050	2.916 ± 0.090	27408.83 ± 19724.23	35.94 ± 3.00	35.84 ± 2.97
BB15-TS-26	17.86	2.768 ± 0.049	0.809 ± 0.030	2.959 ± 0.050	14862.06 ± 4554.09	36.31 ± 1.77	36.26 ± 1.74

Table S3.7f: Results of the LA ^{230}Th/U-dating for sample BB-15. Activity ratios ate indicated by parentheses. BP = before present, i.e., 1950 CE. TS indicates calculated LA ages, LA individually measured ages. NA = no data available.

smpl ID	DFT [cm]	$(^{234}U/^{238}U)$	$(^{230}Th/^{238}U)$	$(^{234}U/^{238}U)_{initial}$	$(^{230}Th/^{232}Th)$	uncorrected age [ka BP]	corrected age [ka BP]
BB15-TS-27	17.88	2.759 ± 0.055	0.796 ± 0.063	2.946 ± 0.058	10351.11 ± 4827.43	35.79 ± 3.30	35.74 ± 3.38
BB15-TS-28	17.90	2.762 ± 0.042	0.810 ± 0.048	2.953 ± 0.045	9334.36 ± 2973.95	36.44 ± 2.57	36.41 ± 2.59
BB15-TS-29	17.92	2.781 ± 0.038	0.799 ± 0.036	2.969 ± 0.039	9253.18 ± 3391.08	35.61 ± 1.92	35.57 ± 1.97
BB15-TS-30	17.94	2.804 ± 0.045	0.813 ± 0.033	2.997 ± 0.047	NA	35.98 ± 1.74	35.93 ± 1.79
BB15-TS-31	17.96	2.808 ± 0.049	0.830 ± 0.059	3.006 ± 0.052	4143.14 ± 1116.21	36.79 ± 3.10	36.73 ± 3.10
BB15-TS-32	17.98	2.863 ± 0.066	0.843 ± 0.066	3.066 ± 0.070	6249.16 ± 2445.85	36.62 ± 3.44	36.57 ± 3.42
BB15-TS-33	18.00	2.911 ± 0.054	0.838 ± 0.030	3.114 ± 0.055	4156.09 ± 1331.63	35.68 ± 1.65	35.62 ± 1.59
BB15-TS-34	18.02	2.976 ± 0.077	0.958 ± 0.064	3.216 ± 0.081	1647.57 ± 289.65	40.61 ± 3.38	40.51 ± 3.43
BB15-TS-35	18.04	2.958 ± 0.083	0.86 ± 0.18	3.167 ± 0.098	N A	36.03 + 8.7413 - 8.1958	35.93 + 9.0564 - 8.1036
BB15-TS-36	18.06	3.05 ± 0.85	0.80 ± 0.19	3.25 ± 0.89	3698.74 ± 1580.52	32.31 + 19.5472 - 10.5735	32.20 + 18.7907 - 10.7291
BB15-TS-37	18.08	2.973 ± 0.080	0.856 ± 0.078	3.182 ± 0.086	11886.17 ± 11541.89	35.83 ± 4.00	35.64 ± 3.96
BB15-TS-38	18.10	2.99 ± 0.10	0.827 ± 0.078	3.19 ± 0.11	3988.88 ± 2553.54	34.24 ± 3.83	34.07 ± 3.89
BB15-TS-39	18.12	3.024 ± 0.067	0.932 ± 0.070	3.258 ± 0.072	5678.61 ± 1396.36	38.74 ± 3.58	38.51 ± 3.41
BB15-TS-40	18.14	3.182 ± 0.082	0.958 ± 0.076	3.427 ± 0.085	9858.83 ± 4059.66	37.58 ± 3.69	37.46 ± 3.59
BB15-TS-41	18.16	3.317 ± 0.070	0.935 ± 0.052	3.556 ± 0.073	10380.12 ± 4842.53	34.89 ± 2.36	34.73 ± 2.38
BB15-TS-42	18.18	3.421 ± 0.079	1.034 ± 0.038	3.693 ± 0.081	6998.56 ± 1806.84	37.70± 1.89	37.57 ± 1.86
BB15-TS-43	18.20	3.420 ± 0.066	1.054 ± 0.055	3.698 ± 0.070	5739.27 ± 2087.22	38.54± 2.38	38.44 ± 2.50
BB15-TS-44	18.22	3.367 ± 0.060	1.086 ± 0.052	3.654 ± 0.063	3229.36 ± 880.68	40.86 ± 2.48	40.50 ± 2.42
BB15-TS-45	18.24	2.96 ± 0.11	0.914 ± 0.063	3.19 ± 0.12	1872.89 ± 416.77	39.02 ± 3.54	38.59 ± 3.50
BB15-TS-46	18.26	2.898 ± 0.089	0.815 ± 0.084	3.094 ± 0.094	359.69 ± 257.39	38.08 + 5.5715 - 4.7787	34.71 ± 4.30
BB15-TS-47	18.54	2.749 ± 0.039	1.082 ± 0.058	3.024 ± 0.045	2052.16 ± 586.89	51.58 ± 3.45	51.57 ± 3.52

Table S3.7f: Results of the LA ^{230}Th/U-dating for sample BB-15. Activity ratios ate indicated by parentheses. BP = before present, i.e., 1950 CE. TS indicates calculated LA ages, LA individually measured ages. NA = no data available.

smpl ID	DFT [cm]	(^{234}U/^{238}U)	(^{230}Th/^{238}U)	(^{234}U/^{238}U)$_{initial}$	(^{230}Th/^{232}Th)	uncorrected age [ka BP]	corrected age [ka BP]
BB15-TS-48	18.56	2.723 ± 0.052	1.088 ± 0.070	2.999 ± 0.057	8759.82 ± 1243.32	52.49 ± 4.38	52.48 ± 4.20
BB15-TS-49	18.58	2.721 ± 0.058	1.087 ± 0.083	2.997 ± 0.066	5348.20 ± 2430.50	52.55 ± 5.10	52.54 ± 5.00
BB15-TS-50	18.60	2.761 ± 0.067	1.075 ± 0.054	3.034 ± 0.070	5507.54 ± 3004.36	50.86 ± 3.50	50.86 ± 3.45
BB15-TS-51	18.62	2.741 ± 0.064	1.049 ± 0.053	3.005 ± 0.067	1510.41 ± 675.33	49.86 ± 3.40	49.84 ± 3.36
BB15-TS-52	18.64	2.707 ± 0.050	1.031 ± 0.068	2.964 ± 0.056	4322.02 ± 1107.52	49.54 ± 4.11	49.53 ± 4.10
BB15-TS-53	18.66	2.740 ± 0.051	1.054 ± 0.069	3.005 ± 0.056	12888.77 ± 15361.63	50.13 ± 4.23	50.13 ± 4.10
BB15-TS-54	18.68	2.74 ± 0.58	1.048 ± 0.049	3.01 ± 0.60	NA	49.77 + 17.5851 - 10.5824	49.75 + 18.5571 - 10.5132
BB15-TS-55	18.70	2.728 ± 0.057	1.073 ± 0.067	2.999 ± 0.062	NA	51.52 ± 4.05	51.52 ± 4.06
BB15-TS-56	18.72	2.662 ± 0.052	1.026 ± 0.044	2.916 ± 0.056	22694.31 ± 19135.12	50.29 ± 2.93	50.27 ± 2.87
BB15-TS-57	18.74	2.626 ± 0.060	1.007 ± 0.065	2.874 ± 0.066	3721.75 ± 1540.69	50.06 ± 4.06	50.03 ± 4.18
BB15-TS-58	18.76	2.567 ± 0.035	0.986 ± 0.066	2.806 ± 0.041	2107.00 ± 548.92	50.14 ± 4.21	50.12 ± 4.20
BB15-TS-59	18.78	2.554 ± 0.058	0.97 ± 0.21	2.788 ± 0.088	1093.42 ± 476.68	49.76 + 13.5522 - 12.3213	49.75 + 13.5507 - 12.1496
BB15-TS-60	18.80	2.558 ± 0.036	0.929 ± 0.035	2.779 ± 0.039	NA	46.92 ± 2.28	46.92 ± 2.26
BB15-TS-61	18.82	2.569 ± 0.040	0.995 ± 0.077	2.811 ± 0.047	18195.08 ± 9032.03	50.64 ± 5.00	50.64 ± 4.74
BB15-TS-62	18.84	2.557 ± 0.061	0.94 ± 0.19	2.781 ± 0.085	6056.63 ± 4451.72	47.57 + 11.9878 - 11.1007	47.46 + 12.5047 - 11.0561
BB15-TS-63	18.86	2.529 ± 0.065	0.975 ± 0.078	2.763 ± 0.069	473.98 ± 143.86	50.47 ± 5.17	50.40 ± 5.23
BB15-TS-64	18.88	2.559 ± 0.042	0.992 ± 0.072	2.800 ± 0.048	278.99 ± 69.98	50.77 ± 4.61	50.73 ± 4.49
BB15-TS-65	18.90	2.556 ± 0.075	1.001 ± 0.045	2.799 ± 0.077	410.38 ± 321.18	51.40 ± 3.39	51.38 ± 3.32
BB15-TS-66	18.92	2.580 ± 0.071	0.931 ± 0.043	2.802 ± 0.075	1945.20 ± 694.33	46.51 ± 3.07	46.50 ± 3.07
BB15-TS-67	18.94	2.649 ± 0.074	0.951 ± 0.062	2.880 ± 0.078	2539.39 ± 1507.91	46.24 ± 3.87	46.21 ± 3.91
BB15-TS-68	18.96	2.578 ± 0.086	1.043 ± 0.073	2.835 ± 0.092	2828.36 ± 924.41	53.54 ± 5.09	53.45 ± 4.96

Table S3.7f: Results of the LA ^{230}Th/U-dating for sample BB-15. Activity ratios ate indicated by parentheses. BP = before present, i.e., 1950 CE. TS indicates calculated LA ages, LA individually measured ages. NA = no data available.

smpl ID	DFT [cm]	(^{234}U/^{238}U)	(^{230}Th/^{238}U)	(^{234}U/^{238}U)$_{initial}$	(^{230}Th/^{232}Th)	uncorrected age [ka BP]	corrected age [ka BP]
BB15-TS-69	18.99	2.686 ± 0.064	0.97 ± 0.27	2.92 ± 0.11	2043.55 ± 840.06	46.44 + 16.6342 - 14.6841	46.37 + 17.3019 - 15.2839
BB15-TS-70	19.00	2.66 ± 0.10	0.895 ± 0.082	2.87 ± 0.11	1530.75 ± 456.65	42.96 ± 5.04	42.76 ± 5.09
BB15-TS-71	19.01	2.581 ± 0.061	1.098 ± 0.085	2.857 ± 0.068	721.30 ± 212.77	56.84 ± 5.66	56.82 ± 5.69
BB15-TS-72	19.03	2.63 ± 0.13	1.012 ± 0.092	2.88 ± 0.13	884.18 ± 274.70	50.31 ± 6.18	50.27 + 6.8297 - 6.1406
BB15-TS-73	19.05	2.677 ± 0.069	1.10 ± 0.10	2.957 ± 0.080	705.37 ± 425.46	54.69 + 6.5986 - 6.0914	54.62 ± 6.57
BB15-TS-74	19.07	2.812 ± 0.032	1.107 ± 0.054	3.097 ± 0.037	7799.08 ± 2814.69	51.56 ± 3.06	51.56 ± 3.06
BB15-TS-75	19.10	2.80 ± 0.14	1.15 ± 0.12	3.10 ± 0.15	8892.68 ± 4238.85	54.15 + 7.644 - 7.124	54.14 + 7.9949 - 7.3818
BB15-TS-76	19.12	2.808 ± 0.080	1.13 ± 0.13	3.101 ± 0.095	2716.18 ± 644.69	53.20 ± 7.69	53.20 ± 7.72
BB15-TS-77	19.14	2.709 ± 0.082	1.19 ± 0.12	3.018 ± 0.094	10260.59 ± 10929.58	58.81 ± 7.89	58.82 + 8.0379 - 7.521
BB15-TS-78	19.16	2.78 ± 0.11	1.15 ± 0.11	3.08 ± 0.12	69901.84 ± 82377.41	54.40 ± 6.99	54.39 + 7.218 - 6.4929
BB15-TS-79	19.18	2.68 ± 0.15	1.25 ± 0.12	3.02 ± 0.16	3216.18 ± 2103.24	63.89 + 9.5883 - 8.5297	63.85 + 9.7009 - 8.3875
BB15-TS-80	19.20	2.63 ± 0.16	1.21 ± 0.31	2.94 ± 0.20	507.86 ± 227.03	62.70 + 22.8604 - 19.3265	62.68 + 23.4686 - 19.5974
BB15-TS-81	19.22	2.48 ± 0.17	1.00 ± 0.33	2.72 ± 0.20	1296.13 ± 737.70	53.14 + 24.6419 - 20.4648	53.12 + 24.8982 - 20.5405
BB15-TS-82	19.24	2.37 ± 0.20	1.39 ± 0.34	2.76 ± 0.26	2012.23 ± 1168.39	86.67 + 37.5209 - 28.2222	86.67 + 37.3212 - 28.1462
BB15-TS-83	19.26	2.4 2± 0.14	1.18 ± 0.22	2.71 ± 0.16	3990.04 ± 2723.89	67.75 + 18.6409 - 15.5429	67.73 + 18.7957 - 15.8711
BB15-TS-84	19.28	2.3 6± 0.11	1.063 ± 0.090	2.62 ± 0.11	1004.51 ± 178.75	61.30 + 8.0624 - 7.177	61.29 + 7.7876 - 7.2303
BB15-TS-85	19.30	2.57 ± 0.11	1.02 ± 0.16	2.82 ± 0.12	2909.03 ± 865.85	52.20 + 11.2196 - 9.9892	52.18 + 10.9524 - 9.7854

Table S3.7f: Results of the LA ^{230}Th/U-dating for sample BB-15. Activity ratios ate indicated by parentheses. BP = before present, i.e., 1950 CE. TS indicates calculated LA ages, LA individually measured ages. NA = no data available.

smpl ID	DFT [cm]	(^{234}U/^{238}U)	(^{230}Th/^{238}U)	(^{234}U/^{238}U)$_{initial}$	(^{230}Th/^{232}Th)	uncorrected age [ka BP]	corrected age [ka BP]
BB15-TS-86	19.32	2.47 ± 0.14	0.993 ± 0.079	2.71 ± 0.14	NA	53.10 + 6.4644 - 5.855	53.08 + 7.0488 - 6.0821
BB15-TS-87	19.34	2.498 ± 0.098	1.15 ± 0.17	2.79 ± 0.12	NA	62.97 + 13.53 - 11.9158	62.96 + 13.9653 - 12.0027
BB15-TS-88	19.36	2.53 ± 0.50	1.098 ± 0.093	2.80 ± 0.52	16004.98 ± 17997.36	58.38 + 21.3902 - 12.8774	58.37 + 20.3437 - 12.8542
BB15-TS-89	19.38	2.62 ± 0.16	1.03 ± 0.21	2.87 ± 0.18	NA	51.61 + 14.1904 - 12.7195	51.60 + 14.5021 - 12.4462
BB15-TS-90	19.40	2.79 ± 0.11	1.12 ± 0.12	3.08 ± 0.12	NA	52.93 ± 6.87	52.93 ± 7.18
BB15-TS-91	19.42	2.761 ± 0.078	1.02 ± 0.22	3.01 ± 0.11	30765.93 ± 37735.63	47.67 + 13.2809 - 11.9665	47.67 + 13.0412 - 11.6285
BB15-TS-92	19.44	2.889 ± 0.079	1.155 ± 0.046	3.19 ± 0.08	NA	52.46 ± 3.12	52.46 ± 3.08
BB15-TS-93	19.47	2.802 ± 0.053	1.242 ± 0.067	3.134 ± 0.061	NA	59.66 ± 4.23	59.66 ± 4.31
BB15-TS-94	19.49	2.896 ± 0.055	1.25 ± 0.28	3.23 ± 0.12	NA	57.34 + 6.673 - 6.0557	57.81 + 18.2332 - 15.2455
BB15-TS-95	19.51	2.79 ± 0.14	1.14 ± 0.12	3.09 ± 0.15	4116.80 ± 1597.33	53.89 + 8.1657 - 7.3081	53.89 + 8.1049 - 7.1036
BB15-TS-96	19.53	2.64 ± 0.35	1.30 ± 0.15	2.99 ± 0.36	3301.55 ± 1794.75	68.26 + 19.0229 - 13.3531	68.18 + 19.1053 - 13.6925
BB15-TS-97	19.55	2.55 ± 0.10	1.207 ± 0.070	2.86 ± 0.11	624.44 ± 223.57	65.15 + 6.4114 - 5.7946	65.08 + 6.3709 - 5.6382
BB15-TS-98	19.57	2.55 ± 0.10	1.30 ± 0.18	2.89 ± 0.13	1271.64 ± 552.00	71.75 + 14.8453 - 12.9958	71.76 + 15.0328 - 13.1687
BB15-TS-99	19.59	2.571 ± 0.090	1.12 ± 0.12	2.85 ± 0.10	NA	58.60 ± 8.22	58.59 + 8.5988 - 7.8748
BB15-TS-100	19.61	2.70 ± 0.11	1.26 ± 0.32	3.04 ± 0.16	NA	63.50 + 23.6524 - 19.3354	63.50 + 22.7613 - 19.4565
BB15-TS-101	19.63	2.74 ± 0.14	1.16 ± 0.12	3.04 ± 0.15	5175.25 ± 2483.16	56.45 + 8.6948 - 7.377	56.44 + 8.3125 - 7.3229
BB15-TS-102	19.65	2.701 ± 0.075	1.10 ± 0.17	2.982 ± 0.098	NA	54.07 + 10.8744 - 10.132	54.03 + 10.8781 - 10.0996

Table S3.7f: Results of the LA ^{230}Th/U-dating for sample BB-15. Activity ratios ate indicated by parentheses. BP = before present, i.e., 1950 CE. TS indicates calculated LA ages, LA individually measured ages. NA = no data available.

smpl ID	DFT [cm]	(^{234}U/^{238}U)	(^{230}Th/^{238}U)	(^{234}U/^{238}U)$_{initial}$	(^{230}Th/^{232}Th)	uncorrected age [ka BP]	corrected age [ka BP]
BB15-TS-103	19.67	2.83 ± 0.54	1.29 ± 0.19	3.18 ± 0.56	1364.18 ± 1103.53	62.07 + 26.168 - 15.8172	61.96 + 25.2134 - 15.6629
BB15-TS-104	19.69	2.810 ± 0.053	1.31 ± 0.41	3.16 ± 0.16	NA	63.29 + 27.6652 - 23.1195	63.29 + 27.475 - 23.3461
BB15-TS-105	19.71	2.83 ± 0.12	1.17 ± 0.13	3.14 ± 0.13	NA	54.62 + 8.4519 - 7.585	54.62 + 8.3231 - 7.4196
BB15-TS-106	19.73	2.728 ± 0.099	1.17 ± 0.11	3.03 ± 0.11	NA	57.02 ± 6.97	57.01 + 7.2719 - 6.7644
BB15-TS-107	19.75	2.79 ± 0.13	1.24 ± 0.27	3.12 ± 0.16	16978.58 ± 11412.71	59.92 + 18.2837 - 16.0589	59.92 + 17.8639 - 15.8789
BB15-TS-108	19.77	2.76 ± 0.13	1.26 ± 0.28	3.10 ± 0.17	NA	62.01 + 18.8944 - 15.8929	62.08 + 18.737 - 17.007
BB15-TS-109	19.80	2.81 ± 0.16	1.31 ± 0.15	3.17 ± 0.18	NA	63.86 + 10.9338 - 9.8307	63.86 + 11.3949 - 10.0034
BB15-TS-110	19.82	2.82 ± 0.11	1.157 ± 0.098	3.12 ± 0.11	5358.62 ± 1041.18	54.17 + 6.553 - 5.8999	54.17 + 6.4257 - 5.6486
BB15-TS-111	19.84	2.76 ± 0.11	1.151 ± 0.076	3.06 ± 0.12	NA	55.31 ± 5.32	55.30 ± 5.29
BB15-TS-112	19.86	2.68 ± 0.16	1.255 ± 0.068	3.02 ± 0.17	NA	63.96 + 7.4467 - 6.1879	63.94 + 7.1601 - 6.1469
BB15-TS-113	19.88	2.73 ± 0.12	1.196 ± 0.054	3.04 ± 0.12	18250.26 ± 18523.78	58.87 + 4.9173 - 4.3835	58.87 + 4.9315 - 4.4161
BB15-TS-114	19.90	2.72 ± 0.12	1.16 ± 0.13	3.02 ± 0.13	NA	56.73 + 9.103 - 8.2878	56.73 + 9.4557 - 8.275
BB15-TS-115	19.92	2.829 ± 0.084	1.141 ± 0.060	3.125 ± 0.087	NA	53.06 ± 3.93	53.06± 3.88
BB15-TS-116	19.94	2.87 ± 0.13	1.188 ± 0.085	3.18 ± 0.13	NA	54.76 ± 5.77	54.76 ± 5.72
BB15-TS-117	19.96	2.720 ± 0.060	1.159 ± 0.062	3.02 ± 0.06	NA	56.84 ± 4.06	56.84 ± 4.11
BB15-TS-118	19.98	2.830 ± 0.094	1.25 ± 0.12	3.17 ± 0.11	NA	59.47 + 8.3813 - 7.6569	59.47 + 8.3492 - 7.6522
BB15-TS-119	20.00	2.77 ± 0.13	1.186 ± 0.085	3.08 ± 0.14	NA	57.20 + 6.4437 - 5.7949	57.20 + 6.5503 - 5.9844

Table S3.7f: Results of the LA ^{230}Th/U-dating for sample BB-15. Activity ratios ate indicated by parentheses. BP = before present, i.e., 1950 CE. TS indicates calculated LA ages, LA individually measured ages. NA = no data available.

smpl ID	DFT [cm]	(^{234}U/^{238}U)	(^{230}Th/^{238}U)	(^{234}U/^{238}U)$_{initial}$	(^{230}Th/^{232}Th)	uncorrected age [ka BP]	corrected age [ka BP]
BB15-TS-120	20.02	2.74 ± 0.13	1.224 ± 0.056	3.07 ± 0.13	NA	60.23 + 5.2456 - 4.6422	60.22 + 5.239 - 4.7376
BB15-TS-121	20.04	2.767 ± 0.098	1.33 ± 0.29	3.13 ± 0.15	NA	66.17 + 20.8686 - 17.6213	66.19 + 20.0799 - 17.7808
BB15-TS-122	20.06	2.75 ± 0.11	1.192 ± 0.076	3.06 ± 0.12	NA	58.58 ± 5.39	58.16 + 6.1757 - 5.2617
BB15-TS-123	20.08	2.646 ± 0.093	1.149 ± 0.071	2.94 ± 0.10	2557.95 ± 747.40	58.25 ± 5.28	58.24 ± 5.10
BB15-TS-124	20.11	2.79 ± 0.14	1.02 ± 0.21	3.04 ± 0.16	NA	47.13 + 12.7686 - 11.5746	47.11 + 12.8101 - 11.3444
BB15-TS-125	20.13	2.67 ± 0.15	0.98 ± 0.15	2.91 ± 0.16	NA	47.14 + 10.2937 - 9.342	47.13 + 10.0078 - 9.0031
BB15-TS-126	20.15	2.64 ± 0.11	1.06 ± 0.13	2.91 ± 0.12	NA	53.08 + 9.1426 - 8.4102	53.06 + 9.1619 - 8.5715
BB15-TS-127	20.17	2.541 ± 0.079	1.21 ± 0.12	2.86 ± 0.09	NA	65.87 + 9.0268 - 8.4389	65.87 + 9.281 - 8.2629
BB15-TS-128	20.19	2.567 ± 0.094	1.14 ± 0.12	2.86 ± 0.10	NA	59.85 + 8.628 - 8.0047	59.84 + 8.5399 - 7.7112
BB15-TS-129	20.21	2.48 ± 0.12	1.06 ± 0.13	2.74 ± 0.13	NA	57.55 + 9.8259 - 9.0776	57.55 + 10.16 - 8.7519
BB15-TS-130	20.23	2.508 ± 0.096	1.20 ± 0.24	2.82 ± 0.13	NA	66.06 + 18.45 - 16.4849	66.07 + 19.2442 - 16.4148
±BB15-TS-131	20.25	2.596 ± 0.091	1.09 ± 0.13	2.87 ± 0.11	NA	55.78 + 9.4271 - 8.463	55.79 + 8.8939 - 8.3656
BB15-TS-132	20.27	2.53 ± 0.12	1.11 ± 0.13	2.81 ± 0.13	NA	59.11 + 9.5865 - 8.9082	59.11 + 9.945 - 8.9251
BB15-TS-133	20.29	2.58 ± 0.13	1.15 ± 0.15	2.87 ± 0.15	NA	60.39 + 11.701 - 10.4543	60.39 + 12.3082 - 10.1518
BB15-TS-134	20.31	2.525 ± 0.100	1.21 ± 0.16	2.84 ± 0.12	NA	65.84 + 12.7429 - 11.347	65.83 + 12.0737 - 11.262
BB15-TS-135	20.33	2.606 ± 0.058	1.28 ± 0.16	2.947 ± 0.086	NA	67.95 + 11.8316 - 10.7682	67.95 ± 11.18
BB15-TS-136	20.35	2.43 ± 0.12	1.12 ± 0.14	2.72 ± 0.13	NA	63.21	63.21

Table S3.7f: Results of the LA ^{230}Th/U-dating for sample BB-15. Activity ratios ate indicated by parentheses. BP = before present, i.e., 1950 CE. TS indicates calculated LA ages, LA individually measured ages. NA = no data available.

smpl ID	DFT [cm]	(^{234}U/^{238}U)	(^{230}Th/^{238}U)	(^{234}U/^{238}U)$_{initial}$	(^{230}Th/^{232}Th)	uncorrected age [ka BP]	corrected age [ka BP]
						+ 10.9367 - 10.0341	+ 11.2583 - 10.1656
BB15-TS-137	20.37	2.609 ± 0.079	1.11 ± 0.22	2.89 ± 0.11	NA	56.97 + 14.8333 - 13.2206	56.96 + 15.3026 - 13.5035
BB15-TS-138	20.39	2.64 ± 0.10	0.98 ± 0.23	2.88 ± 0.13	NA	47.97 + 15.1623 - 13.0585	47.96 + 14.628 - 13.1444
BB15-TS-139	20.41	2.692 ± 0.081	1.059 ± 0.085	2.958 ± 0.088	NA	51.55 ± 5.38	51.54 ± 5.48
BB15-TS-140	20.44	2.635 ± 0.074	1.119 ± 0.080	2.919 ± 0.080	NA	56.69 + 5.6484 - 5.1294	56.70 ± 5.55
BB15-TS-141	20.46	2.66 ± 0.13	1.19 ± 0.10	2.97 ± 0.14	NA	60.74 + 8.2788 - 7.3244	60.73 + 8.1466 - 7.1109
BB15-TS-142	20.48	2.72 ± 0.11	1.16 ± 0.11	3.02 ± 0.12	43687.12 ± 65657.18	56.84 + 7.8189 - 7.1938	56.84 + 7.78 - 7.192
BB15-TS-143	20.50	2.74 ± 0.53	1.23 ± 0.13	3.06 ± 0.55	NA	60.39 + 22.7944 - 13.6187	60.38 + 22.8665 - 13.7438
BB15-TS-144	20.52	2.707 ± 0.078	1.28 ± 0.17	3.05 ± 0.10	NA	64.96 + 11.8624 - 10.5551	64.90 + 11.4049 - 10.5627
BB15-TS-145	20.54	2.67 ± 0.13	1.103 ± 0.071	2.95 ± 0.13	NA	54.83 + 5.8771 - 5.264	54.83 + 5.7137 - 5.2011
BB15-TS-146	20.56	2.82 ± 0.11	1.13 ± 0.14	3.1 ± 0.12	NA	52.91 + 9.2709 - 8.1559	52.91 + 9.1827 - 8.186
BB15-TS-147	20.58	2.74 ± 0.10	1.168 ± 0.088	3.04 ± 0.11	NA	56.93 ± 6.07	56.93 ± 5.96
BB15-TS-148	20.60	2.664 ± 0.084	1.213 ± 0.067	2.982 ± 0.087	18448.40 ± 8971.75	61.84 ± 5.07	61.83 ± 4.89
BB15-TS-149	20.62	2.633 ± 0.079	1.227 ± 0.071	2.956 ± 0.086	NA	63.74 + 5.8746 - 5.0375	63.73 ± 5.33
BB15-TS-150	20.64	2.79 ± 0.11	1.265 ± 0.071	3.13 ± 0.12	23750.75 ± 16512.80	61.53 + 5.8754 - 5.3599	61.51 ± 5.55
BB15-TS-151	20.66	2.74 ± 0.10	1.16 ± 0.16	3.04 ± 0.12	NA	56.76 + 10.9884 - 9.8368	56.75 + 10.7676 - 10.1994
BB15-TS-152	20.68	2.696 ± 0.069	1.127 ± 0.084	2.985 ± 0.075	NA	55.51 ± 5.32	55.5 1± 5.47
BB15-TS-153	20.70	2.747 ± 0.095	1.161 ± 0.059	3.048 ± 0.098	5823.25 ± 1977.88	56.28 ± 4.33	56.27 ± 4.28

Table S3.7f: Results of the LA ^{230}Th/U-dating for sample BB-15. Activity ratios ate indicated by parentheses. BP = before present, i.e., 1950 CE. TS indicates calculated LA ages, LA individually measured ages. NA = no data available.

smpl ID	DFT [cm]	(^{234}U/^{238}U)	(^{230}Th/^{238}U)	(^{234}U/^{238}U)$_{initial}$	(^{230}Th/^{232}Th)	uncorrected age [ka BP]	corrected age [ka BP]
BB15-TS-154	20.72	2.750 ± 0.081	1.13 ± 0.11	3.041 ± 0.088	17169.89 ± 8514.46	54.32 + 7.1785 - 6.5947	54.31 + 7.1392 - 6.4971
BB15-TS-155	20.74	2.798 ± 0.068	1.23 ± 0.12	3.125 ± 0.083	6929.74 ± 2496.03	59.20 + 7.8979 - 7.0015	59.19 ± 7.61
BB15-TS-156	20.76	2.70 ± 0.12	1.235 ± 0.093	3.03 ± 0.12	6120.01 ± 1703.25	62.23 + 7.4261 - 6.4198	62.22 + 7.2559 - 6.6223
BB15-TS-157	20.78	2.699 ± 0.086	1.18 ± 0.10	3.006 ± 0.096	NA	58.73 ± 6.82	58.71 + 7.1799 - 6.4754
BB15-TS-158	20.81	2.85 ± 0.16	1.37 ± 0.10	3.23 ± 0.16	NA	65.91 + 8.519 - 7.6222	65.90 + 8.1708 - 7.4317
BB15-TS-159	20.83	2.79 ± 0.18	1.21 ± 0.11	3.11 ± 0.18	NA	58.09 + 8.6619 - 7.4052	58.19 + 8.5956 - 7.4799
BB15-TS-160	20.85	2.74 ± 0.18	1.20 ± 0.14	3.06 ± 0.19	NA	58.75 + 10.7932 - 9.3105	58.74 + 10.7843 - 9.2339
BB15-TS-161	20.87	2.84 ± 0.60	1.33 ± 0.14	3.20 ± 0.62	NA	63.86 + 28.6183 - 15.3422	63.79 + 27.102 - 15.5325
BB15-TS-162	20.89	2.704 ± 0.091	1.324 ± 0.079	3.064 ± 0.096	3518.08 ± 1384.94	67.81 ± 6.15	67.81 + 6.3897 - 5.859
BB15-TS-163	20.91	2.76 ± 0.11	1.232 ± 0.083	3.09 ± 0.12	7966.17 ± 2308.88	60.12 + 6.1979 - 5.5476	60.11 + 6.4868 - 5.4643
BB15-TS-164	20.93	2.758 ± 0.085	1.233 ± 0.086	3.085 ± 0.091	7153.09 ± 2753.73	60.32 + 6.4009 - 5.4443	60.31 ± 5.74
BB15-TS-165	20.95	2.756 ± 0.093	1.199 ± 0.083	3.071 ± 0.098	NA	59.78 ± 6.05	58.33 + 5,8787 - 5,2752
BB15-TS-166	20.97	2.803 ± 0.084	1.30 ± 0.12	3.156 ± 0.099	937.37 ± 834.24	63.16 + 8.3404 - 7.4366	63.10 + 8,3457 - 7,7693
BB15-TS-167	20.99	2.90 ± 0.12	1.153 ± 0.072	3.20 ± 0.12	4943.90 ± 3787.47	52.30 ± 4.85	52.15 + 5,2334 - 4,6027
BB15-TS-168	21.01	2.80 ± 0.13	1.28 ± 0.29	3.15 ± 0.16	1936.34 ± 1121.26	66.90 + 23.5185 - 19.4566	61.94 + 20,5993 - 17,0356
BB15-TS-169	21.03	2.62 ± 0.56	1.45 ± 0.18	3.03 ± 0.55	37.40 ± 36.57	188.12 + 177.1335 - 60.0512	79.60 + 39,9585 - 22,0163

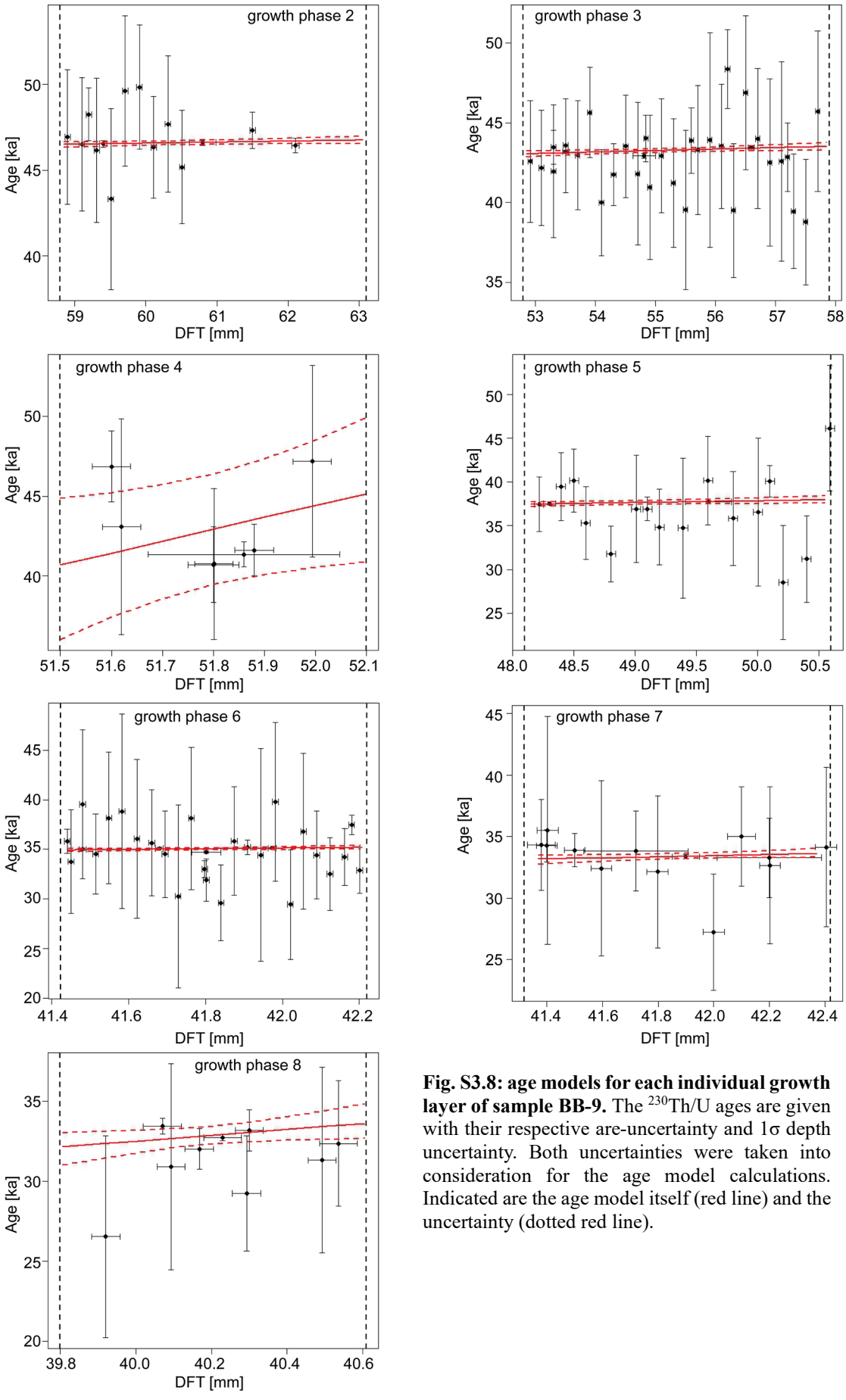

Fig. S3.8: age models for each individual growth layer of sample BB-9. The ^{230}Th/U ages are given with their respective are-uncertainty and 1σ depth uncertainty. Both uncertainties were taken into consideration for the age model calculations. Indicated are the age model itself (red line) and the uncertainty (dotted red line).

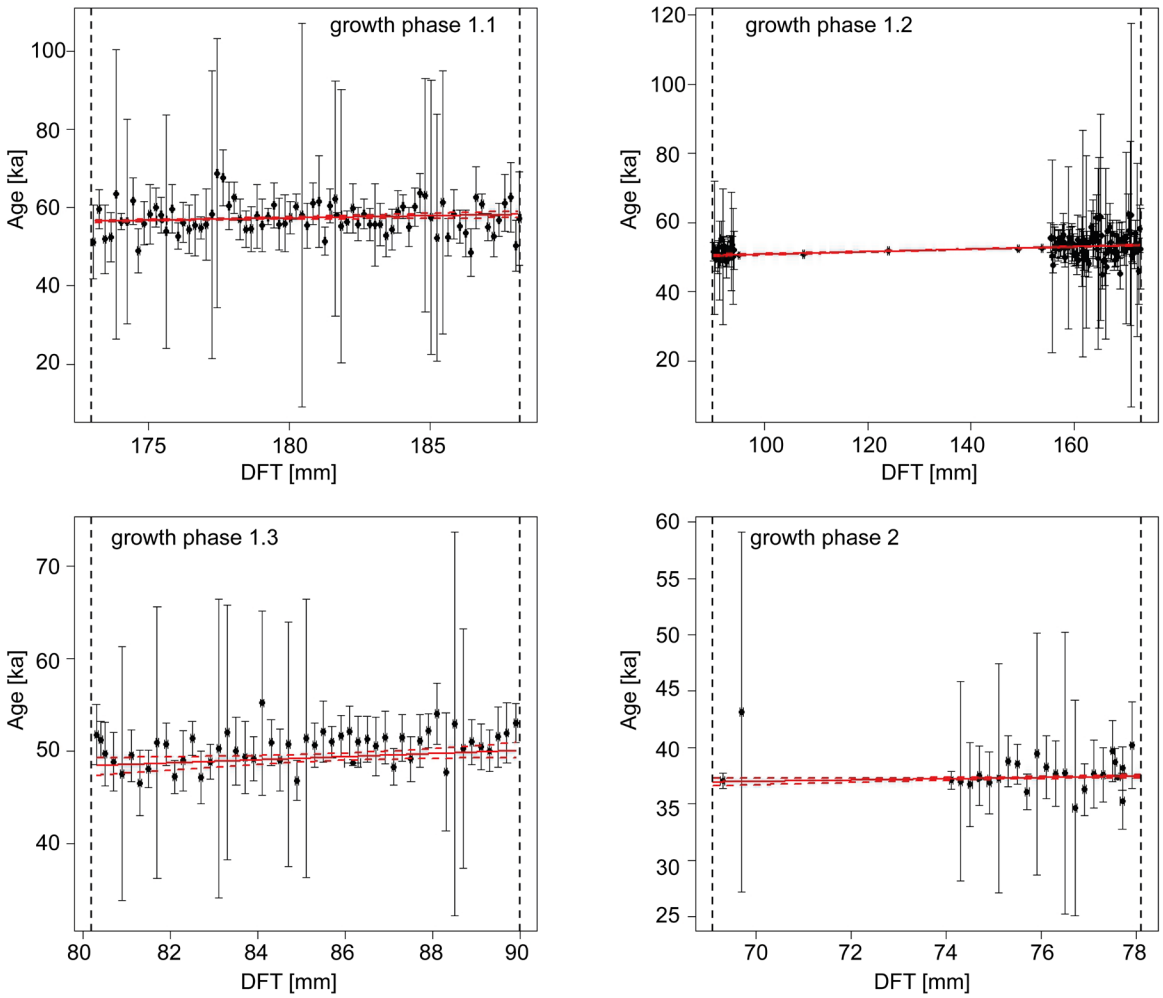

Fig. S3.9: age models for each individual growth layer of sample BB-10. The ^{230}Th/U ages are given with their respective are-uncertainty and 1σ depth uncertainty. Both uncertainties were taken into consideration for the age model calculations. Indicated are the age model itself (red line) and the uncertainty (dotted red line).

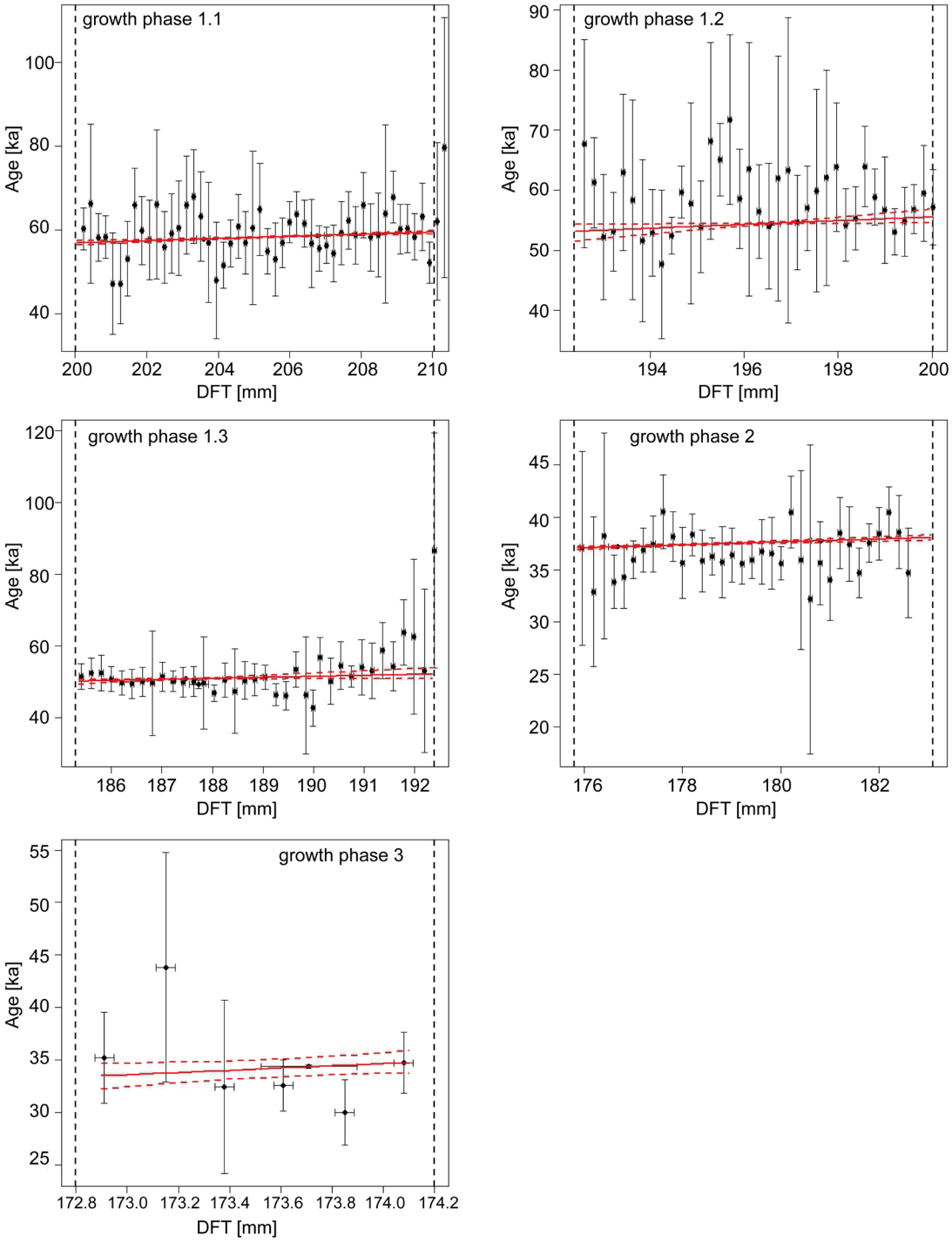

Fig. S3.10: age models for each individual growth layer of sample BB-15. The ^{230}Th/U ages are given with their respective are-uncertainty and 1σ depth uncertainty. Both uncertainties were taken into consideration for the age model calculations. Indicated are the age model itself (red line) and the uncertainty (dotted red line).

Table S3.8: Overview of several parameters used for the age model calculations. Green highlights the used percentage of positive slopes used for the growth phase.

smpl	growth phase	MSWD	MSWD incl. student t	p-value	p-value incl. student t	positive slopes [%]	positive slopes [%] incl. student t
BB9	2	1.32		0.19		49.37	
BB9	3	2.15	0.83	2.07E-04	0.74	99.99	99.09
BB9	4	7.00	0.99	1.49E-06	0.42	0.07	10.82
BB9	5	3.13	0.83	2.18E-05	0.65	93.48	78.11
BB9	6	4.17	0.91	2.06E-12	0.59	93.99	76.55
BB9	7	1.12		0.34		5.54	
BB9	8	2.88	0.99	0.01	0.43	3.02	14.44
BB10	1.1	1.74	0.98	6.35E-05	0.52	99.92	99.14
BB10	1.2		0.87		0.84		100.00
BB10	1.3	2.28	0.88	8.36E-07	0.71	98.71	91.71
BB10	2	0.95		0.53		96.90	
BB15	1.1	1.44	0.98	2.27E-2	0.51	100.00	100.00
BB15	1.2	1.73	0.98	4.05E-3	0.49	82.08	75.48
BB15	1.3	2.08	0.98	1,59E-4	0.51	57.67	55.21
BB15	2	1.84	0.86	2,06E-3	0.70	100.00	100.00
BB15	3	2.80	0.88	0.01	0.49	7.46	22.94

Table S3.9: Depth uncertainties for the ^{230}Th/U-ages based on the sampling method. The Laser ablation value is used for both techniques used in this study.

Sampling method	3σ [mm]	2σ [mm]	1σ [mm]	± 1σ [mm]
Hand held drilling	1.5	0.75	0.375	0.1875
MicroMilling	0.4	0.2	0.10	0.05
Laser Ablation	0.3	0.15	0.075	0.0375

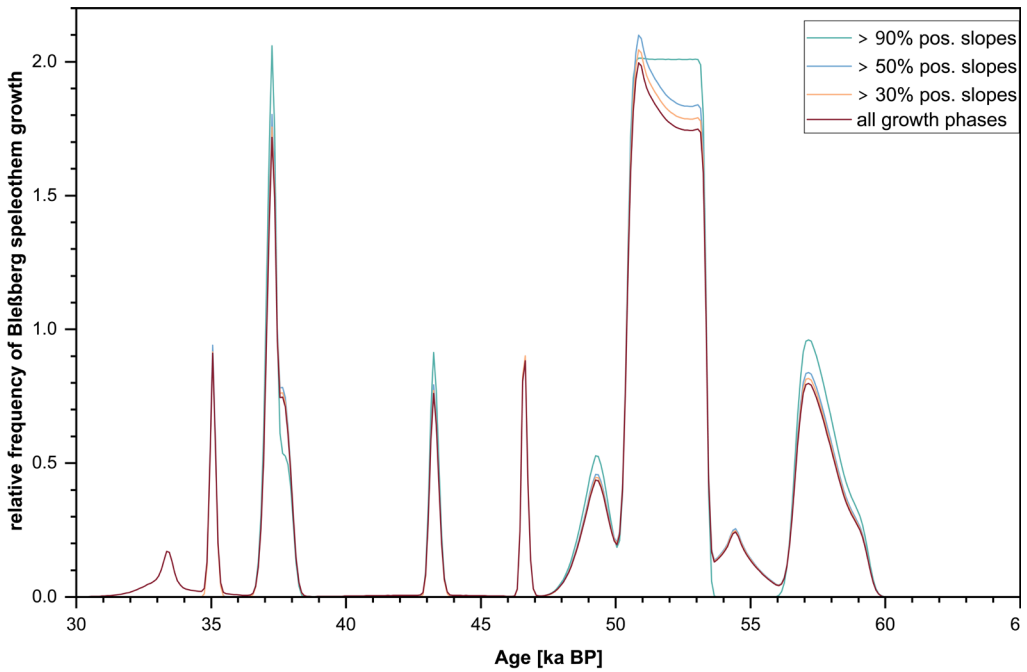

Fig. S3.11: Comparison of the calculated frequency analysis (Fig.3.4) with adjusted data input based on the percentage of positive slopes.

Chapter 4: Manuscript II

The last glacial period in Central Europe – climatic implications recorded by three highly sensitive speleothems from Bleßberg Cave

paper in preparation

Abstract

During Marine Isotope Stage 3 (MIS3, ca. 60 – 30 ka BP), the climate experienced oscillations characterised by rapid temperature increase followed by gradual cooling, known as Dansgaard-Oeschger (DO) events. These events are believed to be linked to rapid ocean and atmosphere circulation changes in the North Atlantic region. Although initially discovered in Greenland ice cores, they have since been found to have a global impact and get connected to have potentially influenced the transition from Neanderthals to modern humans in Eurasia. Speleothem records from Central Europe during MIS 3, however, are very limited due to reoccurring unfavourable conditions for speleothem growth. Therefore, available records are mainly restricted to caves beneath Alpine glaciers or more southern locations.

Here we present three flowstones from Bleßberg Cave, Germany coinciding with several DO events indicating particularly warm periods during MIS 3. We observe a general trend towards colder and drier conditions with ongoing progression of MIS 3. A particular warm period in our record, coinciding with DO14, lasted from ca. 53.4 – 50.4 ka BP. This growth phase recorded the onset of the warm phase and revealed two short-term cold events between 52.1 – 51.4 ka BP, one of them coinciding with Greenland Interstadial 14b.

4.1 Introduction

The last glacial period and especially Marine Isotope Stage 3 (MIS 3, ca. 60 – 30 ka BP (Lisiecki and Raymo, 2005), BP refers to before present where present represents 1950) was characterised by events of abrupt climate change known as Dansgaard-Oeschger (DO) events (Dansgaard et al., 1993; NGRIP Project members, 2004; Rasmussen et al., 2014). Rapid shifts in $\delta^{18}O$ and $\delta^{15}N$ in Greenland ice cores revealed decadal- to millennial-scale events (Rasmussen et al., 2014) when regional temperature increased up to 16.5 ± 3 °C within a few decades (Dansgaard et al., 1993; Kindler et al., 2014). While it seems that these fluctuations were connected to rapid ocean and atmosphere circulation changes in the North Atlantic region (Dansgaard et al., 1993), the main forcing mechanism for DO events remain debated (Baldini et al., 2015; Corrick et al., 2020; Fohlmeister et al., 2023; Vettoretti et al., 2022). The input of freshwater due to sea ice cover melting into the North Atlantic is considered as a major trigger for DO events that affected the strength of the Atlantic meridional overturning circulation (AMOC) (Erhardt et al., 2019) and sea ice cover in the North Atlantic. Climate modelling experiments simulating the temperature changes during the onset of DO events indicate that the extent of the sea-ice cover is indeed a crucial factor for rapid atmospheric changes in the Atlantic sector. A strengthening AMOC with diminishing freshwater input resulted in subsequent warming over Greenland (Knutti et al., 2004). Still, the collapse of the sea ice cover in the North Atlantic might not be the initial trigger for the events (Erhardt et al., 2019).

While first discovered in Greenland, DO events were global in extent (Adolphi et al., 2018; Erhardt et al., 2019), reaching monsoonal regions and the southern hemisphere (Bond et al., 1993; Kathayat et al., 2016; Spötl and Mangini, 2002; Voelker, 2002 and references within). While Greenland ice cores recorded an almost doubling of local snow accumulation (Andersen et al., 2006) and rapid changes in aerosol concentrations (Erhardt et al., 2019), regions dominated by monsoon systems show a strong atmospheric response to shifts in the AMOC. Numerous speleothem records show a strengthening of both the East Asian (Chen et al., 2016; Cheng et al., 2016; Wang et al., 2001) and the Indian (Kathayat et al., 2016) summer monsoon subsystems. In contrast, speleothems from South America reveal a weakening of the South American Monsoon (Cheng et al., 2013). Speleothem records from the Mediterranean (e.g. Constantin et al., 2007; Hodge et al., 2008; Pérez-Mejías et al., 2019) and the European Alps (e.g.Moseley et al., 2020; Moseley

et al., 2014) also show a notable climatic response to DO events but are more complex to interpret due to regionally heterogeneous effects on the precipitation and speleothem $\delta^{18}O$ signals.

The relatively short duration and rapid onset of the warm interstadials render the reconstruction of DO events with paleoclimate records challenging. While the Greenland ice cores are most likely the most sensitive recorder of DO events and also amenable to reconstruct very precise chronologies of individual DOs via layer counting, they have the distinct disadvantage of cumulative dating uncertainty inherent to the layer counting methodology. This leads to absolute dating uncertainties of between ca. 0.8 ka at ca. 27.8 ka BP to > 2.5 ka at ca. 60 ka BP (Rasmussen et al., 2014). Thus, while providing valuable information about the internal progression and duration of DO events, the overall dating uncertainty of the Greenland ice cores often exceeds the duration of DO events (Rasmussen et al., 2014) and precise absolute ages for DO events cannot be derived from the ice cores. This limits precise chronostratigraphic correlations of the ice core DO chronology with other paleoclimate records and hampers the estimation of leads and lags with distal regions. Furthermore, the temporal resolution and the dating accuracy achievable in many other climate archives entail several additional challenges. The reconstruction of DO events in Central Europe is limited to very few well-dated reconstructions for this specific time interval.

Speleothems can provide exceptionally precise and accurate chronologies through U-series dating. Using a compilation of 63 speleothems from the Mediterranean, the Asian Summer Monsoon region, and the South American Monsoon realm, Corrick et al. (2020) constructed the SIOC19 chronology of DO events. They conclude that synchronous climatic changes linked to the onset of the DO events occurred within a century between Europe, Asia and South America. However, their study did not include any speleothems from Central Europe due to the scarcity of available data. A key factor restricting the potential to reconstruct DO events in Central Europe is the occurrence of permafrost. Speleothems cannot grow at sub-zero temperatures that are common in Central Europe during glacial periods like MIS 3. Thus, most European speleothems from MIS 3 originate either from southern (Constantin et al., 2007; Genty et al., 2003; Hodge et al., 2008; Pérez-Mejías et al., 2019) or more coastal (Budsky et al., 2019; Denniston et al., 2018; Kudielka et al., 2019; Stoll et al., 2015) sites that remained unaffected by permafrost. An exception are some alpine regions (e.g. Moseley et al., 2020; Moseley et al., 2014), where subglacial

meltwater and pyrite-bearing host rocks facilitated sulphide oxidation that enabled speleothem growth (Spötl and Mangini, 2002).

Where permafrost did not restrict speleothem formation, Central European caves, located relatively closely to the North Atlantic, are highly sensitive to climatic changes associated with DO events. However, two speleothem records from north-eastern France and eastern Germany either do not provide proxy data (Pons-Branchu et al., 2010) or cover only a short section of MIS 3 with limited chronological detail (Weber et al., 2018). A recent publication discussing a speleothem record from Belgium (Peral et al., 2024) suggests continuous growth for ~ 20 ka during MIS 3. However, the ^{230}Th/U-ages determined for this record primarily align with the warm DO events, and none of them overlaps with the colder stadials in between. Thus, the interpretation of continuous growth of this speleothem could be questioned.

In addition, MIS 3 marks the disappearance of Neanderthals (Higham et al., 2014) and the first appearance of *Homo sapiens* populations around 45 ka BP in Europe (Pederzani et al., 2024). While the exact cause of the replacement of Neanderthals is still a matter of ongoing discussion (e.g. Banks et al., 2008; Degioanni et al., 2019; Smith et al., 2005; Timmermann, 2020), it has also been proposed that abrupt climate change during MIS 3 may have played a role (Staubwasser et al., 2018). This further highlights the importance of precisely dated climate proxy records for Central Europe during MIS 3.

Here we present three precisely dated MIS 3 multi-proxy speleothem records from Bleßberg Cave, Germany, that constrain several distinct growth phases which record favourable growth conditions during DO events in Central Europe. Our records provide new insights into Central European climate dynamics during MIS 3 and reveal exceptionally warm phases during the last glacial, with DO14 (54.24 – 49.62 ka BP) being the most extended warm phase. Our new dataset allows a unique view of the millennial-scale climate evolution in Central Europe during the time leading up to the arrival of modern humans in Europe.

4.2 Cave setting and sample description

4.2.1 Bleßberg Cave

Bleßberg Cave lies at ca. 500 m above sea level in Central Germany (Fig. S4.1). The cave system developed in Triassic marly limestones and is located at 50°25'28'' N and 11°01'13'' E. The NW-SE oriented cave is covered by 12 to 50 m of marly limestone (Lower and Middle Muschelkalk), and the vegetation above the cave is characterised by anthropogenically modified farmland and mixed deciduous and pine forests towards more uphill areas (Breitenbach et al., 2019). The modern climate at Bleßberg Cave can be characterised as Cfb climate in the Köppen-Geiger classification. The cave was first discovered in 2008 during construction works, during which the previously closed cave system was disrupted. The cave atmosphere is relatively stable, although the ventilation is potentially influenced by a stream running through the main passage of the cave (Breitenbach et al., 2019).

4.2.2 Sample description

Three flowstone samples were investigated during this study: BB-9, BB-10, and BB-15 (Fig. S4.2). All three samples grew during parts of MIS 3 and MIS 1, but here we only discuss the MIS 3 sections. BB-9 is a 6.4 cm thick flowstone, and the MIS 3 part of the sample is from 3.4 – 6.4 cm distance from top (DFT). In this section of this sample shows strongly episodic growth, disrupted by detrital layers. The calcite in the lower part is more of a whitish colour. Sample BB-10 is an 18.3 cm thick flowstone that consists of relatively light beige calcite disrupted by two very distinct hiatuses at ~ 6.8 cm DFT and ~ 8 cm distance from top DFT. The MIS 3 part of this sample is between 6.8 – 18.3 cm DFT. The calcite between the hiatuses is of a clear white colour. Sample BB-15 is a ca. 21 cm thick flowstone with three macroscopically visible hiatuses at ca. 17 cm, 17.4 cm, and 18.3 cm DFT, separating MIS 1 from MIS 3 (17 – 18.3 cm DFT). The area between the topmost and second hiatus is of more whitish calcite similar to BB-10, and the lower part shows again darker, beige calcite.

Two additional growth interruptions in samples BB-10 and BB-15, not delineated by visible detrital layers, were identified using the initial ($^{234}U/^{238}U$) activity ratios. More detailed information is given in Klose et al. (in review). In total, BB-9 shows eight growth

phases during MIS 3, BB-10 shows four growth intervals, and BB-15 covers five growth phases within MIS 3. The age chronology of the three flowstones was established by a combination of a solution-based approach with preceding chemical separation of U and Th and subsequential analysis using a MC-ICP-MS and an in-situ approach using a laser ablation system without any chemical processing prior to the MC-ICP-MS analysis. Details are given in Klose et al. (in review). In total 566 ^{230}Th/U-ages were determined.

4.3 Methods

4.3.1 Stable isotope analysis

High-resolution stable oxygen and carbon isotope ratios ($\delta^{18}O$ and $\delta^{13}C$) were obtained from all three flowstone samples. The stable isotope samples from sample BB-9 (n = 236) were sampled at 100 µm resolution and measured at the GeoForschungsZentrum in Potsdam, Germany. Sampling was performed using a Sherline 5400 deluxe MicroMill with digital readout (sample size of around 100 µg), and isotope analyses were conducted using a Thermo Fischer Scientific MAT253 stable isotope mass spectrometer connected to a KIEL IV carbonate device. NBS19 and an internal carbonate reference material were used for quality control and standardization. The external precision is < 0.07 ‰ (1 σ) for both $\delta^{18}O$ and $\delta^{13}C$. All results are reported in delta notation relative to the international Vienna PeeDeeBelemnite (VPDB) standard. The stable isotopes from sample BB-10 (n = 424) were sampled at 150 µm resolution between 6.91 – 7.81 cm DFT and at 325 µm resolution for the bottom section of the sample. Sample BB-15 (n = 542) was subsampled at 135 µm resolution between 17.28 – 18.31 cm DFT, and 50 µm resolution in the bottom section of the sample. For both samples, a Merchantek MicroMilll (NewWave) was used for sampling (sample size of around 100 µg) and the analyses were performed at the Max Planck Institute for Chemistry in Mainz using Delta-V mass spectrometer equipped with a Gasbench II preparation device. In-house standards VICS ($\delta^{13}C$ value of 1.45 ‰ VPDB and a $\delta^{18}O$ value of -5.44 ‰ VPDB) were analysed with each run. The reproducibility of the reference materials is usually better than 0.1 ‰ (1σ) for both $\delta^{18}O$ and $\delta^{13}C$. The results are reported relative to VPDB.

4.3.2 Trace element analysis

Trace element concentrations of Sr, Mg, Ba, and Al of samples BB-9 and BB-10 were determined using an ESI New Wave 193 nm ArF Excimer laser ablation system coupled to an Agilent 7500ce ICP-MS at the Institute for Geosciences, Johannes Gutenberg University, Mainz. We used a rectangular spot size of 130 x 50 µm, a transition rate of 10 µm/s and a laser repetition rate of 10 Hz, resulting in a fluence of 3.5 J/cm^2. For standardization purposes, the NIST SRM 610 glass standard and several other quality control materials (NIST SRM 612, BCR-2G and MACS3) were analysed repeatedly during analyses. For all analyses, ^{43}Ca was used as internal reference, and data evaluation was performed offline following the procedure described in Mischel et al. (2017). A continuous line scan was performed on both samples. Before each data accumulating ablation run, a pre-ablation run was performed to clean the sample surface. We performed principal component analysis (PCA) of the trace element data of both samples using the prcomp() function of the statistical software R (Team, 2023).

4.3.3 Fluid inclusion isotope analysis

Fluid inclusion $\delta^{18}O$ and $\delta^{2}H$ ratios of sample BB-10 (n = 16) were measured at the Max Planck Institute for Chemistry in Mainz, Germany. Flowstone subsamples of ~ 1 g weight were cut using a Dremel Microdrill equipped with a 38 mm diameter diamond-covered circular saw parallel to the growth axis of the sample. The offsets to the growth axis, resulting from the relatively large sample size, were projected to the growth axis by following the growth layer curvature and a mean depth/age relationship was determined (Fig. S4.3). The fluid inclusion water was extracted using a crusher unit and measured on a Picarro L2140i cavity ring-down spectrometer (CRDS) connected to the extraction line. The measurement followed the procedure described by (De Graaf et al., 2020). Isotope data were corrected using a two-point calibration based on two in-house standards (MzTap2022, with a $\delta^{18}O$ value of -8.7 ‰ VSMOW and a $\delta^{2}H$ value of -62.96 ‰ VSMOW, and Kona2022, $\delta^{18}O$ = 1.53 ‰ VSMOW and a $\delta^{2}H$ = 3.48 ‰ VSMOW). The typical 1σ precisions for the technique are based on the water injections of the standards into the system are better than 0.3 ‰ for the $\delta^{18}O$ values and 1.0 ‰ for the $\delta^{2}H$ values (De Graaf et al., 2020). Results are presented as delta values expressed relative to VSMOW.

Temperature estimates were calculated using the fluid inclusion $\delta^{18}O$ value and $\delta^{18}O_{carb}$ of the flowstone. We used the cave-specific water–calcite oxygen isotope equilibrium fractionation factor of Tremaine et al. (2011). In addition, three different approaches were used to verify the calculated temperatures. Two approaches used the $\delta^{2}H$ – $\delta^{18}O$ relationship of the GMWL (and LMWL) and predict the $\delta^{18}O$ value of the fluid inclusion water by projecting the measured $\delta^{2}H$ values onto the modern GMWL and LMWL. The corresponding $\delta^{18}O$ values were then used to estimate temperature following Tremaine et al. (2011). The third approach used a modern local temperature-$\delta^{2}H$ relationship based on the data received from a local GNIP station (Hof, ca. 60 km distance from the cave). Measured fluid inclusion $\delta^{2}H$ values were then used in the established modern precipitation $\delta^{2}H$ – temperature relationship to estimate past temperatures. A comparison of all estimated temperatures is shown in Figure S4.4.

4.3.4 Calcium isotopes

Calcium isotope ratios were analysed on samples BB-9 (n = 10) and BB-10 (n = 13) using a Neptune Plus MC-ICP-MS equipped with an Elemental Scientific Apex Omega HF desolvator system at the Johannes Gutenberg University in Mainz, following Weber et al. (2021). Approximately 1 mg of powdered carbonate was purified using the automated *prep*FAST-MC (ESI Elemental Scientific) system. The Ca fraction was then dried down and re-dissolved in distilled 0.5 mol/L HNO_3 for analysis. A standard bracketing approach was used to correct for mass-dependent fractionation with the samples and reference material being within 10 % of the concentration range of 2 mg/L. Results are presented as delta values ($\delta^{44/42}Ca$) expressed relative to NIST 915a. Additional reference materials (IAPSO, JCp, JCt, MACS3, NanoSr) were analysed for quality control within the same analytical sessions.

4.3.5 Lignin oxidation products

The lignin oxidation products (LOPs) of samples BB-10 (n = 13) and BB-15 (n = 13) were analysed using the procedure of (Homann et al., 2022) at the Department of Chemistry, Johannes Gutenberg University in Mainz. Analyses were performed on an ultra-high performance liquid chromatography (UHPLC) system coupled to a high-resolution mass

spectrometer (HRMS). The subsamples for BB-10 were cut using a diamond band saw and using a precision diamond wire saw for cutting BB-15. The sample sizes averaged around 1 – 2 g.

4.3.6 Soil and host rock analyses

Soil samples (n = 4) from different depths (5 – 15 cm, 15 – 30 cm, 30 – 45 cm, 45 – 50 cm) were collected above Bleßberg Cave. The mineralogy of the soil was analysed a Seifert XRD 3000TT with Cu Kα radiation at 40 kV and 30 mA at the Institute for Geosciences, Johannes Gutenberg University in Mainz. The scanning range was from 5° to 80° (2θ) with a step size of 0.03° (2θ) and a dwell time of 2 s/step. The phases were identified and quantified using the Profex software (Doebelin and Kleeberg, 2015) with the Rietveld refinement (Fig. S4.6).

Soil samples (approx. 0.2 g) from the same depth were also analysed for their element concentrations (Mg, Sr, Ba) following the method as described in Wimpenny et al. (2014). The soil samples and one additional host rock sample were analysed using an iCAP 6500 DUO inductively coupled plasma optical emission spectrometer (ICP-OES, Thermo Fisher Scientific) at the Institute for Geology, Mineralogy and Geophysics, Ruhr-University Bochum. BCS-CRM512 (dolomite, n = 178), BCS-CRM513 (limestone, n = 175) and BCS-CRM 393 (limestone, n = 41) were used as reference materials. The 1σ reproducibility for the reference materials is 0.2 wt%, 0.002 wt% and 0.001 wt% for Mg, 0.002 wt%, 0.0003 wt% and 0.0002 wt% for Sr, and 0.003 wt% for Ba.

4.4 Results

4.4.1 Stable isotopes and trace elements

The stable isotope and trace element data are shown in Fig. 4.1. We divided our MIS 3 record into three phases: early MIS 3 (60 – 48 ka BP), mid MIS 3 (48 – 39.5 ka BP) and late MIS 3 (39.5 – 30 ka BP). These three phases are separated by growth hiatuses that correspond to the Heinrich events 5 (ca. 48.1 – 46.9 ka BP) and 4 (ca. 39.7 – 38.4 ka BP).

The $\delta^{13}C$ record shows a general trend towards less negative values (from ca. -7 to -2 ‰) throughout MIS 3. During early MIS 3 the $\delta^{13}C$ values show pronounced variability and high-frequency variations between -7.8 to -3.5 ‰. Around ~ 53 ka BP, the $\delta^{13}C$ values of sample BB-10 show a rapid decrease from ca. -5.2 to ca. -8.1 ‰. During mid MIS 3, the $\delta^{13}C$ record shows an average of -5.7 ± 0.5 ‰. The variability is between -6.5 to -4.5 ‰, mainly due to the younger growth phase, which shows a rapid decrease from ca. -4.2 to -6.3 ‰ around 43.4 ka BP followed by a rapid increase to -4.8 ‰ shortly after 43.2 ka BP. Late MIS 3 shows generally higher $\delta^{13}C$ values around a mean value of -3.6 ‰ ± 0.9 ‰. The overall individual $\delta^{13}C$ values range between -2.0 to -4.9 ‰ for BB-9, between -1.4 and -7.5 ‰ for BB-10, and between -1.1 and -2.9 ‰ for sample BB-15.

The $\delta^{18}O$ values show a general trend towards more positive values during the progression of MIS 3 from ca. -5.5 to -4.5 ‰ and an average of -4.7 ± 0.4 ‰. Like the $\delta^{13}C$ values, the early MIS 3 phase shows a rapid decrease (from ca. -4.4 to -6.3 ‰) and a subsequent pronounced peak around ~ 53 ka BP in the $\delta^{18}O$ values. The mid phase of MIS 3 shows variations between -6.4 to -5.0 ‰ and an average of -5.6 ± 0.3 ‰. Similarly to the $\delta^{13}C$ values, there is a rapid decrease in the $\delta^{18}O$ values around 53 ka BP from ca. -4.5 to 6.3 ‰. The variability of the younger growth phase around 43 ka BP in this section shows a very strong correlation (r = 0.96) with the $\delta^{13}C$ record and a rapid change from decreasing to increasing values. Late MIS 3 shows $\delta^{18}O$ values around a mean value of -4.6 ± 0.4 ‰. The overall individual $\delta^{18}C$ values range between -4.3 to -6.4 ‰ for BB-9, between -4.4 and -6.3 ‰ for BB-10, and between -3.8 and -6.3 ‰ for sample BB-15.

The Sr concentrations in both samples are relatively high in general and range from ~ 500 to ~ 5000 µg/g. There is a sharp decrease from ~ 5000 to ~ 500 µg/g at ca. 53.2 ka BP, which is followed by a clear trend towards higher concentrations with decreasing age, reaching a peak of ~ 4500 µg/g at ca. 48 ka BP. Similarly to Sr, Mg concentrations are very high in both samples (900 to 5000 µg/g). During early MIS 3, Mg shows an increasing trend between ca. 53.5 – 48 ka BP. Uranium concentrations in both samples are relatively stable (0.4 – 0.5 µg/g) with only a slightly decreasing trend during the progression of MIS 3. The Ba concentration shows no continuous trend, but a short decreasing trend between 52.0 to 48.5 ka BP. The mean Ba concentration is ca. 50 µg/g. The Al concentrations show values of more than a magnitude higher in sample BB-9 (average ~ 675 µg/g) than in sample BB-10 (average ~ 20 µg/g).

4.4.2 Fluid inclusions, Calcium isotopes and LOPs

The $\delta^{18}O$ and $\delta^{2}H$ values of fluid inclusions, $\delta^{44/42}Ca$ values as well as the C/V ratio and Σ8 of the LOPs of sample BB-10 are shown in Figure 2A. The $\delta^{44/42}Ca$ values of sample BB-9 are shown in Figure 2B. The water isotopes of the fluid inclusions show a relatively strong variability between ca. 53 to 50.5 ka BP. The $\delta^{18}O$ values vary between -10 and -8.6 ‰, and the $\delta^{2}H$ values between ca. -71.5 and -64 ‰. Around 53 ka BP, an increase towards more positive values in both water isotopes can be seen and is followed by a short decrease at ca. 51.5 ka BP and a subsequent increase again at 51 ka BP. The general water yield (Fig. S4.5 e) was between 0.02 – 0.47 µL/g and averaged at 0.14 µL/g. The fluid inclusion data plot closely to the GMWL (and even better on the LMWL) (Fig. S4.5). Data points with less than 0.1 µL/g water yield as well as one datapoint highly contaminated by detrital material (outside the scale of Fig. S4B) were discarded. The data shows no drift, indicating that there has been no degassing caused by the crushing of the sample prior to the measurement.

The $\delta^{44/42}Ca$ values of sample BB-10 show a small decreasing trend, with small-scale variations, especially during the beginning and ongoing early phase of MIS 3. The range of the values is ca. 0.50 to 0.65 ‰. The $\delta^{44/42}Ca$ values of sample BB-9 show a larger range of values between ca. 0.06 to 0.36 ‰. However, the trend is strongly influenced by the two values around ~ 33 ka BP. Without these two data points, the same small decreasing trend with the ongoing progression of MIS 3 as seen in BB-10 is notable in sample BB-9.

The Σ8 values of the LOPs of sample BB-10 show a strong increase (up to ca. 55 ng/g) around 51.5 ka BP and a relatively constant level throughout the remaining record. The C/V ratio shows an increase in agreement with the increase of the Σ8 value around 51.5 ka BP.

4.4.3 Soil and host rock analyses

The soil composition of Bleßberg cave predominantly consists of quartz, muscovite and oligoclase. It also includes ferrosilite, illite, chlorite, and goethite (Fig. S4.6). There are no differences in the mineralogical composition of the soil samples from different depths. The element concentrations of the soil samples and the host rock are shown in Table 4.1. The Sr and Ba concentrations are generally higher in the soil samples treated with acetic acid (i.e., acid, which reflects conditions in natural soils, where carbonic acid is produced by

microbial activity) compared to the soils treated with HCl. The Mg concentrations show no significant variation between the soils treated with acetic acid or HCl. The host rock analysis shows generally lower concentrations of Mg, slightly higher concentrations of Sr and also generally lower concentrations in the Ba concentration.

Table 4.1: Element concentrations (Mg, Sr and Ba) of the host rock and soil samples.

sample depth [cm]	material and acid	Mg [µg/g]	Sr [µg/g]	Ba [µg/g]
-	host rock	3695 ± 6	2639 ± 8.4	13.5 ± 0.1
5 – 15	Soil 1 in acetic acid	11200 ± 64	1382 ± 9.7	2640 ± 11.5
15 – 30	Soil 2 in acetic acid	8152 ± 19	1476 ± 3.3	2940 ± 20.1
30 – 45	Soil 3 in acetic acid	10010 ± 35	1916 ± 6.7	3620 ± 32.9
45 – 50	Soil 4 in acetic acid	10280 ± 31	1812.0 ± 9.1	3530 ± 28.6
5 – 15	Soil 1 in HCl	10890 ± 68	136 ± 1.3	751 ± 9.5
15 – 30	Soil 2 in HCl	12110 ± 38	115 ± 1.3	814 ± 4.7
30 – 45	Soil 3 in HCl	9812 ± 50	125 ± 0.6	707 ± 8.4
45 – 50	Soil 4 in HCl	10230 ± 37	110 ± 2.1	723 ± 13.5

4.5 Discussion

4.5.1 Climate during MIS 3

The $\delta^{13}C$ values (Fig. 4.1 a) show a general trend towards more positive values during MIS 3. Long term changes in the $\delta^{13}C$ values could indicate changes in the cave ventilation, which is neglectable in this case, because the cave had no natural entrances prior the discovery in 2008. Therefore, the main influence is contributed to soil development and microbial activity, where more negative values will indicate higher microbial activity due to enhanced CO_2 levels in the soil. The observer trend therefore indicates drier conditions with a potentially less developed soil, decreased microbial activity and vegetation density. This observation is supported by the $\delta^{44/42}Ca$ values (Fig. 4.2c and f), which show a generally decreasing trend towards less negative values indicating prior calcite precipitation (PCP) and therefore drier climate conditions. Calcium has the potential to precipitate prior to speleothem formation, which can result in the enrichment of other trace elements compared to calcite. The lighter calcium isotope (^{42}Ca) is preferentially

incorporated into the solid phase during this process. Therefore, precipitation before speleothem formation can lead to higher values of $\delta^{44/42}Ca$ in the drip water reaching the cave. Accordingly, the Ca isotopes in speleothems would also show higher values.

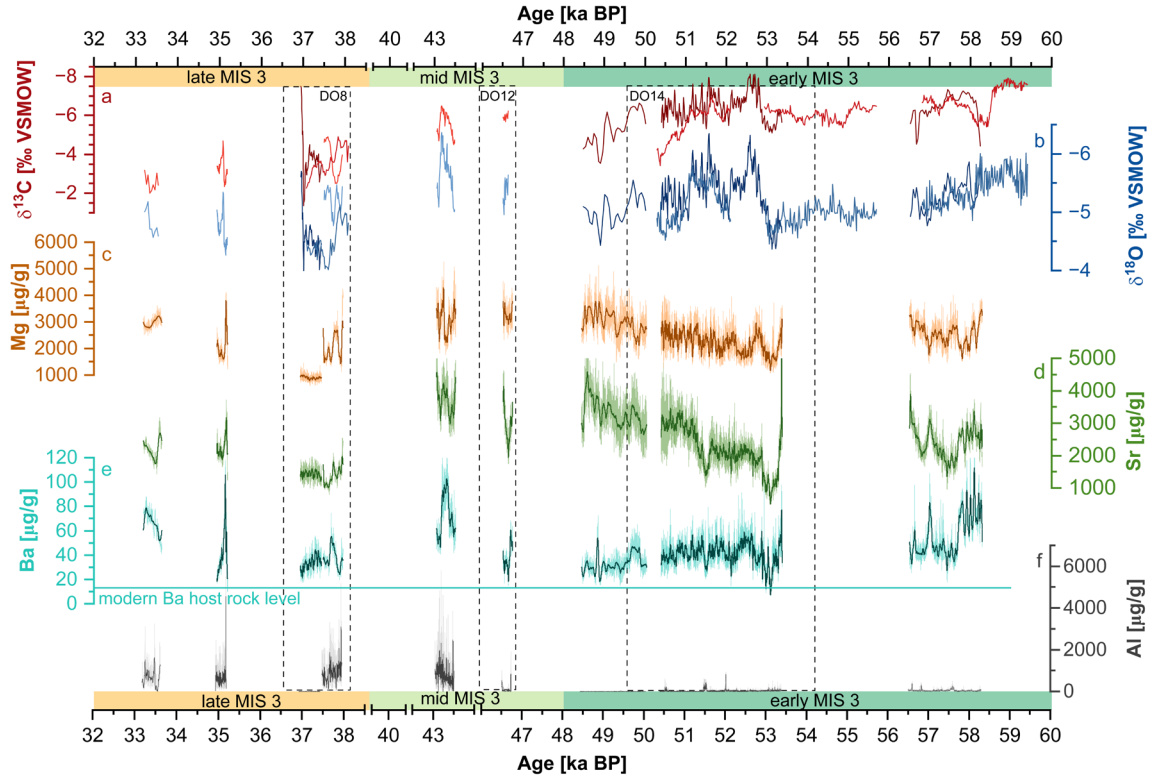

Fig. 4.1: Stable isotopes ($\delta^{13}C$ and $\delta^{18}O$) and trace elements (Mg, Sr, Ba and Al) of the Bleßberg speleothems during MIS3. a $\delta^{13}C$ are given in red (BB-10: dark, BB-15: medium, BB-9: light), b $\delta^{18}O$ are given in blue (BB-10: dark, BB-15: medium, BB-9: light). Trace elements (c – f) are only available for sample BB-9 and BB-10, the light colour shows the high resolution data, the light colour a 100pt mean. The Ba level of the modern host rock (13.3 µg/g) is indicated by the turquoise line. The grey bars indicate DO events 8, 12 and 14.

The general trend of the vegetation reflected by the lignin data during MIS 3 is from non-woody in the very early stage of MIS 3 to a more woody type of vegetation around 53 to 51 ka BP back to a non-woody type in late MIS 3, supporting the suggested trend towards drier climate from early to late MIS 3. The differentiation of vegetation types is based on lignin, a type of biopolymer that is only found in vascular plants. When it is broken down through oxidative digestion, it results in the formation of lignin oxidation products (LOPs). LOPs can be classified into three groups: vanillyl (V), syringyl (S), and cinnamyl (C) (Jex et al., 2014). Based on the comparison of C/V and S/V ratios, it is possible to differentiate between angiosperms, gymnosperms, and woody and non-woody type plants (Hedges and Mann, 1979). The C/V values ranging from 0 to 0.1 indicate woody

vegetation, 0.1 to 0.4 represent a transition zone, and values greater than 0.4 signify non-woody type vegetation. Similarly, the S/V values between 0 to 0.2 indicate gymnosperm plants, 0.2 to 0.9 represent a transition zone, and values greater than 0.9 signify angiosperms. The Σ8 value, which represents the total concentration of all eight analysed LOPs. It can be used as an indicator of the amount of lignin present in the sample and therefore a proxy of the total amount of vegetation.

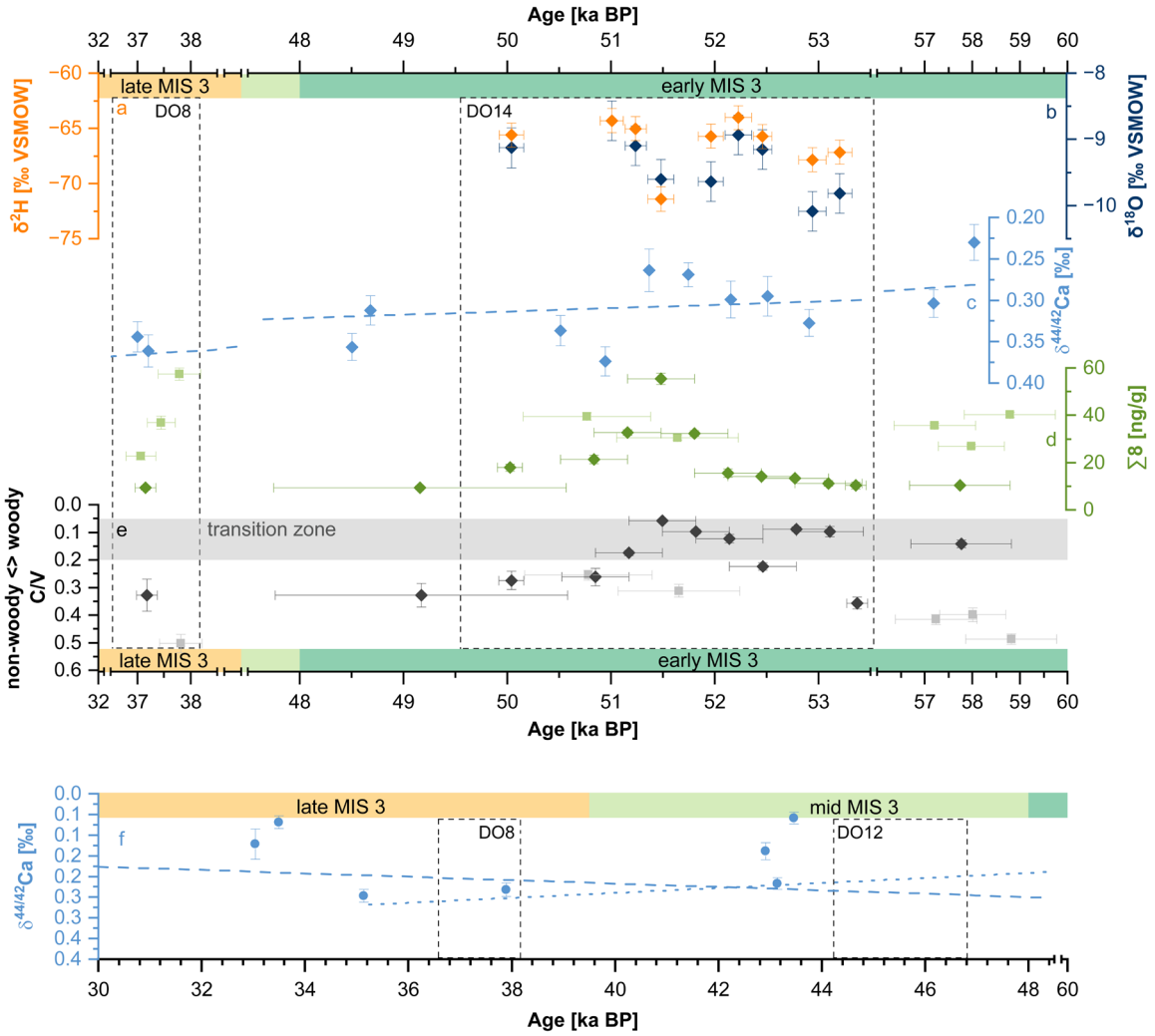

Fig. 4.2: Fluid inclusions $\delta^{18}O$ and $\delta^{2}H$ values, $\delta^{44/42}Ca$ values and two LOP parameters. Please note that diamonds indicate sample BB-10, squares indicate BB-15 and circles indicate BB-9. a and b show the $\delta^{18}O$ and $d^{2}H$ of fluid inclusions of sample BB-10, $\delta^{44/42}Ca$ values indicating wet or dry climate are given for sample BB-10 in c and BB-9 in f. Two lignin parameters indicating overall vegetation density in d and the softwood C/V ratio, both of sample BB-10. The grey bars indicate DO events 8, 12 and 14 as discussed in the main text.

The $\delta^{18}O$ values (Fig. 4.1b) show a general trend towards more positive values during MIS 3, which might indicate colder conditions with ongoing progression of MIS 3. Another potential influence could also be the known sea-level fluctuations during MIS 3 (Siddall et al., 2008), with a progressive reduction of the sea level resulting in more positive $\delta^{18}O$ values in the North Atlantic.

Between ca. 53 and 51 ka BP (aligning with DO14 (54.17 – 48.55 ka BP (Rasmussen et al., 2014)), indicated by a grey box in Fig. 4.1), the $\delta^{13}C$ values show more negative values, hinting towards a stronger soil influence and a particularly well-developed soil during this time frame. During this phase, the LOP data (Σ8 and C/V ratio, Fig. 4.2 d and e) show a peak suggesting increased vegetation density and a well-established woody-type vegetation (Fig. S74.), hinting towards the best-developed vegetation cover throughout MIS 3 with trees of the softwood type (Fig. S4.7). This peak in vegetation also correlates with a negative peak in the $\delta^{44/42}Ca$ values indicating an increased moisture availability.

The LOP data from BB-15 (Fig. 4.2 d) show an additional peak in Σ8 (at ca. 38 ka BP) during DO8 (38.12 – 36.53 ka BP (Rasmussen et al., 2014), indicated by a grey box in Fig. 4.1 and 4.2), which is not visible in the BB-10 LOP data. However, BB-15 started growing earlier during DO8 than BB-10, and the BB-10 data thus reflect a later phase of DO8. In addition, the growth phase of BB-15 lasts for approximately 1 ka, providing more time to establish vegetation. In contrast, BB-10 (and BB-9) display continuous growth for only 0.5 ka. Furthermore, Kindler et al. (2014) describe a preceding slight long-term warming before the start of the rapid temperature increase for DO events subsequent to Heinrich events, like DO8 or 12. Therefore the apparent relatively quick re-establishment of vegetation with the onset of DO8 recorded in BB-15 is most likely a response to this preceding warming. However, the C/V data during DO8 only suggest non-woody type vegetation for both samples. Therefore, the warming during DO8 was either too short or not strong enough (10 °C ± 3 °C Kindler et al., 2014) to establish a more advanced type of vegetation than during DO14 (temperature increase of 12.5 °C ± 3 °C Kindler et al., 2014).

During the mid and late phase of MIS 3, the individual growth phases were generally shorter, and even though DO8 is the only time during MIS 3, where all three samples grew (even if not entirely simultaneously), the vegetation shows only a very brief increase towards non-woody vegetation with a C/V ratio similar to early MIS 3. The longest, continuous growth phase during MIS 3 coincides with DO14 and will therefore be

discussed in more detail in the following. In summary, the proxy data suggest a general trend towards colder and drier conditions during MIS 3.

4.5.2 Comparison with other MIS 3 climate records

Klose et al., (in review) determined the age models for the Bleßberg MIS 3 record and created a composite growth model for all three samples. In total nine growth phases were identified, eight of them distinctively correlating with DO events 16, 14 – 11 and8 – 6. It revealed that the emphasis on long, continuous growth phases was clearly during the early phase of MIS 3. This is supported by this study's proxy data, which suggests that the early MIS 3 period was warmer than the later phases. The data also indicates that the climate conditions during this period were not only warm but also wet, as evidenced by the $\delta^{13}C$ and $\delta^{44/42}Ca$ values.

This observation of a generally warmer early MIS 3 in Europe (especially around 53 – 52 ka BP), is supported by other European records (e.g., Sirocko et al., 2016; Weber et al., 2018). The peak in vegetation density in the Bleßberg record correlates well with a high level of thermophilic *Carpinus* pollen (Fig. 4.3 k) in the Eifel pollen record (Sirocko et al., 2022), which is a hardwood-type tree. The softwood-type trees above Bleßberg cave suggested by the LOP proxy data may be related to a shift in vegetation and climate Western to Eastern Germany, which can also be observed in modern climate. A recent study (Riechelmann et al., 2023) also suggests that a low summer, but high winter insolation leads to warm winters during early MIS 3 promoting vegetation growth in Central Europe, which would further explain the more dominant woody-type vegetation in the Bleßberg record. High and stable sea surface temperatures (SST) at the Iberian margin (Martrat et al., 2007) and the warm conditions in the NALPS speleothem record (Moseley et al., 2014), further support the idea of a warmer early MIS 3. Additionally, the Pa/Th ratios presented in Henry et al. (2016) show the lowest values during early MIS 3. Low Pa/Th ratios are associated with a more vigorous AMOC due to an increased and substantial lateral export of ^{231}Pa caused by a deeper overturning cell. The mean Pa/Th ratio (Fig. 4.3 c, green dotted line) during the entire MIS 3 is reported to be 10 % higher in comparison to the mean of the Holocene (Fig. 4.3 c, grey dotted line). Two phases between 54.1 – 52.3 ka BP and 50.0 – 49.5 ka BP show, however, even lower values than the mean Holocene indicating a similarly strong AMOC. This all demonstrates that the

early phase of MIS 3 created favourable conditions for prolonged speleothem growth due to sufficient water availability, warm temperatures, and increased vegetation cover above the cave.

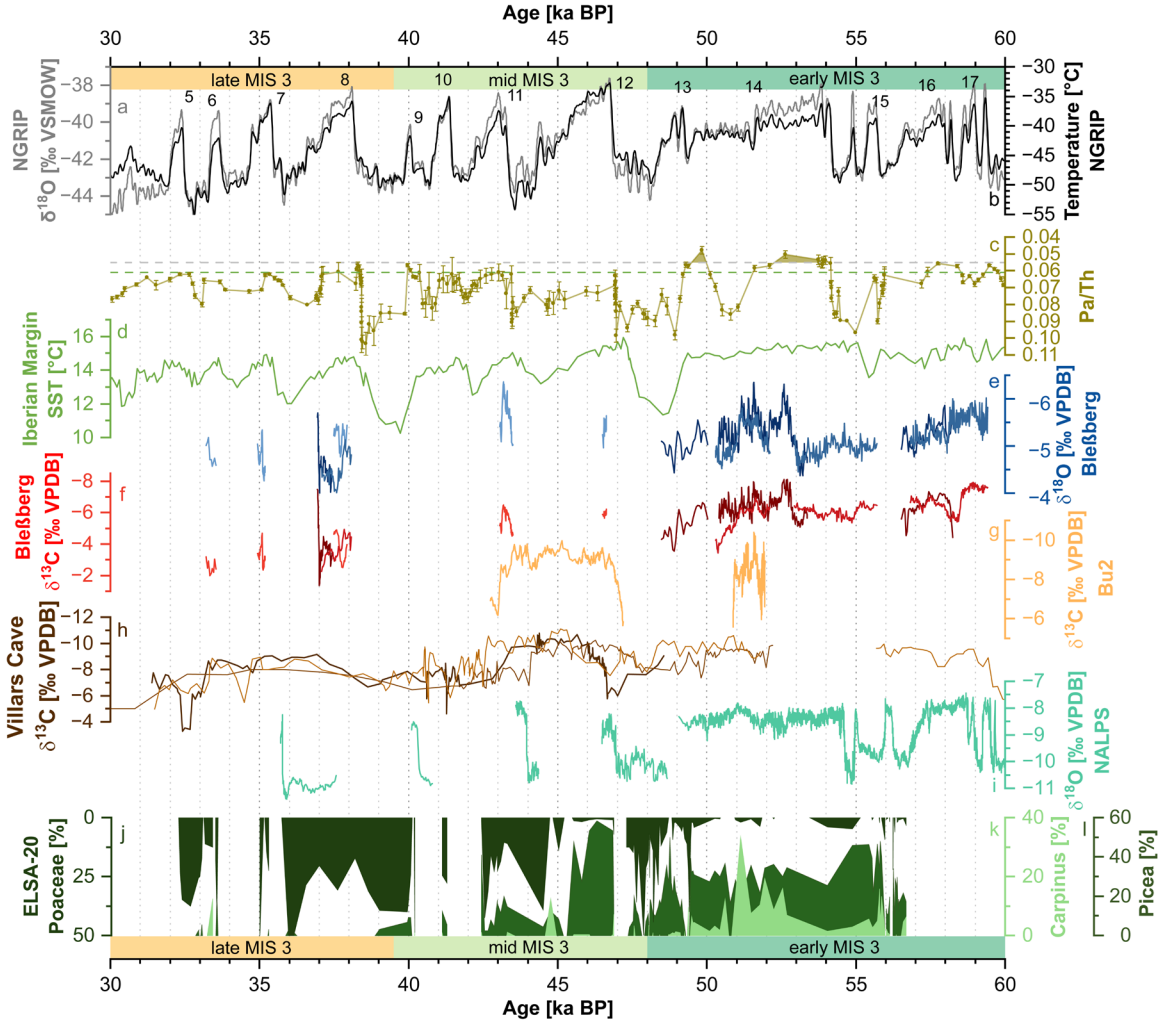

Fig. 4.3: Comparison of Bleßberg stable isotope records with other MIS 3 proxy records. DO events are indicated by the number above the NGRIP $\delta^{18}O$ record (a, grey line (Rasmussen et al., 2018)) and Temperature reconstruction (b, black line (Kindler et al., 2014)). c shows the Bermuda rise Pa/Th record from core CDH19 (Henry et al.,2016) indicating the AMOC strength. The dotted green line indicates the average of MIS 3 (0.0609 ± 0.0074 (2σ)) and the brown dotted lined (Pa/Th = 0.055) indicates the mean Holocene value, the filled area highlights area when the MIS 3 data is higher than this mean value. The green line shows a SST record from the Iberian margin (Martrat et al., 2007), e and f give the Bleßberg stable isotope records in the same colours as in Fig. 4.1. g shows the Bu2 $\delta^{13}C$ record from Bunker Cave (Weber et al., 2018). h shows three $\delta^{13}C$ records from Villars Cave (Vil-09 light brown, Vil-14 brown, Vil-27 dark brown, (Genty et al., 2010)). i shows the composite NALPS $\delta^{18}O$ record (Moseley et al., 2014). And the pollen data j - l is from the ELSA-20 pollen stack from the Eifel region (Sirocko et al., 2022).

The Bleßberg speleothem growth phases correlate with speleothem growth phases in Bunker Cave, Germany (Bu2, Weber et al., 2018), and in Villars Cave, France (Genty et al., 2010) during early MIS 3 (Fig. 4.3). Interestingly, the longest growth period of the Bleßberg speleothems (ca. 53.4 – 50.4 ka BP) is only partly covered by the records from Bunker Cave and Villars Cave. However, Genty et al (2003) described flooding events

occurring during DO14 as potentially preventing speleothem formation in parts of the cave. The recently published record by Peral et al. (2024) shows continuous growth during DO14 but only a weak climate signal with little to no variations in the proxy data. They suggest that this lack of climatic response is caused by a delay between the warm and humid DO event and the onset of speleothem growth. This observation is not necessarily supported by our record. We observe a delay of ~ 1 ka between the onset of our growth phase and the onset of the DO in NGRIP, but in the following, the proxy data show large variability and a good representation of DO14.

The Bleßberg speleothem record only shows two very short growth phases during the mid phase of MIS 3, most likely caused by generally less favourable conditions for speleothem growth. The first growth phase (ca. 46.7 – 46.5 ka BP) correlates and overlaps with the onset of DO12 (44.23 – 46.81 ka BP Rasmussen et al., 2014) within uncertainty. As previously mentioned, Kindler et al. (2014) described a preceding slight long-term warming for DO events following a Heinrich event, like DO12. This explains the timing of the Bleßberg growth phase coinciding with the Greenland onset, without any substantial lag (see Klose et al. (in review) for details). However, even with DO12 being a comparably long DO event in Greenland the growth of the Bleßberg speleothem is relatively short. The Pa/Th ratio during DO12 shows relatively high values for a warm phase and therefore indicates a weaker AMOC. The ratio is noticeably higher than the mean ratio during MIS 3 (Fig. 4.3, green dotted line), with no prominent peaks and a similar level to the stadial period after the DO event. The end of the Bleßberg growth phase also correlates with the end of a growth phase in the NALPS record. The Bunker and Villars Cave records both show continuous growth over a longer period during mid MIS 3, the age model of Bunker Cave, however, might indicate an unresolved growth stop around 45 ka BP and relative growth rate changes in the Villars speleothems were used to identify a cold and dry period between 48.2 to 46.6 ka BP. In addition, Bleßberg Cave is located more continental than both Bunker Cave and Villars Cave, the latter is also located more southern (Fig. S4.1). It is likely that our record is therefore more sensitive to colder and drier periods, which results in the shorter growth phase. Pederzani et al. (2024) report mean annual temperatures around 1 °C for the period between 48 to 45 ka BP and winter temperatures around -10 °C, which supports the theory of generally less-favourable conditions for speleothem growth. The temperature reconstruction is based on $\delta^{18}O$ values from *Equus sp.* teeth from Ilsenhöhle, which is located in close vicinity (ca. 45 km) to Bleßberg Cave.

The second Bleßberg growth phase during the mid phase of MIS 3 started around 43.5 ka BP, coinciding with the onset of DO 11 (43.36 – 42.19 ka BP) within uncertainty and lasted until 43.1 ka BP. The onset of the growth phase also correlates with a rapid increase in the AMOC strength as indicated by rapidly decreasing Pa/Th ratios and high SSTs. Pederzani et al. (2024) describe a particularly cold phase between ca. 45 to 43 ka BP, with temperatures lower by ca. 7 to 15 °C than modern temperatures and a mean annual temperature below freezing. The end of this cold event fits the onset of our growth phase within uncertainty and the Greenland Stadial (GS) 12 (ca. 44.3 – 43.3 ka BP). The Villars record also describes a cooling trend after ca. 45 ka BP, supported by the Bunker Cave (Weber et al., 2018) and Han-sur-Lesse Cave (Peral et al., 2024) records. The Bunker Cave record stops growing shortly after the growth stop in Bleßberg Cave. The Villars speleothem retained to grow but increasing $\delta^{13}C$ values are interpreted as a general deterioration of the climate after 45 ka BP. This general progression of mid MIS 3 is also evident in the pollen record from the Eifel maar lakes with a rapid increase in *Poaceae* and decrease of *Picea* after 45 ka BP.

It is likely that during the mid phase of MIS 3 the climate conditions in Central Europe were, in comparison to early MIS 3, already too cold and/or dry to enable speleothem growth during a long, continuous time period, and the growth phases represented in our record only reflect the warmest/wettest periods of the warm phase and corresponding DO event, i.e., the peaks of the event.

During the late phase of MIS 3, speleothem growth in Bleßberg Cave only occurs during phases with the highest SSTs at the Iberian margin and during the peak of the DO events recorded in NGRIP. The comparison with other European records is hampered by the fact that they either did not grow at all (Bunker Cave, Han-sur-Lesse Cave) or only show a single short growth phase (NALPS) (Fig. 4.3). The Villars Cave record suggests continuous growth, but only has a very low proxy resolution limited by the age model. The lack of other speleothem records from Central Europe during the late phase of MIS 3 emphasizes that the climate conditions became less favourable for speleothem growth during MIS 3 and highlights the sensitivity of the Bleßberg record.

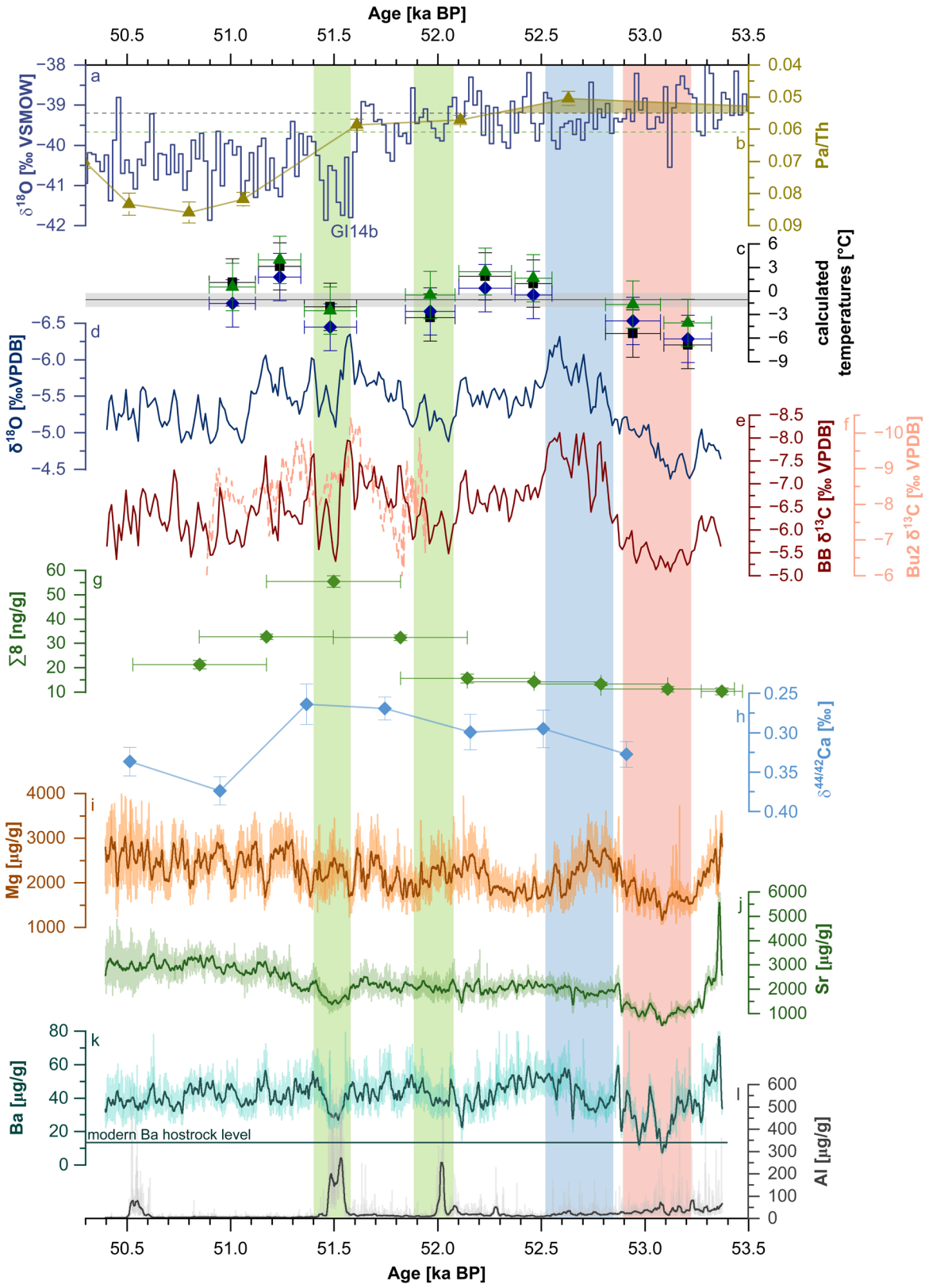

Fig. 4.4: Overview of Bleßberg proxies during DO14. The NGRIP $\delta^{18}O$ record is given in blue (a, Rasmussen et al., 2018) and the Bermuda Rise Pa/Th in olive green (b, Henry et al., 2016). The dotted lines and filled areas are as in Fig. 4.3. The calculated temperatures in c are based on the fluid inclusion data from sample BB-10 and explained in more detail in Fig. S4.4. The stable isotope records from sample BB-10 are given in d and e and for comparisons the Bu2 $\delta^{13}C$ record in f (Weber et al., 2018). g shows the sum of all lignin products, which indicated the vegetation density, and the $\delta^{44/42}$ values (h) indicates wet and dry climate. Four trace elements (Mg, Sr, Ba including the modern Ba host rock level and Al) are given in i – l. The coloured bars indicate the onset of the Central European warm phase (red), the established warm phase (blue) and two cold events (green). The second cold event coincides with GI14b.

4.5.3 DO14

DO14 is the longest DO event recorded in NGRIP during MIS 3, with a duration of 4.62 ka (49.55 – 54.17 ka BP Rasmussen et al., 2014). The Bleßberg growth phase corresponding to DO14 is the longest (ca. 53.4 – 50.4 ka BP) continuous phase recorded in the Bleßberg speleothems (Figs. 4.3 – 4.4) and therefore allows obtaining more detailed information about the climate conditions of a particularly warm phase in Central Europe.

4.5.3.1 Initial Warming (53.5 – 52.5 ka BP)

During the initial 0.2 ka of the Bleßberg growth phase, there is a possibility of observing a mixed signal in both stable isotopes of the speleothem due to permafrost thaw. This could be a result of the beginning of a warm phase, reworking of the system, and input of accumulated detrital material during the hiatus.

Between ca. 53.4 – 52.5 ka BP, the calculated cave air temperatures (usually representing the mean annual surface temperature) show a steady increase from ca. -4.3 to +2.5 °C (± 3 °C). The $\delta^{18}O$ values of the speleothem ($\delta^{18}O_c$) follow this trend and show a steady decrease towards more negative values, most likely indicating the same increase in temperature. The $\delta^{13}C$ values show a generally strong correlation with the $\delta^{18}O_c$ values ($r = 0.89$) during the entire warm phase. The largest discrepancy is, however, observed during this early phase of DO14. Whereas the $\delta^{18}O_c$ values show a steady trend, the $\delta^{13}C$ values, which also show a general trend towards more negative values, show a plateau of ca. 0.3 ka between ca. 53.2 – 52.9 ka BP (red box in Fig.4.4). This might be related to a re-establishment of the soil and the delayed response of soil activity after a cold period and permafrost above the cave. In addition, the vegetation needs time to develop, which influences the $\delta^{13}C$ values. More negative $\delta^{13}C$ values are therefore associated with a better developed soil and increased biological soil activity, more dense vegetation and potentially a higher drip rate. This suggests that both stable isotopes are mainly affected by temperature, but $\delta^{18}O$ is a direct proxy and $\delta^{13}C$ only indirect. Therefore, the correlation between both is relatively high except for the initial phase of re-establishing the soil and vegetation, which causes a lag of the $\delta^{13}C$ values. The sum of lignin (Σ8) shows a prolonged trend towards increasing vegetation, and the lignin C/V ratio indicates a clear non-woody (grassland) vegetation at the beginning of the warm phase switching to a more mixed vegetation in the following. This also supports the idea of the delayed re-establishment soil

and vegetation after the preceding cold period. This hypothesis is further supported by the Ba concentration, which is strongly affected by the host rock because the soil and vegetation still develop, and soil activity is low.

Between ca. 52.8 – 52.5 ka BP (indicated by the blue box in Fig. 4.4), the warm phase is well-established. Both the $\delta^{18}O_c$ and the $\delta^{13}C$ values show a negative peak indicating that the soil is fully "re-developed", and the soil activity is high. The calculated temperatures based on the fluid inclusions still increase after 52.4 ka even though the $\delta^{18}O$ values show a trend towards higher values. The Σ8 data show a slowly increasing trend, supporting the idea of a fully "re-developed" soil, and the $\delta^{44/42}Ca$ values indicate less PCP and thus more humid conditions. The trace elements (especially Mg and Ba) however show a trend towards higher values, which could indicate PCP but might in this case indicate increased soil leaching. The element analysis (Table 4.1) showed that Mg and Ba primarily stem from the soil and are can both already be leached from it with the weaker acetic acid. This acetic acid can be used to mimic conditions in natural soils, where carbonic acid is produced by microbial activity. It demonstrates that with a sufficiently wet climate, both elements can be easily leached from the soil, which would lead to increased values in our record.

4.5.3.2 Transition period (52.5 – 52.1 ka BP)

After ca. 52.5 ka BP, both stable isotope values develop towards more positive values indicating a trend towards colder climate conditions and less soil activity. The calculated temperatures still indicate a slight increase in temperature, but due to the much lower resolution and more importantly the uncertainties, this might not necessarily be contradicting. The $\delta^{44/42}Ca$ values remain stable within uncertainty and indicate no further trend towards wetter conditions. The Ba concentration is still high, further indicating soil leaching, while the Mg concentration decreases. Ba most likely stems from the feldspar and is therefore more easily removed than Mg, which preferably sticks to clay minerals. This might indicate that conditions were drier/colder, and the reduced soil activity is sufficient to leach more Ba but not Mg. That would support the theory of reduced soil activity due to drier conditions.

4.5.3.3 Cold events (52.1 – 51.4 ka BP)

Between ca. 52.1 ka BP and 51.4 ka BP, two cold events are evident (indicated by green boxes in Fig. 4.4) in the Bleßberg warm phase. During both cold events, more positive $\delta^{18}O_c$ values indicate colder temperatures. The $\delta^{13}C$ values are also more positive and indicate less soil activity due to cold stress. Contradicting the LOP data show an ongoing increase in overall vegetation and a trend towards more woody-type vegetation. This trend could be explained with the vegetation reflecting and reacting to summer climate, while the remaining proxies represent an annual signal, and the cold phases show a pronounced seasonality. Both LOP proxies peak during the second cold event, which correlates with the GI14b event in Greenland. We do not have $\delta^{44/42}Ca$ values in the cold phases, but the general trend towards more negative values suggests that those phases were rather wet than dry. This would lead to less PCP and concluding to low element concentrations, which is evident for Sr and Ba during the GI14b cold phase. The water isotopes of the fluid inclusions and the calculated temperatures support the idea of cold events. However, the Al concentrations show increased values during those events. Detrital contamination might affect the fluid inclusion data and measurement and therefore the calculated temperatures. In the case of a strong influence of the Al on the fluid inclusions, it can be expected that the data will shift away from the GMWL (or LMWL), which is not the case here (Fig. S4.5). Nonetheless, the data must be seen as more of a conservative estimate, that supports the data but and is not the decisive factor. The origin of the elevated Al concentrations may be due to flash floods transporting detrital material inside the cave or reflect short term growth stops (Klose et al., in review) or a strongly reduced growth rate.

So far, not much evidence for the GI14b cold event has been found and discussed apart from the Greenland ice cores. Therefore, the comparability with other records is vastly limited. However, we were able to identify the cold phase coinciding with the Greenland GI14b in the $\delta^{13}C$ record from Bunker cave (Weber et al., 2018), which has not been discussed before. A drastic change in the AMOC strength is also clearly noticeable, where a trend towards more positive values in the Pa/Th values coincide with the onset of the event in Greenland (Henry et al., 2016).

4.5.3.4 Termination of the warm phase (51.4 – 50.4 ka BP)

After the second cold event/GI14b, the fluid inclusion data and calculated temperatures indicate a short increase in temperature, while the stable isotopes show a slowly increasing trend towards more positive values. The $\delta^{44/42}$Ca values show a rapid increase towards more positive values as well, indicating the driest conditions during the entire growth phase. The Sr and Mg concentrations support this observation and show an increase in concentrations probably due to PCP being the dominant factor in this phase of the warm event. The Ba concentration shows a slow decreasing trend towards the value of the modern host rock, indicating reduced soil leaching due to dry conditions. Both LOP parameters support this observation and show a decrease in the sum of lignin and vegetation density and a shift towards non-woody vegetation. This indicates that the vegetation most likely did not recover after the GI14b cold phase, even though moisture availability was most likely not the issue during the cold phase. The δ^{13}C values support this observation by showing reduced vegetation cover and soil activity, which also correlates with a strongly reduced AMOC strength. Around 50.8 ka BP the AMOC starts recovering, which is followed by a trend in the stable isotopes, especially the δ^{13}C values, towards more negative values indicating humid climate conditions. The $\delta^{44/42}$Ca values also indicate a decreasing trend towards wetter climate conditions. These climate improvements are not evident in the LOP data, which could be due to the low resolution of the data set or the warming being too short or not warm enough to enable vegetation growth. The growth phase of the Bleßberg speleothem, however, comes to a stop before the AMOC strength is increasing again and reaches the second peak during DO14.

Therefore, the latest phase of this Central European warm phase would be warm and dry, which suggests that PCP may also influence the stable isotope records. The Al concentrations show higher values at the end of the growth and warm phase probably due to detrital material accumulating as the growth of the speleothem comes to a stop. The temperatures are still higher than at the beginning of the warm phase, the stop of speleothem growth, therefore, is probably caused by the direr conditions and the lack of water reaching the cave and the reclining vegetation cover.

4.6 Conclusion

The speleothem samples from Bleßberg Cave offer the great opportunity to investigate the past climate variability of MIS 3 in general and DO14 as a specific pronounced warm event in more detail. The record is highly sensitive to environmental changes and represents the peak warmings during the last glacial period in Central Europe. The record highlights the general trend from humid climate during early MIS 3 towards drier and colder conditions with the progression of MIS 3. The longest warm period recorded in our record coincides with DO14, which was already previously highlighted as a particularly warm and prolonged DO event in numerous paleoclimate archives and records. The Bleßberg record shows, that this particularly warm phase was also significant in the more continental climate of Central Europe and widely influenced vegetation and moisture availability over the continent. Additionally, two distinct short-term cold events were revealed during DO14, one of the coinciding with GI14b, a cold termination recorded in the Greenland ice cores, which has not been shown in terrestrial records before.

MIS 3 marks the timing of the disappearance of the Neanderthals in Europe and the first appearance of the modern human. Pederzani et al. (2024) report the earliest appearance of the *homo sapiens* in Central Europe around ~ 45 ka BP, while Higham et al. (2014) show that the most relevant population of Neanderthals of the Middle Palaeolithic ended latest around 41 – 39 ka BP across Europe. Staubwasser et al., (2018) discussed the theory that a change of climate forced the transition from the Neanderthals to the modern human. They propose that especially GS12 (44.3 – 43.3 ka BP Rasmussen et al., 2014) and the ongoing expansion of steppe biomes during cold and dry stadial periods led to the depopulation of Neanderthals. Modern humans may have been better suited to adapt and track the expanding steppe across Central Europe. Since the Bleßberg Cave record only provides two short growth phases during this transition period, no distinct conclusion can be made about the repetitive depopulation-repopulation cycles of Neanderthals and home sapiens. However, our record supports the idea of dry and unfavourable climate conditions during mid MIS 3 in Central Europe.

4.7 References

Adolphi, F., Bronk Ramsey, C., Erhardt, T., Edwards, R.L., Cheng, H., Turney, C.S.M., Cooper, A., Svensson, A., Rasmussen, S.O., Fischer, H. and Muscheler, R., 2018. Connecting the Greenland ice-core and U/Th timescales via cosmogenic radionuclides: testing the synchroneity of Dansgaard–Oeschger events. Climate of the Past, 14(11): 1755-1781.

Andersen, K.K., Svensson, A., Johnsen, S.J., Rasmussen, S.O., Bigler, M., Röthlisberger, R., Ruth, U., Siggaard-Andersen, M.-L., Peder Steffensen, J. and Dahl-Jensen, D., 2006. The Greenland Ice Core Chronology 2005, 15–42ka. Part 1: constructing the time scale. Quaternary Science Reviews, 25(23-24): 3246-3257.

Baldini, J.U., Brown, R.J. and McElwaine, J.N., 2015. Was millennial scale climate change during the Last Glacial triggered by explosive volcanism? Scientific Reports, 5(1): 17442.

Banks, W.E., d'Errico, F., Peterson, A.T., Kageyama, M., Sima, A. and Sánchez-Goñi, M.-F., 2008. Neanderthal extinction by competitive exclusion. PLoS One, 3(12): e3972.

Bond, G., Broecker, W., Johnsen, S., McManus, J., Labeyrie, L., Jouzel, J. and Bonani, G., 1993. Correlations between climate records from North Atlantic sediments and Greenland ice. Nature, 365(6442): 143-147.

Breitenbach, S.F., Plessen, B., Waltgenbach, S., Tjallingii, R., Leonhardt, J., Jochum, K.P., Meyer, H., Goswami, B., Marwan, N. and Scholz, D., 2019. Holocene interaction of maritime and continental climate in Central Europe: New speleothem evidence from Central Germany. Global and Planetary Change, 176: 144-161.

Budsky, A., Wassenburg, J.A., Mertz-Kraus, R., Spötl, C., Jochum, K.P., Gibert, L. and Scholz, D., 2019. Western Mediterranean climate response to Dansgaard/Oeschger events: New insights from speleothem records. Geophysical Research Letters, 46(15): 9042-9053.

Chen, S., Wang, Y., Cheng, H., Edwards, R.L., Wang, X., Kong, X. and Liu, D., 2016. Strong coupling of Asian Monsoon and Antarctic climates on sub-orbital timescales. Scientific Reports, 6(1): 32995.

Cheng, H., Edwards, R.L., Shen, C.-C., Polyak, V.J., Asmerom, Y., Woodhead, J., Hellstrom, J., Wang, Y., Kong, X. and Spötl, C., 2013. Improvements in ^{230}Th dating, ^{230}Th and ^{234}U half-life values, and U–Th isotopic measurements by multi-collector inductively coupled plasma mass spectrometry. Earth and Planetary Science Letters, 371: 82-91.

Cheng, H., Edwards, R.L., Sinha, A., Spötl, C., Yi, L., Chen, S., Kelly, M., Kathayat, G., Wang, X. and Li, X., 2016. The Asian monsoon over the past 640,000 years and ice age terminations. nature, 534(7609): 640-646.

Constantin, S., Bojar, A.-V., Lauritzen, S.-E. and Lundberg, J., 2007. Holocene and Late Pleistocene climate in the sub-Mediterranean continental environment: A speleothem record from Poleva Cave (Southern Carpathians, Romania). Palaeogeography, Palaeoclimatology, Palaeoecology, 243(3-4): 322-338.

Corrick, E.C., Drysdale, R.N., Hellstrom, J.C., Capron, E., Rasmussen, S.O., Zhang, X., Fleitmann, D., Couchoud, I. and Wolff, E., 2020. Synchronous timing of abrupt climate changes during the last glacial period. Science, 369(6506): 963-969.

Dansgaard, W., Johnsen, S.J., Clausen, H.B., Dahl-Jensen, D., Gundestrup, N.S., Hammer, C.U., Hvidberg, C.S., Steffensen, J.P., Sveinbjörnsdottir, A.E., Jouzel, J. and Bond, G., 1993. Evidence for general instability of past climate from a 250-kyr ice-core record. Nature, 364: 218 - 220.

De Graaf, S., Lüders, V., Banks, D.A., Sośnicka, M., Reijmer, J.J., Kaden, H. and Vonhof, H.B., 2020. Fluid evolution and ore deposition in the Harz Mountains revisited: isotope and crush-leach analyses of fluid inclusions. Mineralium Deposita, 55: 47-62.

Degioanni, A., Bonenfant, C., Cabut, S. and Condemi, S., 2019. Living on the edge: Was demographic weakness the cause of Neanderthal demise? PLoS One, 14(5): e0216742.

Denniston, R.F., Houts, A.N., Asmerom, Y., Wanamaker Jr, A.D., Haws, J.A., Polyak, V.J., Thatcher, D.L., Altan-Ochir, S., Borowske, A.C. and Breitenbach, S.F., 2018. A stalagmite test of North Atlantic SST and Iberian hydroclimate linkages over the last two glacial cycles. Climate of the Past, 14(12): 1893-1913.

Doebelin, N. and Kleeberg, R., 2015. Profex: a graphical user interface for the Rietveld refinement program BGMN. Journal of applied crystallography, 48(5): 1573-1580.

Erhardt, T., Capron, E., Rasmussen, S.O., Schüpbach, S., Bigler, M., Adolphi, F. and Fischer, H., 2019. Decadal-scale progression of the onset of Dansgaard–Oeschger warming events. Clim. Past, 15(2): 811-825.

Fohlmeister, J., Sekhon, N., Columbu, A., Vettoretti, G., Weitzel, N., Rehfeld, K., Veiga-Pires, C., Ben-Yami, M., Marwan, N. and Boers, N., 2023. Global reorganization of atmospheric circulation during Dansgaard–Oeschger cycles. Proceedings of the National Academy of Sciences, 120(36): e2302283120.

Genty, D., Blamart, D., Ouahdi, R., Gilmour, M., Baker, A., Jouzel, J. and Van-Exter, S., 2003. Precise dating of Dansgaard–Oeschger climate oscillations in western Europe from stalagmite data. Nature, 421(6925): 833-837.

Genty, D., Combourieu-Nebout, N., Peyron, O., Blamart, D., Wainer, K., Mansuri, F., Ghaleb, B., Isabello, L., Dormoy, I. and von Grafenstein, U., 2010. Isotopic characterization of rapid climatic events during OIS3 and OIS4 in Villars Cave stalagmites (SW-France) and correlation with Atlantic and Mediterranean pollen records. Quaternary Science Reviews, 29(19-20): 2799-2820.

Hedges, J.I. and Mann, D.C., 1979. The characterization of plant tissues by their lignin oxidation products. Geochimica et Cosmochimica Acta, 43(11): 1803-1807.

Henry, L., McManus, J., Curry, W., Roberts, N., Piotrowski, A. and Keigwin, L., 2016. North Atlantic ocean circulation and abrupt climate change during the last glaciation. Science, 353(6298): 470-474.

Higham, T., Douka, K., Wood, R., Ramsey, C.B., Brock, F., Basell, L., Camps, M., Arrizabalaga, A., Baena, J. and Barroso-Ruíz, C., 2014. The timing and spatiotemporal patterning of Neanderthal disappearance. Nature, 512(7514): 306-309.

Hodge, E.J., Richards, D.A., Smart, P.L., Andreo, B., Hoffmann, D.L., Mattey, D.P. and González-Ramón, A., 2008. Effective precipitation in southern Spain (~ 266 to 46 ka) based on a speleothem stable carbon isotope record. Quaternary Research, 69(3): 447-457.

Homann, J., Zirbes, M., Arndt-Engelbart, M., Scholz, D., Waldvogel, S.R. and Hoffmann, T., 2022. Development of a Method for Anodic Degradation of Lignin for the Analysis of Paleo-Vegetation Proxies in Speleothems. ChemElectroChem, 9(6): e202101312.

Jex, C.N., Pate, G.H., Blyth, A.J., Spencer, R.G., Hernes, P.J., Khan, S.J. and Baker, A., 2014. Lignin biogeochemistry: from modern processes to Quaternary archives. Quaternary Science Reviews, 87: 46-59.

Kathayat, G., Cheng, H., Sinha, A., Spötl, C., Edwards, R., Zhang, H., Li, X., Yi, L., Ning, Y. and Cai, Y., 2016. Indian monsoon variability on millennial-orbital timescales, Sci. Rep., 6, 24374.

Kindler, P., Guillevic, M., Baumgartner, M., Schwander, J., Landais, A. and Leuenberger, M., 2014. Temperature reconstruction from 10 to 120 kyr b2k from the NGRIP ice core. Clim. Past, 10(2): 887-902.

Knutti, R., Flückiger, J., Stocker, T. and Timmermann, A., 2004. Strong hemispheric coupling of glacial climate through freshwater discharge and ocean circulation. Nature, 430(7002): 851-856.

Kudielka, G., Bar-Matthews, M., Gilmour, M., Ayalon, A., Koeberl, C. and Montanari, A., 2019. Implications for central Italy paleoclimate from 95,000 yr BP until the early Holocene as evident from Frasassi Cave speleothems.

Lisiecki, L.E. and Raymo, M.E., 2005. A Pliocene-Pleistocene stack of 57 globally distributed benthic δ18O records. Paleoceanography, 20(1).

Martrat, B., Grimalt, J.O., Shackleton, N.J., de Abreu, L., Hutterli, M.A. and Stocker, T.F., 2007. Four climate cycles of recurring deep and surface water destabilizations on the Iberian margin. Science, 317(5837): 502-507.

Mischel, S.A., Mertz-Kraus, R., Jochum, K.P. and Scholz, D., 2017. TERMITE: An R script for fast reduction of laser ablation inductively coupled plasma mass spectrometry data and its application to trace element measurements. Rapid Communications in Mass Spectrometry, 31(13): 1079-1087.

Moseley, G.E., Spötl, C., Brandstätter, S., Erhardt, T., Luetscher, M. and Edwards, R.L., 2020. NALPS19: Sub-orbital-scale climate variability recorded in northern Alpine speleothems during the last glacial period. Climate of the Past, 16(1): 29-50.

Moseley, G.E., Spötl, C., Svensson, A., Cheng, H., Brandstätter, S. and Edwards, R.L., 2014. Multi-speleothem record reveals tightly coupled climate between central Europe and Greenland during Marine Isotope Stage 3. Geology, 42(12): 1043-1046.

NGRIP Project members, 2004. High-resolution record of Northern Hemisphere climate extending into the last interglacial period. Nature, 431(7005): 147-151.

Pederzani, S., Britton, K., Trost, M., Fewlass, H., Bourgon, N., McCormack, J., Jaouen, K., Dietl, H., Döhle, H.-J. and Kirchner, A., 2024. Stable isotopes show Homo sapiens dispersed into cold steppes~ 45,000 years ago at Ilsenhöhle in Ranis, Germany. Nature ecology & evolution: 1-11.

Peral, M., Marchegiano, M., Verheyden, S., Goderis, S., Van Helden, T., Vanhaecke, F., Van Acker, T., Jia, X., Cheng, H. and Fiebig, J., 2024. A new insight of the MIS 3 Dansgaard-Oeschger climate oscillations in western Europe from the study of a Belgium isotopically equilibrated speleothem. Quaternary Science Reviews, 329: 108564.

Pérez-Mejías, C., Moreno, A., Sancho, C., Martín-García, R., Spötl, C., Cacho, I., Cheng, H. and Edwards, R.L., 2019. Orbital-to-millennial scale climate variability during Marine Isotope Stages 5 to 3 in northeast Iberia. Quaternary Science Reviews, 224: 105946.

Pons-Branchu, E., Hamelin, B., Losson, B., Jaillet, S. and Brulhet, J., 2010. Speleothem evidence of warm episodes in northeast France during Marine Oxygen Isotope Stage 3 and implications for permafrost distribution in northern Europe. Quaternary Research, 74(2): 246-251.

Rasmussen, S.O., Bigler, M., Blockley, S.P., Blunier, T., Buchardt, S.L., Clausen, H.B., Cvijanovic, I., Dahl-Jensen, D., Johnsen, S.J., Fischer, H., Gkinis, V., Guillevic, M., Hoek, W.Z., Lowe, J.J., Pedro, J.B., Popp, T., Seierstad, I.K., Steffensen, J.P., Svensson, A.M., Vallelonga, P., Vinther, B.M., Walker, M.J.C., Wheatley, J.J. and Winstrup, M., 2014. A stratigraphic framework for abrupt climatic changes during the Last Glacial period based on three synchronized Greenland ice-core records: refining and extending the INTIMATE event stratigraphy. Quaternary Science Reviews, 106: 14-28.

Riechelmann, D.F., Albert, J., Britzius, S., Krebsbach, F., Scholz, D., Schenk, F., Jochum, K.P. and Sirocko, F., 2023. Bioproductivity and vegetation changes documented in Eifel maar lake sediments (western Germany) compared with speleothem growth indicating three warm phases during the last glacial cycle. Quaternary International, 673: 1-17.

Siddall, M., Rohling, E.J., Thompson, W.G. and Waelbroeck, C., 2008. Marine isotope stage 3 sea level fluctuations: Data synthesis and new outlook. Reviews of Geophysics, 46(4).

Sirocko, F., Albert, J., Britzius, S., Dreher, F., Martínez-García, A., Dosseto, A., Burger, J., Terberger, T. and Haug, G., 2022. Thresholds for the presence of glacial megafauna in central Europe during the last 60,000 years. Scientific reports, 12(1): 20055.

Sirocko, F., Knapp, H., Dreher, F., Förster, M., Albert, J., Brunck, H., Veres, D., Dietrich, S., Zech, M. and Hambach, U., 2016. The ELSA-Vegetation-Stack: Reconstruction of Landscape Evolution Zones (LEZ) from laminated Eifel maar sediments of the last 60,000 years. Global and Planetary Change, 142: 108-135.

Smith, F.H., Janković, I. and Karavanić, I., 2005. The assimilation model, modern human origins in Europe, and the extinction of Neandertals. Quaternary International, 137(1): 7-19.

Spötl, C. and Mangini, A., 2002. Stalagmite from the Austrian Alps reveals Dansgaard–Oeschger events during isotope stage 3:: Implications for the absolute chronology of Greenland ice cores. Earth and Planetary Science Letters, 203(1): 507-518.

Staubwasser, M., Drăguşin, V., Onac, B.P., Assonov, S., Ersek, V., Hoffmann, D.L. and Veres, D., 2018. Impact of climate change on the transition of Neanderthals to modern humans in Europe. Proceedings of the National Academy of Sciences, 115(37): 9116-9121.

Stoll, H., Mendez-Vicente, A., Gonzalez-Lemos, S., Moreno, A., Cacho, I., Cheng, H. and Edwards, R.L., 2015. Interpretation of orbital scale variability in mid-latitude speleothem δ18O: Significance of growth rate controlled kinetic fractionation effects. Quaternary Science Reviews, 127: 215-228.

Team, R.C., 2023. R Development Core Team R: A Language and Environment for Statistical Computing 2023. R Core Team: Vienna, Austria.

Timmermann, A., 2020. Quantifying the potential causes of Neanderthal extinction: Abrupt climate change versus competition and interbreeding. Quaternary Science Reviews, 238: 106331.

Tremaine, D.M., Froelich, P.N. and Wang, Y., 2011. Speleothem calcite farmed in situ: Modern calibration of $\delta^{18}O$ and $\delta^{13}C$ paleoclimate proxies in a continuously-monitored natural cave system. Geochimica et Cosmochimica Acta, 75(17): 4929-4950.

Vettoretti, G., Ditlevsen, P., Jochum, M. and Rasmussen, S.O., 2022. Atmospheric CO_2 control of spontaneous millennial-scale ice age climate oscillations. Nature Geoscience, 15(4): 300-306.

Voelker, A.H., 2002. Global distribution of centennial-scale records for Marine Isotope Stage (MIS) 3: a database. Quaternary Science Reviews, 21(10): 1185-1212.

Wang, Y.-J., Cheng, H., Edwards, R.L., An, Z., Wu, J., Shen, C.-C. and Dorale, J.A., 2001. A high-resolution absolute-dated late Pleistocene monsoon record from Hulu Cave, China. Science, 294(5550): 2345-2348.

Weber, K., Weber, M., Menneken, M., Kral, A.G., Mertz-Kraus, R., Geisler, T., Vogl, J. and Tütken, T., 2021. Diagenetic stability of non-traditional stable isotope systems (Ca, Sr, Mg, Zn) in teeth–An in-vitro alteration experiment of biogenic apatite in isotopically enriched tracer solution. Chemical Geology, 572: 120196.

Weber, M., Scholz, D., Schröder-Ritzrau, A., Deininger, M., Spötl, C., Lugli, F., Mertz-Kraus, R., Jochum, K.P., Fohlmeister, J., Stumpf, C.F. and Riechelmann, D.F.C., 2018. Evidence of warm and humid interstadials in central Europe during early MIS 3 revealed by a multi-proxy speleothem record. Quaternary Science Reviews, 200: 276-286.

Wimpenny, J., Colla, C.A., Yin, Q.-Z., Rustad, J.R. and Casey, W.H., 2014. Investigating the behaviour of Mg isotopes during the formation of clay minerals. Geochimica et Cosmochimica Acta, 128: 178-194.

Supplementary Material for

The last glacial period in Central Europe – climatic implications recorded by three highly sensitive speleothems from Bleßberg Cave

paper in preparation

4.8 Supplementary Material

Cave site

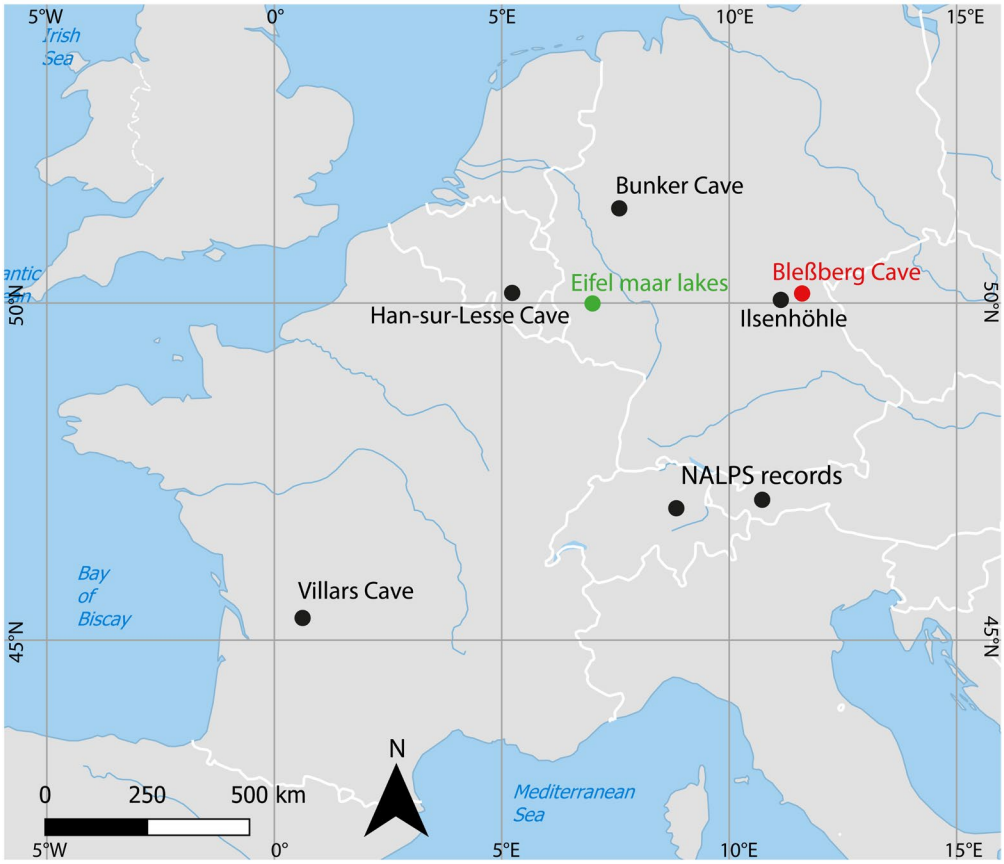

Fig. S4.1: Map of Central Europe showing the cave site and location of other records used.

Samples

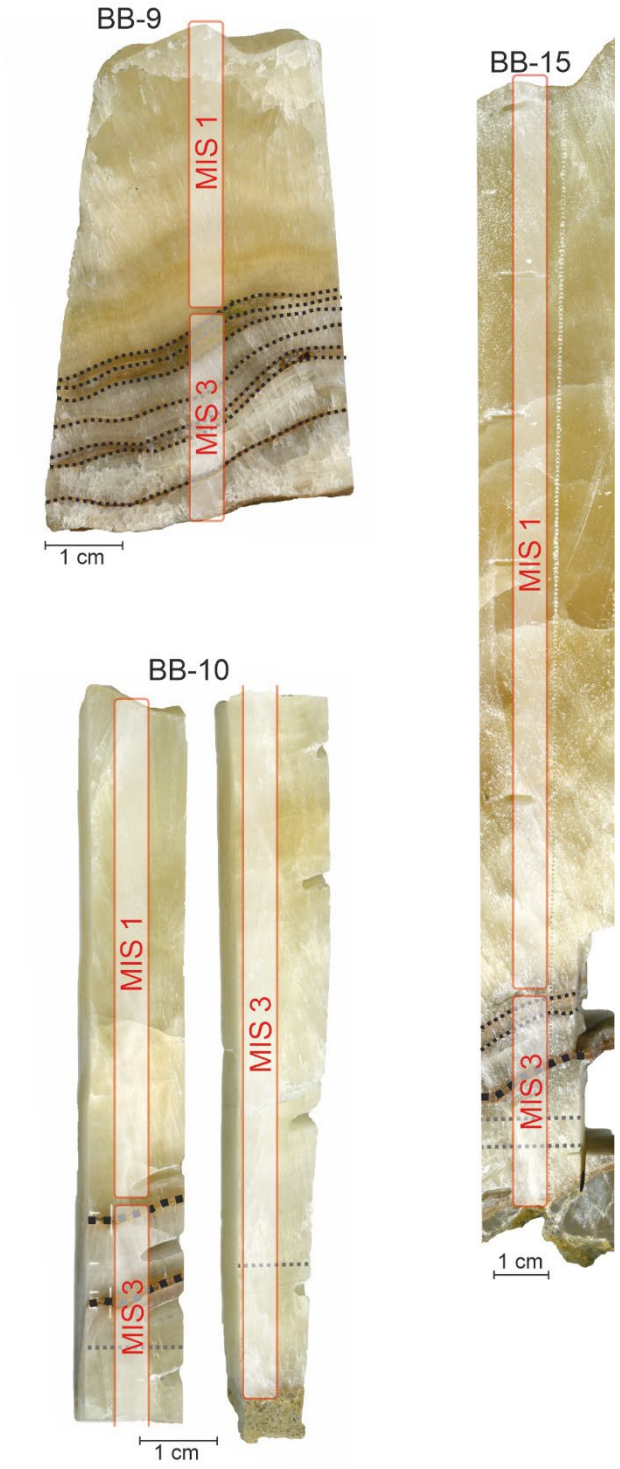

Fig. S4.2: Scans of samples BB-9, BB-10 and BB-15. MIS 1 and MIS 3 parts are indicated by the boxes. Dotted lines indicate growth stops, where black shows growth stops, which are visually detectable and grey lines indicate growth stops, which were defined though the ^{230}Th/U-ages and resulting age models. The growth stops identified during MIS 3 were determined based on the initial ^{238}U/^{234}U activity ratios (see Klose et al., in prep for details).

Establishing the main age/depth axis

Flowstones are typically characterised by episodic growth patterns, which often results in very narrow growth layers. Additionally, due to their growth from a thin, flowing water film, instead of a dripping point as for instance stalagmites, the growth layers tend to have a variable thickness and uneven surface. Therefore, flowstones are often considered less suitable for paleoclimate reconstructions because the sampling is challenging.

The main age/depth axis (Fig. S4.3, indicated in red) is the axis where the stable isotopes and trace elements were measured. All the remaining proxies, as well as the ^{230}Th/U-ages were sampled with a certain distance from this axis. Due to the growth characteristics the DFTs for the same growth layer but measured further away (Fig. S4.3, indicated in blue) from this main age/depth axis, can be highly variable. Therefore, all ^{230}Th/U-ages and proxies were projected on the main axis as visualised in Figure S4.3 relative to their position in the growth layer under consideration, that the thickness of layers can vary.

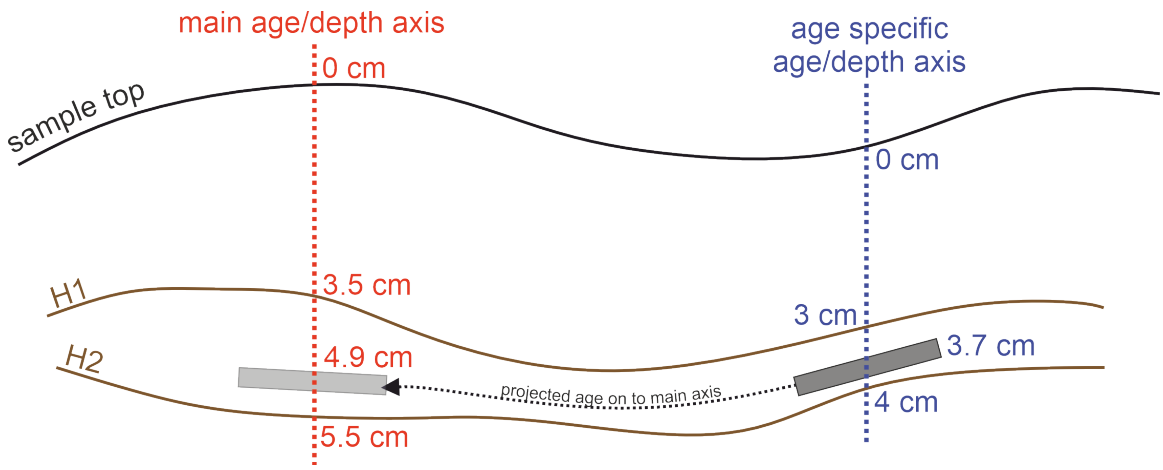

Fig. S4.3: Schematic illustration on the establishment of the main age/depth axis. This method was applied on all samples and all proxies, which were not sampled on the main axis. H1 and H2 indicate two hiatuses, i.e., two growth stops.

Calculation and comparison of the Fluid inclusion temperatures

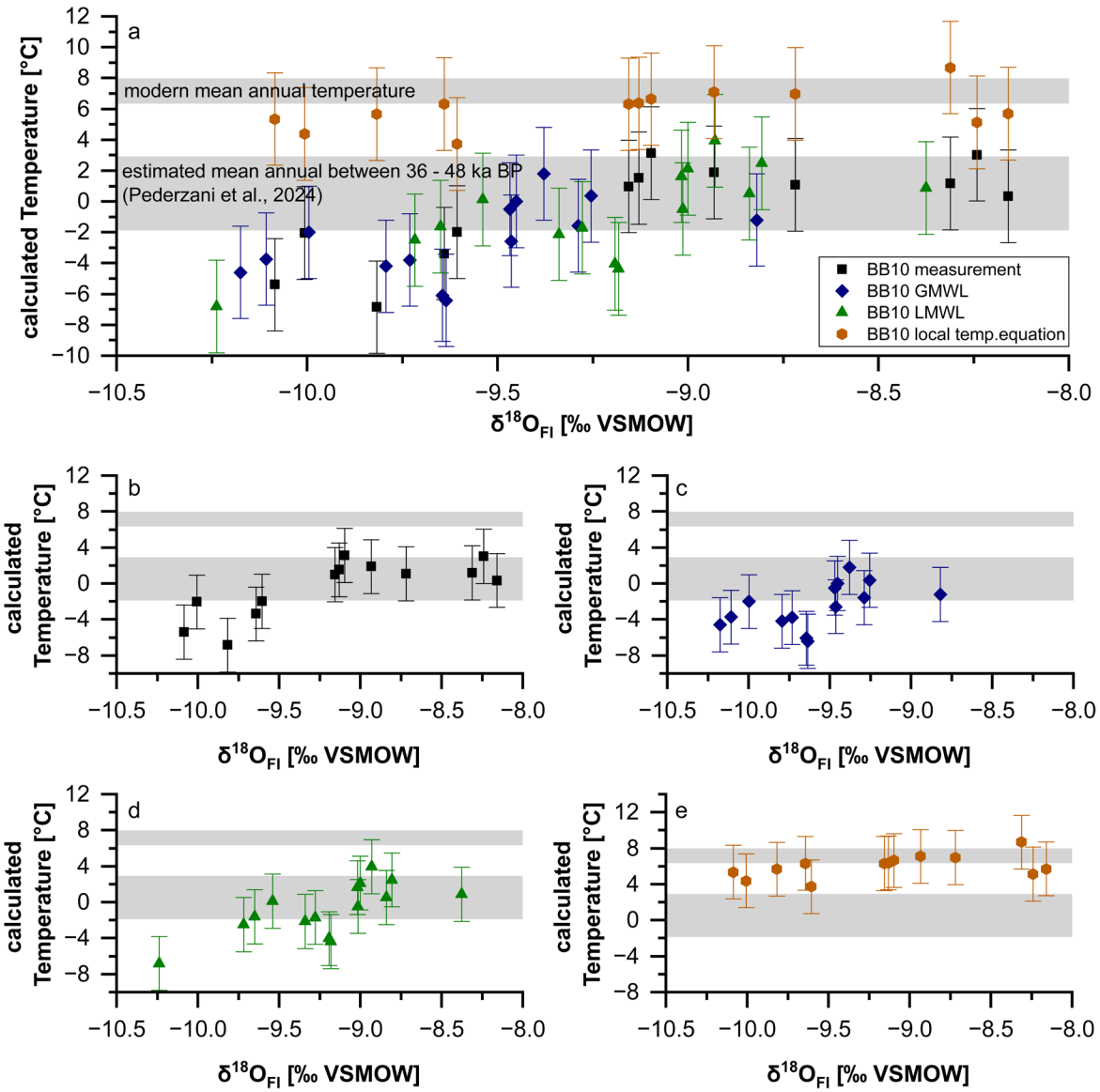

Fig. S4.4: Comparison of calculated temperatures relative to $\delta^{18}O_{FI}$ for MIS 3. We compare four approaches: (b) estimates based on the measured $\delta^{18}O$ values of fluid inclusions and the speleothem carbonate using the cave-specific water–calcite oxygen isotope fractionation of (Tremaine et al., 2011); (c) estimates based on measured $\delta^{2}H$ values projected to fit on the GMWL, and (d) estimates based on the LMWL and both shifted values were used to estimate a potentially more precise $\delta^{18}O$ value, which was then used for the calculations based on Tremaine et al. (2011). For the last approach (e), a modern local $\delta^{2}H/T$ relationship was established and used for the calculations. Modern mean annual temperature refers to the average temperature in Germany at present, and the estimated mean annual temperature between 36 ka and 48 ka BP is based on the study by Pederzani et al. (2024). Fluid inclusion data were obtained from sample BB-10.

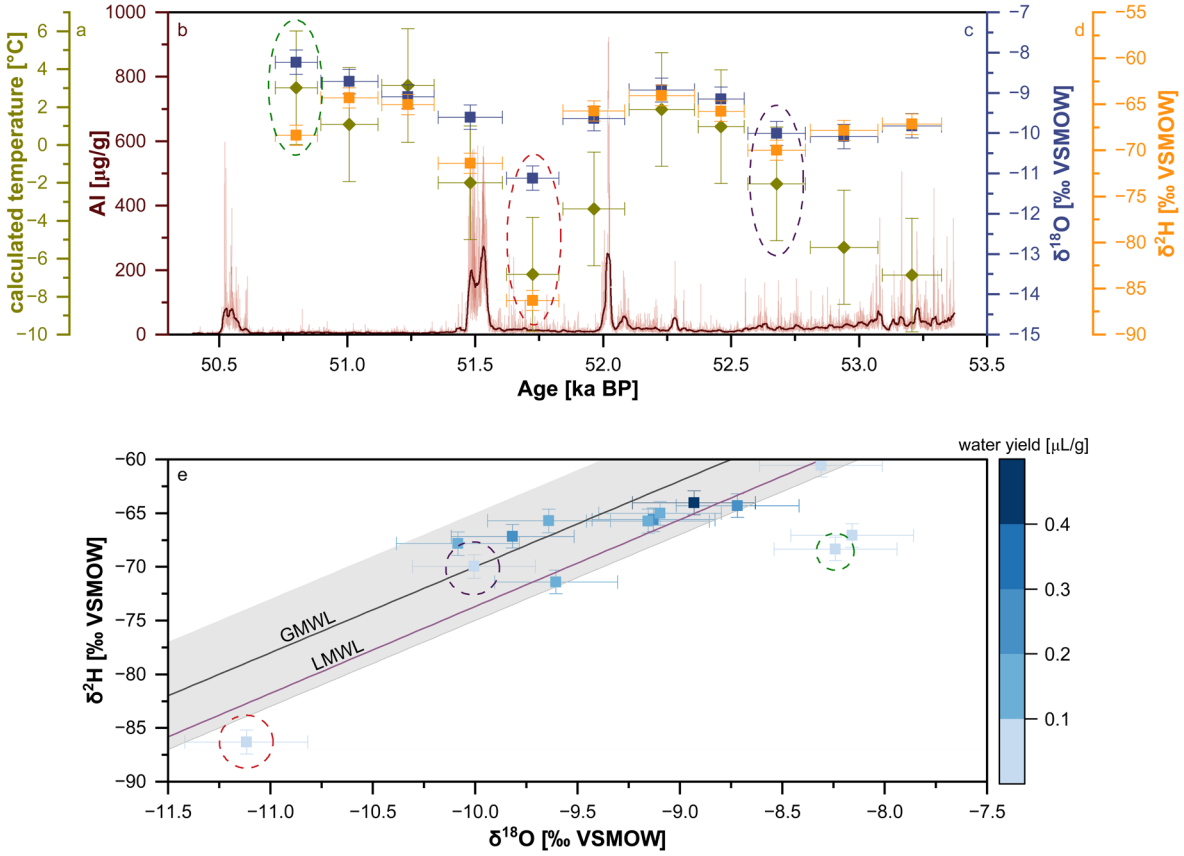

Fig. S4.5: Overview of estimated temperatures, fluid inclusion water isotopes, and Al concentration during DO14, and all fluid inclusion $\delta^{18}O$ and $\delta^{2}H$ ratios observed during MIS 3. All measurements are based on sample BB-10. Estimated temperatures in a are based on measured fluid inclusion $\delta^{18}O$ (c and d, see Fig. S4.2 for details). Highest Al concentrations (b) align with two fluid inclusion/temperature data points (at ca. 52 ka and 51.5 ka BP), which might result in an unreliable measurement and therefore calculated temperature. Another reason for unreliable data in fluid inclusions is shown in e. Measurements with < 0.1 µL/g water yield were discarded because these low water concentrations are at the limit of the method. Those data points often plot far off the GMWL or LMWL. The three data points with < 0.1 µL/g water yield are indicated by circles in the upper graph.

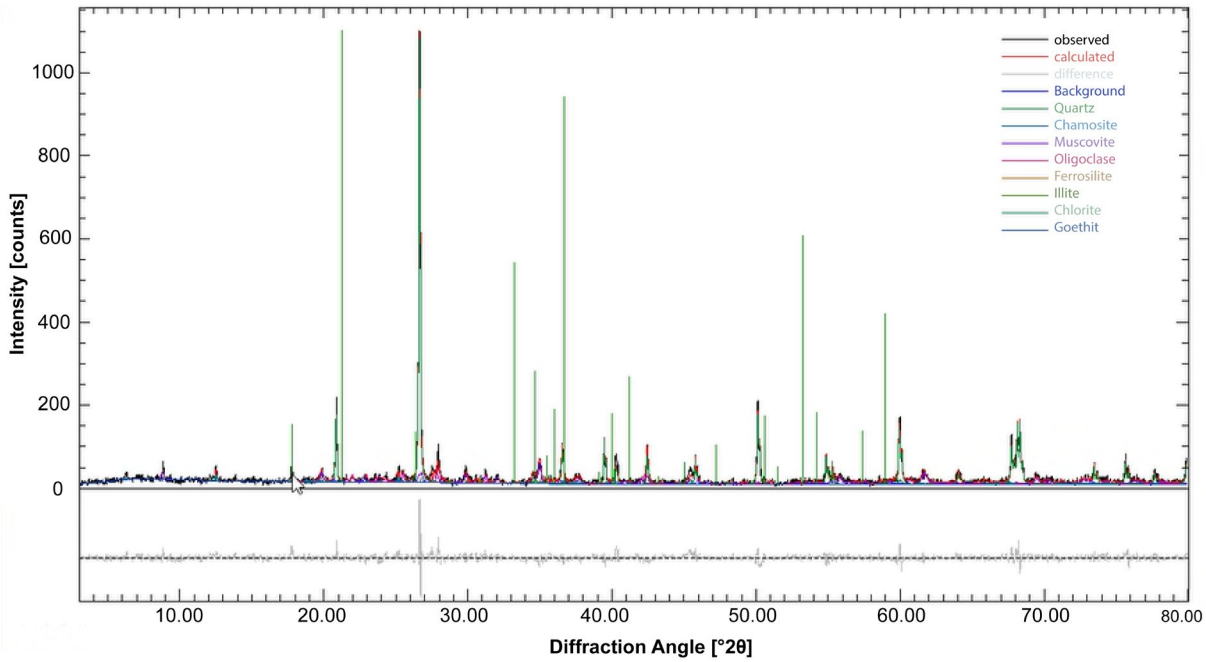

Fig. S4.6: XRD spectrum of soil sample. The peaks are listed on the side.

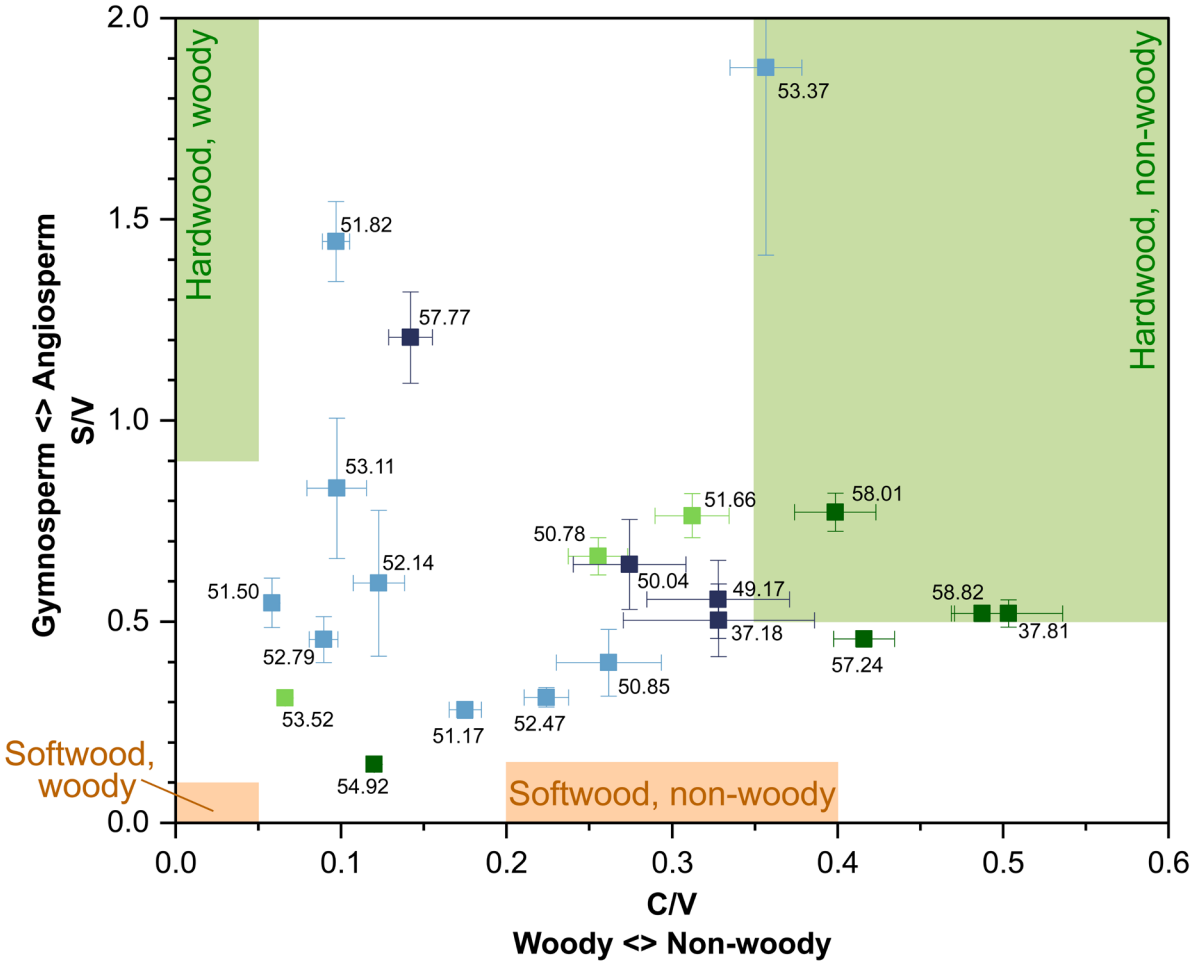

Fig. S4.7: S/V and C/V ratios of lignin oxidation products in sample BB-10 (green) and BB-15 (blue) during MIS 3. Vegetation types are indicated by shaded boxes, based on the experimental differentiation of (Hedges and Mann, 1979). Numbers below data points indicate mean sample age. Data points during DO14 are in a lighter shade of colour.

Chapter 5: Manuscript III

A high-resolution multi-proxy speleothem record covering the last 14 ka – the progression of Termination I and the Holocene in Central Europe

paper in preparation

Abstract

The Holocene and Termination I are phases of the paleoclimate that have been intensively studied over the course of last decades. Even though the general climate of the last 15 ka is relatively well understood, short-term climate oscillations during this time period and internal structures of centennial- to millennial-scale events like the Younger Dryas (12.8 – 11.7 ka BP) are still a matter of ongoing debate.

Here we present a precisely dated multi-proxy speleothem record from Bleßberg Cave, Germany covering the Bølling/Allerød, Younger Dryas and the Holocene. We observe several cold short-term climate events like the Older Dryas and Intra–Allerød cold period as events with enhanced microbial activity in the soil and increases in vegetation density despite reported temperature decreases in the North Atlantic. We furthermore find potential evidence for a two-phased Younger Dryas in Central Europe and a seasonal influence on the discussed discrepancy that is the Holocene temperature conundrum and Holocene thermal maximum evident in proxy data but not in climate models.

5.1 Introduction

The transition (Termination I, ca 15 – 10 ka BP) from the last glacial period to the recent interglacial was characterised by several climate oscillations with varying extent and significant effects on both marine and terrestrial environments (Ammann et al., 1994; Brauer et al., 2000; Hughen et al., 1996; Karpuz and Jansen, 1992; Litt et al., 2003; Lowe et al., 1994). The climate improved after the last cold event of the late Glacial period (Heinrich 1). This led to the Bølling/Allerød interstadial (ca. 14.7 – 2.8 ka BP), followed by the Younger Dryas cold phase (YD, 12.8 ka (Reinig et al., 2021) – 11.7 ka BP) and finally, the transition to the Holocene (11.7 ka BP – recent). Over the last decades, a great effort has been put into investigating these past climate changes and climatic events, with the YD being one of the most extensively studied events. Although significant improvement regarding its timing and the question of a globally synchronous onset has been made recently (Reinig et al., 2021), the internal structure of this event remains relatively poorly constrained (Zhang et al., 2022). For instance, proxy records from continental Europe revealed a rapid increase in temperature in the middle of the event, potentially caused by a northward shift of the westerlies and interpreted as a strengthening of the Atlantic Meridional Overturning Circulation (AMOC) (Lane et al., 2013).

The trigger of the YD is most likely the influx of meltwater from the Laurentide ice sheet into the North Atlantic, which resulted in an abrupt weakening of the AMOC and subsequently a cooling in the North Atlantic region (e.g. Schenk et al., 2018). The cooling of the North Atlantic was accompanied by an extension of sea ice (Denton et al., 2005; Lowe et al., 1994; Steffensen et al., 2008), southwards shifts in Northern hemisphere atmospheric circulations (Denton et al., 2010), drier conditions (Björck, 2007; Muschitiello et al., 2015; Rach et al., 2014) and generally more continental climate conditions (Schenk et al., 2018) in the North Atlantic realm. Evidence for the YD in Central Europe stems primarily from lake sediment records indicating cold mean annual air temperatures from $\delta^{18}O$ records (e.g. Lauterbach et al., 2011; Van Raden et al., 2013). Other studies also revealed the previously mentioned regaining strength of the AMOC with an ongoing progression of the YD (Bakke et al., 2009; Elmore and Wright, 2011) resulting in a northward shift of the oceanic polar front around 12.3 ka BP (Pearce et al., 2013) and two phases of the YD evident in European lake sediment records (Bakke et al., 2009; Lane et al., 2013; Neugebauer et al., 2012).

Another more recent topic of debate is the so-called Holocene temperature conundrum, which describes the unresolved disagreement between proxy-based climate reconstructions and climate model simulations of the Holocene (Büntgen, 2022; Cartapanis et al., 2022; Essell et al., 2024; Hertzberg, 2021; Thompson et al., 2022). While proxy records hint towards a Holocene thermal maximum between 10.0 – 5.5 ka BP and a peak in temperature (2 – 3 °C warmer than today) around 7 ka BP (Wanner, 2021), climate models show no such thermal maximum (Kaufman and Broadman, 2023). This might be caused by the fact that climate models reconstruct mean annual temperatures, while the proxy-based reconstructions primarily stem from archives and proxy records, which are biased towards the warm season (Hertzberg, 2021), such as pollen records (Rehfeld et al., 2016) or sea surface temperatures (Bova et al., 2021). Two main potential hypotheses have been proposed to address this topic: (i) the Holocene thermal maximum is only a warm seasonal climate trend, driven by high latitudinal summer insolation (Bova et al., 2021; Wanner, 2021) or (ii) most climate models do not include the sufficient climate forcing, such as vegetation changes. This highlights the need for well-dated proxy records, which represent annual climate.

Speleothems provide a great opportunity for reconstructing annual climate and have been established as a valuable, terrestrial source for paleoclimate reconstructions in the past decades. They can be dated very precisely using U-series disequilibrium methods (Richards and Dorale, 2003; Scholz and Hoffmann, 2008) and provide a wide range of environmental and climatic proxies (Fairchild and Baker, 2012), allowing for multi-proxy analyses. Here we present three precisely dated multi-proxy speleothem records from Bleßberg Cave, Germany. All three samples grew during phases of the Last Glacial, covering the Bølling/Allerød, one sample the YD itself, and all samples the early to mid-Holocene. Previous studies (Breitenbach et al., 2019) focusing on two mid- to late-Holocene speleothem samples from the same cave allow us to generate a continuous paleoclimate record from the late Glacial (ca. 14.5 ka BP) to recent (0.6 ka BP), which will enhance our understanding of the climate variability of Central Europe during this period.

5.2 Cave setting and sample description

5.2.1 Bleßberg Cave

Bleßberg Cave is located at approximately 500 m above sea level on the southern edge of the Thuringian schist mountains. The cave system was formed in Triassic marly limestones and can be found near the town of Eisfeld in Germany, at coordinates 50°25'28'' N and 11°01'13'' E. The cave runs in an NW-SE direction and is covered by 12 to 50 m of marly limestone from the Lower and Middle Muschelkalk periods. The vegetation surrounding the cave is mainly a mix of anthropogenically modified farmland and mixed deciduous and pine forests on the uphill areas (Breitenbach et al., 2019). The modern climate in the region of Bleßberg Cave falls under the Cfb classification in the Köppen-Geiger system. The cave was discovered for the first time in 2008 due to railway construction activities that caused the previously closed cave system to be disrupted. Although the ventilation of the cave is potentially affected by a stream that flows through its main passage, the cave atmosphere is considered to be relatively stable (Breitenbach et al., 2019).

5.2.2 Speleothem samples

Three flowstone samples were investigated during this study: BB-9, BB-10, and BB-15 (Fig. S5.1). All three samples grew during parts of MIS 1 and MIS 3. The MIS 3 part of the samples has been discussed in detail in Klose et al., 2024 (in review and prep). BB-9 is a 6.4 cm long flowstone and consists of beige calcite in the upper part (upper 3.4 cm), which grew during MIS 1 and shows strongly episodic growth disrupted by detrital layers and several growth stops in the lower, more whitish MIS 3 part of the sample. Sample BB-10 is a flowstone that measures 18.3 cm in length. It is made up of relatively light beige calcite that is interrupted by two distinctive hiatuses located at approximately 6.8 cm DFT and 8 cm DFT. The calcite between these two hiatuses is white and clear in colour. The upper part of the sample, up to the first hiatus from the top, covers MIS 1, while the remaining bottom part covers MIS 3. Sample BB-15 is a flowstone that measures approximately 21 cm in length. Three visible hiatuses can be observed at depths of approximately 17 cm, 17.4 cm, and 18.3 cm DFT. The upper part of the sample consists of beige calcite, while the area between the first two hiatuses, counting from the top, is composed of more whitish calcite

that is similar in appearance to BB-10. The lower portion of the sample once again shows darker, more beige calcite.

5.3 Methods

5.3.1 ^{230}Th/U-dating

The ^{230}Th/U-ages for all samples were determined at the Johannes Gutenberg University and the Max Planck Institute for Chemistry (MPIC) in Mainz. In total 20 ^{230}Th/U-ages were determined, 8 for sample BB-9, 6 for sample BB-10 and 6 for sample BB-15. 18 samples were drilled with a handheld dental drill and the samples were subsequently prepared for ^{230}Th/U-dating using a multi-collector inductively coupled mass spectrometer (MC-ICP-MS) using slightly different approaches. The remaining 2 ^{230}Th/U-ages were obtained by in-situ analyses using an MC-ICP-MS coupled to an ESI New Wave NWR 193 nm ArF excimer laser ablation system, the procedure is in detail described in Klose et al., 2014 (in prep).

For the analyses (n = 5) performed at the MPIC approximately 0.3 g were used. Subsequently, U and Th were dissolved in 7N HNO_3, mixed with a ^{229}Th-^{235}U-^{236}U spike (see Gibert et al., 2016) and chemically separated by ion-exchange columns chemistry following the procedure as described in (Hoffmann, 2008) with the adjustments as stated in (Yang et al., 2015). U and Th were measured separately using a standard-bracketing procedure to account for mass fractionation, ion counter gain and tailing. The measurement followed the procedure as described in Obert et al. (2016). A CETAC Aridus II was used as the desolvating nebulizer system connected to Nu Plasma MC-ICP-MS.

For the adjusted analyses (n = 13) at the Johannes Gutenberg University only approximately 50 mg of sample material was used. U and Th were also dissolved in 7N HNO_3, mixed with a ^{229}Th-^{235}U-^{236}U spike (see Klose et al., 2024 (in prep) for calibration details) and chemically separated by ion-exchange columns chemistry, but followed the procedure as described in Klose et al., 2024 (in prep). Again, a standard-bracketing procedure was used (see Klose et al., 2024 (in prep) for details on calibrations and the measurement). The analysis used an Elemental Scientific Apex Omega HF introduction system coupled to a Thermo Fischer Scientific Neptune Plus MC-ICP-MS.

All of the resulting ages were used for the calculations of the age-depth relationship (Fig. 5.1) of the samples using the StalAge age-modelling algorithm (Scholz and Hoffmann, 2011).

5.3.2 Stable isotope analysis

High-resolution stable oxygen and carbon isotope values ($\delta^{18}O$ and $\delta^{13}C$) were obtained for all three flowstone samples and all results are reported relative to VPDB.

Sample BB-9 (n = 207) was analysed for stable isotopes with a resolution of 200 µm. The sampling was done at the GeoForschungsZentrum in Potsdam using a MicroMill device. A Finnigan MAT253 stable isotope mass spectrometer system by Thermo Fischer Scientific, connected to an automated carbonate-reaction device (KIEL IV), was used for the analysis. Quality control was ensured by using NBS19 and an internal reference material. The external precision for both stable isotope ratios is < 0.07 ‰ (1 σ).

The stable isotopes for sample BB-10 (n = 141) were sampled at 450 µm resolution. A MicroMill device was used for sampling (sample size of around 100 – 200 µg) and the analysis was performed at the MPIC in Mainz using a Thermo Delta V continuous flow isotope ratio mass spectrometer equipped with a Gasbench II. Quality control was ensured by using NBS19 and an internal lab $CaCO_3$ reference material. For both isotopes the external precision is < 0.11 ‰ (1 σ).

For sample BB-15 the samples (n = 216) were taken and measured at the Leibniz Institut für Angewandte Geophysik (LIAG) in Hannover. The sample resolution is 800 µm and the analysis was performed using a ThermoFinnigan Delta XP ratio mass spectrometer equipped with a Gasbench II. Due to remeasurements of the bottom MIS 3 part of the sample, parts of MIS 1 (16.50 – 16.59 cm DFT) were also remeasured. The samples (n = 33) were drilled in a 300 µm resolution using a MicroMill device and the analysis was done at the Max Planck Institute for Chemistry in Mainz and followed the same procedure as sample BB-10.

5.3.3 Trace element analysis

Trace element concentrations of Sr for samples BB-9 and -10 were determined by LA-ICP-MS. The samples were analysed at the Institute for Geosciences, Johannes Gutenberg University Mainz, using an ESI New Wave 193 nm ArF Excimer laser system coupled to an Agilent 7500ce ICP-MS. The used laser parameters are the following: a rectangular spot size of 130 x 50 µm, a transition rate of 10 µm/s, and a laser repetition rate of 10 Hz. These values resulted in a fluence of 3.5 J/cm^2. We performed multiple analyses on a NIST SRM 610 and other quality control materials (NIST SRM 612, BCR-2G, and MACS3) for calibration purposes. ^{43}Ca was used as an internal reference for all analyses and data evaluation was performed offline following the procedure described in (Mischel et al., 2017). Both samples were analysed using a continuous line scan method, preceded by a pre-ablation process.

5.3.4 Fluid inclusion isotope analysis

Fluid inclusions were analysed at the MPIC in Mainz for sample BB-10 (n = 11) by measuring $\delta^{18}O$ and $\delta^{2}H$. The sample was divided into approximately 1 g pieces using a Dremel Microdrill with a 38 mm diameter diamond-covered circular saw. The cuts were made parallel to the growth axis of the sample. The Fluid inclusions were measured using a crusher unit connected to a Picarro L2140i cavity ring-down spectrometer (CRDS). The measurement followed the procedure as described in (De Graaf et al., 2020) and the isotope data were corrected using a two-point calibration based on two in-house standards (MzTap2022 ($\delta^{18}O$ value of -8.7 ‰ and $\delta^{2}H$ value of -62.96 ‰) and Kona2022 ($\delta^{18}O$ value of 1.53 ‰ and $\delta^{2}H$ values of 3.48 ‰). The 1σ precisions of the analyses are based on the water injections of the standards into the system and aim better than 0.3 ‰ for the $\delta^{18}O$ values and 1.0 ‰ for the $\delta^{2}H$ values (De Graaf et al., 2020). The results are presented as delta values expressed relative to VSMOW.

Paleotemperatures were calculated based on the $\delta^{18}O$ of the fluid inclusions and the $CaCO_3$ of the speleothem according to the cave-specific water–calcite oxygen isotope equilibrium fractionation presented in (Tremaine et al., 2011).

5.3.5 Calcium isotopes

Calcium isotope ratios were analysed for samples BB-9 (n = 9) and -10 (n = 7) at the Johannes Gutenberg University in Mainz using a Neptune Plus MC-ICP-MS equipped with an Elemental Scientific Apex Omega HF desolvator system following the method described in Weber et al. (2021). Prior to analysis ca. 1 mg of sample material was purified using an automated prepFAST-MC (ESI Elemental Scientific) system. Approximately 1 mg of sample material was purified using the automated *prep*FAST-MC (ESI Elemental Scientific) system. For the analysis, the Ca fraction was subsequently dried down and re-dissolved in distilled 0.5 mol/L HNO_3. A standard bracketing approach was used to correct for mass dependent fractionation with the samples and reference material being within 10 % of the concentration range of 2 mg/L. The results are presented as delta values ($\delta^{44/42}Ca$) expressed relative to NIST 915a. For quality control five additional reference materials (IAPSO, JCp, JCt, MACS3, NanoSr) were analysed control within the same analytical sessions.

5.3.6 Strontium isotopes

Strontium isotope ratios were analysed using solution MC-ICP-MS and LA-MC-ICP-MS for samples BB-9 (solution-based n = 2, LA-based n = 7) and BB-10 (solution-based n = 1, LA-based n = 9) at the Johannes Gutenberg University in Mainz. For the solution-based analysis a Neptune Plus MC-ICP-MS equipped with an Elemental Scientific Apex Omega HF desolvator system was used. For the LA-MC-ICP-MS the same Neptune Plus MC-ICP-MS setup was used coupled to an ArF Excimer 193 nm laser system (ESI NWR193). The methods, and sample preparation for the solution-based analysis, followed the procedures as described in (Weber et al., 2020) and (Weber et al., 2017). The results are provided as $^{87}Sr/^{86}Sr$ ratios corrected for NIST SRM 987 ratio of 0.710248 (McArthur et al., 2001) for the solution-based analyses and for JCp-1 ratio of 0.709164 (Weber et al., 2018) for the LA-based analyses.

5.3.7 Lignin oxidation products

The lignin oxidation products (LOPs) of samples BB-10 (n = 6) and -15 (n = 61) were analysed at the Johannes at the Johannes Gutenberg University in Mainz and followed the procedure as described in (Homann et al., 2022). For the analysis an ultra-high performance liquid chromatography (UHPLC) system coupled to a high-resolution mass spectrometer (HRMS) was used. The samples for BB-10 were cut using a diamond band saw and a precision diamond wire saw for BB-15. The sample sizes were between 1 – 2 g.

5.4 Results

5.4.1 ^{230}Th/U-dating and age modelling

The results of the ^{230}Th/U-dating are presented in Table 5.1. The ^{230}Th/U-ages as presented in the following only refer to the MIS 1 part of the samples. The MIS 3 parts of all three samples have been previously published in Klose et al. (in prep).

The ^{238}U concentrations of the samples are relatively similar and average at 0.476 ± 0.003 µg/g, with the concentrations generally increasing with increasing age. The ^{232}Th concentrations, which can be used as an indicator for the degree of detrital contamination and therefore potential growth stops, have an average of 0.726 ± 0.006 ng/g. Only five samples show slightly elevated ^{232}Th levels between 1.19 ± 0.01 ng/g and 2.27 ± 0.01 ng/g. Those detrital concentrations do not indicate growth stops, however, based on the ^{230}Th/U-ages and resulting age models (Fig. 5.1) one undetected growth stop was identified for samples BB-9 (at 0.8 cm DFT) and BB-10 (at 4.1 cm DFT) respectively.

Based on the age models the first growth phase of sample BB-9 (in the following referred to as growth phase 9.1) started at 14.5 ± 0.2 ka BP and ended at 13.24 ± 0.5 ka BP, the second growth (in the following referred to as growth phase 9.2) phase started at 9.7 ± 0.3 ka BP and ended at 8.7 ± 0.2 ka BP. Resulting in a growth stop duration of ca. 4.8 ka. The first growth phase of ample BB-10 (in the following referred to as growth phase 3.1) started at 14.0 ± 0.1 ka BP and ended at 13.84 ± 0.06 ka BP, the second growth (in the following referred to as growth phase 3.2) phase started at 11.9 ± 0.3 ka BP and ended at 6.64 ± 0.03 ka BP. This results in a disruption of growth of ca. 2.1 ka. BB-15

shows one continuous growth phase, which started at 14.4 ± 0.3 ka BP and ended at 7.1 ± 0.8 ka BP.

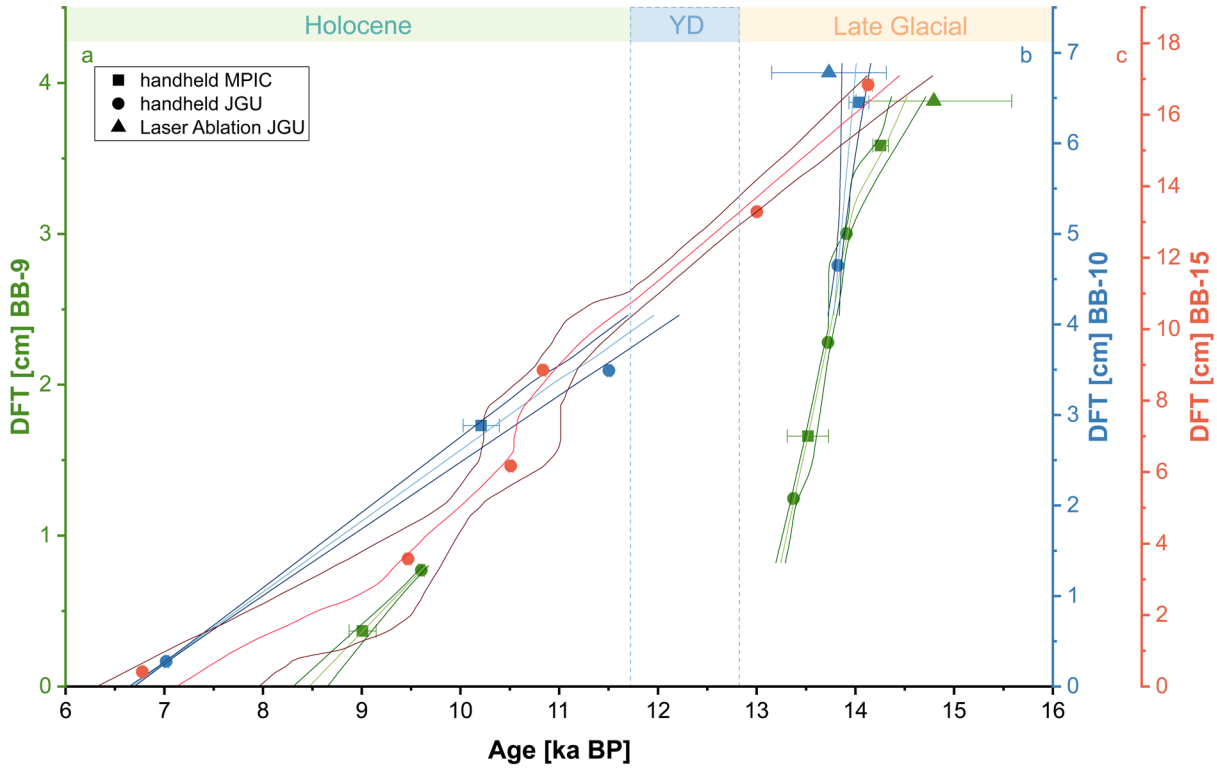

Fig. 5.1: Age models of sample BB-9, BB-10 and BB-15. a the age model of sample BB-9 is shown in green, b the age model for sample BB-10 is shown in yellow and c BB-15 in red. The individual ^{230}Th/U-age symbols are given in the legend. The 95%-confidence intervals are indicated by the darker line.

Table 5.1: Results of the ^{230}Th/U-dating. Activity ratios ate indicated by parentheses. Asterisks (*) indicate samples measured with the MPIC setup.

Sample ID	DFT [cm]	^{238}U [µg/g]	^{232}Th [ng/g]	(^{234}U/^{238}U)	(^{230}Th/^{238}U)	(^{234}U/^{238}U)$_{initial}$	uncorrected age [ka BP]	corrected age [ka BP]
BB-9								
BB9-1*	0.37	0.4531 ± 0.0027	0.1029 ± 0.0025	2.8860 ± 0.0058	0.2322 ± 0.0033	2.9350 ± 0.0057	9.02 ± 0.13	9.01 ± 0.14
JK129	0.77	0.2829 ± 0.0026	0.4384 ± 0.0041	2.9445 ± 0.0011	0.25227 ± 0.00072	2.9984 ± 0.0011	9.619 ± 0.028	9.604 ± 0.029
LL193	1.25	0.4498 ± 0.0028	0.07912 ± 0.00055	3.1351 ± 0.0010	0.36837 ± 0.00076	3.2177 ± 0.0011	13.376 ± 0.029	13.374 ± 0.030
BB9-Top*	1.67	0.4695 ± 0.0028	0.0752 ± 0.0096	3.2614 ± 0.0069	0.3868 ± 0.0056	3.3501 ± 0.0072	13.53 ± 0.21	13.52 ± 0.21
LL194	2.29	0.5261 ± 0.0033	0.3948 ± 0.0025	3.4155 ± 0.0010	0.41146 ± 0.00071	3.5114 ± 0.0010	13.731 ± 0.026	13.72 ± 0.025
LL195	3.02	0.4526 ± 0.0028	1.2918 ± 0.0081	3.3486 ± 0.0016	0.40855 ± 0.00091	3.4431 ± 0.0016	13.935 ± 0.032	13.912 ± 0.033
BB9-2*	3.6	0.5412 ± 0.0032	2.225 ± 0.022	3.5577 ± 0.0064	0.4438 ± 0.0022	3.6634 ± 0.0064	14.294 ± 0.079	14.256 ± 0.079
BB9-1 (LA)	3.88	na	na	3.631 ± 0.038	0.457 ± 0.024	3.747 ± 0.039	14.68 ± 0.79	14.87 ± 0.79
BB-10								
LL196	0.28	0.4931 ± 0.0030	0.2072 ± 0.0013	2.81287 ± 0.00091	0.17831 ± 0.00050	2.84953 ± 0.00090	7.026 ± 0.020	7.021 ± 0.020
BB10-Top*	2.88	0.4497 ± 0.0026	0.2474 ± 0.0072	3.1122 ± 0.0056	0.2829 ± 0.0050	3.1749 ± 0.0058	10.24 ± 0.19	10.21 ± 0.19
LL197	3.49	0.5350 ± 0.0032	1.3479 ± 0.0081	3.1594 ± 0.0012	0.32196 ± 0.00058	3.2312 ± 0.0012	11.534 ± 0.020	11.506 ± 0.022
JK 124	4.65	0.5401 ± 0.0037	1.1894 ± 0.0081	3.4862 ± 0.0012	0.42297 ± 0.00093	3.5857 ± 0.0012	13.843 ± 0.032	13.823 ± 0.032
BB10-1*	6.42	0.5452 ± 0.0037	1.055 ± 0.010	3.571 ± 0.013	0.4397 ± 0.0026	3.676 ± 0.013	14.08 ± 0.10	14.03 ± 0.10
BB10-1 (LA)	6.78	na	na	3.603 ± 0.023	0.434 ± 0.017	3.707 ± 0.023	13.32 ± 0.61	13.80 ± 0.58
BB-15								
SB1	0.3	0.5921 ± 0.0036	0.14581 ± 0.00090	2.80437 ± 0.00065	0.17187 ± 0.00028	2.83960 ± 0.00070	6.783 ± 0.012	6.780 ± 0.012
SB11	3.5	0.3919 ± 0.0024	0 .6643 ± 0.0040	2.9331 ± 0.0011	0.24805 ± 0.00072	2.9859 ± 0.0011	9.491 ± 0.028	9.470 ± 0.029
SB2	6.2	0.3695 ± 0.0022	0.2849 ± 0.0017	3.13856 ± 0.00079	0.29324 ± 0.00062	3.2034 ± 0.0008	10.518 ± 0.024	10.509 ± 0.023
SB12	8.9	0.5190 ± 0.0032	0.3532 ± 0.0022	3.20693 ± 0.00088	0.30855 ± 0.00070	3.27593 ± 0.00090	10.844 ± 0.026	10.837 ± 0.026
SB3	13.5	0.5219 ± 0.0032	0.5429 ± 0.0033	3.37238 ± 0.00074	0.38604 ± 0.00055	3.46157 ± 0.00080	13.014 ± 0.020	13.003 ± 0.020
SB4	17.2	0.3699 ± 0.0024	2.267 ± 0.015	3.5158 ± 0.0023	0.4359 ± 0.0011	3.6188 ± 0.0023	14.192 ± 0.036	14.131 ± 0.040

BP = before present, i.e., 1950 CE, LA = Laser Ablation, na = data is not available.

5.4.2 Stable isotopes and trace elements

The stable isotope values and the Sr and Ba trance element records are shown in Fig. 5.3. Please note that the dotted records in Fig. 5.3 stem from two previously published records from Bleßberg Cave (sample BB-1 and BB-3, (Breitenbach et al., 2019)) and are not part of this study.

The total range in the $\delta^{13}C$ values (Fig. 5.3 a) across the entire record is from ca. -9.9 ‰ at around 6.7 ka BP to ca. -3.5 ‰ at around 14.4 ka BP, resulting in an amplitude of ~ 6.2 ‰ and a decreasing trend towards more negative values from the late Glacial to the Holocene. The general trend is interrupted by a rapid increase from ca. -8.3 ‰ at around 12.5 ka BP to ca.-5.1 ‰ at around 12.3 ka BP evident in sample BB-15, which is the only sample with continuous growth during this time period coinciding with the YD. For the individual samples, the range in values is from ca. -3.9 to -8.7 ‰ for sample BB-9, from ca. -5.3 ‰ to -9.9 ‰ for sample BB-10 and from ca. -3.5 to -9.3 ‰ for sample BB-15.

The overall range of the $\delta^{18}O$ values (Fig. 5.3 b) is from ca. -7.1 ‰ at around 13.2 ka BP to ca. -4.1 ‰ at around 14.4 ka BP, resulting in an overall amplitude of ~ 3.1 ‰ and therefore a generally smaller amplitude than in the $\delta^{13}C$ record. An overall decreasing trend with decreasing age is visible, as in the $\delta^{13}C$ record. The trend, however, is more distinct during the late Glacial and YD until the beginning of the Holocene, i.e., from ca 14.5 until 11.7 ka BP. With the start of the Holocene, the values show a short increasing trend from approx. -6.8 to approx. -5.3 ‰ around 10.9 ka BP, bevor declining to a slow decreasing trend. The range of the individual samples is ca.-4.7 to -7.1 ‰ for sample BB-9, from ca. -5.4 to -6.8 ‰ for sample BB-10 and from ca. -4.1 to -7.2 ‰ for sample BB-15.

The Strontium concentrations across the entire record, as well as the individual range of sample BB-9 and -10, vary between ca. 500 and 7000 µg/g and are therefore generally high. During the late Glacial a rapid decrease from ca. 3000 to 1000 µg/g is evident between 4.5 to 13.7 ka BP, followed by a slow increase in concentration until the end of the growth phase. During the Holocene a long-term trend towards higher concentrations from ca. 1000 to 7000 µg/g is visible. The range of the Barium concentrations is ca. 90 to 10 µg/g for the entire record as well as the individual range of sample BB-10, the individual range for sample BB-9 is slightly smaller and only varies from 70 to 10 µg/g. The values are highest during the late Glacial part of the record and show a similar, but

reversed, trend as observed in the Sr record. At the end of the growth phase, the values reach the level of the Ba concentration of the modern host rock (13.3 µg/g (Klose et al., in prep)). No long-term trend is evident in the Ba record during the Holocene. The transition from YD to Holocene is characterised by a sharp increase from modern host rock level to ca. 40 µg/g. The remaining record shows only small term variations.

5.4.3 Ca and Sr isotopes

The $\delta^{44/42}$Ca values exhibit a variation between 0.21 ± 0.02 ‰ to 0.38 ± 0.02 ‰ throughout the entire record. The largest fluctuations occurred during the last glacial period, whereas the Holocene period only showed a range between 0.30 ± 0.03 ‰ to 0.38 ± 0.02 ‰, with small term trends. The values during the late Glacial first show an increase between the beginning of the growth phase around 14.4 ka BP until 14 ka BP, followed by a rapid decrease in value (from 0.32 ± 0.02 ‰ to 0.21 ± 0.02 ‰) within ~ 0.2 ka BP, between ca.14 ka BP to 13.8 ka BP. The remaining part of the growth phase is characterised by a slowly increasing trend of the $\delta^{44/42}$Ca values.

The $^{87}Sr/^{86}Sr$ ratios show a trend towards lower ratios, with a larger variation from the late Glacial to the Holocene with no significant variations. The late Glacial shows $^{87}Sr/^{86}Sr$

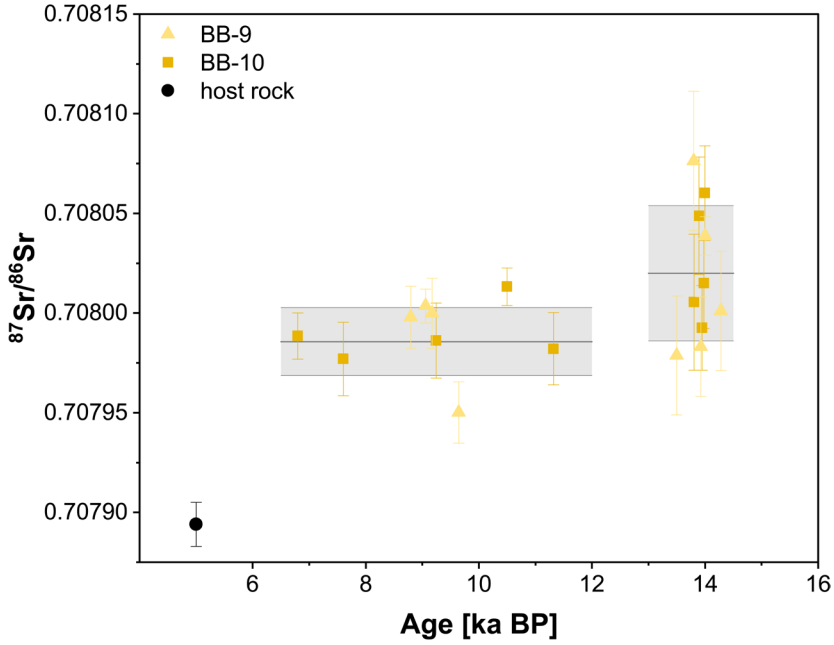

Fig. 5.2: Strontium isotope ratios of the late Glacial and early Holocene and a modern host rock sample. The symbols for the individual samples are given in the legend. The mean value for both phases is shown as a black line, the grey boxes indicate the 1σ SD.

ratios between 0.70798 ± 0.00003 and 0.70808 ± 0.00004 (mean value = 0.70802 ± 0.00004 SD 1σ), while the Holocene shows $^{87}Sr/^{86}Sr$ ratios between 0.70795 ± 0.00003 and 0.70800 ± 0.00003 (mean value = 0.70799 ± 0.00002 SD 1σ). The Triassic limestone at Bleßberg Cave has an $^{87}Sr/^{86}Sr$ ratio of 0.07894 ± 0.00001 (2σ, Fig. 5.2), which is in agreement with the Sr-isotope value expected from the seawater evolution curve (McArthur et al., 2001) and results in more radiogenic samples indicating a stronger soil influence.

5.4.4 Fluid inclusions and LOPs

The fluid inclusion samples from BB-10 have a water yield ranging from 0.03 to 0.27 µL/g (Fig. S5.2 d). However, the majority of the samples yielded less than 0.1 µL/g, which might affect the precision of the data. The fluid inclusion water isotope ranged from -11.2 ± 0.3 ‰ to -9.3 ± 0.3 ‰ in $\delta^{18}O$ and from -83.9 ± 1.1 ‰ to -63.2 ± 1.1 ‰ in $\delta^{2}H$ (Fig. S5.2 b and c). The data plots in agreement with the Global Meteoric Water Line (GMWL) and the site specific Local Meteoric Water Line (LMWL) (Fig. S5.2 d), indicating that the speleothem grew in thermal isotopic equilibrium and was not affected by re-equilibration. Therefore, the fluid inclusion data will reflect the precipitation reaching the cave (Dennis et al., 2001; Schwarcz et al., 1976). The fluid inclusion water isotopes indicate a significant increase in values during the late Glacial period, rising rapidly by approximately 15 ‰ ($\delta^{2}H$) and 1 ‰ ($\delta^{18}O$) between ca. 14.0 ka BP and 13.8 ka BP. During the Holocene growth phase, the $\delta^{2}H$ and $\delta^{18}O$ values increased by around 10 ‰ and 1 ‰ respectively between approximately 11.4 ka BP and 8.5 ka BP. This was followed by a subsequent decrease in the values. The temperatures calculated based on the fluid inclusion data and the $\delta^{18}O$ of speleothem $CaCO_3$ show a range of -3.8 ± 3 °C to 3.1 ± 3 °C and follow the general trend of the water isotopes of the fluid inclusions.

The LOPs of sample BB-15 show a large range in the C/V ratio (between 0.13 ± 0.01 and 4.2 ± 2.1), while the S/V ratio varies between 0.19 ± 0.04 and 1.3 ± 0.5. The defined maximum value for the C/V ratio in softwood type plants is 1.2, which several (n = 6) measured values exceed. The data points with C/V ratios > 1.2 are therefore highlighted in Figs. 5.3 and 5.4. The general trend of the C/V and S/V ratios of BB-10 hint towards generally non-woody type vegetation, with most of the data points falling either in the transition zone or angiosperm type of the C/V ratio (Fig. S5.3). The Σ8 values (i.e., the sum of all eight analysed LOPs). range between 3.5 ± 0.1 ng/g and 41.8 ± 0.1.2 ng/g. The

highest Σ8 values, i.e., the highest density vegetation, can be found during the late Glacial growth phase around 14 and 13 ka BP. The general trend of the data shows decreasing values with decreasing age.

5.5 Discussion

5.5.1 Timing of the growth phases

All three samples started growing during the late Glacial and more precisely during the Bølling/Allerød (B/A) interstadial. The onset of the B/A interstadial around 14.7 ka BP marks the end of the last cold climate period of the last Glacial, the Heinrich (H) stadial 1. The transition from the H1 event to the B/A interstadial is characterised by drastic changes in vegetation (type, density, and expansion), and generally increasing sea surface temperatures (SST) in the North-Atlantic mid-latitudes (Naughton et al., 2007). The internal structure of the B/A interstadial can be divided into several short-term warm and cold periods, recorded in the Greenland ice cores (Lowe et al., 2008) and numerous terrestrial (Fletcher et al., 2010; Lotter et al., 2012; Peyron et al., 2005; Van Raden et al., 2013; Wohlfarth et al., 2001) and marine (Broecker, 1990; Moreno et al., 2012) records. It has been proposed that the trigger of the short cold periods during the B/A was periodic meltwater input from retreating Laurentide ice sheets, leading to climatic fluctuations due to a weakening of the AMOC (Donnelly et al., 2005; Lehman and Keigwin, 1992; McManus et al., 2004).

Two of the speleothems from Bleßberg Cave started growing shortly after the onset of the B/A interstadial, at 14.5 ± 0.2 ka BP (BB-9) and 14.4 ± 0.3 ka BP (BB-15), resulting in a lag of ~ 0.25 ka between the reported onset of the B/A warm period and speleothem growth in Bleßberg Cave. Speleothems require liquid water (with the potential to dissolve the host rock) and a sufficient soil and vegetation cover above the cave to grow. Previous studies (Richter and Riechelmann, 2008) revealed Cryocalcites (i.e., cryogenic calcites, that require a body of ice inside the cave to form) in Germany TIMS dated to 15.61 ± 0.20 ka BP and 14.48 ± 0.12 ka BP, showing that permafrost conditions lasted until the onset of the B/A interstadial. Klose et al., (in prep) proposed that Bleßberg Cave speleothem growth phases can serve as a proxy for favourable conditions for speleothem growth, based on the MIS 3 parts of the samples used in this study. Therefore, the growth

of samples BB-9 and BB-15 likely indicates the threshold for favourable conditions in Central Europe after the H1 stadial. Sample BB-10 started growing ~ 0.5 ka later than the other two samples at 14.0 ± 0.1 ka BP. The growth phase of this sample is relatively short (~ 0.15 ka, until 13.84 ± 0.06 ka BP), which implies the theory of only the most favourable conditions recorded in this sample. Sample BB-9 stops growing during a more progressed phase of the B/A interstadial (at 13.24 ± 0.5 ka BP). This sample likely recorded most of the B/A interstadial and reclined growth with worsened climate conditions towards the transition to the YD. This is also supported by the proxy data and will be discussed in Chapter 5.2 in more detail. BB-15 continued to grow during the YD cold event, which shows that no permafrost conditions were re-enabled during the YD.

All three samples grew during parts of the early and mid Holocene. However, while sample BB-10 started growing coinciding with the transition from the YD to the early Holocene (at 11.9 ± 0.3 ka BP), sample BB-9 only started growing again at 9.7 ± 0.3 ka BP not coinciding with any climatic event.

In general, the growth rates of samples BB-9 and -10 show a decrease from the B/A interstadial, on average 27.6 µm/a for BB-9 and 122 µm/a for sample BB-10, to the Holocene, which on average are 6.8 µm/a for BB-9 and 7.7 µm/a for sample BB-10. The growth rate of sample BB-10 during the B/A is exceptionally fast, especially for a flowstone, which usually tends to show slow and episodic growth. This further highlights the potential of reflecting the most favourable conditions for speleothem growth during the B/A interstadial and in general the warmer/wetter climate conditions during the B/A interstadial in comparison to the early Holocene in Central Europe.

The growth rate of sample BB-15 shows an average of 28 µm/a, with a slightly faster growth rate during the Holocene (33.5 µm/a) than during the B/A interstadial (23.2 µm/a) and shows an inversed trend than the other two samples. However, the ^{230}Th/U-dating of this sample could still be improved and the age model and therefore growth rate of the Late Glacial growth phase only relies on two individual ^{230}Th/U-ages. It can also be assumed that the growth rate during the YD would show a distinct decline.

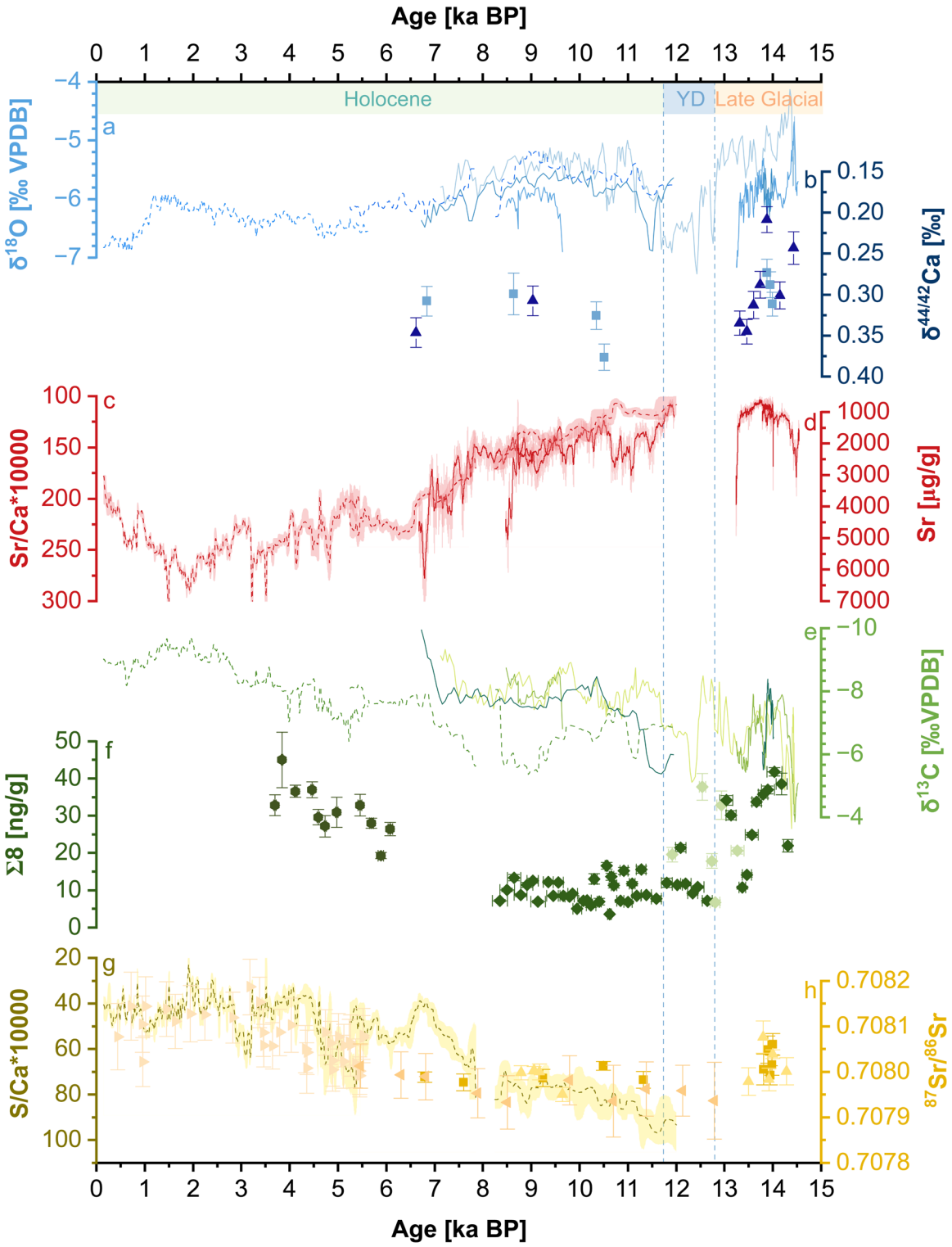

Fig. 5.3: The Bleßberg Cave Holocene record. The data from this study are given as solid lines, the dotted lines show data from a previously published Bleßberg Cave record from the Holocene (BB1 and BB-3, Breitenbach et al., 2019). a shows the $\delta^{18}O$ record, b the $\delta^{44/42}Ca$ record (triangles indicate BB-9 and squares BB-10) and the red lines indicate Sr trace element data, please note the different axis for the different samples due to different applied techniques (µXRD and Laser Ablation). e shows the $\delta^{13}C$ data and f the sum of LOPs. The light green values are out of the common range for softwood C/V ratios and therefore presumably less precise and therefore highlighted. g shows the BB-1 and BB-3 S/Ca*1000 values and h the Sr isotope ratios. Triangles indicate BB-9 and squares BB-10. The tilted triangles are unpublished Sr isotopes ratios from samples BB-1 and BB-3.

5.5.2 Climate progression during the Holocene

The Holocene record presented in Fig. 5.3 consists of the records of this study and the previously published Bleßberg Cave Holocene record by Breitenbach et al. (2019). They will therefore be discussed as one continuous record.

Breitenbach et al. (2019) interpret the $\delta^{13}C$ values, Sr/Ca and S/Ca ratios in the Bleßberg record as proxies for changes in the composition and density of vegetation, microbial soil activity and development and changes in infiltration (Lechleitner et al., 2017). The $\delta^{13}C$ values can, especially in a temperate climate zone, be influenced by all parameters mentioned above and often reflect a combination of all the contributing factors (Fairchild and Baker, 2012; Genty et al., 2001; Genty and Massault, 1999). Another potential factor influencing the $\delta^{13}C$ signal is changes in the ventilation of the cave and CO_2 degassing inside the cave. A long-term trend towards more negative values can observed with the ongoing progression of the Holocene. This significant change in the values would require a progressive reduction in ventilation (Scholz et al., 2012) throughout the Holocene. This is unlikely since the cave had no natural entrance prior to the discovery in 2008 and ventilation and degassing processes are therefore likely to have only minor influences on the $\delta^{13}C$ values.

The study site during the Holocene is generally characterised by higher microbial activity during the spring and summer, while the main infiltration season is during the winter (Breitenbach et al., 2019), which will be indicated by generally more negative $\delta^{13}C$ values due to enhanced CO_2 levels in the soil. These $\delta^{13}C$ values, however, can be influenced by the residence time of the percolating water in the aquifer. Longer residence times would lead to more positive values, approaching the values of the host rock limestone, which shows $\delta^{13}C$ values between +1 to -2 ‰ (Breitenbach et al., 2019). Thus, with the recorded values between -5 to -10 ‰ a strong influence of vegetation and microbial activity can be assumed. Generally, better developed soil is characterised by enhanced organic matter and microbial activity leading to high soil pCO_2 and consequently more negative $\delta^{13}C$ values (Cerling, 1984). Therefore, changes in the soil thickness and vegetation density, affecting the soil pCO_2 by root respiration, greatly affect the $\delta^{13}C$ signature of the percolating water (Scholz et al., 2012).

Further information on the vegetation density and composition can be gained from the LOP signal in speleothems. LOPs can be classified into three groups: vanillyl (V),

syringyl (S), and cinnamyl (C) (Jex et al., 2014). It is possible to differentiate between angiosperms (hardwood), gymnosperms (softwood), woody, and non-woody plants by comparing their C/V and S/V ratios (Hedges and Mann, 1979). The values of C/V that range from 0 to 0.1 indicate the presence of woody vegetation. A ratio between 0.1 – 0.4 represents a transition zone, while ratios > 0.4 indicate non-woody vegetation. Similarly, the S/V ratios between 0 – 0.2 indicate the presence of gymnosperm plants. A ratio between 0.2 – 0.9 represents a transition zone, while ratios > 0.9 signify the presence of angiosperms. However, unfortunately, it is common for the ratios to fall within the transition zone. To gain information on the vegetation density, the sum of all eight LOPs (Σ8) can be used, with high values indicating a high amount of vegetation above the cave.

Additional information regarding soil development can be derived from S/Ca ratios (μXRF trace element data). While several sources for the S in speleothems are possible (e.g. Frisia et al., 2005; Wolff et al., 2017; Wynn et al., 2010), inorganic and organic S can also derive from weathering and organic matter decomposition (Edwards, 1998). The predominant form of S in aerobic soils is easy-leachable sulphate, SO_4^{2-}. Increased contact time between S and the soil results in reduced SO_4^{2-} leaching directly to the cave due to absorption and/or transformation of S to less mobile components. The soil above the Bleßberg Cave can be classified as brown soil, a well-drained soil with a low pH-value and high water holding capacity, which promotes prolonged S and soil interaction time. A better developed soil, therefore, results in reduced SO_4^{2-} leaching and improved retention of S and leads to lower S/Ca ratios in the speleothem.

A great addition to the S/Ca ratios is the $^{87}Sr/^{86}Sr$ ratios obtained for this study. They can be used to provide insight into the residence time of the water in the aquifer (Banner et al., 1996; Oster et al., 2010) and the response of soil and host rock in relation to weathering processes due to rainfall (Avigour et al., 1990). Sr^{2+} ions can get incorporated as a substitute for Ca^{2+} ions in the crystal lattice of speleothem $CaCO_3$ (Banner, 2004). So far, no isotopic fractionation of the Sr isotopes has been observed during the substitution process and during the precipitation of speleothems. Therefore, it is assumed that $^{87}Sr/^{86}Sr$ ratio of the speleothem reflects that of the parent solution (Banner and Kaufman, 1994), where more radiogenic ratios usually indicate a stronger soil signature. The proposed underlying process is the addition of an external radiogenic source incorporated into the soil above the

cave (e.g., deposition of atmospheric dust (Banner et al., 1996; Zhou et al., 2009)), which has a varying contribution with changes in the soil pCO_2 (Banner et al., 1996). As mentioned before, better developed soil and increased vegetation density will lead to increased microbial activity in the soil and hence enhanced weathering of silicate material. The soil above Bleßberg Cave is characterised by a high level (50 %) of SiO_2 and therefore due to the enhanced weathering of the soil it will lead to increased radiogenic Sr in the percolating water and subsequently the speleothem. Therefore, better developed soil with increased microbial activity is indicated by more radiogenic (i.e., increased) $^{87}Sr/^{86}Sr$ ratios, stronger S retention indicated by lower S/Ca values, and most likely also more negative $\delta^{13}C$ values and a higher vegetation density indicated by higher Σ8 values.

Visually, the S/Ca and $^{87}Sr/^{86}Sr$ ratios show a general negative correlation with ongoing progression of the Holocene, except for a jump towards lower values of the S/Ca ratios around 7 ka BP, which is not recorded in the $^{87}Sr/^{86}Sr$ ratios but could be due the much lower resolution of the $^{87}Sr/^{86}Sr$ ratios. Both values indicate underdeveloped soil with minimal microbial activity during the early Holocene, with only a minimal improvement towards lower S/Ca values. During the mid Holocene a clear development towards better developed soil and more microbial activity is evident, as well as the previously mentioned peak in the S/Ca around 7 ka BP, which might hint towards the Holocene thermal maximum. However, since the microbial activity in the temperate region of Bleßberg Cave is generally higher during the spring and summer, the Holocene thermal maximum still might be a seasonal signal. During the late Holocene $^{87}Sr/^{86}Sr$ ratios reach the highest (most radiogenic) values, while the S/Ca values reach the lowest level of the entire Holocene. Interestingly, the $^{87}Sr/^{86}Sr$ ratios available of the late glacial, coinciding with the Bølling/Allerød warm period, are similarly high than during the transition from mid to late Holocene, and demonstrate the favourable conditions, with higher microbial activity with well-developed soil during the Bølling/Allerød.

The $\delta^{13}C$ and Σ8 values generally support the observation made based on the S/Ca and $^{87}Sr/^{86}Sr$ ratios. The trends observed are relatively similar with a more plateau-like structure during the early Holocene, indicating only developing vegetation cover and more reduced microbial activity as observed by the S/Ca and $^{87}Sr/^{86}Sr$ ratios. Around 7 ka BP a jump towards rapidly decreasing $\delta^{13}C$ values similar to the S/Ca ratios is evident. During the late Holocene, a continuous trend towards more negative values is shown by both signals, until ca. 1.6 ka BP, where the $\delta^{13}C$ values start to increase.

Calcium can precipitate prior to the formation of speleothems (prior calcite precipitation, PCP), leading to the enrichment of other trace elements, like Sr, in comparison to calcite. During this process, the lighter calcium isotope (^{42}Ca) gets incorporated into the solid phase. This can result in higher $\delta^{44/42}Ca$ values in the drip water that reaches the cave, and consequently, the Ca isotopes in speleothems also exhibit higher values. This is often used as an indicator of drier climatic conditions and increased PCP, with lower $\delta^{44/42}Ca$ values indicating wetter climate conditions.

The Sr/Ca ratios (μXRF trace element data) and Sr values (LA trace element data) of speleothems can be a sensitive proxy for changes in infiltration, where higher ratios are recorded during periods of reduced moisture availability (Fairchild and Treble, 2009). Breitenbach et al. (2019) showed that while there is no climate seasonality in the region of Bleßberg Cave, the effective infiltration peaks during the winter months, due to increased evapotranspiration during the warmer months. Infiltration-sensitive proxies like Sr could therefore be used to reconstruct the changes in the infiltration, with a strong bias towards the warm season, by indicating PCP.

The Sr trace element data shows a general trend towards higher values during the early and mid Holocene indicating increasing summer PCP. Two distinctive peaks interrupt the general at the beginning of the early Holocene (ca. 11.7 – 10.6 ka BP) and during the end mid Holocene (ca. 6.7 – 5.5 ka BP) and indicate intense periods of moisture reduction with increased PCP. Both of these positive peaks are supported by higher $\delta^{44/42}Ca$ values indicating drier climate conditions. During the early Holocene, the Sr values show a stronger centennial variability and several short-term periods of moisture reduction, around 3.5 ka, 3.2 ka and 1.5 ka BP as identified by Breitenbach et al. (2019). Unfortunately, no $\delta^{44/42}Ca$ values are available for this section of the Holocene. The general trend towards more positive values/more summer PCP during the early Holocene stops around 2 ka BP and progresses towards lower values and therefore less PCP and potentially drier climate conditions.

There are many contributing factors, which can influence the $\delta^{18}O$ values of drip water and speleothems. The precipitation reaching Bleßberg cave stems mainly from the North Atlantic region, with no seasonal maximum but the highest effective infiltration during the winter months. Breitenbach et al. (2019) extensively discussed the regional factors controlling the $\delta^{18}O$ values in precipitation ($\delta^{18}O_p$), local factors controlling the $\delta^{18}O$ values

in the infiltrating water and the $\delta^{18}O$ of Bleßberg speleothems ($\delta^{18}O_{spel}$) as a proxy of atmospheric circulation and thus the reader is referred to the publication for more detailed coverage of the potential influences. They conclude, based on modern meteorological data obtained close to the cave, that the regional signal of the $\delta^{18}O_p$ values is strongly influenced by air temperature and the NAO mode (Baldini et al., 2008), whereas higher temperatures and a positive NAO mode are represented by more positive $\delta^{18}O_p$ values. They further show that the reason for the relatively stable collected modern drip water $\delta^{18}O$ is due to mixing of infiltration water in the karst aquifer. Concluding, the Bleßberg Cave $\delta^{18}O_{spel}$ record combines the $\delta^{18}O_p$ history, seasonal changes in the effective infiltration, temperature, and long-term pan-regional environmental dynamics.

The general progression of the $\delta^{18}O_{spel}$ record is towards more negative values indicating a cooling trend with potentially increased winter precipitation during the early phase of the Holocene. In addition, the $\delta^{18}O_{spel}$ values follow the trend of the $\delta^{44/42}Ca$ values during the early Holocene. Breitenbach et al. (2019) proposed, that a positive NAO would lead to a stronger atmospheric vortex and deepened low pressure cell over the North Pole and therefore a positive Arctic Oscillation. This would lead to strong Westerlies and a reduced branching of the jet stream and finally the transport of warmer moisture from the North Atlantic towards Europe. Therefore, the positive NAO and warm temperatures might also indicate wetter climate conditions to peak around 9 ka BP, which is supported by our $\delta^{44/42}Ca$ record. The reimaging $\delta^{18}O_{spe}$ record shows only small variations hinting towards a slight increasing trend and a slight temperature increase until ca. 1 ka BP before reclining back towards a negative trend and decreasing temperatures and a negative NAO mode.

5.5.3 Centennial-scale climate oscillations during Termination I

5.5.3.1 Bølling warm period (14.64 – 14.03)

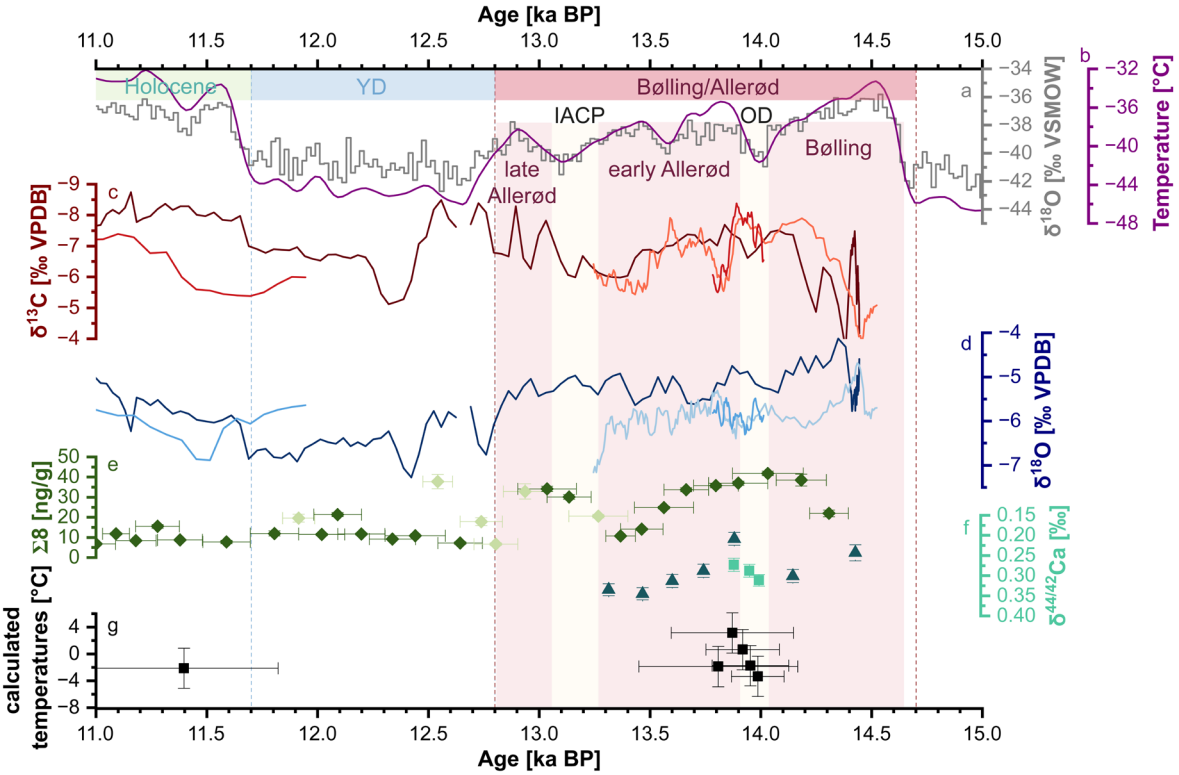

Fig. 5.4: The Bleßberg Cave Late Glacial record and Transition I record. The NGRIP $\delta^{18}O$ (black line, Rasmussen et al., 2014) and Temperatures record (purple line, Kindler et al., 2014) are given in a and b. The stable isotopes records of the Bleßberg flowstones are given in c and d, the light colour indicates sample BB-9, the medium one BB-10 and the dark BB-15 in both records. The LOP data Σ8 is shown in e and highlighted as described in the main text and Fig. 5.3, $\delta^{44/42}Ca$ values are given for sample BB-9 (dark turquoise triangles) and BB-10 (light turquoise squares. The calculated temperatures in g are based on the fluid inclusion data of sample BB-10. The red and yellow boxes indicate subevents of the Bølling/Allerød warm period, where red indicates a warm and yellow a cold period. The names of the event are given, OD stands for Older Dryas and IACP is abbreviated for Intra-Allerød cold period.

A rapid decrease of the $\delta^{13}C$ values (Fig. 5.4 c) of samples BB-9 and BB-15 marks the onset of the Bølling warm period (GI-1e in the Greenland GICC05 chronology (Rasmussen et al., 2014)) and indicates a re-establishment of soil activity and vegetation, which is supported by rapid increase in vegetation density (Fig. 5.4 e) and hints towards a general increase in temperature and moisture availability. This trend of re-establishing vegetation is also evident in other European records which report, for instance, birch woodland in the Meerfelder Maar region in Germany (Litt et al., 2001) and open forest type vegetation in N-W Romania with a generally humid climate (Wohlfarth et al., 2001). Surprisingly, the transition from a dry to a wet climate is not indicated by the Ca isotopes (Fig. 5.4 f).

However, the resolution of $\delta^{44/42}$Ca values is relatively low during the Bølling period and the distinct dry to wet transition may therefore not be recorded.

Regarding the progression of the Bølling warm period, it has been shown, that while the Greenland ice core records (Fig. 5.4 a and b) show a gradual decline in temperature and a peak during the onset of the event (Jouzel et al., 2007), mid-latitude records often rather indicate continuous warming (Fletcher et al., 2010). Lotter et al., (2012) presented a quantitative July temperature reconstruction from Gerzensee, Switzerland using fossil chironomid, a type of aquatic insect, and pollen data, which showed those opposite trends. While the pollen-based temperatures followed the decreasing trend of the Greenland ice core after the initial warming, the chironomid-based record indicated gradual temperature increase throughout the entire interstadial period, suggesting that the different trend might be a seasonal bias represented by some, but not all, records.

The isotope records of the Bleßberg flowstones show decreasing values with the progress of the Bølling warm period and reach a negative peak around 14.2 ka BP followed by a slight short-term increase until the end of the Bølling period. Both stable isotope records follow the variability of the Greenland ice core and while δ^{13}C represents the microbial soil activity as a response to increasing vegetation density, δ^{18}O acts as a more direct temperature proxy. Therefore, the temperature rapidly increases with the onset of the event but follows the gradual cooling as shown in the Greenland ice cores after 14.4 ka BP.

The $\delta^{44/42}$Ca values indicate slightly drier conditions towards the end of the Bølling warm period. However, even though the temperatures decrease, and the climate develops towards generally drier conditions with the ongoing progression of the Bølling warm period, the total amount of vegetation reaches a peak at the end of the warm phase, indicating that the climate conditions were still favourable for continued vegetation growth.

5.5.3.2 Older Dryas cold period (14.03 – 13.9)

The Older Dryas cold period (GI-1d in the Greenland GICC05 chronology (Rasmussen et al., 2014)) is characterised by decreasing δ^{13}C and δ^{18}O values, indicating a cold period with increased microbial soil activity. This observation is supported by the amount of vegetation staying at a constant high level, slowly increasing $\delta^{44/42}$Ca values as well as temperatures calculated from fluid inclusions (Fig. 5.4 g). Wolfarth et al. (2001) described

an increase in tree cover in N-W Romania and Litt et al. (2001) open woodland with birch-type trees supporting our observations for Central Europe. Studies from the western Mediterranean (Fletcher et al., 2010), however, describe drier conditions and a declining temperate forest. The proposed underlying process is based on a weakening of the thermohaline circulation resulting in jet stream intensifications and an extension of cyclonic activity, resulting in wet climate conditions, towards more continental Europe and vice versa. This would create an opposed hydrological pattern between the Western Mediterranean and Central Europe and explain the conditions as shown in our record.

5.5.3.3 Allerød warm period (13.9 – 12.8 ka BP)

The Allerød warm period (GI-1c – a in the Greenland GICC05 chronology (Rasmussen et al., 2014)) can be divided into an early (GI-1c, 13.9 – 13.26) and late phase (GI-1a, 13.05 – 12.85) interrupted by the Intra–Allerød cold period (IACP, GI-1b, 13.26 – 13.05). The onset of this warm phase shows a negative peak in the $\delta^{13}C$ values, as well as the $\delta^{44/42}Ca$ values, which mark the lowest values for both proxies during the entire Termination I phase. These negative peaks are accompanied by a slightly delayed negative peak in the $\delta^{18}O$ values, a slowly decreasing vegetation amount and the highest calculated temperatures of the entire Termination I. The onset of this warm period is therefore characterised by a very warm and humid climate.

The general trend during this warm period is towards a colder and drier climate, with reduced vegetation and soil activity. The stable isotope records observe two short-term oscillations around 13.7 ka BP and 13.6 ka BP, coinciding with the GI-1c1 and GI-1c2 sub-events, which are not recorded by the other proxies due to a much lower resolution. These cold events show decreasing values in both stable isotope records and therefore the same climate signature as the Older Dryas cold period, but on a much smaller amplitude.

After 13.5 ka BP, the $\delta^{13}C$ values start to increase and reach a plateau around 13.4 ka BP. Alongside this decrease in soil activity and an increase in $\delta^{44/42}Ca$ values, indicating drier climate conditions. The decrease of the $\delta^{18}O$ values is 0.2 ka delayed, showing that while the climate conditions got drier the temperature remained high. Shortly before the IACP, the $\delta^{13}C$ values start to decrease again, as well as the $\delta^{18}O$ values of sample BB-9. The stable oxygen isotope record of sample BB-15 has a much larger resolution and

therefore shows less short-term variability in the $\delta^{18}O$ record. The vegetation amount shows an increase during the IACP.

5.5.3.4 Younger Dryas cold period (12.8 – 11.7 ka BP)

The Younger Dryas (YD, GS-1 in the Greenland GICC05 chronology (Rasmussen et al., 2014)) is unfortunately only represented by sample BB-15 in our record, which has the lowest proxy resolution and the least precise age model. This synchronous cold phase is characterised by an abrupt change to continuously very low $\delta^{18}O$ values and temperatures in the Greenland ice core and enhanced seasonality with a colder and/or drier climate in Europe (Brauer et al., 1999; Heiri et al., 2014; Schenk et al., 2018).

The onset of the YD in our record shows a continuation of a gradual trend of the stable isotope records from the Allerød warm period towards more negative values. This would imply that not only the onset of the event in Central Europe was gradual and not abrupt but also characterised by a warm climate with high microbial activity in the soil. As mentioned before, the age model precision of this sample is relatively low, due to the low spatial resolution of $^{230}Th/U$-ages. Therefore, it is not unlikely that this early part of the YD might in fact be the latest part of the Allerød warm period and the abrupt increase in the $\delta^{13}C$ values between 12.6 to 12.4 ka BP might represent the actual onset of the YD in our record. If that were the case, we would observe a transition towards a warmer climate with increasing vegetation and microbial activity at 0.2 ka BP (based on the available age model) after the onset of the event. However, a precise discussion of the data, potential conclusions about the internal structure of the event and comparisons with other records are hampered by the age model which needs improvement.

5.6 Conclusion

The speleothems BB-9, BB-10, and BB-15 from Bleßberg Cave are used to reconstruct the transition from the late Glacial to the Holocene. All three flowstones cover at least parts of the Bølling/Allerød interstadial and one sample maintained growth throughout the Younger Dryas stadial. By combining our record with a previously published record from

Bleßberg Cave (Breitenbach et al., 2019), we were able to create a continuous multi-proxy record of the Holocene until 0.6 ka BP.

Several centennial-scale climate oscillations were observed during the Bølling/Allerød interstadial, which shows the high sensitivity of the speleothems from Bleßberg Cave. Three cold events were recorded during which our speleothems recorded cooler temperatures but a remaining well working environment, indicated by high microbial activity in the soil and increasing vegetation density. The internal structure of the Younger Dryas is less well represented, due to the much lower resolution of the age model and proxies of sample BB-15. However, a two-phase structure of the cold phase can be observed but needs further work to justify the conclusion. The Holocene record revealed a general cooling trend with ongoing progression, but an increase in vegetation, soil development and microbial activity in the soil, especially at the beginning of the mid Holocene. Additionally, an increase in PCP is observed hinting towards drier climate conditions until ca. 2 ka BP where the trend shifts towards less PCP and wetter climate conditions. The theory of Holocene thermal maximum around 7 ka BP might be supported by our record, which shows a jump towards a well-developed soil and high microbial activity alongside wet climate conditions. However, we do not observe a clear trend in our temperature data, which supports the idea that the Holocene thermal maximum might be a solely seasonal signal.

5.7 Outlook

Several improvements could and should be made to optimise the paleoclimate record presented in this study. Especially the late Glacial part has the potential to reveal further short-term climate oscillations during the Younger Dryas and answer relevant questions for the paleoclimate community. Additionally, as for the current state of the age models the stable isotope records of samples BB-9 and BB-10 show a different climatic signal during the B/A cold phases than sample BB-15. During the Older Dryas, samples BB-9 and BB-10 show more negative values in both stable isotopes, indicating colder climate conditions with enhanced microbial activity, which fits the opposed hydrological pattern between the Western Mediterranean and Central Europe theory proposed by Fletcher et al. (2010). However, BB-15 shows more positive values in both stable isotopes. The most likely explanation is based on the less precise age model of BB-15, which could easily be

improved by additional ^{230}Th/U-ages. Due to the independent age models but still great agreement of the δ^{13}C records of BB-9 and BB-10 those records presumably show the accurate signal. Nevertheless, both options are visualised in Figs. 5.5and 5.6 and indicate a potential shift of the records. These two options, however, would result in significant changes in the interpretation of the stable isotope records. Another time period which might improve with a revised age model for BB-15 would be the onset of the Younger Dryas (Fig. 5.7)

In addition to an improved age model for sample BB-15 several additional new proxies, which are already available for sample BB-9 and BB-10, would significantly improve the reconstruction of the late Glacial, but especially the Younger Dryas. The proxies best suited would be trace elements and Ca isotopes. Also, based on the reworked age model and new growth rate, it might be helpful to obtain the stable isotopes in a higher resolution. It is a great opportunity to have a (precisely dated) speleothem sample from the Younger Dryas and the new proxies might help answer the question of the existence of a two-phase Younger Dryas in Europe.

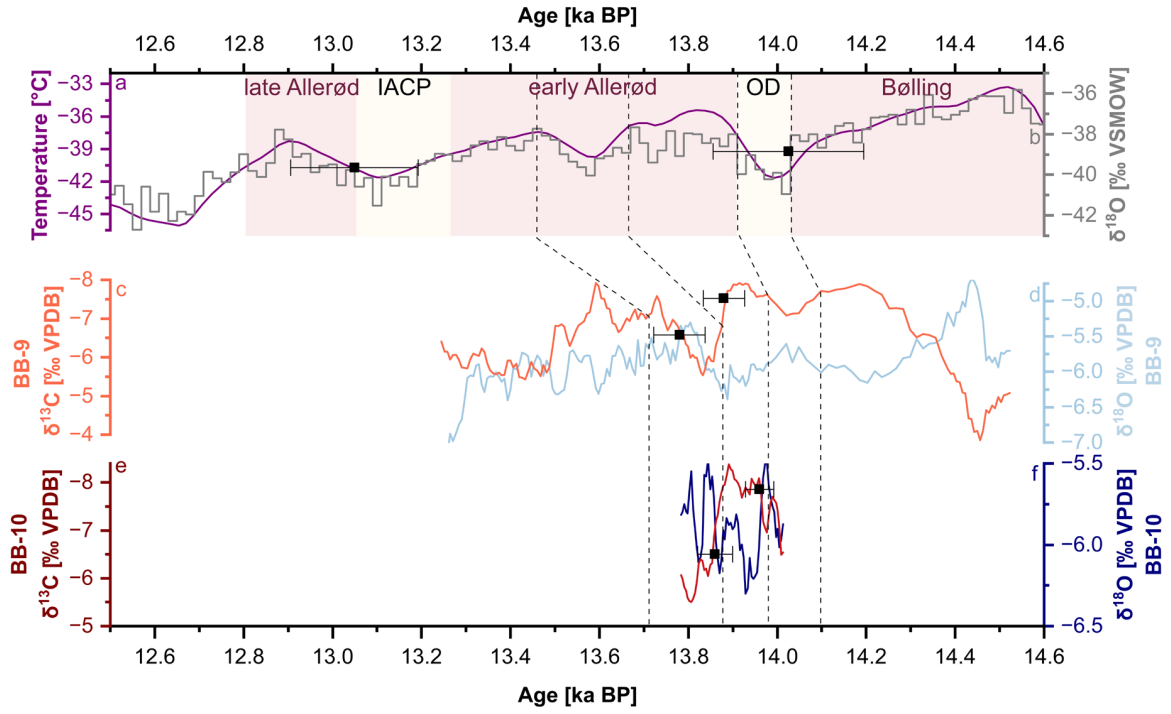

Fig. 5.5: Option no. 1 to shift the BB-9 and BB-10 proxies during the Bølling/Allerød interstadial. The NGRIP records are given in a (Temperatures, purple line, (Kindler et al., 2014)) and b (δ^{18}O, grey line, (Rasmussen et al., 2014)). The stable isotope records of BB-9 are given in c and d, the stable isotope records of BB-10 are given in e and f. For both Bleßberg records two ages from the proxy age model are given with the corresponding uncertainty (2σ), and for the NGRIP record based on the counting uncertainty given in Rasmussen et al., (2014). The dotted lines indicate the potential shifts. The subevents Bølling/Allerød period are indicated by red (warm phase) and yellow (cold phase) boxes and labelled. OD refers to the Older Dryas and IACD for Intra-Allerød cold period.

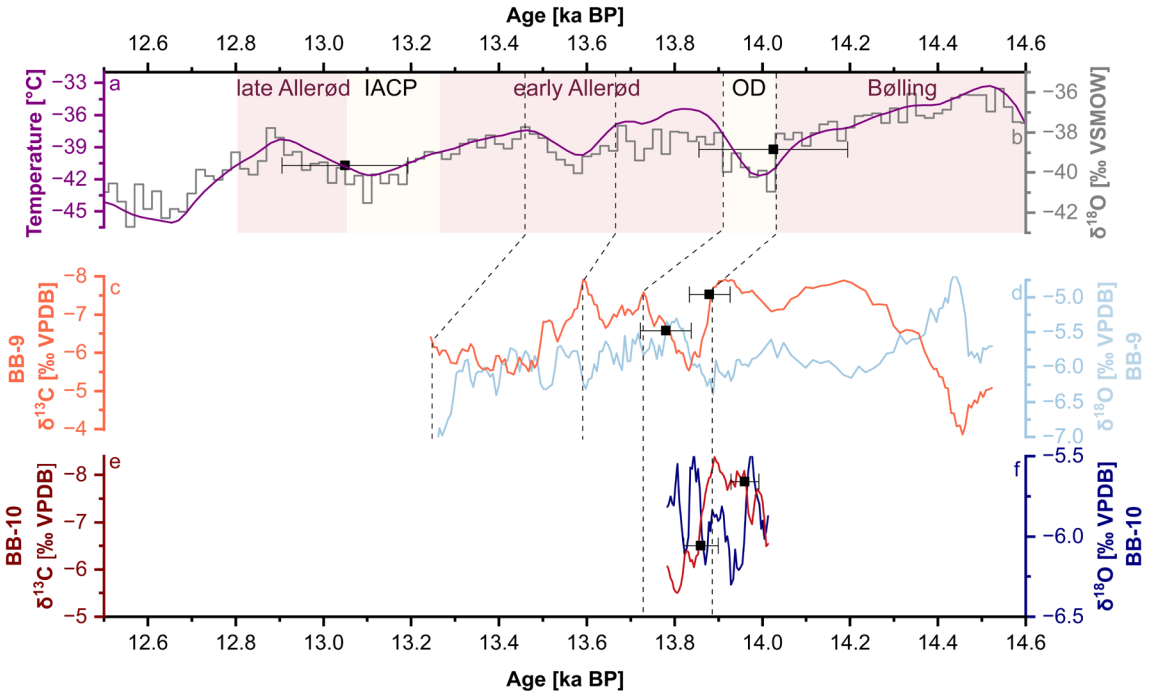

Fig. 5.6: Option no. 2 to shift the BB-9 and BB-10 proxies during the Bølling/Allerød interstadial. The NGRIP records are given in a (Temperatures, purple line, (Kindler et al., 2014)) and b ($\delta^{18}O$, grey line, (Rasmussen et al., 2014)). The stable isotope records of BB-9 are given in c and d, the stable isotope records of BB-10 are given in e and f. For both Bleßberg records two ages from the proxy age model are given with the corresponding uncertainty (2σ) and for the NGRIP record based on the counting uncertainty given in Rasmussen et al., (2014). The dotted lines indicate the potential shifts. The subevents Bølling/Allerød period are indicated by red (warm phase) and yellow (cold phase) boxes and labelled. OD refers to the Older Dryas and IACD for Intra-Allerød cold period.

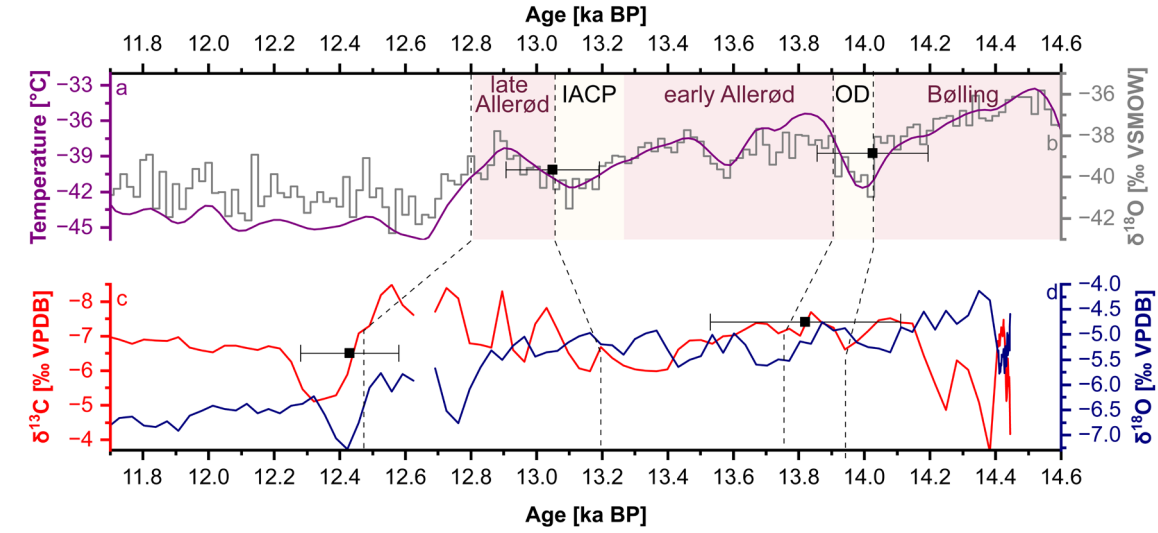

Fig. 5.7: The potential option to shift the BB-15 during the Bølling/Allerød interstadial. The NGRIP records are given in a (Temperatures, purple line, (Kindler et al., 2014)) and b ($\delta^{18}O$, grey line, (Rasmussen et al., 2014)). The stable isotope record of BB-15 is given in c and d. Two ages from the proxy age model are given with the corresponding uncertainty (2σ) and for the NGRIP record based on the counting uncertainty given in Rasmussen et al., (2014). The dotted lines indicate the potential shifts. The subevents Bølling/Allerød period are indicated by red (warm phase) and yellow (cold phase) boxes and labelled. OD refers to the Older Dryas and IACD for Intra-Allerød cold period.

5.8 References

Ammann, B., Lotter, A.F., Eicher, U., Gaillard, M.J., Wohlfarth, B., Haeberli, W., Lister, G., Maisch, M., Niessen, F. and Schlüchter, C., 1994. The Würmian Late-glacial in Iowland Switzerland. Journal of Quaternary Science, 9(2): 119-125.

Avigour, A., Magaritz, M., Issar, A. and Dodson, M., 1990. Sr isotope study of vein and cave calcites from southern Israel. Chemical geology, 82: 69-81.

Bakke, J., Lie, Ø., Heegaard, E., Dokken, T., Haug, G.H., Birks, H.H., Dulski, P. and Nilsen, T., 2009. Rapid oceanic and atmospheric changes during the Younger Dryas cold period. Nature Geoscience, 2(3): 202-205.

Baldini, L.M., McDermott, F., Foley, A.M. and Baldini, J.U., 2008. Spatial variability in the European winter precipitation δ^{18}O-NAO relationship: Implications for reconstructing NAO-mode climate variability in the Holocene. Geophysical Research Letters, 35(4).

Banner, J.L., 2004. Radiogenic isotopes: systematics and applications to earth surface processes and chemical stratigraphy. Earth-Science Reviews, 65(3-4): 141-194.

Banner, J.L. and Kaufman, J., 1994. The isotopic record of ocean chemistry and diagenesis preserved in non-luminescent brachiopods from Mississippian carbonate rocks, Illinois and Missouri. Geological Society of America Bulletin, 106(8): 1074-1082.

Banner, J.L., Musgrove, M., Asmerom, Y., Edwards, R.L. and Hoff, J.A., 1996. High-resolution temporal record of Holocene ground-water chemistry: Tracing links between climate and hydrology. Geology, 24(11): 1049-1053.

Björck, S., 2007. Younger Dryas oscillation, global evidence, Encyclopedia of Quaternary science. Elsevier, pp. 1987-1994.

Bova, S., Rosenthal, Y., Liu, Z., Godad, S.P. and Yan, M., 2021. Seasonal origin of the thermal maxima at the Holocene and the last interglacial. Nature, 589(7843): 548-553.

Brauer, A., Endres, C., Günter, C., Litt, T., Stebich, M. and Negendank, J.F., 1999. High resolution sediment and vegetation responses to Younger Dryas climate change in varved lake sediments from Meerfelder Maar, Germany. Quaternary Science Reviews, 18(3): 321-329.

Brauer, A., Günter, C., Johnsen, S. and Negendank, J.F., 2000. Land-ice teleconnections of cold climatic periods during the last Glacial/Interglacial transition. Climate Dynamics, 16: 229-239.

Breitenbach, S.F., Plessen, B., Waltgenbach, S., Tjallingii, R., Leonhardt, J., Jochum, K.P., Meyer, H., Goswami, B., Marwan, N. and Scholz, D., 2019. Holocene interaction of maritime and continental climate in Central Europe: New speleothem evidence from Central Germany. Global and Planetary Change, 176: 144-161.

Broecker, W.S., 1990. Salinity history of the northern Atlantic during the last deglaciation. Paleoceanography, 5(4): 459-467.

Büntgen, U., 2022. Scrutinizing tree-ring parameters for Holocene climate reconstructions. Wiley Interdisciplinary Reviews: Climate Change, 13(4): e778.

Cartapanis, O., Jonkers, L., Moffa-Sanchez, P., Jaccard, S.L. and de Vernal, A., 2022. Complex spatio-temporal structure of the Holocene Thermal Maximum. Nature Communications, 13(1): 5662.

Cerling, T.E., 1984. The stable isotopic composition of modern soil carbonate and its relationship to climate. Earth and Planetary science letters, 71(2): 229-240.

De Graaf, S., Lüders, V., Banks, D.A., Sośnicka, M., Reijmer, J.J., Kaden, H. and Vonhof, H.B., 2020. Fluid evolution and ore deposition in the Harz Mountains revisited: isotope and crush-leach analyses of fluid inclusions. Mineralium Deposita, 55: 47-62.

Dennis, P., Rowe, P. and Atkinson, T., 2001. The recovery and isotopic measurement of water from fluid inclusions in speleothems. Geochimica et Cosmochimica Acta, 65(6): 871-884.

Denton, G.H., Alley, R.B., Comer, G.C. and Broecker, W.S., 2005. The role of seasonality in abrupt climate change. Quaternary Science Reviews, 24(10-11): 1159-1182.

Denton, G.H., Anderson, R.F., Toggweiler, J., Edwards, R., Schaefer, J. and Putnam, A., 2010. The last glacial termination. science, 328(5986): 1652-1656.

Donnelly, J.P., Driscoll, N.W., Uchupi, E., Keigwin, L.D., Schwab, W.C., Thieler, E.R. and Swift, S.A., 2005. Catastrophic meltwater discharge down the Hudson Valley: A potential trigger for the Intra-Allerød cold period. Geology, 33(2): 89-92.

Edwards, P.J., 1998. Sulfur cycling, retention, and mobility in soils: a review.

Elmore, A.C. and Wright, J.D., 2011. North Atlantic Deep Water and climate variability during the Younger Dryas cold period. Geology, 39(2): 107-110.

Essell, H., Esper, J., Wanner, H. and Büntgen, U., 2024. Rethinking the Holocene temperature conundrum. Climate Research, 92: 61-64.

Fairchild, I.J. and Baker, A., 2012. Speleothem science: from process to past environments. John Wiley & Sons.

Fairchild, I.J. and Treble, P.C., 2009. Trace elements in speleothems as recorders of environmental change. Quaternary Science Reviews, 28(5-6): 449-468.

Fletcher, W.J., Sánchez Goñi, M.F., Peyron, O. and Dormoy, I., 2010. Abrupt climate changes of the last deglaciation detected in a Western Mediterranean forest record. Climate of the Past, 6(2): 245-264.

Frisia, S., Borsato, A., Spötl, C., Villa, I.M. and Cucchi, F., 2005. Climate variability in the SE Alps of Italy over the past 17 000 years reconstructed from a stalagmite record. Boreas, 34(4): 445-455.

Genty, D., Baker, A., Massault, M., Proctor, C., Gilmour, M., Pons-Branchu, E. and Hamelin, B., 2001. Dead carbon in stalagmites: carbonate bedrock paleodissolution vs. ageing of soil organic matter. Implications for ^{13}C variations in speleothems. Geochimica et Cosmochimica Acta, 65(20): 3443-3457.

Genty, D. and Massault, M., 1999. Carbon transfer dynamics from bomb-^{14}C and δ*C time series of a laminated stalagmite from SW France—modelling and comparison with other stalagmite records. Geochimica et Cosmochimica Acta, 63(10): 1537-1548.

Gibert, L., Scott, G.R., Scholz, D., Budsky, A., Ferràndez, C., Ribot, F., Martin, R.A. and Lería, M., 2016. Chronology for the Cueva Victoria fossil site (SE Spain): evidence for early Pleistocene Afro-Iberian dispersals. Journal of human evolution, 90: 183-197.

Hedges, J.I. and Mann, D.C., 1979. The characterization of plant tissues by their lignin oxidation products. Geochimica et Cosmochimica Acta, 43(11): 1803-1807.

Heiri, O., Brooks, S.J., Renssen, H., Bedford, A., Hazekamp, M., Ilyashuk, B., Jeffers, E.S., Lang, B., Kirilova, E. and Kuiper, S., 2014. Validation of climate model-inferred regional temperature change for late-glacial Europe. Nature communications, 5(1): 4914.

Hertzberg, J., 2021. Palaeoclimate puzzle explained by seasonal variation. Nature Publishing Group UK London.

Hoffmann, D.L., 2008. ^{230}Th isotope measurements of femtogram quantities for U-series dating using multi ion counting (MIC) MC-ICPMS. International Journal of Mass Spectrometry, 275(1-3): 75-79.

Homann, J., Zirbes, M., Arndt-Engelbart, M., Scholz, D., Waldvogel, S.R. and Hoffmann, T., 2022. Development of a Method for Anodic Degradation of Lignin for the Analysis of Paleo-Vegetation Proxies in Speleothems. ChemElectroChem, 9(6): e202101312.

Hughen, K.A., Overpeck, J.T., Peterson, L.C. and Trumbore, S., 1996. Rapid climate changes in the tropical Atlantic region during the last deglaciation. Nature, 380(6569): 51-54.

Jex, C.N., Pate, G.H., Blyth, A.J., Spencer, R.G., Hernes, P.J., Khan, S.J. and Baker, A., 2014. Lignin biogeochemistry: from modern processes to Quaternary archives. Quaternary Science Reviews, 87: 46-59.

Jouzel, J., Stiévenard, M., Johnsen, S., Landais, A., Masson-Delmotte, V., Sveinbjornsdottir, A., Vimeux, F., Von Grafenstein, U. and White, J.C., 2007. The GRIP deuterium-excess record. Quaternary Science Reviews, 26(1-2): 1-17.

Karpuz, N.K. and Jansen, E., 1992. A high-resolution diatom record of the last deglaciation from the SE Norwegian Sea: Documentation of rapid climatic changes. Paleoceanography, 7(4): 499-520.

Kaufman, D.S. and Broadman, E., 2023. Revisiting the Holocene global temperature conundrum. Nature, 614(7948): 425-435.

Lane, C.S., Brauer, A., Blockley, S.P. and Dulski, P., 2013. Volcanic ash reveals time-transgressive abrupt climate change during the Younger Dryas. Geology, 41(12): 1251-1254.

Lauterbach, S., Brauer, A., Andersen, N., Danielopol, D.L., Dulski, P., Hüls, M., Milecka, K., Namiotko, T., Obremska, M. and Von Grafenstein, U., 2011. Environmental responses to Lateglacial climatic fluctuations recorded in the sediments of pre-Alpine Lake Mondsee (northeastern Alps). Journal of Quaternary Science, 26(3): 253-267.

Lechleitner, F.A., Breitenbach, S.F., Cheng, H., Plessen, B., Rehfeld, K., Goswami, B., Marwan, N., Eroglu, D., Adkins, J. and Haug, G., 2017. Climatic and in-cave influences on $\delta^{18}O$ and $\delta^{13}C$ in a stalagmite from northeastern India through the last deglaciation. Quaternary Research, 88(3): 458-471.

Lehman, S.J. and Keigwin, L.D., 1992. Sudden changes in North Atlantic circulation during the last deglaciation. Nature, 356(6372): 757-762.

Litt, T., Brauer, A., Goslar, T., Merkt, J., Bałaga, K., Müller, H., Ralska-Jasiewiczowa, M., Stebich, M. and Negendank, J.F., 2001. Correlation and synchronisation of Lateglacial continental sequences in northern central Europe based on annually laminated lacustrine sediments. Quaternary Science Reviews, 20(11): 1233-1249.

Litt, T., Schmincke, H.-U. and Kromer, B., 2003. Environmental response to climatic and volcanic events in central Europe during the Weichselian Lateglacial. Quaternary Science Reviews, 22(1): 7-32.

Lotter, A.F., Heiri, O., Brooks, S., van Leeuwen, J.F., Eicher, U. and Ammann, B., 2012. Rapid summer temperature changes during Termination 1a: high-resolution multi-proxy climate reconstructions from Gerzensee (Switzerland). Quaternary Science Reviews, 36: 103-113.

Lowe, J.J., Ammann, B., Birks, H., Björck, S., Coope, G., Cwynar, L., De Beaulieu, J.L., Mott, R., Peteet, D. and Walker, M., 1994. Climatic changes in areas adjacent to the North Atlantic during the last glacial-interglacial transition (14-9 ka BP): a contribution to IGCP-253. Journal of Quaternary Science, 9(2): 185-198.

Lowe, J.J., Rasmussen, S.O., Björck, S., Hoek, W.Z., Steffensen, J.P., Walker, M.J., Yu, Z. and Group, I., 2008. Synchronisation of palaeoenvironmental events in the North Atlantic region during the Last Termination: a revised protocol recommended by the INTIMATE group. Quaternary Science Reviews, 27(1-2): 6-17.

McArthur, J.M., Howarth, R. and Bailey, T., 2001. Strontium isotope stratigraphy: LOWESS version 3: best fit to the marine Sr-isotope curve for 0–509 Ma and accompanying look-up table for deriving numerical age. The Journal of Geology, 109(2): 155-170.

McManus, J.F., Francois, R., Gherardi, J.-M., Keigwin, L.D. and Brown-Leger, S., 2004. Collapse and rapid resumption of Atlantic meridional circulation linked to deglacial climate changes. nature, 428(6985): 834-837.

Mischel, S.A., Mertz-Kraus, R., Jochum, K.P. and Scholz, D., 2017. TERMITE: An R script for fast reduction of laser ablation inductively coupled plasma mass spectrometry data and its application to trace element measurements. Rapid Communications in Mass Spectrometry, 31(13): 1079-1087.

Moreno, A., González-Sampériz, P., Morellón, M., Valero-Garcés, B.L. and Fletcher, W.J., 2012. Northern Iberian abrupt climate change dynamics during the last glacial cycle: a view from lacustrine sediments. Quaternary Science Reviews, 36: 139-153.

Muschitiello, F., Pausata, F.S., Watson, J.E., Smittenberg, R.H., Salih, A.A., Brooks, S.J., Whitehouse, N.J., Karlatou-Charalampopoulou, A. and Wohlfarth, B., 2015. Fennoscandian freshwater control on Greenland hydroclimate shifts at the onset of the Younger Dryas. Nature Communications, 6(1): 8939.

Naughton, F., Goñi, M.S., Desprat, S., Turon, J.-L., Duprat, J., Malaizé, B., Joli, C., Cortijo, E., Drago, T. and Freitas, M., 2007. Present-day and past (last 25 000 years) marine pollen signal off western Iberia. Marine Micropaleontology, 62(2): 91-114.

Neugebauer, I., Brauer, A., Dräger, N., Dulski, P., Wulf, S., Plessen, B., Mingram, J., Herzschuh, U. and Brande, A., 2012. A Younger Dryas varve chronology from the Rehwiese palaeolake record in NE-Germany. Quaternary Science Reviews, 36: 91-102.

Obert, J.C., Scholz, D., Felis, T., Brocas, W.M., Jochum, K.P. and Andreae, M.O., 2016. ^{230}Th/U dating of Last Interglacial brain corals from Bonaire (southern Caribbean) using bulk and theca wall material. Geochimica et Cosmochimica Acta, 178: 20-40.

Oster, J.L., Montanez, I.P., Guilderson, T.P., Sharp, W.D. and Banner, J.L., 2010. Modeling speleothem δ^{13}C variability in a central Sierra Nevada cave using 14C and 87Sr/86Sr. Geochimica et Cosmochimica Acta, 74(18): 5228-5242.

Pearce, C., Seidenkrantz, M.-S., Kuijpers, A., Massé, G., Reynisson, N.F. and Kristiansen, S.M., 2013. Ocean lead at the termination of the Younger Dryas cold spell. Nature communications, 4(1): 1664.

Peyron, O., Bégeot, C., Brewer, S., Heiri, O., Magny, M., Millet, L., Ruffaldi, P., Van Campo, E. and Yu, G., 2005. Late-Glacial climatic changes in Eastern France (Lake Lautrey) from pollen, lake-levels, and chironomids. Quaternary Research, 64(2): 197-211.

Rach, O., Brauer, A., Wilkes, H. and Sachse, D., 2014. Delayed hydrological response to Greenland cooling at the onset of the Younger Dryas in western Europe. Nature Geoscience, 7(2): 109-112.

Rasmussen, S.O., Bigler, M., Blockley, S.P., Blunier, T., Buchardt, S.L., Clausen, H.B., Cvijanovic, I., Dahl-Jensen, D., Johnsen, S.J., Fischer, H., Gkinis, V., Guillevic, M., Hoek, W.Z., Lowe, J.J., Pedro, J.B., Popp, T., Seierstad, I.K., Steffensen, J.P., Svensson, A.M., Vallelonga, P., Vinther, B.M., Walker, M.J.C., Wheatley, J.J. and Winstrup, M., 2014. A stratigraphic framework for abrupt climatic changes during the Last Glacial period based on three synchronized Greenland ice-core records: refining and extending the INTIMATE event stratigraphy. Quaternary Science Reviews, 106: 14-28.

Rehfeld, K., Trachsel, M., Telford, R.J. and Laepple, T., 2016. Assessing performance and seasonal bias of pollen-based climate reconstructions in a perfect model world. Climate of the Past, 12(12): 2255-2270.

Reinig, F., Wacker, L., Jöris, O., Oppenheimer, C., Guidobaldi, G., Nievergelt, D., Adolphi, F., Cherubini, P., Engels, S. and Esper, J., 2021. Precise date for the Laacher See eruption synchronizes the Younger Dryas. Nature, 595(7865): 66-69.

Richards, D.A. and Dorale, J.A., 2003. Uranium-series chronology and environmental applications of speleothems. Reviews in Mineralogy and Geochemistry, 52(1): 407-460.

Richter, D.K. and Riechelmann, D.F.C., 2008. Late Pleistocene cryogenic calcite spherolites from the Malachitdom Cave (NE Rhenish Slate Mountains, Germany): origin, unusual internal structure and stable CO isotope composition. International Journal of Speleology, 37(2): 5.

Schenk, F., Väliranta, M., Muschitiello, F., Tarasov, L., Heikkilä, M., Björck, S., Brandefelt, J., Johansson, A.V., Näslund, J.-O. and Wohlfarth, B., 2018. Warm summers during the Younger Dryas cold reversal. Nature Communications, 9(1): 1634.

Scholz, D., Frisia, S., Borsato, A., Spötl, C., Fohlmeister, J., Mudelsee, M., Miorandi, R. and Mangini, A., 2012. Holocene climate variability in north-eastern Italy: potential influence of the NAO and solar activity recorded by speleothem data. Climate of the Past, 8(4): 1367-1383.

Scholz, D. and Hoffmann, D., 2008. ^{230}Th/U-dating of fossil corals and speleothems. E&G Quaternary Science Journal, 57(1/2): 52-76.

Scholz, D. and Hoffmann, D.L., 2011. StalAge–An algorithm designed for construction of speleothem age models. Quaternary Geochronology, 6(3-4): 369-382.

Schwarcz, H.P., Harmon, R.S., Thompson, P. and Ford, D.C., 1976. Stable isotope studies of fluid inclusions in speleothems and their paleoclimatic significance. Geochimica et Cosmochimica Acta, 40(6): 657-665.

Steffensen, J.P., Andersen, K.K., Bigler, M., Clausen, H.B., Dahl-Jensen, D., Fischer, H., Goto-Azuma, K., Hansson, M., Johnsen, S.s.J. and Jouzel, J., 2008. High-resolution Greenland ice core data show abrupt climate change happens in few years. Science, 321(5889): 680-684.

Thompson, A.J., Zhu, J., Poulsen, C.J., Tierney, J.E. and Skinner, C.B., 2022. Northern Hemisphere vegetation change drives a Holocene thermal maximum. Science advances, 8(15): eabj6535.

Tremaine, D.M., Froelich, P.N. and Wang, Y., 2011. Speleothem calcite farmed in situ: Modern calibration of $\delta^{18}O$ and $\delta^{13}C$ paleoclimate proxies in a continuously-monitored natural cave system. Geochimica et Cosmochimica Acta, 75(17): 4929-4950.

Van Raden, U.J., Colombaroli, D., Gilli, A., Schwander, J., Bernasconi, S.M., van Leeuwen, J., Leuenberger, M. and Eicher, U., 2013. High-resolution late-glacial chronology for the Gerzensee lake record (Switzerland): $\delta^{18}O$ correlation between a Gerzensee-stack and NGRIP. Palaeogeography, Palaeoclimatology, Palaeoecology, 391: 13-24.

Wanner, H., 2021. Late-Holocene: cooler or warmer? The Holocene, 31(9): 1501-1506.

Weber, K., Weber, M., Menneken, M., Kral, A.G., Mertz-Kraus, R., Geisler, T., Vogl, J. and Tütken, T., 2021. Diagenetic stability of non-traditional stable isotope systems (Ca, Sr, Mg, Zn) in teeth–An in-vitro alteration experiment of biogenic apatite in isotopically enriched tracer solution. Chemical Geology, 572: 120196.

Weber, M., Lugli, F., Jochum, K.P., Cipriani, A. and Scholz, D., 2018. Calcium carbonate and phosphate reference materials for monitoring bulk and microanalytical determination of Sr isotopes. Geostandards and Geoanalytical Research, 42(1): 77-89.

Weber, M., Tacail, T., Lugli, F., Clauss, M., Weber, K., Leichliter, J., Winkler, D.E., Mertz-Kraus, R. and Tütken, T., 2020. Strontium uptake and intra-population 87Sr/86Sr variability of bones and teeth—controlled feeding experiments with rodents (Rattus norvegicus, Cavia porcellus). Frontiers in Ecology and Evolution, 8: 569940.

Weber, M., Wassenburg, J.A., Jochum, K.P., Breitenbach, S.F., Oster, J. and Scholz, D., 2017. Sr-isotope analysis of speleothems by LA-MC-ICP-MS: High temporal resolution and fast data acquisition. Chemical Geology, 468: 63-74.

Wohlfarth, B., Hannon, G., Feurdean, A., Ghergari, L., Onac, B.P. and Possnert, G., 2001. Reconstruction of climatic and environmental changes in NW Romania during the early part of the last deglaciation (~ 15,000–13,600 cal yr BP). Quaternary Science Reviews, 20(18): 1897-1914.

Wolff, C., Plessen, B., Dudashvilli, A.S., Breitenbach, S.F., Cheng, H., Edwards, L.R. and Strecker, M.R., 2017. Precipitation evolution of Central Asia during the last 5000 years. The Holocene, 27(1): 142-154.

Wynn, P.M., Fairchild, I.J., Frisia, S., Spötl, C., Baker, A. and Borsato, A., 2010. High-resolution sulphur isotope analysis of speleothem carbonate by secondary ionisation mass spectrometry. Chemical Geology, 271(3-4): 101-107.

Yang, Q., Scholz, D., Jochum, K.P., Hoffmann, D.L., Stoll, B., Weis, U., Schwager, B. and Andreae, M.O., 2015. Lead isotope variability in speleothems—A promising new proxy for hydrological change? First results from a stalagmite from western Germany. Chemical Geology, 396: 143-151.

Zhang, W., Wu, H., Cheng, J., Geng, J., Li, Q., Sun, Y., Yu, Y., Lu, H. and Guo, Z., 2022. Holocene seasonal temperature evolution and spatial variability over the Northern Hemisphere landmass. Nature Communications, 13(1): 5334.

Zhou, H., Feng, Y.-x., Zhao, J.-x., Shen, C.-C., You, C.-F. and Lin, Y., 2009. Deglacial variations of Sr and 87Sr/86Sr ratio recorded by a stalagmite from Central China and their association with past climate and environment. Chemical Geology, 268(3-4): 233-247.

Supplementary Material for

A high-resolution multi-proxy speleothem record covering the last 14 ka – the progression of Termination I and the Holocene in Central Europe

paper in preparation

5.9 Supplementary material

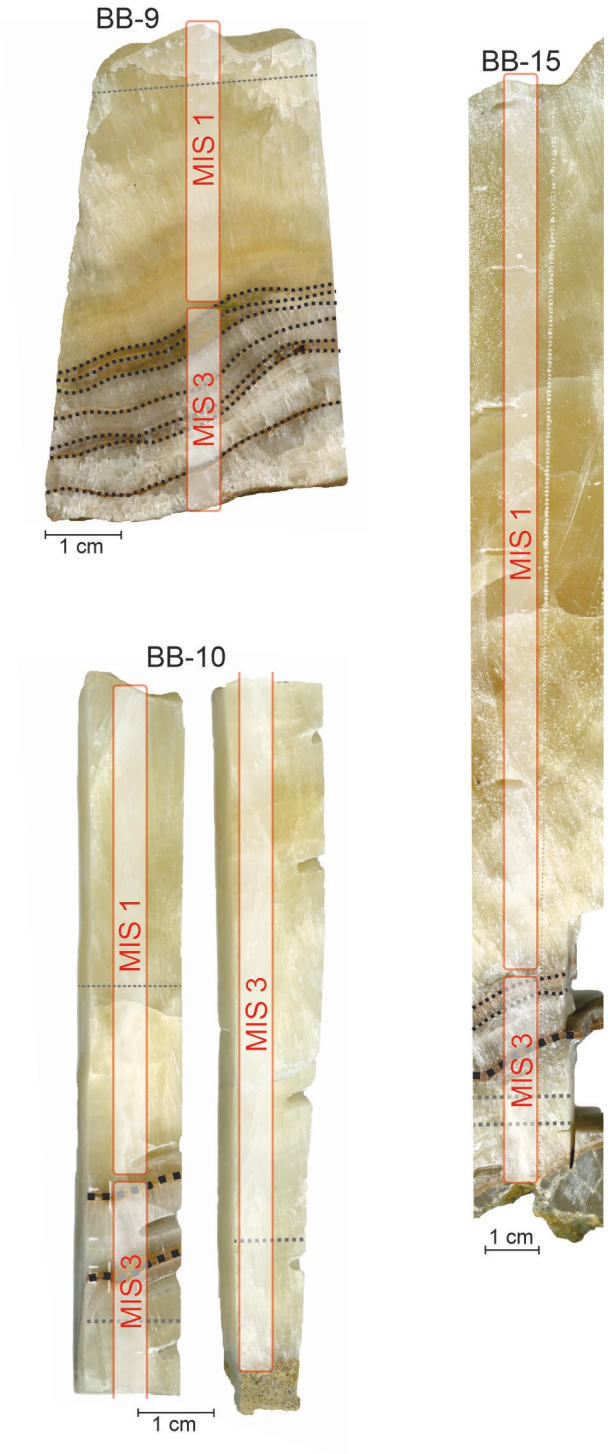

Fig. S5.1: Scans of samples BB-9, BB-10 and BB-15. All growth stops of the samples are highlighted, the black dotted lines indicate growth stops, which are visually detectable, the grey dotted lines indicate growth stops identified based on the ^{230}Th/U-ages and age models. MIS 1 und MIS 3 areas of the samples are indicated with the boxes.

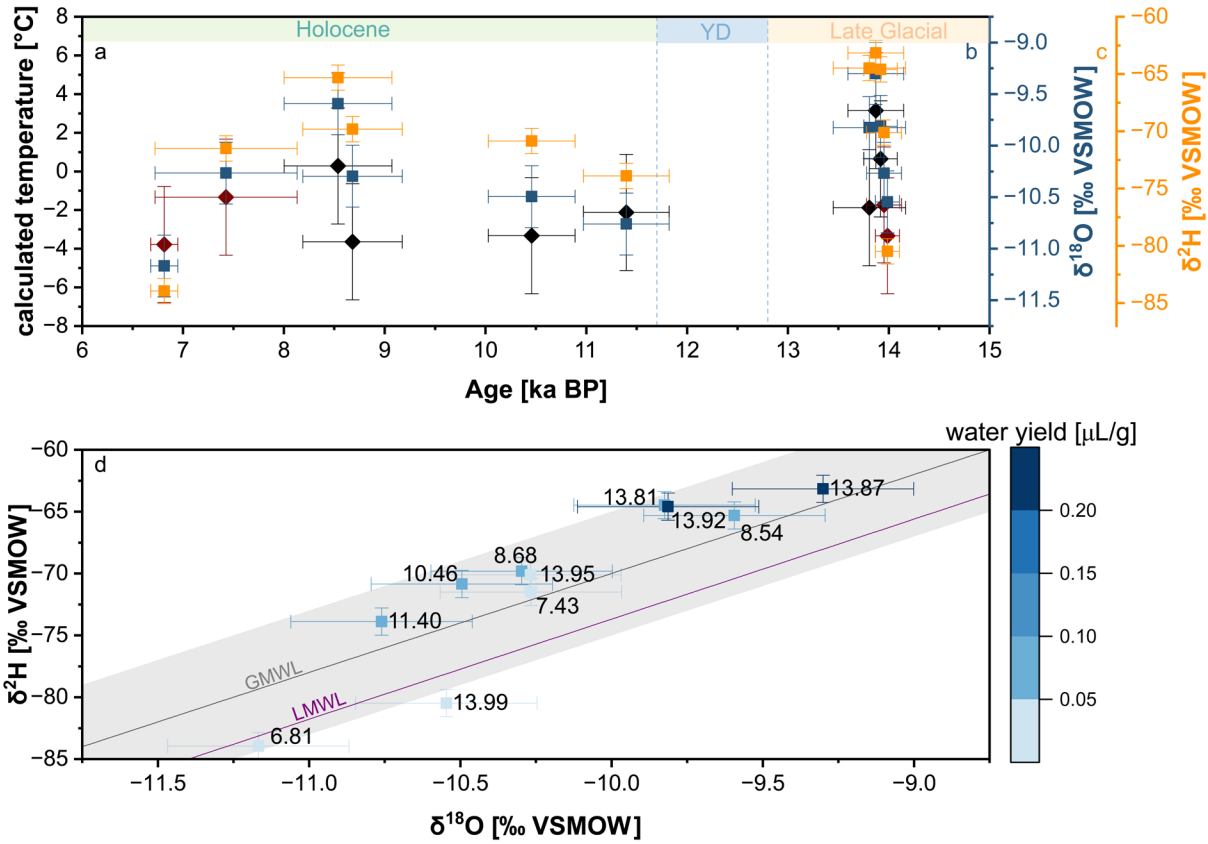

Fig. S5.2: Overview of estimated temperatures and fluid inclusion $\delta^{18}O$ and $\delta^{2}H$ of sample BB-10. All measurements are based on sample BB-10. Estimated temperatures in a are based on measured fluid inclusion $\delta^{18}O$ (b and c) Measurements with < 0.05 µL/g water yield were indicated in red in a because these low water concentrations are at the limit of the method. Those data points often plot far off the GMWL or LMWL, which is the case for two out of four. The remaining data plots close to the GMWL/LMWL, even though the water yield is generally low and are therefore included in the study.

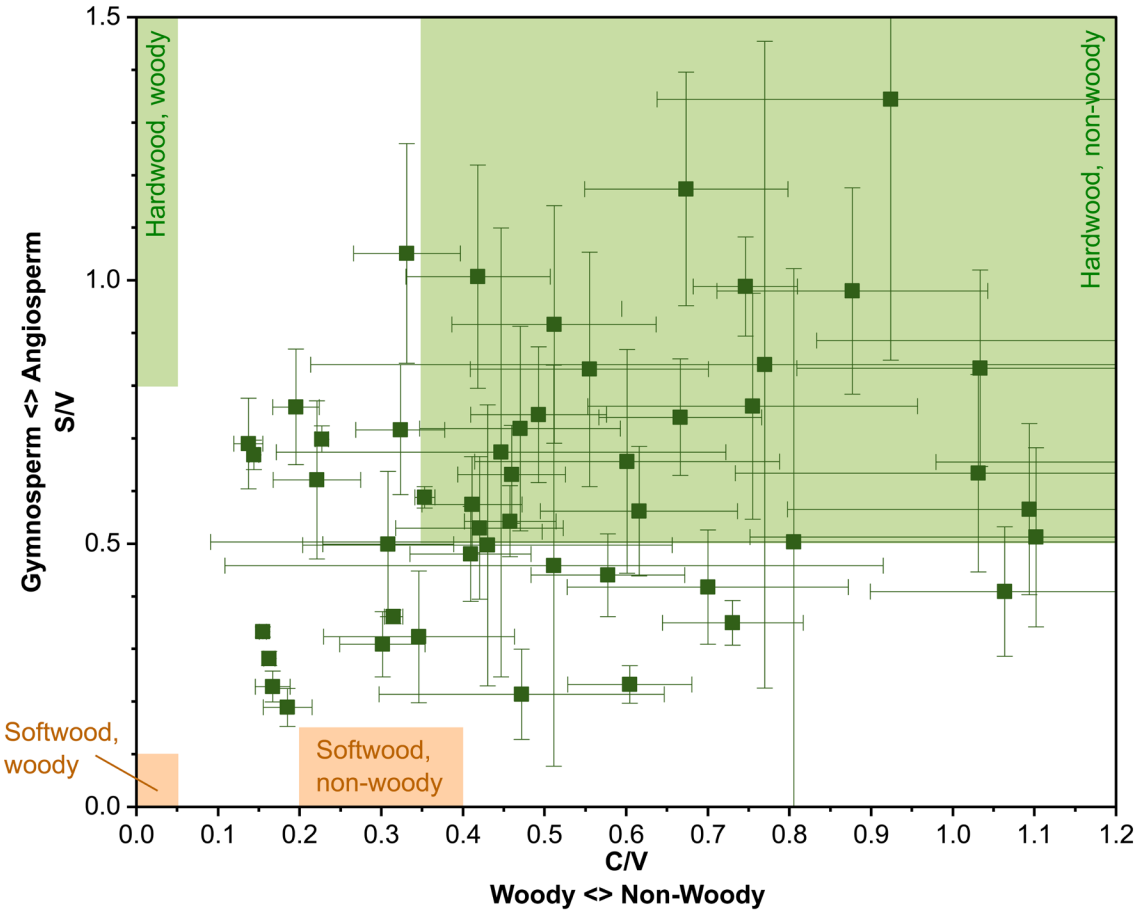

Fig. S5.3: S/V and C/V ratios of lignin oxidation products in sample BB-15 during the Holocene and late Glacial. Vegetation types are indicated by shaded boxes, based on the experimental differentiation of (Hedges and Mann, 1979).

Chapter 6: Manuscript IV

ITL dating of speleothems – A case study from Bleßberg cave, Germany

Junjie Zhang[1*], Jennifer Klose[2], Sumiko Tsukamoto[1], Denis Scholz[2], Norbert Marwan[3], Sebastian F. M. Breitenbach[4], Lutz Katzschmann[5], Dennis Kraemer[6]

*corresponding author: Junjie.Zhang@leibniz-liag.de

[1] Leibniz Institute for Applied Geophysics (LIAG), 30655 Hannover, Germany

[2] Institute for Geosciences, University of Mainz, 55128 Mainz, Germany

[3] Potsdam Institute for Climate Impact Research (PIK), Member of the Leibniz Association, 14473 Potsdam, Germany

[4] Department of Geography and Environmental Sciences, Northumbria University, Newcastle, UK

[5] Thuringian State office for the Environment, Mining and Nature Conservation (TLUBN), 07745 Jena, Germany

[6] Federal Institute for Geosciences and Natural Resources (BGR), 30655 Hannover, Germany

submitted in similar form to Quaternary Geochronology

Abstract

Speleothems are a key archive of past climatic and environmental changes. ^{230}Th/U dating is the most commonly used method to determine speleothem ages. However, incorporation of non-radiogenic thorium may hamper ^{230}Th/U dating, and samples older than 600 ka also remain out-of-reach. Calcite exhibits a thermoluminescence (TL) signal at 280 °C with a high characteristic saturation dose, and provides great potential to date carbonate samples over several million years. Hitherto, the application of TL dating has been hindered by two key factors: 1) a spurious TL signal occurring in the high temperature range, and 2) unstable dose rate due to U-series disequilibrium.

Here we test an isothermal TL (ITL) dating method on a speleothem sample from Bleßberg cave, Germany, which has been accurately dated by the ^{230}Th/U-method between 425.6 ± 3.9 and 321.6 ± 2.0 ka. ITL signal measured at 235 °C can completely remove the 280 °C TL peak with a negligible TL contribution from the higher temperature range, thus reducing the influence from the spurious signal. The time-dependent dose rate variation is simulated using the initial radioactivity of ^{238}U, ^{234}U, ^{230}Th and their decay constants. For four subsamples tested with the ITL method, three of them have ITL ages consistent with the ^{230}Th/U ages at isochronous sampling positions.

6.1 Introduction

Speleothems are secondary carbonate precipitated from dripwater in caves mostly in limestone or dolomite bedrock (Moore, 1952). The wide distribution of speleothems and their exceptional suitability for high accuracy and precision ^{230}Th/U dating make them extraordinary terrestrial archives of past climatic and environmental changes (Henderson, 2006; Scholz and Hoffmann, 2008; Cheng et al., 2016). However, ^{230}Th/U dating has an upper limit of approximately 600 ka (e.g., Scholz and Hoffmann, 2008; Cheng et al., 2016), and it is not applicable for samples older than 600 ka and for samples with incorporation of non-radiogenic thorium. U-Pb dating is also applicable for speleothem samples with millions of years in ages (Richards et al., 1998; Woodhead et al., 2006; Pickering et al., 2010; Woodhead and Petrus, 2019). However, U-Pb requires samples with high U and low common Pb, and the majority of speleothem samples is not suitable for U-Pb dating.

Thermoluminescence (TL) dating has been performed on calcite from various geological backgrounds, such as speleothem, limestone, calcite vein, and biogenic carbonate (Aitken and Bussell, 1982; Aitken and Wintle, 1977; Debenham, 1983; Duller et al., 2009; Engin and Guven, 1997; Franklin et al., 1988; Ninagawa et al., 1992; Ninagawa et al., 1994; Wintle, 1975, 1978). Its characteristic TL peak at ~280 °C (with a heating rate of 5 °C/s) is mostly applied for dating. Despite of the low precision of TL dating compared to the ^{230}Th/U dating method, TL dating has the potential to date over millions of years because of the high saturation dose (up to 5000 Gy) of the TL signal (Wintle, 1978; Debenham, 1983; Debenham and Aitken, 1984; Duller et al., 2009; Stirling et al., 2012; Zhang and Wang, 2020). However, several drawbacks of TL dating with calcite have hindered its application. One obstacle is the existence of a spurious TL signal at the high temperature range (Wintle, 1975; Bangert and Henning, 1979; Pagonis et al., 1997). The spurious TL signal is not related to radiation, and its existence will result in overestimation of the equivalent dose (D_e). Some studies suggested that the spurious TL signal was caused by the mechanic damage of the grain surface during the pretreatment of the calcite sample, such as grinding, and applying acetic etching to remove the surface layer of the calcite grains indeed helped to suppress the spurious signal (Wintle, 1975, 1978; Ninagawa et al., 1988). However, in some studies, the etching treatment failed to remove the spurious TL signal completely (Bangert and Hennig, 1979; Pagonis et al., 1997), and other hypotheses have been proposed for the origin of the spurious TL signal, such as the presence of trapped

organic matter (Bangert and Hennig, 1979; Rogue et al., 2001; Liao et al., 2014), oxygen absorption and desorption (Bangert and Hennig, 1979) and carbonate decomposition during heating (Rogue et al., 2001). It has also been suggested that after being removed by heating, the spurious TL signal can still be regenerated after several days of storage (Pagonis et al., 1997). Another drawback for TL dating of calcite is that the multiple-aliquot additive-dose protocol (MAAD) is usually needed for D_e measurements (Wintle, 1978; Debenham, 1983; Debenham and Aitken, 1984; Yee and Mo, 2018), as heating to a high temperature (e.g. 400 °C) will change the luminescence sensitivity significantly. The MAAD protocol consumes large amounts of sample, and has a larger error in D_e estimation. Moreover, as the MAAD applies extrapolation to get the D_e, it is not applicable to very old samples (e.g. >1 Ma). A third drawback is the difficulty in dose rate calculation for calcite samples, especially for speleothems, as the dose rate can change significantly over time due to U-series disequilibrium. In addition, for calcite samples, the alpha dose rate usually contributes most to the total dose rate, while very scattered alpha efficiency values have been reported for speleothem samples (Debenham and Aitken, 1984; Wintle, 1978).

Instead of heating the aliquots to a high temperature (e.g. 400 °C) to obtain the 280 °C TL peak, the aliquots can be kept at a relatively lower temperature (e.g. 230 °C) for long time to measure an isothermal TL (ITL) signal which is equivalent to the 280 °C TL peak. The ITL dating protocol has been widely applied for quartz (Murray and Wintle, 2000; Buylaert et al., 2006; Choi et al., 2006; Tsukamoto et al., 2007; Vandenberghe et al., 2009; Tang and Li, 2015; Rahimzadeh et al., 2023). As the ITL signals are measured at relatively lower temperatures, the luminescence sensitivity change is smaller and the single-aliquot regenerative-dose (SAR) protocol can be applied, which improves the accuracy and precision of D_e estimation compared to the MAAD protocol used for TL dating. Recent studies applied ITL measurements at 230 to 240 °C on calcite samples, and reported that the ITL SAR protocol has great potential to measure D_e accurately with negligible influence from the spurious signal (Zhang and Wang, 2020; Huang et al., 2022). However, hitherto the reliability of the ITL SAR protocol in dating calcite has not been tested on samples with independent age control.

In this study, we test the ITL SAR protocol on a speleothem sample from Bleßberg cave, Germany. ^{230}Th-U dating is performed on this speleothem sample which provides precise independent age control. The characteristics of the ITL signal and the 280 °C TL peak, such as signal stability and dose response curve, are studied. We apply both the ITL

SAR and TL MAAD protocols and compare their performance on D_e measurements. To obtain ITL ages, we calculate the annual dose year by year based on the initial radioactivity of ^{238}U, ^{234}U, ^{230}Th and their decay constants. Finally, the ITL ages are compared with the $^{230}Th/U$ ages to discuss the reliability of ITL dating.

6.2 Sample details

The Bleßberg cave is located in Thuringia, Germany (50°25′28″ N, 11°01′13″ E) (Fig. S6.1). The cave was discovered in March 2008 during the construction of a tunnel for the new railway line. The cave is overlain by 12 to 50 m thickness of Triassic marly limestone (Lower Muschelkalk/Anisium) (Breitenbach et al., 2019). Inside the cave, speleothems are widely developed. The cave had no natural entrances before the discovery in 2008, and had not been disturbed by animal or human activities, providing an ideal place for paleoclimate and paleoenvironmental reconstructions (Breitenbach et al., 2019). A heart shaped sample (BB2-1) was collected from the wall of the cave in 2008. The sample was cut into slices to reveal the growth bandings. Slices were prepared for different analyses, such as trace element mapping, isotopic analysis, $^{230}Th/U$ dating and ITL dating. The slice used for ITL dating is shown on Fig. 6.1.

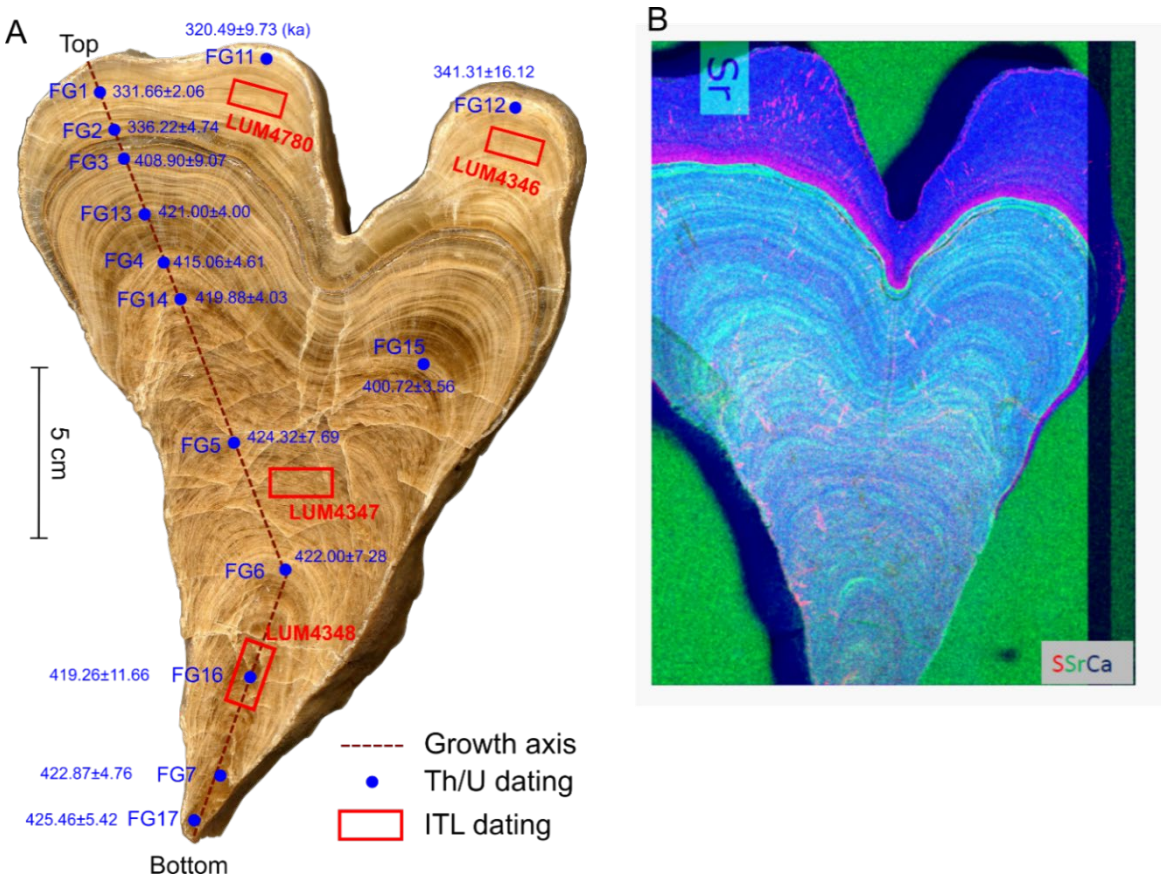

Fig. 6.1. The speleothem sample used in this study. A) Blue dots indicate sampling positions for ^{230}Th/U dating, and red squares indicate sampling positions for TL/ITL dating. B) Elements distribution revealed by μ-EDXRF analysis.

6.3 Petrologic study and trace elements mapping

Four subsamples were collected from one slice of BB2-1 (the same slice used for ITL dating), to perform X-ray diffraction (XRD) analyses with a PANalytical MPD Pro XRD equipment at the Federal Institute for Geosciences and Natural Resources (BGR), Hannover, Germany. Results show that the speleothem sample is pure calcite (Fig. S6.2). Two thin sections were prepared and observed under a petrographic microscope. The sample is compact and the grain sizes of the calcite crystals vary significantly at different positions, ranging from <100 μm to larger than 500 μm (Fig. S6.3).

Micro-energy dispersive X-ray fluorescence (μ-EDXRF) can generate 2D element distribution images that provide textural and spatially resolved chemical information

(Rammlmair et al., 2006). One slice of the speleothem was polished on the surface, and used for µ-EDXRF analysis. The X-ray was excited with an Rh tube with 50 kV and 600 µA. The beam diameter was 18 µm, and the element distribution images were recorded at a measuring distance of 40 µm with a measuring time of 1 ms per measuring point. The growth layers are clearly visible from the element distribution, and two major growth phases can be identified by their different element concentrations (Fig. 6.1B).

6.4 ^{230}Th/U-dating

^{230}Th/U dating was conducted at the Institute for Geosciences, Johannes Gutenberg University (JGU) Mainz. In total, fourteen ^{230}Th/U-ages were determined. Approximately 50 mg of sample material was drilled using a handheld drill and processed in a clean laboratory to separate U and Th. The samples were weighed, dissolved in 7N HNO_3 and subsequently spiked with a previously calibrated ^{229}Th-^{233}U-^{236}U spike solution. The samples were dried down, treated with concentrated HNO_3, HCl and H_2O_2 to destroy potential organic material and then again evaporated and dissolved in 7N HNO_3. The samples were further passed through ion exchange columns filled with 1.5 mL of Bio-Rad AG 1-X8 (200 – 400 mesh size) anion exchange resin following the procedure described in Klose et al. (in review). Mass spectrometric analyses of U and Th were conducted using a Thermo Fisher Neptune Plus multi-collector inductively coupled plasma mass spectrometer (MC-ICP-MS) equipped with an Elemental Scientific Apex Omega HF desolvator. U and Th were measured separately in a standard-bracketing procedure, and the data were corrected offline using an in-house R-script (R Core Team, 2022). All activity ratios and ages were calculated using the decay constants of Cheng et al. (2013). To account for potential detrital contamination, the ages were corrected assuming an upper continental crust ^{232}Th/^{238}U weight ratio of 3.8 ± 1.9 (Wedepohl, 1995) and secular equilibrium between ^{230}Th, ^{234}U, and ^{238}U. Details of the measurements can be found in Klose et al (in review).

The Th/U results are summarised in Table 1. Ten Th/U ages are from Marine Isotope Stage (MIS) 11 and four ages are from MIS 9.

Table 6.1. Results of the ^{230}Th/U-dating. Activity ratios are indicated by []. $[^{234}U/^{238}U]_0$ is the initial activity ratio of ^{234}U and ^{238}U when the speleothem crystallised. Age errors are 2σ.

Sample ID	^{238}U (ppm)	^{232}Th (ppb)	$[^{234}U/^{238}U]$	$[^{230}Th/^{238}U]$	$[^{234}U/^{238}U]_0$	$age_{uncorrected}$ (ka)	$age_{corrected}$ (ka)
FG1	0.5325 ± 0.0036	5.134 ± 0.035	1.6035 ± 0.0009	1.7178 ± 0.0020	2.54 ± 0.01	331.77 ± 1.76	331.66 ± 2.06
FG2	0.2815 ± 0.0021	8.272 ± 0.062	1.8593 ± 0.0034	2.0487 ± 0.0049	3.22 ± 0.03	336.47 ± 2.26	336.22 ± 4.74
FG3	0.5658 ± 0.0034	22.45 ± 0.137	1.4975 ± 0.0026	1.6415 ± 0.0038	2.58 ± 0.04	409.33 ± 3.61	408.90 ± 9.07
FG4	0.8743 ± 0.0075	5.677 ± 0.049	1.5180 ± 0.0007	1.6723 ± 0.0023	2.67 ± 0.02	415.13 ± 4.26	415.06 ± 4.61
FG5	0.8868 ± 0.0057	24.83 ± 0.160	1.5283 ± 0.0020	1.6911 ± 0.0030	2.75 ± 0.03	424.61 ± 3.38	424.32 ± 7.69
FG6	0.8312 ± 0.0060	21.85 ± 0.158	1.5318 ± 0.0018	1.6947 ± 0.0029	2.75 ± 0.03	422.27 ± 3.48	422.00 ± 7.28
FG7	0.9150 ± 0.0057	12.12 ± 0.075	1.5521 ± 0.0011	1.7224 ± 0.0021	2.82 ± 0.02	423.00 ± 3.46	422.87 ± 4.76
FG11	0.3875 ± 0.0023	35.36 ± 0.213	1.5195 ± 0.0062	1.5994 ± 0.0074	2.28 ± 0.03	321.61 ± 1.97	320.49 ± 9.73
FG12	0.4120 ± 0.0026	53.11 ± 0.341	1.5240 ± 0.0089	1.6265 ± 0.0108	2.37 ± 0.05	342.86 ± 2.34	341.31 ± 16.12
FG13	0.5553 ± 0.0032	3.934 ± 0.022	1.5393 ± 0.0007	1.7042 ± 0.0019	2.77 ± 0.02	421.07 ± 3.56	421.00 ± 4.00
FG14	0.8164 ± 0.0056	5.195 ± 0.036	1.5294 ± 0.0007	1.6903 ± 0.0019	2.73 ± 0.02	419.95 ± 3.68	419.88 ± 4.03
FG15	0.6938 ± 0.0062	2.487 ± 0.022	1.5161 ± 0.0006	1.6615 ± 0.0020	2.60 ± 0.02	400.76 ± 3.40	400.72 ± 3.56
FG16	0.8940 ± 0.0053	41.30 ± 0.244	1.5572 ± 0.0033	1.7273 ± 0.0047	2.82 ± 0.05	419.72 ± 3.54	419.26 ± 11.66
FG17	0.8187 ± 0.0048	12.35 ± 0.072	1.5584 ± 0.0012	1.7323 ± 0.0023	2.86 ± 0.03	425.60 ± 3.87	425.46 ± 5.42

6.5 Luminescence dating

6.5.1 Sample preparation and instrumentation

Sample preparation and luminescence measurements were performed at the Leibniz Institute for Applied Geophysics (LIAG), Hannover. Four subsamples (LUM4346, 4347, 4348, 4780) were cut with a saw from the center, middle and outer rim of one slice of speleothem BB2-1 (Fig. 6.1A). Sample preparation was performed under subdued red light. The surface of the subsamples was etched with hydrochloric acid (10 %) to avoid effects of light exposure. The remaining pieces were gently crushed under water and wet sieved to separate grains with a size of 100 to 200 μm. These grains were mounted on stainless steel discs, to prepare the aliquots (6 mm diameter) for luminescence measurements. Measurements were performed on a Risø TL/OSL DA 15 reader. A $^{90}Sr/^{90}Y$ beta source is mounted inside the reader, with a dose rate of 0.121 Gy/s for coarse grains. The TL glow curves and the ITL signals were measured in an N_2 atmosphere. Heating rates were 5 °C/s if not specified otherwise. The signals were detected through a single 4-mm thick Schott BG-39 filter (transmission band of 350 to 600 nm).

6.5.2 Equivalent dose measurements

6.5.2.1 MAAD protocol

The MAAD protocol was tested with the TL peak signal at 280 °C (details in Table 6.2). Weights of aliquots were measured for mass normalisation (Debenham and Aitken, 1984; Wintle, 1978). Meanwhile, two kinds of low-temperature TL peak normalisation methods were tested for LUM4347. The aliquots were firstly given a small test dose (5 Gy), followed by heating to 200 °C to measure the corresponding low-temperature TL peak at ca. 100 °C (T_1). The aliquots were then divided into several groups, given different additive doses (from 0 to 600 Gy). Aliquots were heated to 250 °C to remove the unstable low-temperature TL signal. Small test doses (5 Gy) were then administered again. TL glow curves were measured at up to 400 °C with background subtraction. In this step, the glow curve contains the 280 °C TL peak (L_x) corresponding to the natural plus additive dose and the 100 °C TL

peak corresponding to the small dose (T_2) (Fig. 6.2). The T_1 and T_2 signals were integrated from 80 to 120 °C, and the L_x signals from 270 to 290 °C.

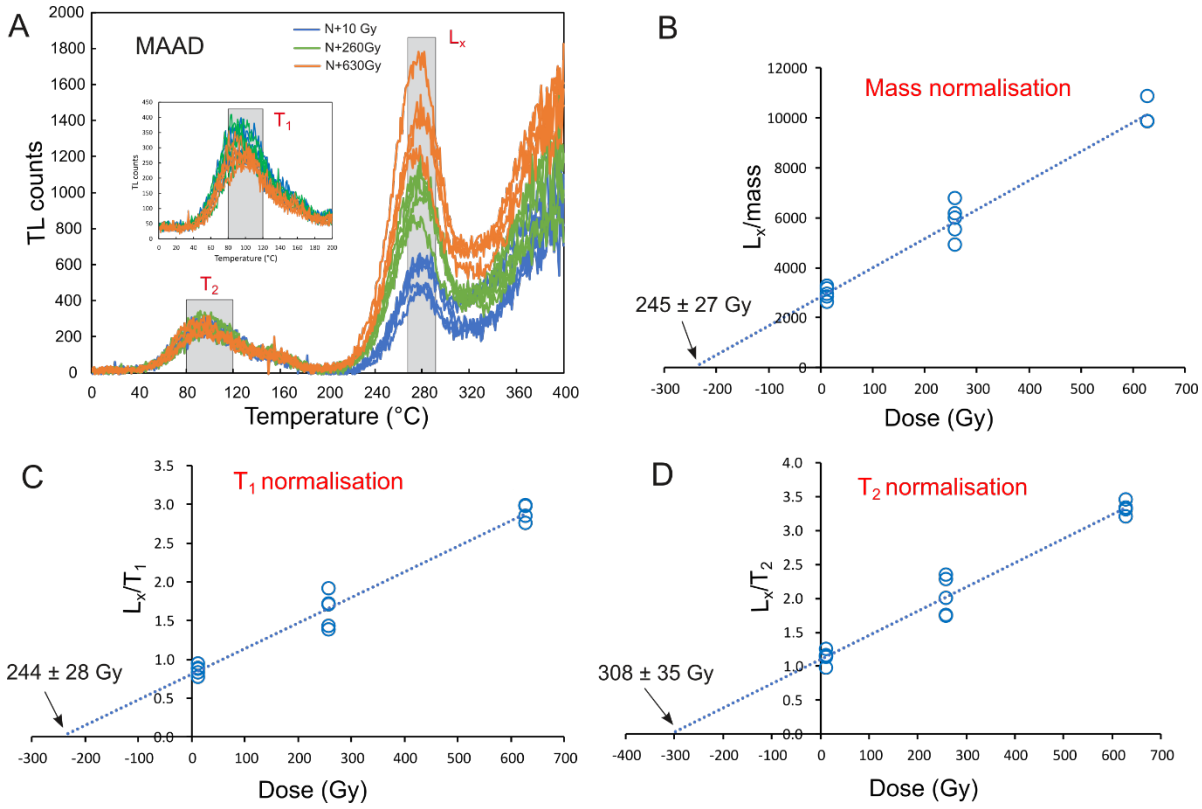

Fig. 6.2. MAAD D_e estimation for the 280 °C TL peak of LUM4347. A) TL curves of aliquots with different additive doses. The low-temperature TL peak at ~100 °C corresponds to a small dose (5 Gy). D_e estimation with mass normalisation (B), T_1 normalisation (C) and T_2 normalisation (D).

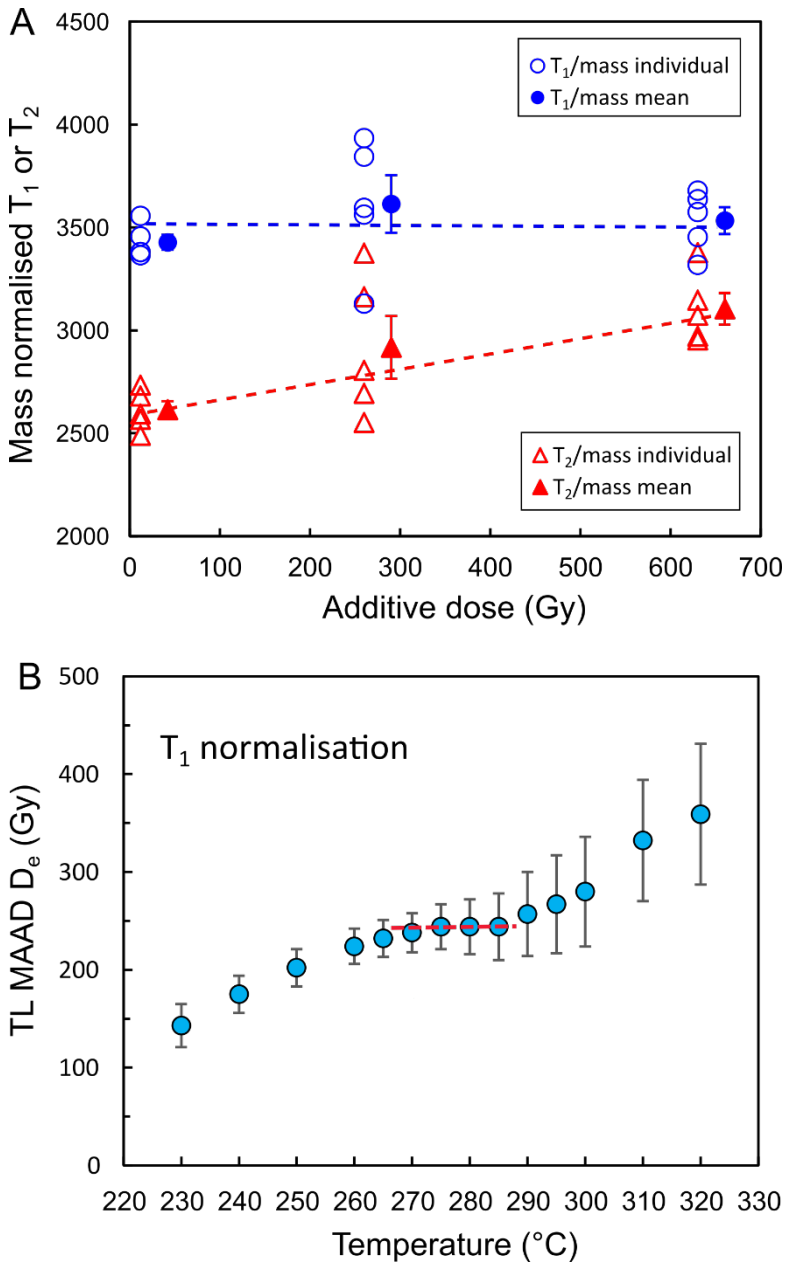

Fig. 6.3. A) Mass normalised T_1 and T_2 for LUM4347. Note that the sensitivity of T_2 increases with larger additive dose. B) MAAD D_e values for TL signals from different temperature ranges. Note that there is a D_e plateau between the temperature range between 270 and 285 °C.

The T_1 normalisation procedure is straightforward. T_1 represents the TL response to a fixed dose, which can represent the mass of the aliquot (Zhang and Tsukamoto, 2022). The T_2 normalisation is also called the zero glow monitoring (ZGM) technique (Aitken and

Bussell, 1979; Duller et al., 2009). An advantage of the ZGM normalisation is that the 280 °C TL peak used for dating and the 100 °C TL peak used for normalisation can be shown in the same glow curve (Fig. 6.2A). D_e was estimated with three different normalisation methods: mass normalisation, T_1 normalisation and T_2 normalisation (Fig. 6.2B-D). The two small test doses (a total of 10 Gy) were added to the additive doses when estimating the D_e values. The D_e results are 245 ± 27 Gy and 244 ± 28 Gy with mass normalisation and T1 normalisation, respectively, which are identical to each other. However, the T_2 normalisation gives a higher De of 308 ± 35 Gy, indicating that the T_2 normalisation (ZGM) is not a reliable method. Mass normalised T_1 is independent of the additive doses while mass normalised T_2 increases with larger additive doses (Fig. 6.3A). As the T_2 signal is measured after the additive dose administration, its intensity is influenced by the preceding additive dose. Such kind of 'pre-dose effect' on T_2 results in an underestimated slope on the L_x/T_2 vs. dose plot, and consequently an overestimated De. As the T_1 signal is measured before any treatments with all aliquots in their initial states, the T_1 normalisation is equivalent to mass normalisation in D_e estimation. However, T_1 normalisation is a more practical method as weighing aliquots is laborious and may risk grain loss.

Table 6.2. The MAAD protocol for D_e measurement with TL signal, and the SAR protocol for ITL_{235} signal.

MAAD			SAR		
Step	Treatments	Signal	Step	Treatments	Signal
1	Give a small test dose (5 Gy)		1	Regeneration dose (D_i, 0 Gy for the first cycle)	
2	Heat to 200 °C	T_1	2	Heat to 245 ºC	
3	Give additive dose, for different groups of aliquots		3	Isothermal TL at 235 ºC for 200s	L_x
4	Preheat to 250 °C		4	Test dose	
5	Give a small test dose (5 Gy)		5	Heat to 245 ºC	
6	TL to 400 °C with BG subtraction	T_2, L_x	6	Isothermal TL at 235 ºC for 200s	T_x
			7	Return to step 1	

With T_1 normalisation, MAAD D_e values were estimated with TL signals at different temperature intervals (T ± 10 °C, T from 230 to 320) for LUM4347. A De plateau is reached

when T is between 270 and 285 °C (Fig. 6.3B). The smaller D_e values in the lower temperature range are a result of lower thermal stability of the signals, whereas the larger D_e values in the higher temperature range are likely a consequence of a spurious TL signal. In this study, the samples underwent only mild crushing. Consequently, the impact of spurious TL signals on the 280 °C TL peak is minimal, allowing us to maintain a D_e plateau within the 270–285 °C range. MAAD D_e values were also measured for LUM4346 and LUM4348 with the T_1 normalisation method (Table 6.3).

Table 6.3. Results of TL/ITL dating. U concentrations are from line scan LA-ICP-MS measurements. The simulated and iterated ITL ages are calculated based on the ITL_{235} D_e. Errors of $^{230}Th/U$ ages are 2σ. Errors of ITL ages are 1σ.

LUM ID	Th/U ID	$[^{234}U/^{238}U]_0$	U (ppm)	$^{230}Th/U$ age (ka)	280°C TL D_e (Gy)	ITL_{235} D_e (Gy)	Iterated ITL age (ka)	Simulated ITL age (ka)
LUM4780	FG1	2.54 ± 0.01	0.42 ± 0.02	331.66 ± 2.06	na	99 ± 4	316 ± 21	316 ± 23
LUM4346	FG12	2.37 ± 0.05	0.65 ± 0.03	341.31 ± 16.12	169 ± 29	179 ± 6	381 ± 23	381 ± 24
LUM4347	FG5	2.75 ± 0.03	0.67 ± 0.02	424.32 ± 7.69	244 ± 28	236 ± 15	413 ± 32	413 ± 33
LUM4348	FG16	2.82 ± 0.05	0.87 ± 0.03	419.26 ± 11.66	264 ± 33	244 ± 10	350 ± 22	350 ± 23

6.5.2.1 SAR protocol

The net TL loss removed by ITL measurements at 235 °C (ITL_{235}) over 200 s is shown in Fig. 6.4A. The ITL_{235} signal can perfectly isolate the 280 °C TL peak with negligible contribution from the higher temperature range. The SAR dating protocol with the ITL measurement is listed in Table 6.2. It is adapted from Zhang and Wang (2020) with small modifications. The duration of ITL measurement is reduced from 500 s to 200 s, and the cleaning step at the end of each cycle (heated to 400 °C) in Zhang and Wang (2020) was also removed, as the ITL_{235} for 200 s can completely remove the 280 °C TL peak (Fig. 6.4A). The ITL_{235} curves of one aliquot of LUM4346 are shown on Fig. 6.4B, together with the dose-response curve (DRC) and the sensitivity changes between the SAR cycles. The ITL signals increase in the first 5 s because of the thermal lag between the heating plate and the disc, thus the 6 to 15 s signal is integrated for D_e estimation with the last 181 to 200 s signal subtracted as background. The DRC can be fitted with a single saturating exponential function which pass through origin, and the recycling ratio is very close to unity (Fig. 6.4B).

SAR D_e values were measured at different ITL temperatures for sample LUM4346, with 4 to 8 aliquots for each temperature. The SAR D_e values reach a plateau at the ITL temperature range between 230 and 240 °C (Fig. 6.4C). It is equivalent to the MAAD D_e plateau between 270 and 285 °C for the TL signal (Fig. 6.3B). Similarly, the smaller ITL D_e values below 230 °C can be attributed to lower thermal stability, whereas the larger D_e values observed above 240 °C are due to the influence of a spurious signal.

Dose recovery tests were performed on LUM4346 with a single aliquot regenerative additive dose (SARA) protocol. Three groups of aliquots were given doses of 120, 240, and 360 Gy on top of the natural dose. The aliquots were measured with the ITL_{235} SAR procedure. The recovered doses were plotted against the additive doses in Fig. 6.4D. The dose recovery ratio (DRR) is 0.99±0.02, indicating the reliability of D_e measurements for the ITL_{235} SAR protocol. SAR D_e values were also measured with the ITL_{235} signal for the other three subsamples (Table 6.3).

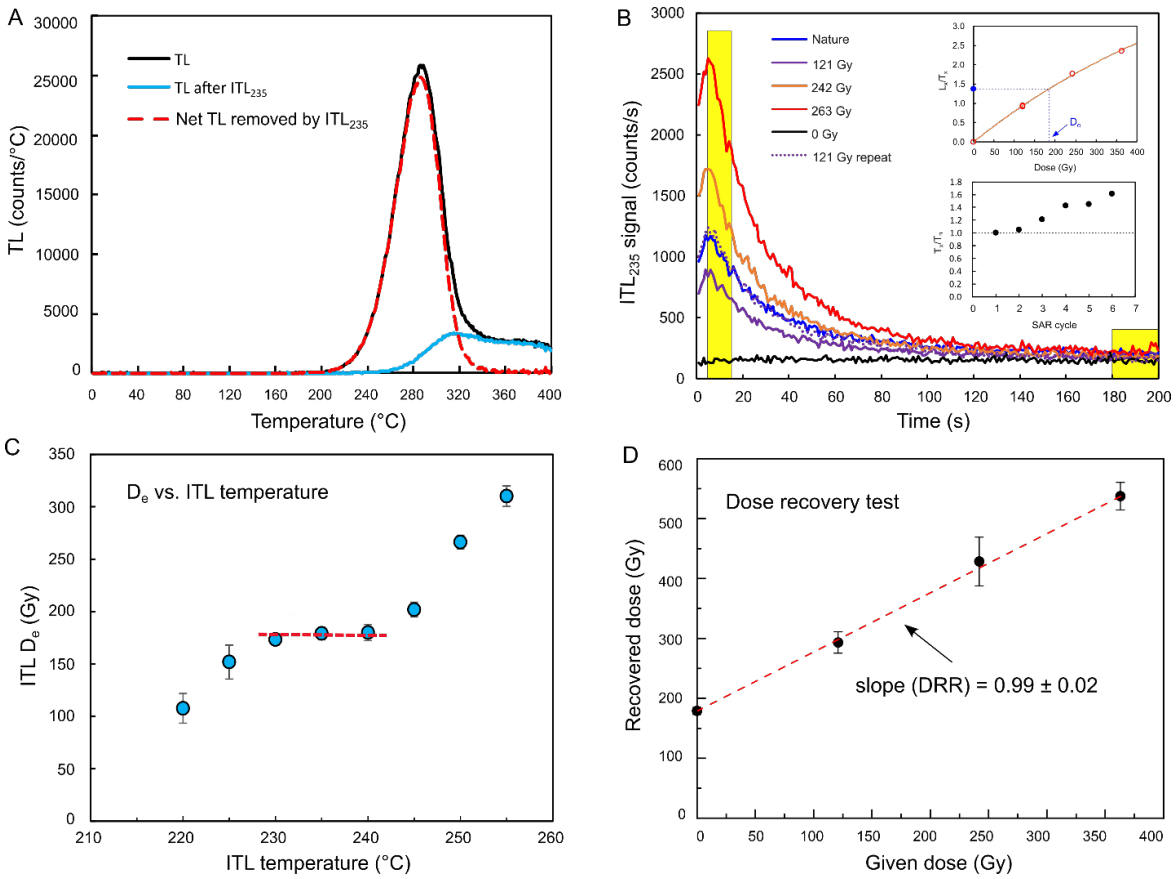

Fig. 6.4. A) Net TL signal removed by ITL measurement at 235 °C (ITL_{235}) for 200 s on an aliquot of LUM4347. The TL signal corresponds to a given dose of 120 Gy. B) ITL_{235} signals for an aliquot of LUM4346. Inset graphs are the dose-response curves of the aliquot,

and the sensitivity change with the cycles. C) SAR D_e values with ITL signals at different temperatures for LUM4346. The D_e at each temperature is an average of 4 – 8 aliquots. Error bar is 1σ. D) Dose recovery tests with the SARA protocol for ITL_{235} signal of sample LUM4346. Each data point is an average of 5 aliquots. Error bar is 1σ. The slope is the dose recovery ratio (DRR).

6.5.3 Luminescence characteristics

6.5.3.1 Thermal lifetime

Low thermal stability of a luminescence signal will result in age underestimation. To study the thermal lifetime of the 280 °C TL peak of the speleothem sample, the trap kinetic parameters were determined by both peak shifting and isothermal annealing methods. For peak shifting, two aliquots from sample LUM4347 were used. Aliquots were heated to 400 °C to remove the natural signals. A fixed regenerative dose of 360 Gy was administered to the aliquots. After being preheated to 250 °C (5 °C/s), the TL signals were measured up to 400 °C (with background subtraction) at various heating rates of 1.6, 0.8, 0.4, 0.2, and 0.1 °C/s (Fig. 6.5A). Heating rates used here are relatively low to minimise the thermal lag between the heating plate and the steel disc. The trap depths (E) are 1.76 and 1.77 eV, and the frequency factors (s) are 7.4×10^{15} and 1.1×10^{16} s^{-1} for the measured two aliquots, respectively. The mean temperature inside the Bleßberg cave is 8.7 ± 0.1 °C (Breitenbach et al., 2019). The calculated lifetimes of the 280 °C TL peak for the two aliquots are 74 and 93 Ma respectively, at a temperature of 10 °C.

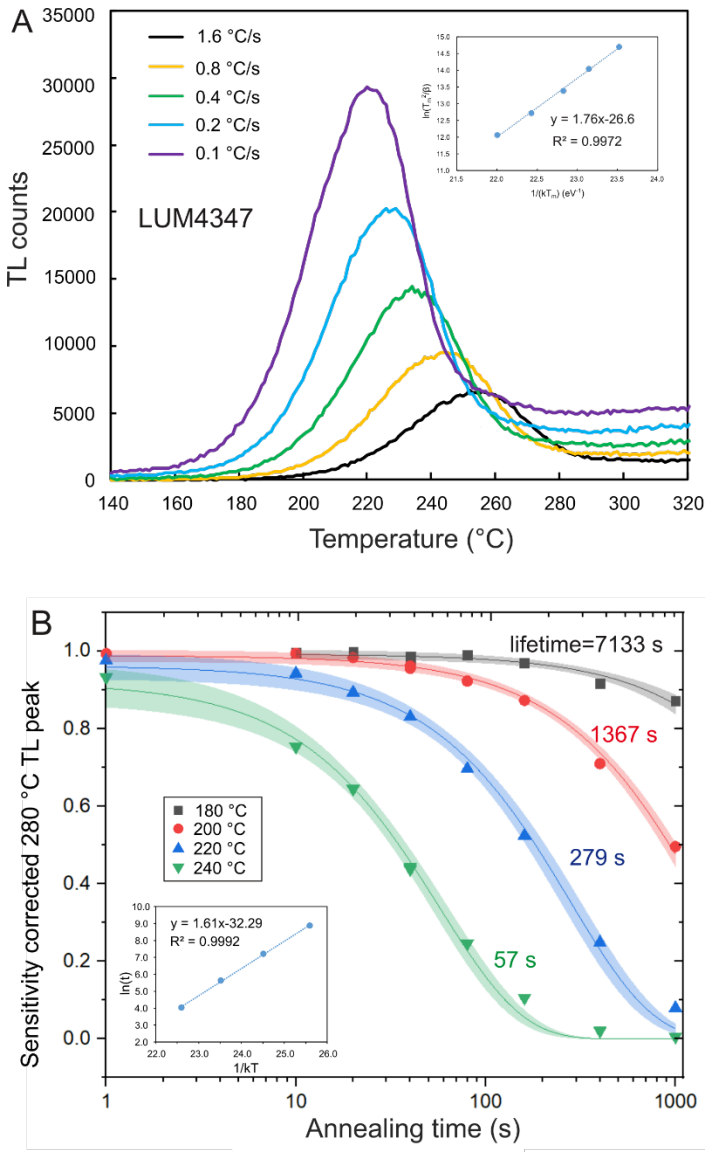

Fig. 6.5. Thermal lifetime measurements for the 280 °C TL peak. A) TL curves at different heating rates of one aliquot of LUM4347. The inset plot is to obtain the trap depth (E) and frequency factor (*s*). B) Isothermal annealing result for the same aliquot used in (A).

The same two aliquots were also applied for isothermal annealing tests to measure the thermal lifetime of the 280 °C TL peak. The regenerative dose and test dose were fixed at 120 Gy for the aliquots. After being preheated to 250 °C, the aliquots were exposed to different temperatures (180, 200, 220, and 240 °C) for different periods (1, 10, 20, 40, 80, 160, 400, 1000, and repeat 40 s), and the TL signals (up to 400 °C at 5°C/s) were measured afterwards. For the test dose signal, TL signals were measured directly after being preheated to 250 °C. The sensitivity corrected 280 °C TL peak signal decreased with longer annealing

time (Fig. 6.5B). With the isothermal annealing experiments, the E values for the 280 °C TL peak are 1.61 and 1.60 eV, and the *s* values are 1.06×10^{14} and 1.02×10^{14} s^{-1} for the two aliquots, respectively. The calculated lifetimes at 10 °C are 13 and 10 Ma, respectively.

We applied the arithmetic mean of E and geometric mean of *s* of the two aliquots to calculate the mean lifetime in each method for the 280 °C TL peak. The results are listed in Table S6.1, together with the lifetimes of the 280 °C TL peak reported by previous studies (Debenham, 1983; Engin and Guven, 1997; Stirling et al., 2012; Wintle, 1974; Wintle, 1977). The reported lifetimes of the 280 °C TL peak varied by two orders of magnitude, from 2 Ma to 200 Ma at 10 °C, which might be sample-dependent. In our study, the mean lifetime of 280 °C TL peak is 83 Ma with the peak shifting method or 12 Ma with the isothermal annealing method. The reason for the discrepancy between the lifetimes measured by two different methods is not clear. Assuming a lifetime of 12 Ma, the signal is still sufficiently stable for samples younger than 1.2 Ma. In case the sample age is older than 1.2 Ma, a lifetime correction procedure can be applied (Adamiec et al., 2010; Duller et al., 2015; Liu et al., 2016; Tsukamoto et al., 2018; Richter et al., 2020).

6.5.3.2 Anomalous fading

Anomalous fading is the athermal loss of signal, which is common for the TL and IRSL signals of feldspar (Wintle, 1973; Visocekas, 1985; Spooner, 1992, 1994;). The existence of anomalous fading will result in age underestimation. We performed fading tests for both the 280 °C TL peak and the ITL_{235} signal.

For the 280 °C TL peak, the multiple-aliquot method was applied. A total of 25 aliquots of LUM4346 were heated to 400 °C to remove the TL signal. The aliquots were irradiated with 240 Gy, preheated to 250 °C, and divided into 4 groups. After different delay times at room temperature for the four groups, the aliquots were heated to 400 °C to record the TL signals (L_x). Then, the aliquots were given a test dose of 120 Gy, preheated to 250 °C and immediately heated to 400 °C to record the TL signals (T_x). The sensitivity corrected signals (L_x/T_x) of the 280 °C TL peak of the aliquots were re-normalised by the mean L_x/T_x of the first group (with the shortest delay time, t_c), and the re-normalised signals were plotted against the delay times (Fig. S6.4A). The fading rate (g-value) was obtained from the slope

of the fitted linear regression. The g-value (t_c=0.3 h) obtained in this protocol is 0.53 ± 0.69 %.

The fading rate of the ITL_{235} signal was measured following the SAR procedure (Auclair et al., 2003). After being given 240 Gy and preheated to 245 °C, the aliquot was held at room temperature for different delay times, and the ITL_{235} signal was measured (Fig. S6.4B). A test dose of 240 Gy was given, and the ITL_{235} signal of the test dose was applied for sensitivity correction. A total of five aliquots of LUM4346 were measured with this procedure. The estimated g-values (t_c=0.3 h) varied between –2.4 %/decade to 2.2 %/decade, with a mean value of 0.03 ± 0.72 %/decade.

The fading rates of both the 280 °C TL peak and the IL_{235} signal are close to 0, indicating that the TL or ITL signals have no fading. Debenham and Aitken (1984) observed no measurable signal loss of the 280 °C TL peak of stalagmitic calcite within eight months after artificial irradiation. Huang et al. (2022) reported no detectable fading of the ITL_{235} signal for vein calcite crystals from a geological structure fracture. Our fading tests are consistent with previous studies, indicating that calcite samples are free of fading.

6.5.3.3 Saturation dose

DRCs were built for the 280 °C TL peak and the ITL_{235} signal of sample LUM4346. For the 280 °C TL peak, the multiple-aliquot regenerative-dose protocol (MAR) was applied. Five aliquots were heated to 400 °C to remove the natural signal. A small dose of 5 Gy is given to the aliquots and heated to 200 °C to record low-temperature TL signal, which would be used for inter-aliquot normalisation (T_1 normalisation). The aliquots were given doses of 0, 600, 1200, 2400, and 4800 Gy respectively, preheated to 250 °C, then heated to 400 °C (with BG subtraction) to record the 280 °C TL peak. The corresponding signal and the doses can be well fitted with a single saturating exponential function: $I=I_0*(1-\exp(-D/D_0))$, where I is the TL peak intensity, I_0 is the saturated signal, and D_0 is the characteristic saturation dose. The D_0 value of the 280 °C TL peak is 3950 ± 350 Gy (Fig. 6.6). For the ITL_{235} signal, DRCs were built with the SAR procedure with two different test doses (T_d) of 120 Gy and 360 Gy. With a T_d value of 120 Gy, the D_0 value is 1650 ± 110 Gy, which is significantly smaller than the D_0 of the 280 °C TL peak. However, with a T_d value of 360 Gy, D_0 is 3740 ± 250 Gy, close to the 280 °C TL peak.

The increase of D_0 with larger T_d indicates that the pre-dose effect can be reduced by a larger test dose.

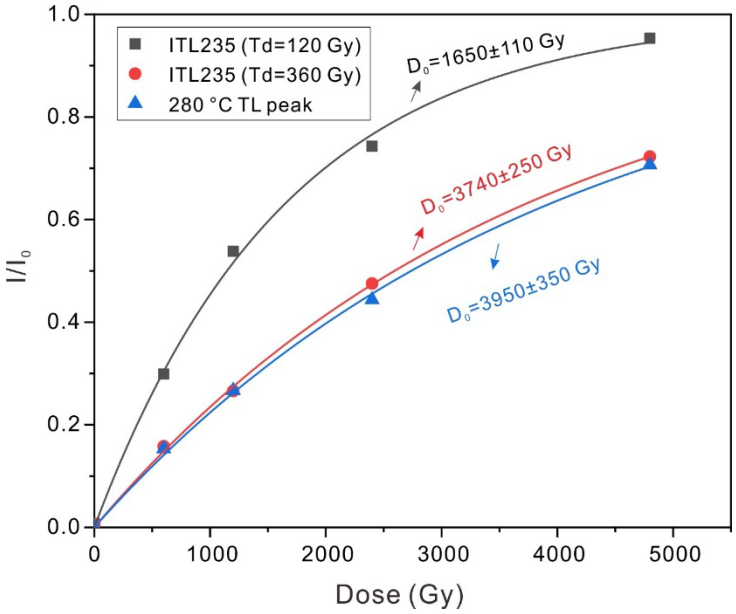

Fig. 6.6. Dose-response curves of the 280 °C TL peak and the ITL_{235} signal, fitted with a single saturating exponential function: $I=I_0*(1-\exp(-D/D_0))$. The characteristic saturation dose (D_0) of the 280 °C TL peak is 3950 ± 350 Gy. For the ITL_{235} signal, the D_0 is 1650 ± 110 Gy with a test dose of 120 Gy, and 3740 ± 250 Gy with a test dose of 360 Gy.

DRCs of the 280 °C TL peak have also been studied for snail opercula and the D_0 values of ~1500 Gy and ~13000 Gy were reported with two different SAR protocols (Duller et al., 2009; Stirling et al., 2012). DRCs for both 280 °C TL peak and ITL_{240} signal have been built with two travertine samples and two limestone samples in Zhang and Wang (2020), and the D_0 values are in the range of 3000 to 5000 Gy. Huang et al. (2022) reported D_0 values of 2000 to 2400 Gy for ITL signals at 230 and 235 °C for a limestone sample and a vein calcite sample. The D_0 values of the speleothem sample in this study (ca. 4000 Gy) are within the range of the previous studies, indicating the overall high saturation dose for calcite with different origins. Assuming a dating limit of $2*D_0$ (Wintle and Murray, 2006), the maximum D_e which can be measured with high reliability could be up to 8000 Gy for the speleothem samples. As the dose rates of speleothems are mostly smaller than 1.0 Gy/ka, the maximum dating range could reach 8 Ma, although lifetime correction might be needed in this case.

6.5.4 Dose rate and age estimation

6.5.4.1 U, Th, K measurements

6.5.4.1.1 "Whole rock" ICP-MS

To measure the U, Th and K concentrations, four subsamples which are adjacent to the ITL subsamples were analysed with an ICPMS instrument in the Laboratory of the Geochemistry Research Unit at BGR. The subsamples were ground into powder in an agate mortar. After drying at 110°C for a minimum of 12 hours, powder aliquots were digested with 5M HNO_3 to selectively decompose the carbonate fraction (Kraemer et al. 2021). For this, 250 mg aliquots of the dried powders were weighed into acid-cleaned Savillex PTFE beakers and 10 ml of 5 M HNO_3 (suprapure grade) were slowly added to each beaker. The beakers were closed and the suspension was heated to 70 °C on a hotplate for 2 hours. After cooling down to room temperature, the suspensions were filtered with acid/DI-cleaned filter syringes with a pore size of 0.2 µm. The filtered solutions were then diluted with DI to a final molarity of 1M HNO_3. For quality control, the certified reference material J-Ls1 (limestone; issued by the Geological Survey of Japan) was digested along with the samples. The carbonate extractions were measured with a Thermo Fisher iCAP TQ ICP-MS. Potassium was determined on m/z=39 in triple quadrupole mode with oxygen as reaction gas, whilst Th and U were measured in single quadrupole mode on m/z=232 and 238 in KED mode (kinetic energy discrimination) with He as cell gas. The elements Ru and Bi were used for internal standardisation. The measured concentrations of K in the reference standard were 63 ppm (reference: 25 to 83 ppm; georem Database; accessed on 12.05.2023). The measured concentrations of Th and U were 0.015 and 1.80 ppm (published literature values are 0.016 and 1.83 ppm; Dulski, 2001).

Table 6.4. Dose rates (Ḋ) at U-series equilibrium.

LUM ID	U* (ppm)	U[#] (ppm)	Th* (ppm)	K* (%)	Cosmic ray (Gy/ka)	Alpha (Gy/ka)	Beta (Gy/ka)	Gamma (Gy/ka)	Gamma[&] (Gy/ka)	Ḋ (Gy/ka)	1σ (Gy/ka)
LUM4780	0.65 ± 0.01	0.42 ± 0.02	0.007	0.0076	0.011	0.149	0.068	0.049	0.010	0.237	0.012
LUM4346	0.71 ± 0.02	0.65 ± 0.03	0.025	0.0077	0.011	0.232	0.102	0.076	0.015	0.360	0.019
LUM4347	1.03 ± 0.02	0.67 ± 0.02	0.012	0.0067	0.011	0.238	0.103	0.077	0.039	0.391	0.017
LUM4348	1.02 ± 0.01	0.87 ± 0.03	0.008	0.0060	0.011	0.308	0.132	0.099	0.020	0.471	0.022

*U, Th, K concentrations from 'whole rock' ICPMS measurements.

[#] U concentrations from line scan LA-ICP-MS measurements, which are used for dose rate calculation.

[&]For LUM4780, LUM4346, LUM4348, the gamma dose rates were taken as 20 % of the gamma dose rates in infinite medium. For LUM4347, the gamma dose rate was taken as 50 % of the gamma dose rate in infinite medium.

U concentrations range from 0.65 to 1.03 ppm for the four subsamples (Table 6.4). The concentrations of Th and K are very low, with Th concentrations between 0.007 and 0.025 ppm and K concentrations of 60 to 77 ppm. The dose rates from ^{232}Th series are 0.0013 to 0.0045 Gy/ka and the dose rates from K are 0.0063 to 0.0081 Gy/ka for the four subsamples, which are negligible. The major contribution to the dose rate thus stems from the U series. However, the subsamples used for ICP-MS analysis are adjacent to the subsamples used for ITL dating and the homogeneity of uranium distribution within the speleothem sample remains uncertain.

6.5.4.1.2 Line scan LA-ICP-MS

High-resolution trace element analysis of U and Th was conducted at the Institute for Geosciences, JGU Mainz, by laser ablation inductively coupled plasma mass spectrometry (LA-ICP-MS) using an ESI New Wave NWR 193 nm ArF Excimer laser system coupled to an Agilent 7700ce ICP-MS. The analyses were conducted using the continuous line scan method with a spot size of 100 µm, a laser repetition rate of 10 Hz, a scan speed of 10 µm/s and a fluence of approximately 3.5 J/cm². For calibration, the reference material NIST SRM 610 as well as other quality control materials (NIST SRM 612, MACS-3, BCR-2G) were analysed several times during the analysis. The reproducibility based on the analyses of NIST SRM 610 was 7.2 % for Th and 12.2 % for U (1 RSD). ^{43}Ca was used as an internal reference to calculate the trace element concentrations, and the offline data evaluation followed the calculations described in Mischel et al. (2017). For further details, the reader is referred to Jochum et al. (2012). The line scan was performed on another slice of speleothem BB2-1 which is opposite to the slice used for ITL dating. Four lines were chosen, which pass through the sampling regions of the four ITL subsamples (Fig. S6.5).

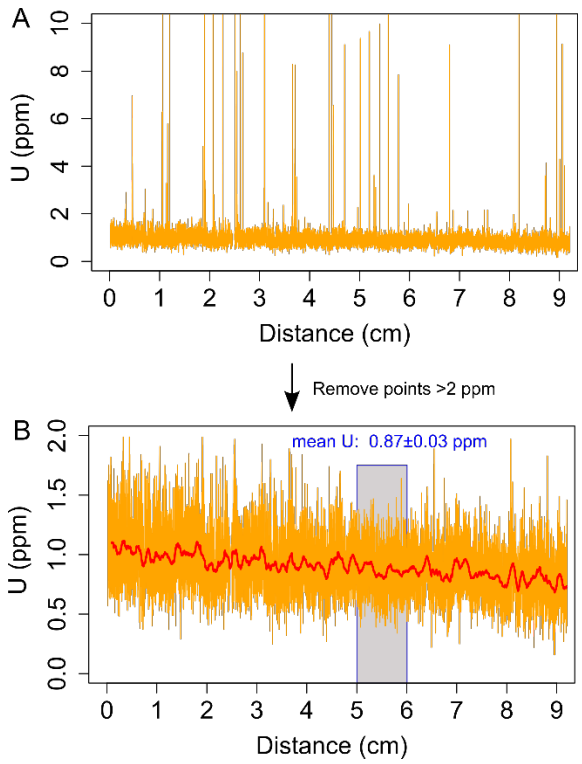

Fig. 6.7. A) U concentrations from the line scan LA-ICP-MS measurements. The line passes through the sampling position of LUM4348 (at the distance of 5 – 6 cm). B) U concentrations after removing the data points higher than 2 ppm. The red line indicates the average values of U concentrations over each 1 mm. The mean U for LUM4348 is calculated from the U concentrations between 5 and 6 cm.

Line scan measurements show that the U concentrations are mostly lower than 1.0 ppm for the sample, and the Th concentrations are mostly lower than 0.2 ppm. However, there are high U, Th concentrations in the detected lines which can reach tens of or hundreds of ppm (Fig. S6.5). These high U and Th concentrations tend to occur in pairs and generally correspond to high Th/U ratios (Fig. S6.5), which may indicate the existence of detrital minerals that are abundant in U and Th. Such high U and Th spots will increase the overall U and Th concentrations. However, as the alpha particle can only penetrate 20 to 30 μm inside the crystal, these radioactive 'hotspots' provide a negligible contribution to the total dose rate. Thus, to calculate the dose rate, U concentrations exceeding 2 ppm were excluded and the remaining 'background' U concentrations were averaged (Fig. 6.7). After removing the spikes, the U concentrations are generally stable along the detection lines and an infinite homogeneous medium can be assumed for alpha and beta dose rate calculations. The U concentrations obtained in this way are 65 – 92% of the U concentrations from the 'whole-rock' ICP-MS measurements for the four subsamples.

6.5.4.2 Alpha efficiency

As the speleothem sample is pure calcite, U is generally uniformly distributed inside and outside the grains. Consequently, the alpha dose rate has a high contribution to the total dose rate, making the alpha efficiency factor an important parameter. Previously reported a-values or k-values for the 280 °C TL peak of calcite vary substantially between samples (Wintle, 1978; Debenham and Aitken, 1984; Theocaris et al., 1997; Roque et al., 2001; Ogata et al., 2017; Yee and Mo, 2018; Zhang and Wang, 2020) (Fig. S6). Especially, Debenham and Aitken (1984) reported a-values for 27 stalagmites from two caves, which ranged from 0.09 to 0.55. Such scattered a-values among speleothem samples render the use of a mean a-value for dose rate calculation implausible. In this study, the alpha efficiency of the four subsamples used for ITL dating was measured individually.

Instead of the a-value system, the Sa value system (Guérin and Valladas, 1980), which can directly convert the alpha flux into dose rate was applied here. The measurements of Sa values were performed in the luminescence laboratory in University Bordeaux Montaigne, with an inhouse-built alpha irradiator (^{241}Am foil source). The alpha flux rate of the source has been accurately calibrated to be 1.9*105 α-particles $s^{-1}cm^{-2}$ (Kreutzer et al., 2018). The speleothem samples were ground into fine grained powders and the 4 to 11 μm fraction was separated following Stokes law. Aliquots were prepared with steel cups from Freiberg Instruments, with ca. 0.6 mg sample on each cup. In this way, the covered cup surface is thin-layered, with an average surface density of 1 mg cm^{-2} (Kreutzer et al., 2018).

The luminescence measurements were performed on a Lexsyg smart TL/OSL reader (always with N_2 flow). The built-in beta source of the reader is 0.133 Gy/s for fine grains (4 to 11 μm) on the steel cups. The aliquots were heated to 450 °C (5 °C/s) for four times (without background subtraction) to remove the natural signal and the spurious signal completely. Afterwards, the aliquots were given a dose of ca. 88 Gy and heated to 450 °C. Repeat the dosing and heating step for two more times. In this way, the aliquots were 'stabilised' and sensitivity change in the following measurements will be smaller. The stabilised aliquots were put under the alpha source for irradiation of 12 hours. The alpha flux received by the aliquots was 8.21*109 α-particles cm^{-2}. After alpha irradiation, the corresponded beta D_e was measured following a TL SAR protocol (Table S6.2). As these aliquots were already stabilised by repeated dosing and heating, the SAR protocol can still

be applied for TL D_e measurements. To reduce the influence of regenerated spurious signal, which can regenerate during the storage (Pagonis et al., 1997), the time lag between the alpha irradiation and D_e measurements was less than one day. The heating rate was set as 1 °C/s, to make the 280 °C TL peak (with heating rate of 5 °C/s) shifted to approximately 245 °C, to further reduce the influence of spurious TL signal (Fig. S6.7). The beta De was divided by the given alpha flux to get the Sa value (Table S6.3). For the four subsamples, the Sa values are quite close to each other, ranging from 19.4 to 21.9 uGy/(1000α*cm^{-2}). The mean Sa value of the four subsamples is 20.8 ± 0.5 µGy/(1000α*cm^{-2}). We suspect that the variation of the Sa values between the four subsamples results from the random error of measurements, as only 2 to 3 aliquots were measured for each subsample. Thus, the mean Sa value was applied for dose rate calculation. If converting the Sa value into k-value system, the mean effective k-value for U (keff_U) would be 0.126 ± 0.003, and for Th (keff_Th) 0.140 ± 0.003 (details of conversion in Table S6.3 notes).

6.5.4.3 Dose rates at equilibrium

Alpha and beta dose rates were calculated based on an infinite homogeneous medium. We used the conversion factors from Guérin et al. (2011). Attenuation of the gamma dose rate should be considered because the speleothem sample is not big enough in size, and cannot be treated as an infinite homogeneous medium for gamma ray which has a travelling length of around 30 cm in rocks. As the ^{230}Th/U ages at the top of the speleothem approximate around 330 ka, we can assume the shape of the speleothem remained unchanged for most of the time, and so did the gamma attenuation factors. Thus, we deduced the gamma attenuation factors based on the present shape of the speleothem sample. However, due to its irregular shape, accurate gamma attenuation factors for the four subsamples are difficult to estimate. Approximately, we applied a gamma attenuation factor of 0.2 for the three subsamples at the rim (LUM4346, LUM4348, LUM4780) and of 0.5 for the subsample in the centre (LUM4347). To account for the large uncertainty, a relative error of 50 % was assumed for the gamma dose rate. As the gamma dose rate assuming an infinite medium contributes only ~13 % to the total dose rate, the ages are not sensitive to the gamma attenuation factors. Cosmic ray dose rate is calculated based on the latitude, longitude, elevation and the overburden (Prescott and Hutton, 1994). As the cave has a roof of 12 to

50 m, the cosmic ray was only 0.011 Gy/ka based on a depth of 40 m. Although Th and K have very small contribution to the total dose rate (0.008 – 0.013 Gy/ka) due to their low concentrations, they were still considered in the dose rate calculation. However, the concentration of U is key for dose rate calculation. The U concentrations measured along lines with the LA-ICP-MS method were used for dose rate calculation. The total dose rates at U-series equilibrium are presented in Table 6.4. For all the four subsamples, the alpha dose rate contributes to 62 to 65 % of the total dose rate (Fig. S6.8).

6.5.4.4 Dose rate simulation and ages

The total dose rate is mainly determined by the ^{238}U series. However, the ^{238}U decay chain cannot be assumed to be in secular equilibrium since ^{230}Th was absent at the time of speleothem crystallisation, and the initial activity ratio of ^{234}U and ^{238}U ($[^{234}U/^{238}U]_0$) in dripwater can be much higher than 1 (Cowart and Osmond, 1977; Osmond et al., 1983; Plater et al., 1992; Tripathi et al., 2013). As a result, the dose rate changes with time. Here we applied two methods to tackle the problem of dose rate variation.

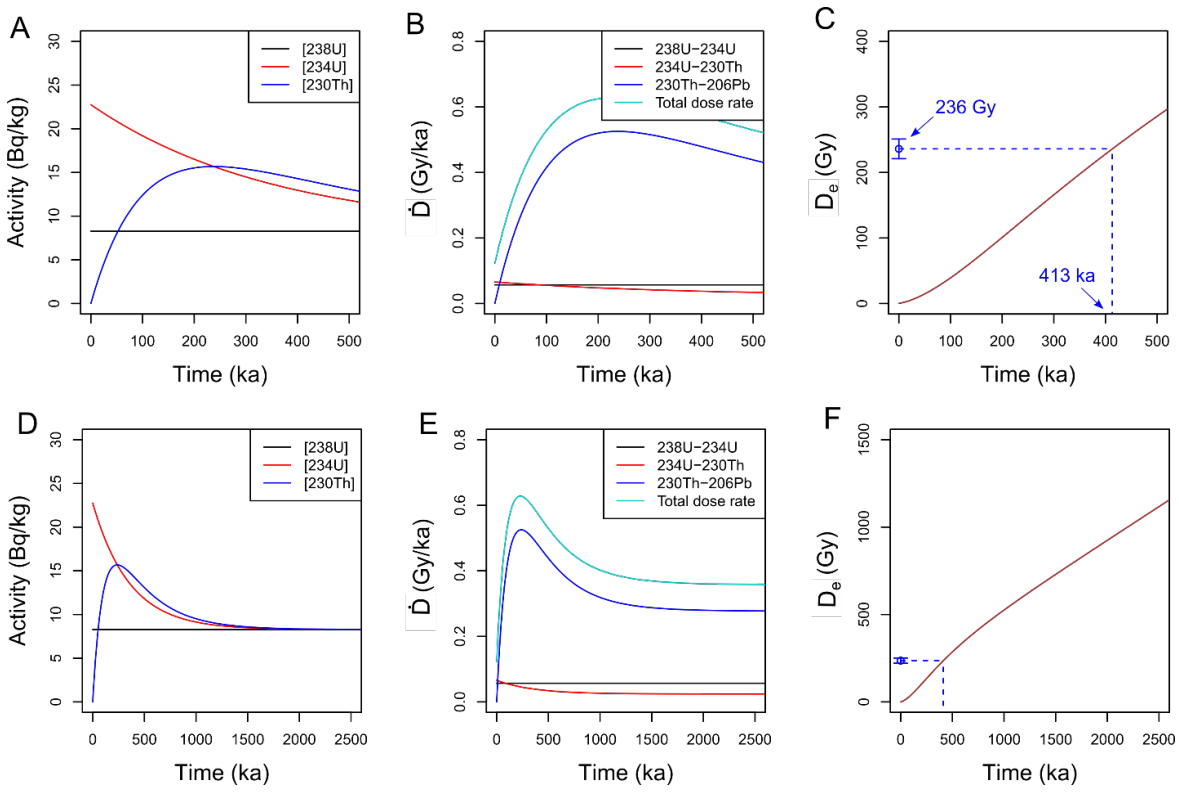

Fig. 6.8. Dose rate simulation for LUM4347. A) Radioisotope activities of ^{238}U, ^{234}U and ^{230}Th with time. The $[^{234}U/^{238}U]_0$ is 2.75; B) Time-dependent variation of dose rates

within the three segments (^{238}U to ^{234}U, ^{234}U to ^{230}Th, ^{230}Th to ^{206}Pb) of the ^{238}U decay chain; C) Growth of equivalent dose (D_e) with time. D-F are the same as A-C, but with longer time. Note that the U-series reach equilibrium only after ca. 1.5 Ma, and the dose rates become stable afterwards.

One method is to directly model the dose rate variation with time. We simulated the radioactivity of the ^{238}U, ^{234}U and ^{230}Th isotopes with a step of one year using numerical simulation, following the initial activities and decay constants. The [^{238}U] activity is almost a constant. Since the [^{234}U/^{238}U]$_0$ is larger than 1, the [^{234}U] decreases with time, and consequently the [^{230}Th] initially increases and then decreases with time (Fig. 6.8A). The dose rate of the ^{238}U decay chain was calculated by dividing the chain into three segments (^{238}U to ^{234}U, ^{234}U to ^{230}Th, ^{230}Th to the ^{206}Pb), and corresponding conversion factors (Guérin et al., 2011) in each segment were used. As the two daughter isotopes between ^{238}U and ^{234}U, and all daughter isotopes behind ^{230}Th have short half-lives compared to the sample age, instant equilibrium can be assumed for each segment. The dose rate of each segment is calculated and summed up to get the dose rate of the whole ^{238}U series (Fig. 6.8B). The dose rate from ^{232}Th series, ^{40}K and the cosmic dose rate were also calculated and added to get the total dose rate (annual dose). For sample LUM4347, the annual rate was 0.15 Gy/ka at the crystallisation of speleothem. Then it increased with time and reached 0.65 Gy/ka at 230 ka. Afterwards, it decreased again and will eventually reach a steady state of 0.39 Gy/ka. By adding up those annual doses, the growth pattern of D_e with age can be obtained (Fig. 6.8C). The measured D_e of LUM4347 is 236 Gy, which corresponds to an age of 413 ka. For the error of the ages, the Monte Carlo method was applied, taking into consideration of three normal distributions: the U concentration, the [^{234}U/^{238}U]$_0$ and the D_e value. The ITL ages deduced in this way are termed *simulated ages*. Note that the ^{226}Ra behind ^{230}Th has a half-life of 1602 years, which is not sufficiently short for very young samples (e.g. <10 ka). Dose rate simulation with 4-segment division was tested and the *simulated ages* increased by less than 2 ka, which is negligible considering the sample ages in this study. As a result, 3-segment simulation is used throughout this study.

The other method is the age iteration method modified from Ikeya and Ohmura (1983). Firstly, the total dose rate at U-series equilibrium (Ḋ) was calculated. An initial age was calculated dividing the measured D_e with Ḋ. The following iterative calculation was performed:

1) Calculated the D_e_cal with equation:

$$D_{e\,cal} = \dot{D} * \text{age} + \dot{D}_{234} * (r_0 - 1) * (1 - e^{-\lambda^{234} age})/\lambda^{234} - \dot{D}_{230} * \{(1 - e^{-\lambda^{230} age})/\lambda^{230} - 1/\lambda^{234} * (r_0 - 1) * [1 - (\lambda^{230} * e^{-\lambda^{234} age} - \lambda^{234} * e^{-\lambda^{230} age})/(\lambda^{230} - \lambda^{234})]\} \quad (6.1)$$

where $\dot{D}_{234}$ is the dose rate in the decay chain between the ^{234}U and ^{230}Th, and $\dot{D}_{230}$ is the dose rate in the decay chain after ^{230}Th. The λ^{234} and λ^{230} are the decay constants of the ^{234}U and ^{230}Th, respectively and r_0 is the $[^{234}U/^{238}U]_0$.

2) Calculated a new age:

$$age = age * D_e/D_e\_cal \quad (6.2)$$

where D_e is the measured value, which is a constant.

3) Back to step 1.

The age became stable after approximately five times of iteration. Ages obtained in this way are termed *iterated ages*, and we assume the same relative errors for the *iterated ages* as the initial ages.

The iterated ages and simulated ages of all subsamples based on the ITL_{235} signal are shown in Table 6.3.

6.6 Discussion

The D_e values obtained by the MAAD protocol with the 280 °C TL peak and the SAR protocol with the ITL_{235} signal agree well with each other. However, the ITL_{235} SAR D_e values have much smaller errors compared to the TL MAAD D_e values, as the SAR protocol avoids the error stemming from inter-aliquot variation. For the samples in this study, the spurious TL signal in the high temperature range is not significant, so the accurate MAAD D_e estimation with the 280 °C TL peak is still achievable.

The ITL_{235} ages obtained by both the dose rate simulation method and age iteration method are identical, which further proves the reliability of the two correction methods. Mathematically, the age iteration method and the dose rate simulation method are similar. The iteration method uses integration, which theoretically divides the time into infinitely small intervals. In the dose rate simulation method, we divide the time into 1-year intervals. The consistent age estimates indicate that the 1-year interval in dose rate simulation has a sufficiently high resolution. The age iteration method is more convenient compared to the dose rate simulation. However, the age iteration method can only be applied to closed systems, while the dose rate simulation method is more flexible and offers potential to incorporate U-uptake, Rn loss, etc.

The ITL ages are plotted against the Th/U ages in Fig. 6.9. For three of the samples, the ITL ages agree with the Th/U ages within 10 % uncertainty. The much higher errors of the ITL ages makes ITL dating not competitive when compared to ^{230}Th/U dating for speleothem samples younger than 600 ka and without detrital Th contamination. However, because of the high saturation dose of the TL/ITL signal of calcite, it is applicable to samples older than 600 ka, i.e., beyond the limit of the Th/U dating method. Moreover, Th contamination is not a drawback but rather an advantage for TL/ITL dating as it reduces the relative error of the total dose rate brought in by U-series disequilibrium.

As shown in the above section, accurate ITL age estimation requires the $[^{234}U/^{238}U]_0$ value. Because of the long residence time of U in seawater, the $[^{234}U]/[^{238}U]$ in seawater remains to be around 1.14 (Chen et al., 1986). However, terrestrial waters have variable $[^{234}U]/[^{238}U]$ values depending on weathering and infiltration conditions, which can range from 0 to more than 10, with the majority of the values between 1 and 3 (Cowart and Osmond, 1977; Osmond et al., 1983). If ignoring the U-series disequilibrium and simply

applying the dose rate at secular equilibrium for age estimation, the age can thus be substantially over- or underestimated (Fig. S6.9).

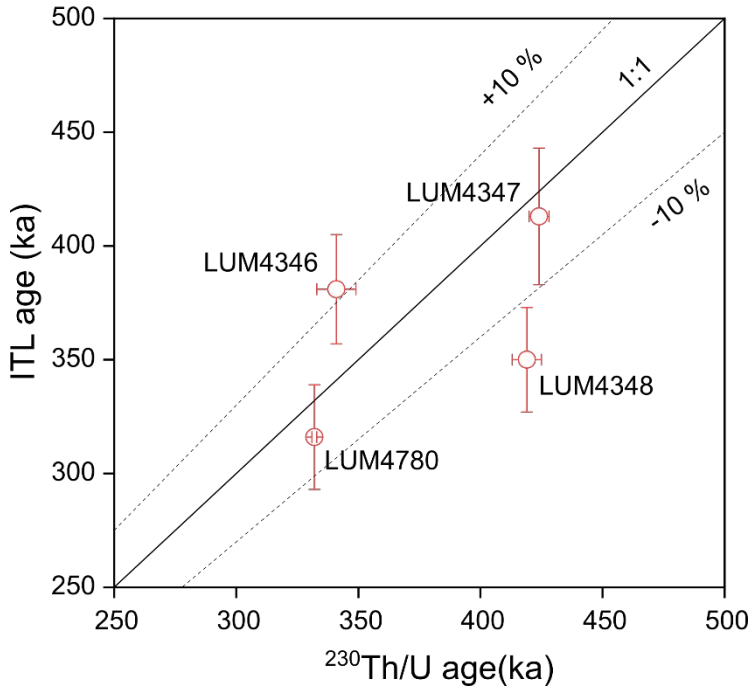

Fig. 6.9. Comparison of the ITL ages with the ^{230}Th/U ages. Error bars are 1σ for both ages.

To obtain the $[^{234}U/^{238}U]_0$ value, accurate measurements of the present concentrations of ^{234}U, ^{238}U and ^{230}Th are needed. However, with these measurements, the ^{230}Th/U ages would be already available, rendering ITL dating unnecessary. The advantage of ITL dating is its application to old speleothem samples which exceed the dating limit of ^{230}Th/U dating. The ideal application case would thus be speleothem samples which have both a younger part suitable for ^{230}Th/U dating and an older part amenable to ITL dating (Fig. 6.10). From ^{230}Th/U dating on the younger part, a $[^{234}U/^{238}U]_0$ value can be obtained. If the $[^{234}U/^{238}U]_0$ does not change much with time for the same speleothem sample, $[^{234}U/^{238}U]_0$ of the younger part of the speleothem can be used when applying ITL dating on the older part.

For speleothem samples which have no younger part suitable for ^{230}Th/U dating, a feasible way is to estimate the $[^{234}U/^{238}U]_0$ value and combine ^{234}U/^{238}U dating and ITL dating. With the guessed $[^{234}U/^{238}U]_0$ value and modern $[^{234}U/^{238}U]$, an ^{234}U/^{238}U age can be calculated. Meanwhile, an ITL age can also be obtained with the $[^{234}U/^{238}U]_0$. With a higher $[^{234}U/^{238}U]_0$, the ^{234}U/^{238}U age would be higher, while the ITL age would be lower due to the overall higher dose rate. If the ^{234}U/^{238}U age is older than ITL age, it means that the guessed $[^{234}U/^{238}U]_0$ is too high, and vice visa. We can moderate the $[^{234}U/^{238}U]_0$ value

until the $^{234}U/^{238}U$ age and the ITL age agree with each other. This method is only valid for samples within the dating range of the $^{234}U/^{238}U$ dating method (i.e. <1.5 Ma).

6.7 Conclusion

The ITL_{235} signal can isolate the 280 °C TL peak with little contribution of TL signals from the higher temperature range, which is advantageous for dating calcite samples with highly spurious signals. The speleothem sample tested here has only a limited spurious signal, thus the SAR D_e values of the ITL_{235} signal are consistent with the MAAD D_e of the 280 °C TL peak. However, the use of the single-aliquot technique results in much smaller error estimates for the ITL_{235} SAR D_e values.

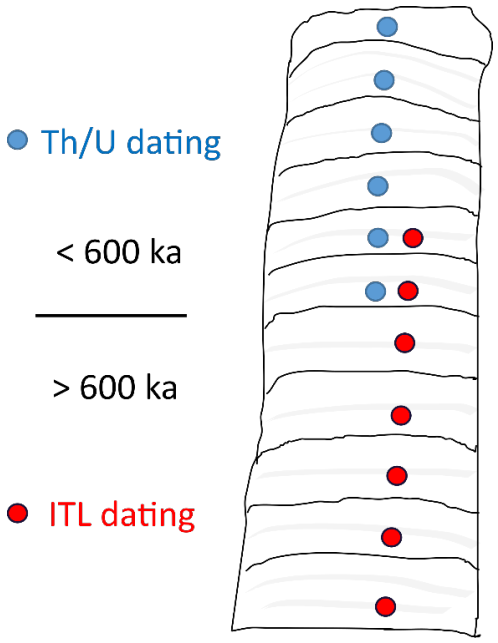

Fig. 6.10. An ideal speleothem sample which can be dated by both $^{230}Th/U$ and ITL. The $[^{234}U/^{238}U]_0$ value deduced from $^{230}Th/U$ dating in the younger part (<600 ka) of the speleothem sample can be used for the older part with ITL dating.

Alpha efficiencies of the four subsamples are quite close to each other, with a mean S_a value of 20.8±0.5 μGy/(1000α*cm^{-2}). Line scan LA-ICP-MS measurements show spikes in U distribution. Removing these high U concentrations, the dose rate can be calculated using an infinite homogeneous medium. The dose rate variation due to U-series disequilibrium can be simulated with the initial ^{238}U, ^{234}U, ^{230}Th activities and their decay constants. For three of the four tested subsamples, the ITL_{235} ages are consistent

with ^{230}Th/U ages. Due to the higher uncertainties, ITL dating is not comparable to ^{230}Th/U dating for samples younger than 600 ka. However, ITL dating provides a new avenue for dating speleothem samples older than the U/Th dating limit and samples with detrital Th contamination (in case of U-Th dating) and common lead contamination (in case of U-Pb dating). This method offers an alternative promising approach for deep-time speleothem-based geochronology.

6.8 Acknowledgements

The authors sincerely thank Nobert Mercier, Sebastian Kreutzer and Chantal Tribolo for their help and fruitful discussion about alpha efficiency measurements and evaluation. D. Scholz and J. Klose are thankful to M. Großkopf, M. Weber, and V. Blumrich for assistance during U-series dating at the University of Mainz. This study is funded by the Deutsche Forschungsgemeinschaft (DFG, German Research Foundation) as project number 508966574 (MA 4759/18-1, SCHO 1274/17-1, ZH 1184/2-1).

6.9 References

Adamiec, G., Duller, G.A.T., Roberts, H.M., Wintle, A.G., 2010. Improving the TT-OSL SAR protocol through source trap characterisation. Radiat Meas 45, 768-777.

Aitken, M.J., 1985. Thermoluminescence Dating. Academic Press, London.

Aitken, M.J., Bussell, G.D., 1979. Zero-glow monitoring (ZGM). Ancient TL 6, 13-15.

Aitken, M.J., Bussell, G.D., 1982. TL dating of fallen stalactites. PACT 6, 550-554.

Aitken, M.J., Wintle, A.G., 1977. Thermoluminescence Dating of Calcite and Burnt Flint - Age Relation for Slices. Archaeometry 19, 100-105.

Auclair, M., Lamothe, M., Huot, S., 2003. Measurement of anomalous fading for feldspar IRSL using SAR. Radiat Meas 37, 487-492.

Bangert, U., Henning, G.J., 1979. Effect of sample preparation and the influence of clay impurities on the TL-dating of calcitic cave deposits. PACT 3, 281-289.

Breitenbach, S.F.M., Plessen, B., Waltgenbach, S., Tjallingii, R., Leonhardt, J., Jochum, K.P., Meyer, H., Goswami, B., Marwan, N., Scholz, D., 2019. Holocene interaction of maritime and continental climate in Central Europe: New speleothem evidence from Central Germany. Global and Planetary Change 176, 144-161.

Buylaert, J.P., Murray, A.S., Huot, S., Vriend, M.G.A., Vandenberghe, D., De Corte, F., Van den haute, P., 2006. A comparison of quartz OSL and isothermal TL measurements on Chinese loess. Radiat Prot Dosim 119, 474-478.

Chen, J.H., Lawrence Edwards, R., Wasserburg, G.J., 1986. ^{238}U, ^{234}U and ^{232}Th in seawater. Earth and Planetary Science Letters 80, 241-251.

Cheng, H., Edwards, R.L., Shen, C.-C., Polyak, V.J., Asmerom, Y., Woodhead, J., Hellstrom, J., Wang, Y., Kong, X. and Spötl, C. (2013) Improvements in ^{230}Th dating, ^{230}Th and ^{234}U half-life values, and U–Th isotopic measurements by multi-collector inductively coupled plasma mass spectrometry. Earth and Planetary Science Letters 371, 82-91.

Cheng, H., Edwards, R.L., Sinha, A., Spotl, C., Yi, L., Chen, S.T., Kelly, M., Kathayat, G., Wang, X.F., Li, X.L., Kong, X.G., Wang, Y.J., Ning, Y.F., Zhang, H.W., 2016. The Asian monsoon over the past 640,000 years and ice age terminations. Nature 534, 640-646.

Choi, J.H., Murray, A.S., Cheong, C.S., Hong, D.G., Chang, H.W., 2006. Estimation of equivalent dose using quartz isothermal TL and the SAR procedure. Quat Geochronol 1, 101-108.

Clemens, S.C., Prell, W.L., Sun, Y., 2010. Orbital-scale timing and mechanisms driving Late Pleistocene Indo-Asian summer monsoons: Reinterpreting cave speleothem $\delta^{18}O$. Paleoceanography 25.

Cowart, J.B., Osmond, J.K., 1977. Uranium Isotopes in Groundwater: Their Use in Prospecting for Sandstone-Type Uranium Deposits, In: Butt, C.R.M., Wilding, I.G.P. (Eds.), Developments in Economic Geology. Elsevier, pp. 365-379.

Debenham, N.C., 1983. Reliability of thermoluminescence dating of stalagmitic calcite. Nature 304, 154-156.

Debenham, N.C., Aitken, M.J., 1984. Thermoluminescence dating of stalagmitic calcite. Archaeometry 26, 155-170.

Duller, G.A.T., Penkman, K.E.H., Wintle, A.G., 2009. Assessing the potential for using biogenic calcites as dosemeters for luminescence dating. Radiat Meas 44, 429-433.

Duller, G.A.T., Tooth, S., Barham, L., Tsukamoto, S., 2015. New investigations at Kalambo Falls, Zambia: Luminescence chronology, site formation, and archaeological significance. Journal of Human Evolution 85, 111-125.

Dulski, P., 2001. Reference Materials for Geochemical Studies: New Analytical Data by ICP-MS and Critical Discussion of Reference Values. Geostandards and Geoanalytical Research 25, 87–125.

Engin, B., Guven, O., 1997. Thermoluminescence dating of Denizli travertines from the southwestern part of Turkey. Appl Radiat Isotopes 48, 1257-1264.

Franklin, A.D., Hornyak, W.F., Tschirgi, A.A., 1988. Thermo-Luminescence Dating of Tertiary Period Calcite. Quaternary Sci Rev 7, 361-365.

Henderson, G.M., 2006. Caving in to new chronologies. Science 313, 620-622.

Huang, C., Zhang, J., Wang, L., Zhao, H., Li, S.-H., 2022. Equivalent dose estimation of calcite using isothermal thermoluminescence signals. Quaternary Geochronology 70, 101310.

Ikeya, M., Ohmura, K., 1983. Comparison of ESR ages of corals from marine terraces with ^{14}C and $^{230}Th/^{234}U$ ages. Earth and Planetary Science Letters 65, 34-38.

Jochum, K.P., Scholz, D., Stoll, B., Weis, U., Wilson, S.A., Yang, Q., Schwalb, A., Börner, N., Jacob, D.E. and Andreae, M.O. (2012) Accurate trace element analysis of speleothems and biogenic calcium carbonates by LA-ICP-MS. Chemical Geology 318-319, 31-44.

Klose et al., in review

Kraemer, D., Frei, R., Ernst, D.M., Bau, M., Melchiorre, E., 2021. Serpentinization in the Archean and Early Phanerozoic – Insights from chromium isotope and REY systematics of the Mg Cr hydroxycarbonate stichtite and associated host serpentinites. Chemical Geology 565, 120055.

Kreutzer, S., Martin, L., Dubernet, S., Mercier, N., 2018. The IR-RF alpha-Efficiency of K-feldspar. Radiation Measurements 120, 148–156.

Liao, J., Hu, C., Li, C., Zhang, G., Gao, J., Huang, J., 2014. Spurious Thermoluminescence from Stalagmite:A New Paleoenvironmental Proxy. . Earth Science 23(4), 443-450.

Liritzis, I., Stamoulis, K., Papachristodoulou, C., Ioannides, K., 2013. A re-evaluation of radiation dose-rate conversion factors. Mediterranean Archaeology and Archaeometry 13, 1-15.

Liu, J.F., Murray, A.S., Buylaert, J.P., Jain, M., Chen, J., Lu, Y., 2016. Stability of fine-grained TT-OSL and post-IR IRSL signals from a c. 1 Ma sequence of aeolian and lacustrine deposits from the Nihewan Basin (northern China). Boreas 45, 703-714.

Mischel, S.A., Mertz-Kraus, R., Jochum, K.P. and Scholz, D. (2017) TERMITE - An R script for fast reduction of LA-ICPMS data and its application to trace element measurements. Rapid Communications in Mass Spectrometry 31, 1079-1087.

Moore, G.W., 1952. Speleothem—a new cave term. National Speleological Society News 10, 2.

Murray, A.S., Wintle, A.G., 2000. Application of the single-aliquot regenerative-dose protocol to the 375 degrees C quartz TL signal. Radiat Meas 32, 579-583.

Ninagawa, K., Adachi, K., Uchimura, N., Yamamoto, I., Wada, T., Yamashita, Y., Takashima, I., Sekimoto, K., Hasegawa, H., 1992. Thermoluminescence Dating of Calcite Shells in the Pectinidae Family. Quaternary Sci Rev 11, 121-126.

Ninagawa, K., Matsukuma, Y., Fukuda, T., Sato, A., Hoshinoo, N., Nakagawa, M., Yamamoto, I., Wada, T., Yamashita, Y., Sekimoto, K., Komura, K., 1994. Thermoluminescence Dating of a Calcite Shell, Crassostrea-Gigas (Thunberg) in the Ostreidae Family. Quaternary Sci Rev 13, 589-593.

Ninagawa, K., Takahashi, N., Wada, T., Yamamoto, I., Yamashita, N., Yamashita, Y., 1988. Thermo-Luminescence Measurements of a Calcite Shell for Dating. Quaternary Sci Rev 7, 367-371.

Ogata, M., Hasebe, N., Fujii, N., Yamakawa, M., 2017. Measuring apparent dose rate factors using beta and gamma rays, and alpha efficiency for precise thermoluminescence dating of calcite. J Miner Petrol Sci 112, 336-345.

Osmond, J.K., Cowart, J.B., Ivanovich, M., 1983. Uranium isotopic disequilibrium in ground water as an indicator of anomalies. The International Journal of Applied Radiation and Isotopes 34, 283-308.

Pagonis, V., Maniatis, Y., Michael, C., Bassiakos, Y., 1997. Spurious and regenerated thermoluminescence in calcite powder samples. Radiat Meas 27, 37-42.

Pickering, R., Kramers, J.D., Partridge, T., Kodolanyi, J., Pettke, T., 2010. U–Pb dating of calcite–aragonite layers in speleothems from hominin sites in South Africa by MC-ICP-MS. Quaternary Geochronology 5, 544–558.

Plater, A.J., Ivanovich, M., Dugdale, R.E., 1992. Uranium series disequilibrium in river sediments and waters: the significance of anomalous activity ratios. Applied Geochemistry 7, 101-110.

Prescott, J.R., Hutton, J.T., 1994. Cosmic-Ray Contributions to Dose-Rates for Luminescence and Esr Dating - Large Depths and Long-Term Time Variations. Radiat Meas 23, 497-500.

R Core Team (2022). R: A language and environment for statistical computing. R Foundation for Statistical Computing, Vienna, Austria.

Rahimzadeh, N., Zhang, J., Tsukamoto, S., Long, H., 2023. Characteristics of the quartz isothermal thermoluminescence (ITL) signal from the 375 °C peak and its potential for extending the age limit of quartz dating. Radiation Measurements 161, 106899.

Richards, D.A., Bottrell, S.H., Cliff, R.A., Ströhle, K., Rowe, P.J., 1998. U-Pb dating of a speleothem of Quaternary age. Geochimica et Cosmochimica Acta 62, 3683–3688.

Richter, M., Tsukamoto, S., Long, H., 2020. ESR dating of Chinese loess using the quartz Ti centre: A comparison with independent age control. Quaternary International 556, 159-164.

Rogue, C., Guibert, P., Vartanian, E., Bechtel, F., Schvoerer, M., 2001. Thermoluminescence-dating of calcite: study of heated limestone fragments from Upper Paleolithic layers at Combe Sauniere, Dordogne, France. Quaternary Sci Rev 20, 935-938.

Roque, C., Guibert, P., Vartanian, E., Bechtel, F., Schvoerer, M., 2001. Thermoluminescence — dating of calcite: study of heated limestone fragments from Upper Paleolithic layers at Combe Sauniere, Dordogne, France. Quaternary Sci Rev 20, 935-938.

Scholz, D., Hoffmann, D., 2008. ^{230}Th/U-dating of fossil corals and speleothems. E&G Quaternary Science Journal 57, 52-76.

Spooner, N.A., 1992. Optical dating: Preliminary results on the anomalous fading of luminescence from feldspars. Quaternary Sci Rev 11, 139-145.

Spooner, N.A., 1994. The Anomalous Fading of Infrared-Stimulated Luminescence from Feldspars. Radiat Meas 23, 625-632.

Stirling, R.J., Duller, G.A.T., Roberts, H.M., 2012. Developing a single-aliquot protocol for measuring equivalent dose in biogenic carbonates. Radiat Meas 47, 725-731.

Tang, S.L., Li, S.H., 2015. Low temperature thermochronology using thermoluminescence signals from quartz. Radiat Meas 81, 92-97.

Theocaris, P.S., Liritzis, I., Galloway, R.B., 1997. Dating of Two Hellenic Pyramids by a Novel Application of Thermoluminescence. Journal of Archaeological Science 24, 399-405.

Tripathi, R.M., Sahoo, S.K., Mohapatra, S., Lenka, P., Dubey, J.S., Puranik, V.D., 2013. Study of uranium isotopic composition in groundwater and deviation from secular equilibrium condition. Journal of Radioanalytical and Nuclear Chemistry 295, 1195-1200.

Tsukamoto, S., Long, H., Richter, M., Li, Y., King, G.E., He, Z., Yang, L., Zhang, J., Lambert, R., 2018. Quartz natural and laboratory ESR dose response curves: A first attempt from Chinese loess. Radiat Meas 120, 137-142.

Tsukamoto, S., Murray, A.S., Huot, S., Watanuki, T., Denby, P.M., Bøtter-Jensen, L., 2007. Luminescence property of volcanic quartz and the use of red isothermal TL for dating tephras. Radiat Meas 42, 190-197.

Vandenberghe, D.A.G., Jain, M., Murray, A.S., 2009. Equivalent dose determination using a quartz isothermal TL signal. Radiat Meas 44, 439-444.

Visocekas, R., 1985. Tunneling Radiative Recombination in Labradorite - Its Association with Anomalous Fading of Thermo-Luminescence. Nucl Tracks Rad Meas 10, 521-529.

Wedepohl, K.H. (1995) The composition of the continental crust. Geochimica et Cosmochimica Acta 59, 1217-1232.

Wintle, A.G., 1973. Anomalous Fading of Thermoluminescence in Mineral Samples. Nature 245, 143-144.

Wintle, A.G., 1974. Factors determining the thermoluminescence of chronologically significant materials. PhD thesis, University of Oxford.

Wintle, A.G., 1975. Effects of sample preparation on the thermoluminescence characteristics of calcite. Modern Geology 5, 165-167.

Wintle, A.G., 1977. Thermoluminescence dating of minerals—traps for the unwary. Journal of Electrostatics 3, 281-288.

Wintle, A.G., 1978. A thermoluminescence dating study of some Quaternary calcite: potential and problems. Can. J. Earth Sci. 15, 1977-1986.

Wintle, A.G., Murray, A.S., 2006. A review of quartz optically stimulated luminescence characteristics and their relevance in single-aliquot regeneration dating protocols. Radiat Meas 41, 369-391.

Woodhead, J., Hellstrom, J., Maas, R., Drysdale, R., Zanchetta, G., Devine, P., Taylor, E., 2006. U–Pb geochronology of speleothems by MC-ICPMS. Quaternary Geochronology 1, 208–221.

Woodhead, J., Petrus, J., 2019. Exploring the advantages and limitations of in situ U–Pb carbonate geochronology using speleothems. Geochronology 1, 69–84.

Yee, K.P., Mo, R.H., 2018. Thermoluminescence dating of stalactitic calcite from the Early Paleolithic occupation at Tongamdong site. J. Archaeol. Sci. Rep. 19, 405-410.

Zhang, J., Wang, L., 2020. Thermoluminescence dating of calcite – Alpha effectiveness and measurement protocols. J Lumin 223, 117205.

Zhang, J., Tsukamoto, S., 2022. A simplified multiple aliquot regenerative dose protocol to extend the dating limit of K-feldspar pIRIR signal. Radiation Measurements 157, 106827.

Zimmerman, D.W., 1971. Thermoluminescent dating using fine grains from pottery. Archaeometry 13, 29-52.

Supplementary Material for

ITL dating of speleothems – A case study from Bleßberg cave, Germany

Junjie Zhang[1*], Jennifer Klose[2], Sumiko Tsukamoto[1], Denis Scholz[2], Norbert Marwan[3], Sebastian F. M. Breitenbach[4], Lutz Katzschmann[5], Dennis Kraemer[6]

*corresponding author: Junjie.Zhang@leibniz-liag.de

[1] Leibniz Institute for Applied Geophysics (LIAG), 30655 Hannover, Germany

[2] Institute for Geosciences, University of Mainz, 55128 Mainz, Germany

[3] Potsdam Institute for Climate Impact Research (PIK), Member of the Leibniz Association, 14473 Potsdam, Germany

[4] Department of Geography and Environmental Sciences, Northumbria University, Newcastle, UK

[5] Thuringian State office for the Environment, Mining and Nature Conservation (TLUBN), 07745 Jena, Germany

[6] Federal Institute for Geosciences and Natural Resources (BGR), 30655 Hannover, Germany

submitted in similar form to Quaternary Geochronology

6.10 Supplementary Material

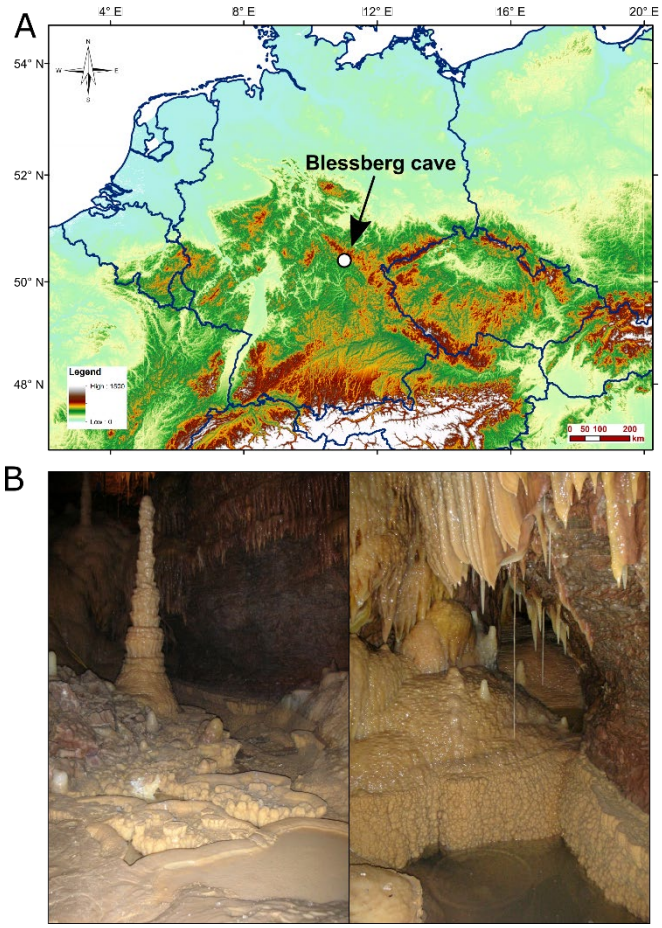

Fig. S6.1. A) Location of the Blessberg cave, Germany. B) Speleothems inside the Blessberg cave.

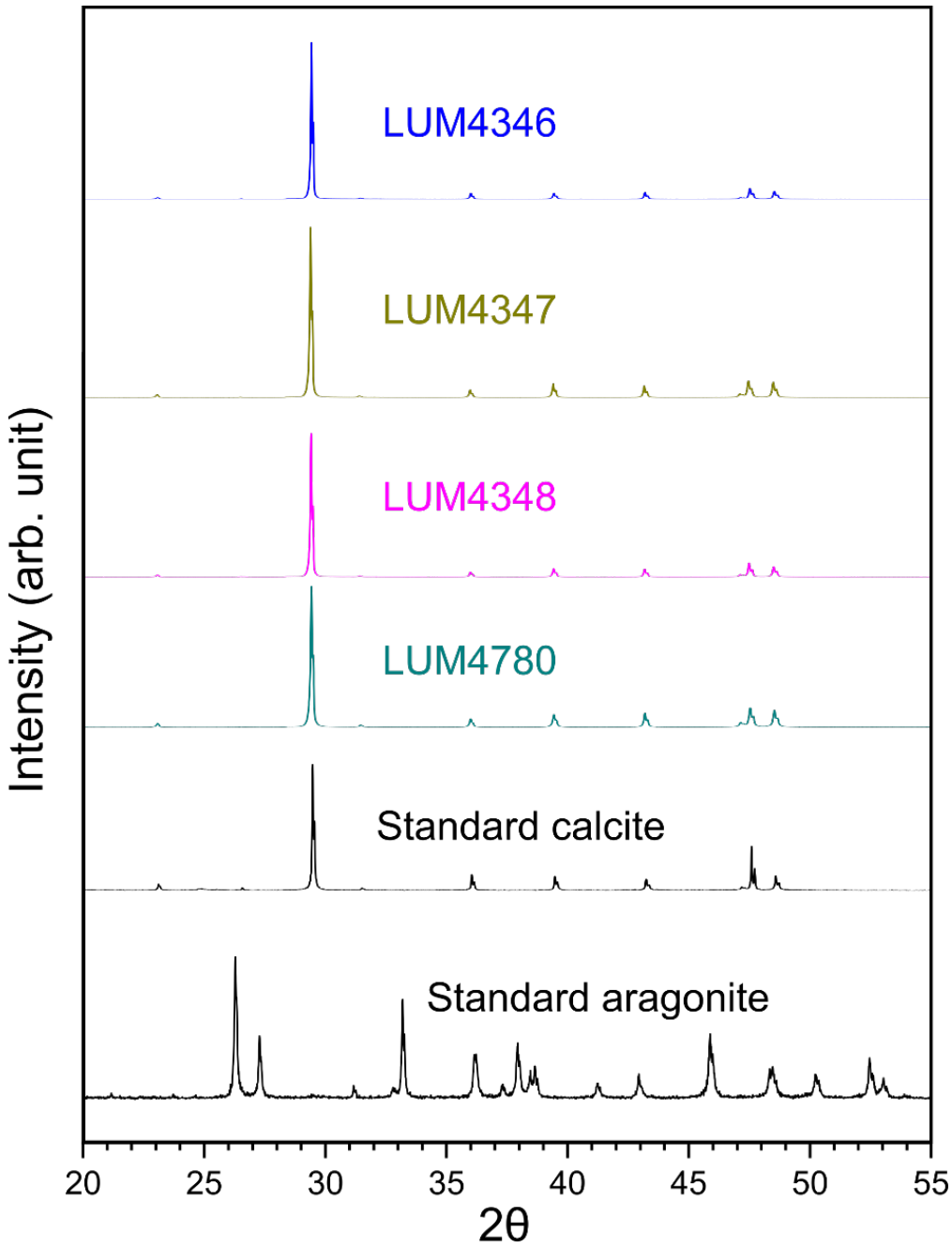

Fig. S6.2. X-ray diffraction analyses (XRD) results for the 4 subsamples used for ITL dating. The standard XRD curves for calcite (R040070) and aragonite (R040078) are from the RRUFF database (https://rruff.info).

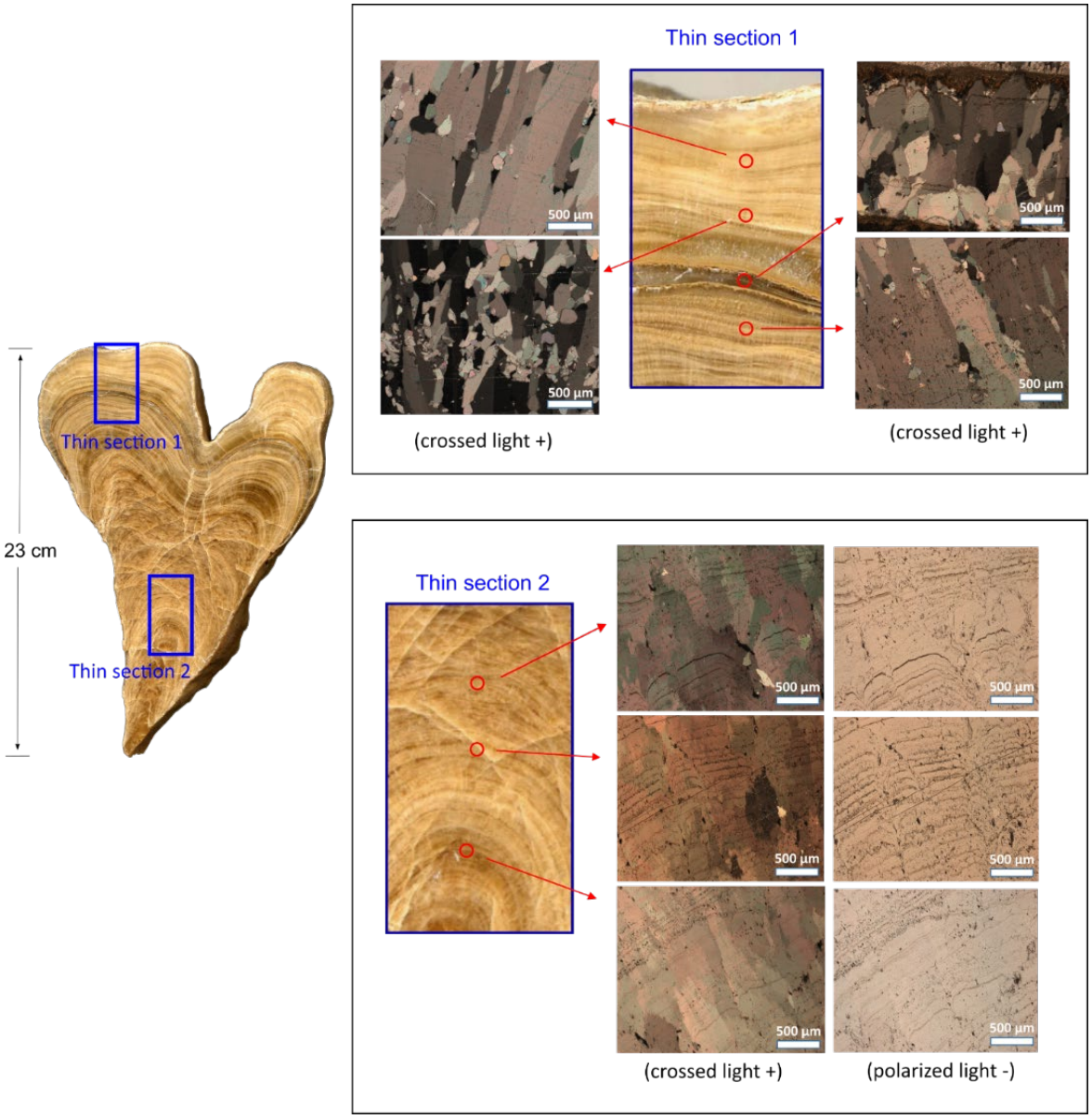

Fig. S6.3. Thin section photographs of the speleothem sample.

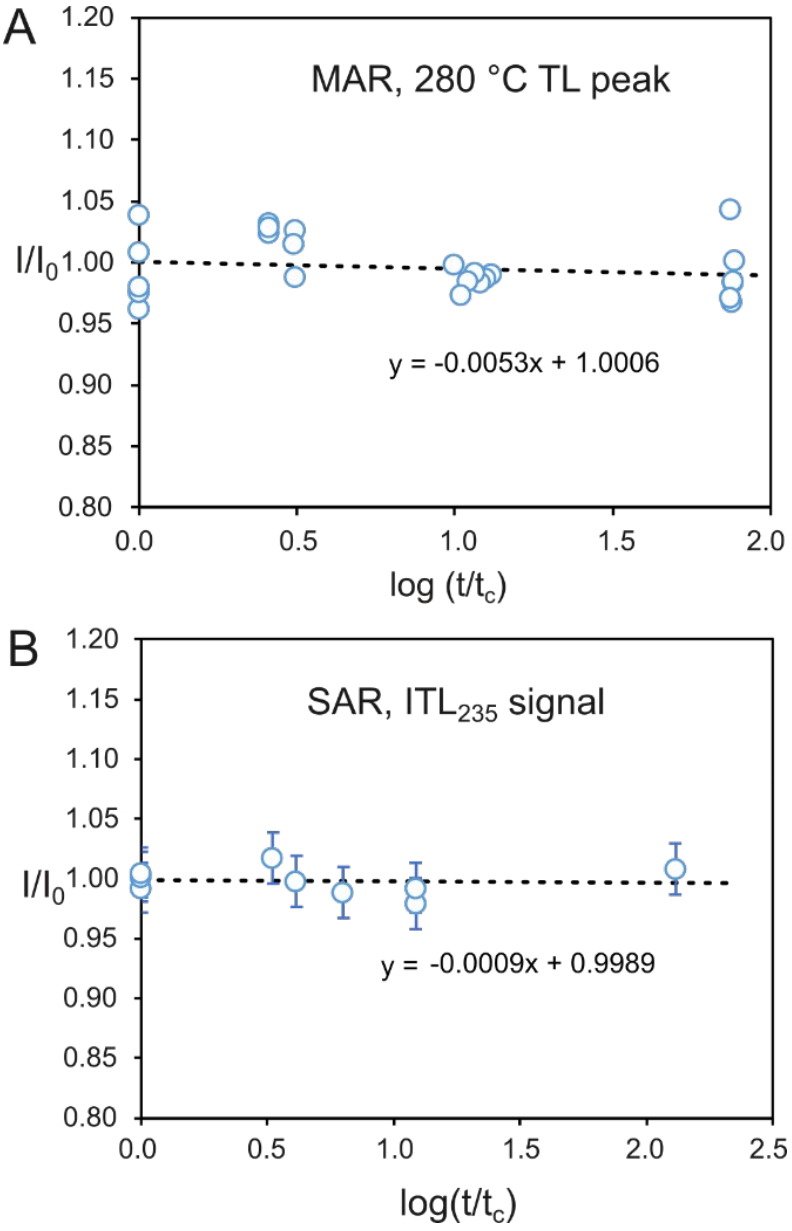

Fig. S6.4. A) Fading rate of the 280 °C TL peak with the MAR protocol. B) Fading rate of the ITL_{235} signal with the SAR protocol for one aliquot of LUM4346. Note that the slopes are very close to zero, indicating no fading.

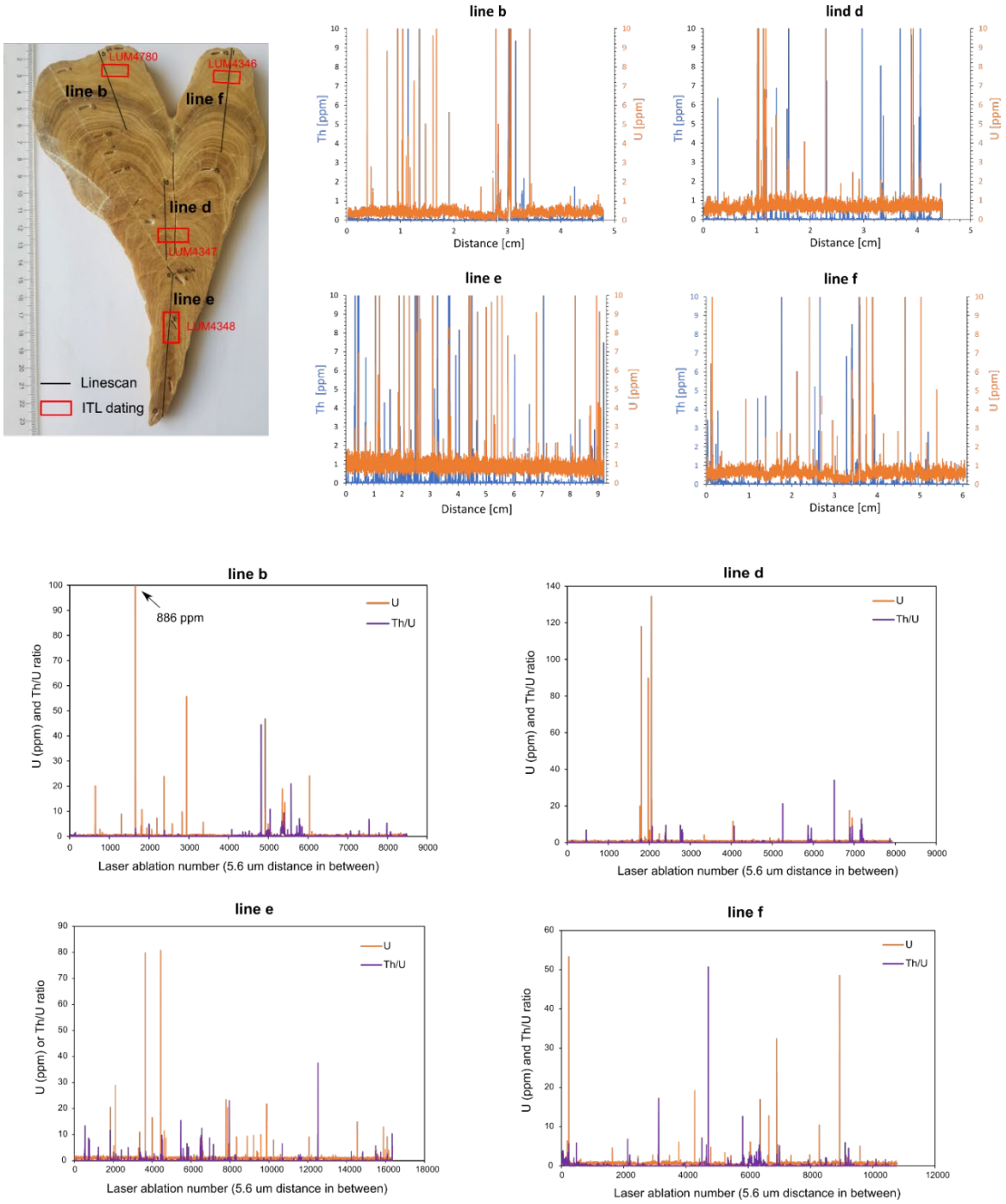

Fig. S6.5. U, Th concentrations from the Line scan LC-ICP-MS analyses. Note that there are many spikes in U, Th concentrations, and these high U, Th concentrations generally correspond to high Th/U ratios.

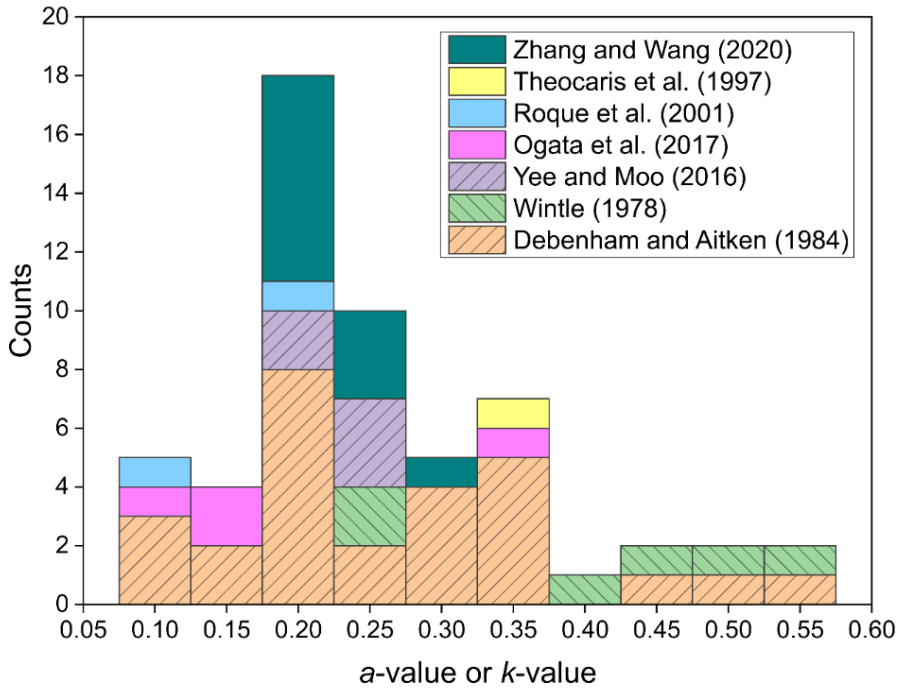

Fig. S6.6. Summary of *a*-values or *k*-values of calcite published in previous studies. The columns with slash lines indicate speleothem samples.

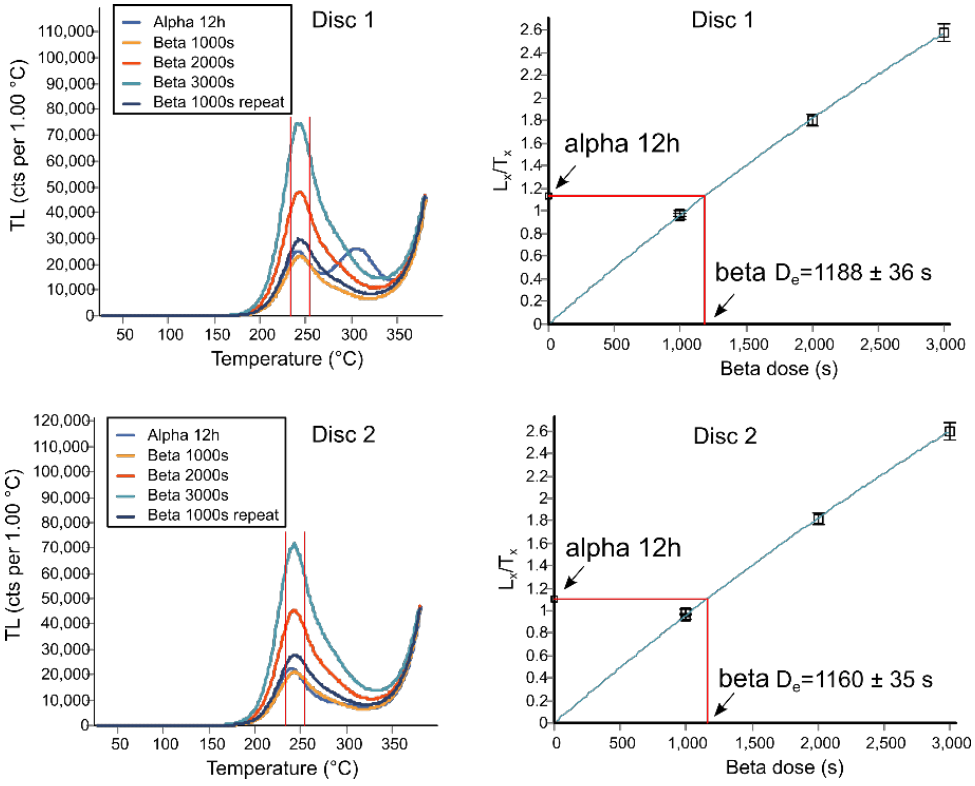

Fig. S6.7. Estimation for S_a value of LUM4346. Heating rate is 1 °C/s, and the TL peak is at 245 °C. Signal of 235–255 °C is used. In disc 1, there is a peak at 320 °C which might be spurious signal. The alpha flux rate is $1.9*10^5$ α-particles s^{-1} cm^{-2}. The beta source inside the Lexsyg reader has a dose rate of 0.133 Gy/s.

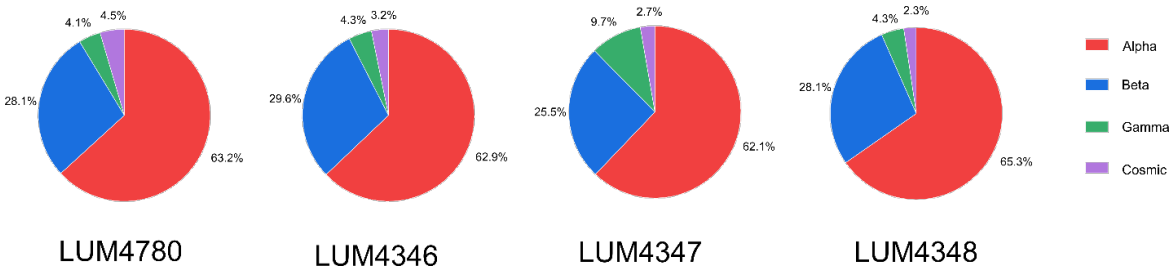

Fig. S6.8. Pie charts showing the contributions of alpha, beta, gamma and cosmic ray to the total dose rate.

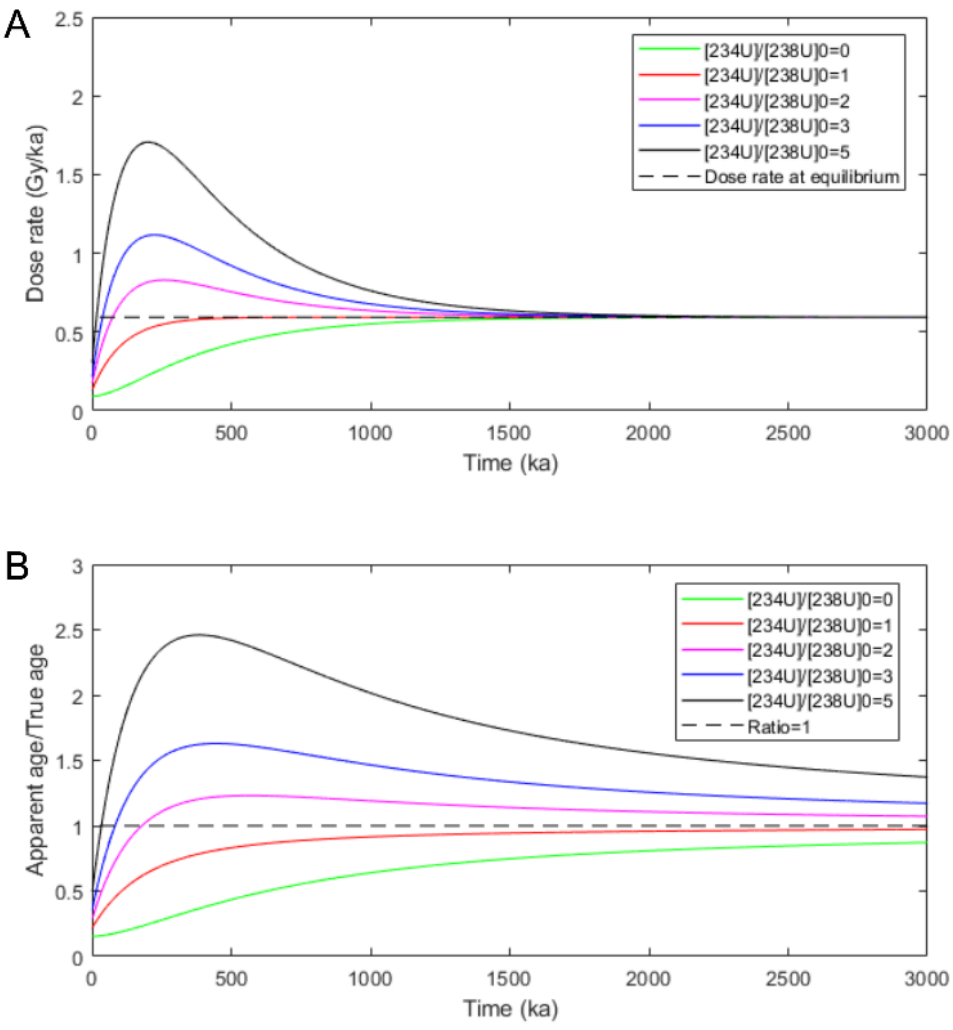

Fig. S6.9. A) Modelled dose rate (1 ppm ^{238}U) variation over time with different $[^{234}U/^{238}U]_0$ values; B) Ratio of apparent age (assuming secular equilibrium since crystallisation) and true age with time.

Table S6.1. Summary of the thermal lifetimes of the 280 °C TL peak.

Reference	Sample	Signal	Method	Trap depth (eV)	Frequency factor (s^{-1})	Lifetime at 10 °C (Ma)
Wintle (1974)	Limestone	285 °C peak	Peak shifting	1.52	2.0×10^{13}	2
Wintle (1977)	Speleothem	275 °C peak	Peak shifting	1.75	4.0×10^{15}	110
Debenham (1983)	Speleothem	280 °C peak	Peak shifting	1.56	5.0×10^{13}	4
Stirling et al. (2012)	Snail operculum	275 °C peak	Peak shifting	1.73	9.6×10^{14}	200
Engin and Guven (1997)	Travertine	280 °C peak	Peak shifting	1.73	1.4×10^{15}	137
		280 °C peak	Initial rise	1.70	7.3×10^{14}	77
		280 °C peak	Isothermal annealing	1.68	2.5×10^{14}	99
This study	Speleothem	280 °C peak	Peak shifting	1.76	9.1×10^{15}	83
		280 °C peak	Isothermal annealing	1.61	1.0×10^{14}	12

Table S6.2. TL SAR protocols for S_a value measurements.

Step	Treatments	Signal
1	Alpha irradiation 12h for first cycle beta irradiation (1000, 2000, or 3000 s) for other cycles	
2	Preheat to 250 °C (5°C/s)	
3	TL to 400 °C (1°C/s)	L_x
4	Test dose (beta irradiation 1000 s)	
5	Preheat to 250 °C (5°C/s)	
6	TL to 400 °C (1°C/s)	T_x

Table S6.3. Summary of S_a values and the converted effective k-values for U (k_{eff}_U) and Th (k_{eff}_Th).

Sample ID	LUM4346		LUM4347		LUM4348		LUM4780	
	S_a	1σ	S_a	1σ	S_a	1σ	S_a	1σ
Disc 1	19.2	0.5	22.1	0.5	20.0	0.6	20.1	0.6
Disc 2	19.6	0.5	21.6	0.6	21.5	0.6	22.5	0.6
Disc 3	19.5	0.5						
Mean of each sample	19.4±0.1		21.9±0.2		20.7±0.7		21.3±1.2	
Mean S_a of the four subsamples	**20.8±0.52 µGy/(1000α*cm^{-2})**							
Mean k_{eff}_U	**0.126±0.003**							
Mean k_{eff}_Th	**0.140±0.004**							

Table notes: Converting S_a to effective k-values.

Ranges of alpha particles in calcite (ρ=2.71 g/cm^3) are from the software of 'The Stopping and Range of Ions in Matter' (SRIM version 2013). With the alpha ranges, alpha flux of U and Th in calcite are calculated:

Alpha flux for 1 ppm U in calcite: 18468 cm^{-2}*year^{-1}
Alpha flux for 1 ppm Th in calcite: 5166 cm^{-2}*year^{-1}

From conversion factors from Guérin et al. (2011):

Alpha dose rate for 1 ppm U: 2.795 Gy/ka
Alpha dose rate for 1 ppm Th: 0.7375 Gy/ka

Alpha dose rate of U = Alpha dose rate of U
$18468*0.92*S_a = 2.795*k_{eff}$_U
→ **k_{eff}_U = S_a/165**

Alpha dose rate of Th = Alpha dose rate of Th
$5166*0.96*S_a = 0.7375*k_{eff}$_Th
→ **k_{eff}_Th = S_a/149**

Note that the factors of 0.92 for U and 0.96 for Th in the left side of the equations are due to the difference between the alpha particle energy spectrum of the home-made alpha source in the University Bordeaux Montaigne and the alpha spectrum in nature. These two factors are simulated by Norbert Mercier from the University Bordeaux Montaigne.

Chapter 7: Conclusion & Outlook

The main part of this study, focussed on improving ^{230}Th/U-dating for flowstones. While the initial idea for this project was to use the standard procedure for the sampling, chemical separation of U and Th and measurement of the ^{230}Th/U-ages and create a high-resolution multi-proxy paleoclimate record, it became clear that either a high-resolution record will not be feasible, or significantly more effort will be necessary to create a reliable age chronology. The first attempt to improve the sampling precision and minimise detrital contamination of the sample powder was to use a MicroMill device. The ^{230}Th/U-ages obtained with this approach were the most precise, in terms of age uncertainty, obtained during this study. This highlights, that even if more time consuming, this sampling approach should more regularly be taken into consideration.

Due to the very narrow and uneven growth layers of the flowstones, especially sample BB-9, the sampling area was very limited, and it was often not possible to avoid detrital contamination even with the MicroMill. The LA approach solved this problem to some extent, however, the general limitations of the ^{230}Th/U-dating method were aggravated. The Bleßberg samples have a medium – high ^{238}U concentration between 0.3 – 0.5 µg/g and are old enough that a sufficient level of ^{230}Th is present. Therefore, only approximately 50 mg of sample material was needed to obtain very precise solution-based ^{230}Th/U-ages. However, the sample size is drastically reduced when using LA. The ages obtained with the in-situ LA approach were the most precise in terms of spatial resolution, however, the age uncertainty was larger by a factor of > 10 compared to the solution ages. This shows, that not only do the U and Th concentrations play an even more crucial role when using LA, but also that the LA ^{230}Th/U-ages alone will only very rarely produce a precise age model. Therefore, it greatly depends on the purposes of the study. If the goal is to test, if the ^{230}Th/U-method is generally applicable i.e., test for sufficient U and Th content or if the sample is out of range, LA ^{230}Th/U-dating is very useful. If the goal is to establish a first approximate on the age or if a precise age estimate is not needed to answer the research question, LA ^{230}Th/U-dating offers a cost efficient, less destructive, and fast possibility to do so. It is also possible to gain valuable information about the structure of the speleothem, potential U loss or gain, which will greatly affect the dating of the sample or the extent of hiatuses. A summary of parameters gained from one LA measurements (with two parallel line scans) is shown in Figure 7.1.

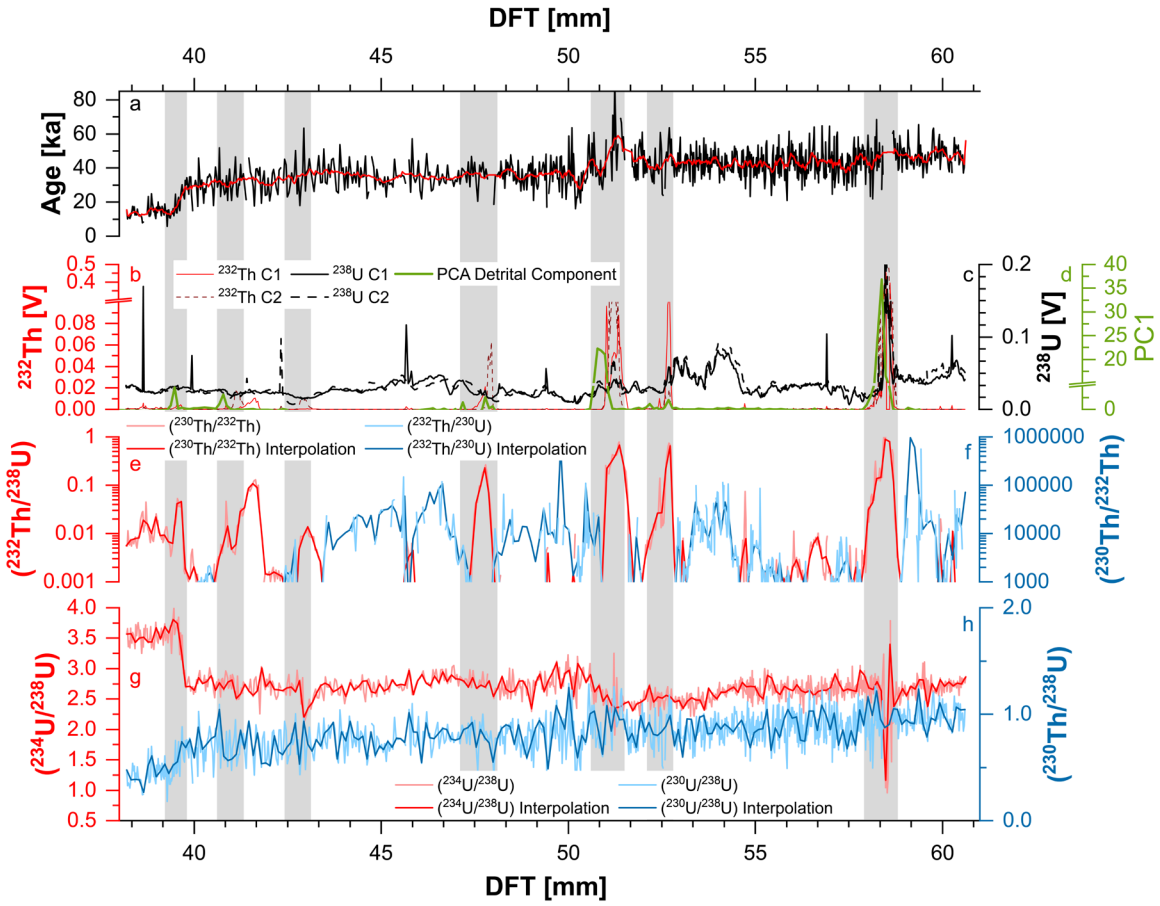

Fig. 7.1: Exemplary overview on several parameters and results obtained by continuous line scans LA ^{230}Th/U-dating. In a the final age chronology is shown in high-resolution (black) and smoothed (red). b and c showcased the variation between two cycles of measurements, e and f highlights the potential to identify hiatuses (high (^{232}Th/^{238}U) and low (^{230}Th/^{232}Th)) and their extent. The hiatuses are also indicated by the grey bars and the detrital component of a trace element PCA in d. g and h show the date obtained, which is needed for the final age calculations in a. This continuous record can also be used to calculate individual ^{230}Th/U-ages.

In this study, the LA approach was used to combine a large amount of unprecise LA ^{230}Th/U-ages in a very high spatial resolution (0.2 mm) with few, but precise solution-based ^{230}Th/U-ages. This approach proved to be very useful for samples of this type and it was possible to calculate precise age models for most of the individual growth layers of the flowstones. However, conventionally used methods for age-depth modelling do not work with this dating setup. Due to the characteristics of the flowstones a modified error-weighted linear regression model, was used for the age-depth modelling, but it will most likely be further adjusted for a larger variety of samples with other characteristics, e.g., samples where no linear growth rate can be assumed.

Another potential improvement of the method is regarding the measurement itself. Due to the low abundance of the decay products ^{234}U and ^{230}Th, the central ion counter was needed to monitor both isotopes Therefore, two separate line scans were necessary to

calculate ^{230}Th ages with the instrumental setup during this study. The effect is visible in Fig.7.1 b and c, which shows the data from both line scans. A setup where a parallel measurement is possible could therefore significantly improve the method.

The paleoclimate records obtained during this study are very promising. The flowstones are very sensitive to even centennial- to millennial-scale climate oscillations., which allows to investigate the internal structure of events, in addition to general climatic trends and developments.

The MIS 3 record established during this study proved that the climate conditions in Central Europe were favourable for speleothem growth throughout the entire MIS. While the early phase of MIS 3 (and especially DO14) was clearly the most humid, several growth phases during the mid and late MIS 3 were recorded as well. A lag to the DO onset recorded in the Greenland ice cores is evident for most of the Bleßberg growth phases. Surprisingly, an exception to this observation is, for instance, the growth phases coinciding with DO event 8 and 12, which occurred after the Heinrich events 4 and 5. Kindler et al. (2014) described a slight long-term, more gradual warming prior to the onset of the warm event in Greenland, rather than the rapid warming typical for the events. While the Bleßberg record cannot provide DO structure-like proxy records, they are very sensitive to changes in the North Atlantic and the growth phases were therefore established as a proxy for Central European warm phases during MIS 3.

The late Glacial and Holocene records further support the general observation, that the Bleßberg Cave record has the potential to precisely reconstruct several short-term events and their internal structure. This part of the study has, however, still many options to be improved, which was already discussed in Chapter 5.7.

This thesis highlights the importance and potential of combining the standard solution-based approach of ^{230}Th/U-dating with LA techniques. It allows for a fast data acquisition and less destructive sampling in a very high resolution, which can be a valuable and powerful tool to use on samples, where the spatial resolution will not allow more than the sampling for one or two solution-based ^{230}Th/U-ages. By combining these methods, it is possible to create precise age models for samples like the Bleßberg flowstones, which would not have been possible without the addition of the LA techniques.

7.1 References

Kindler, P., Guillevic, M., Baumgartner, M., Schwander, J., Landais, A. and Leuenberger, M., 2014. Temperature reconstruction from 10 to 120 kyr b2k from the NGRIP ice core. Clim. Past, 10(2): 887-902.

Acknowledgements